UNIVERSITÉ DENIS DIDEROT

Paris VII

THÈSE

presentée par

Mohammad Ijaz AYYAZ

pour obtenir
le titre de Docteur de l'Université de Paris VII
(Spécialité Physique et Technologie des Grands Instruments)

SUJET

Measurement of the Proton Structure Function $F_2(x, Q^2)$ at low x and low Q^2 with the H1 Detector at HERA.

Soutenue le 24 juin 1999 devant le jury composé de:

M.	Banner	
U.	Bassler	
M.-C.	Cousinou	
C.	Guyot	Rapporteur
M.	Jaffre	Rapporteur
F.	Vannucci	Président

Resumé

Dans cette thèse la mesure de la fonction de structure du proton $F_2(x, Q^2)$ est présentée, effectuée avec les données prises en 1995 par l'expérience H1 auprès du collisionneur HERA dans le domaine cinématique de $10^{-5} \leq x \leq 10^{-2}$ et de $0.85 \leq Q^2 \leq 20\ GeV^2$. Cette mesure est faite avec les premières données prises après que les détecteurs "arrières" de H1 aient été améliorés, avec l'installation d'un calorimètre de type SpaCal, et l'adjonction d'une chambre à dérive à 4 plans, la BDC. Ces deux détecteurs et leurs performances sont décrits en détail en parallèle avec les autres sous-détecteurs utilisés dans l'analyse. De nouvelles techniques d'analyse concernant la calibration, la reconstruction cinématique et la suppression du bruit dans le SpaCal sont présentées. Les résultats obtenus sur F_2 sont en bon accord avec les mesures précédentes faites à HERA, et ont une précision meilleure dans la région de Q^2 entre 3 et 10 GeV^2, dans laquelle le régime perturbatif de la Chromodynamique Quantique est atteint. La validité des équations d'évolution à l'ordre "Next-to-Leading" de la QCD est montré.

Abstract

In this thesis the measurement of the proton structure function $F_2(x, Q^2)$ is presented in the kinematic domain of $10^{-5} \leq x \leq 10^{-2}$ and of $0.85 \leq Q^2 \leq 20\ GeV^2$ with the H1 experiment at the electron-proton collider HERA using data taken during the year 1995. This measurement is done with the first H1 data after the "backward" detectors were upgraded with a new calorimeter of the SpaCal type, and a new drift chamber (BDC) in front of it. Both these detectors and their performances are described in detail along with the other detector components used in the analysis. New analysis techniques are presented, concerning the calibration, the kinematic reconstruction and the noise suppression in the SpaCal calorimeter. The F_2 results are in good agreement with previous HERA data, and have an improved precision in the region of Q^2 between 3 and 10 GeV^2, in which the perturbative regime of QCD is reached. The validity of Next to Leading Order QCD to explain the rise at low x of the F_2 proton cross-section is shown.

Introduction

The most direct way to study the structure of the nucleon consists in breaking up the proton by scattering energetic leptons off it. This type of interaction, called Deep Inelastic Scattering (DIS), revealed about thirty years ago the compositeness of the proton, and in the following its constituents: quarks and gluons and their interaction, described by the theory of QuantumChromoDynamics (QCD). Until the early nineties, DIS experiments were performed in the fixed target mode by shooting electron, muon or neutrino beams on Hydrogen, Deuterium or, especially for neutrino scattering, on heavy targets like carbon or even lead, which allow not only to study the proton structure, but also the neutron structure and the different effects of their binding in the nucleon. From double differential cross-section measurements of these lepton-nucleon interactions, structure functions can be determined, which can be interpreted as the sum of the various quark densities in the nucleon and be linked by their evolution in the phase space to the gluon density. Although the evolution of the parton densities can be established in different models in one dimension of the phase space, precise experimental measurements are necessary to determine their shape and to verify the validity of different assumptions made by the various models.

With HERA (Hadron-Electron Ring Accelerator) at DESY (Deutsches Electronen SYnchrotron) a collider of leptons and hadrons was built for the first time: in 1992 the first collisions between 26.7 GeV electrons and 820 GeV hadrons were performed and observed by the H1 and ZEUS experiments. The increase of the center of mass energy $\sqrt{s} \simeq 300\ GeV$, obtained by the collider mode, presents an important increase in the kinematic region accessible for the proton structure studies. Figure 0.1 shows a comparison of the accessible regions between HERA and various fixed target experiments in the two kinematic variables, mostly used for the description of the proton structure: x, the fractional momentum of the struck quark in the infinite momentum frame of the proton, and Q^2, the squared momentum transfer between the scattered lepton and the proton. HERA allowed to extend the measurement of the proton structure towards low x and at high Q^2, by roughly three orders of magnitude. In 1992, the first year of operation of HERA, the rise of the structure function F_2 with decreasing x was established and related to an increase of the gluon density. In the following years, the increase in luminosity allowed for a more precise quantification of this effect, as well as for the study of consequent predictions for exclusive processes, as for example the contribution from charm production to the structure function.

In 1995, the H1 collaboration replaced detector components in the backward re-

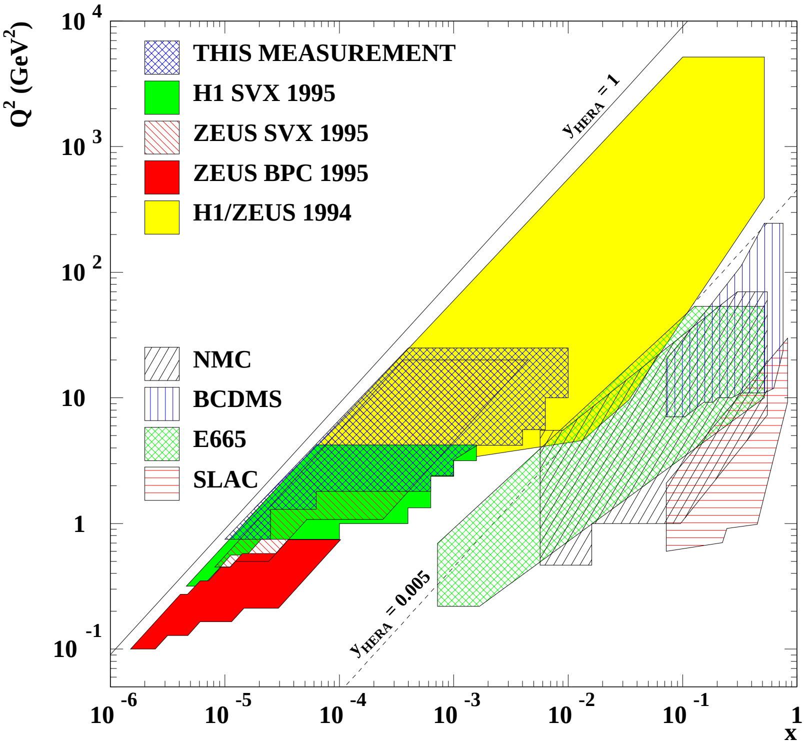

Figure 0.1: *Kinematic plane of the accessible region for Proton Structure Function measurements comparing HERA and various fixed target experiments.*

gion [1], which is the most relevant region for the detection of the scattered electron at low x and low Q^2, by a Backward Drift Chamber (BDC) and a SpaCal Calorimeter, allowing for an extension of the measurable kinematic region towards lower x and lower Q^2. Most of the 1995 running was devoted to the commissioning of these new subdetectors, but enough data was taken in order to improve the previous measurements in the region of Q^2 between 1 and 10 GeV^2, which will be described in this thesis. A period of data taking was devoted in 1995 to explore the region down to $Q^2 = 0.35\ GeV^2$, by shifting the interaction vertex in the proton beam direction. These two measurements allowed for a more precise description of the transition region between real photon exchange (photoproduction) and virtual photon exchange (DIS), in which the breakdown of the validity of perturbative developments of QCD is expected.

After a brief description of the theoretical background of Deep Inelastic Scattering in chapter 1, the experimental setup is presented in chapter 2. The various steps of the event selection (chapter 3), the calibration and correction procedures used for the cross-section measurement (chapter 4) are discussed. The chapter 5 is devoted to the F_2 measurement and to a brief interpretation of the results.

---

[1] At HERA, the positive z-axis is defined in the direction of the proton beam.

Contents

Chapter 1

Deep Inelastic Scattering and F_2

Deep inelastic scattering (DIS) of electrons off protons has revealed in the late sixties the partonic structure of the proton [1, 2, 3]: the scattering can in fact be thought of as between the electron and one of the constituents of the proton. The structure of the proton is translated into measurable quantities called the structure functions. From these functions one can study different properties as the composition and the behaviour of the proton constituents. QuantumChromoDynamics (QCD) describes the so called "strong interaction" among these constituents. The perturbative development of QCD (pQCD) can be tested by measuring the structure functions in different kinematic regions and studying their variations.

This chapter presents the definition of the structure functions from the cross section and their interpretation in the Quark Parton Model (QPM) and in pQCD. In section 1.1 the event kinematics are defined. In section 1.2 the structure functions and their relation to the cross section are presented. In section 1.3 the interpretation of the structure functions in the framework of the QPM is developed. Section 1.4 establishes the DGLAP evolution equations of the parton densities in the QCD frame. In section 1.5 the QCD fits to the structure functions are discussed along with parameterization schemes of the parton densities. In section 1.6 models describing the transition between photoproduction and DIS are presented.

1.1 The Kinematics of Deep Inelastic Scattering

The deep inelastic scattering of an electron off a proton can be described at the lowest order by the diagram in figure 1.1. An incident electron of 4-momentum $k(E, 0, 0, \sqrt{E^2 - m_e^2})$ interacts with a proton of 4-momentum $p(E_p, 0, 0, -\sqrt{E_p^2 - m_p^2})$. At HERA, the energy of the incoming electron and proton is $E = 27.6\ GeV$ and $E_p = 820\ GeV$ respectively, so we can neglect the masses of the particles in the following. In neutral current events the electron and the proton exchange a boson γ or Z^o with 4-momentum $q(\nu, \vec{q})$. After the scattering, the 4-momentum of the electron can be written as $k'(E', \vec{k}')$, while the proton generally breaks up in several particles, forming the hadronic final state X. In charged current events, the outgoing lepton is a neutrino and the exchanged particle a charged W boson.

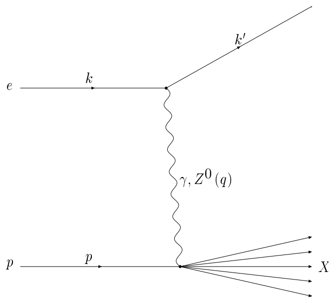

Figure 1.1: *Diagram for DIS ep-scattering.*

We define three Lorenz invariant quantities Q^2, x and y in order to describe the interaction, as

$$Q^2 = -q^2 = -(k-k')^2 \tag{1.1}$$

$$x = Q^2/2p.q \tag{1.2}$$

$$y = p.q/p.k \tag{1.3}$$

In DIS, the boson propagator is always space-like, therefore, we define a positive quantity Q^2, the squared momentum transfer, as the virtuality of the exchanged boson. As the Z and the W bosons are massive, their exchange is only relevant at large Q^2 (of the order of $M^2 \sim 10^4\ GeV^2$) and not treated in the following, since the measurement takes place at $Q^2 \sim 10\ GeV^2$. The influence of the Z exchange on the F_2 structure function is about 1% at $Q^2 \sim 1000 GeV^2$. x is the Bjorken variable, which can be interpreted in the frame of infinite momentum of the proton, as the fractional proton momentum carried by the struck quark. The third quantity y, usually termed as inelasticity, is the fractional electron energy carried by the virtual photon in the proton rest frame. Further two useful quantities are defined as,

$$s = (k+p)^2 \tag{1.4}$$

$$W^2 = (q+p)^2 \tag{1.5}$$

s, the total ep center of mass energy squared, is characteristic of the accelerator and the hadronic final state mass W, is the total $\gamma^* p$ center of mass energy. Using the 4-momentum of the incoming particles and neglecting the masses of the electron m_e and the proton m_p, s becomes

$$s = 4EE_p \tag{1.6}$$

leading to a center of mass energy $\sqrt{s}$ of about 300 GeV which is related to the other kinematic variables by

$$Q^2 = sxy \tag{1.7}$$

Within this approximation we obtain W^2 as,

$$W^2 = \frac{(1-x)}{x} Q^2 \tag{1.8}$$

1.2 The Inclusive Cross-Section and the Structure Functions

The double differential cross section for DIS of non-polarized electrons and protons (ep) exchanging a photon is given by [4, 5]

$$\frac{d^2\sigma}{d\Omega dE'} = \frac{\alpha^2}{Q^4}(\frac{E'}{E})L^{\mu\nu}W_{\mu\nu} \tag{1.9}$$

Here $\alpha = \frac{e^2}{4\pi}$ is the electromagnetic coupling constant. The angular phase space of the scattered electron is described by $d\Omega$, i.e.

$$d\Omega = \sin\theta d\theta d\phi \tag{1.10}$$

The leptonic tensor $L^{\mu\nu}$ describes the electron-photon interaction and is completely known following the point-like nature of the electron. It is given by

$$L_{\mu\nu} \equiv \frac{1}{2}tr(\not{k}'\gamma_\mu \not{k}\gamma_\nu) = 2(k_\mu k'_\nu + k'_\mu k_\nu + \frac{q^2}{2}g_{\mu\nu}) \tag{1.11}$$

for an electromagnetic interaction of a non-polarized spin 1/2 particle. Here γ are the four 4×4 Dirac matrices and $g_{\mu\nu}$ is the completely symmetric tensor. The hadronic tensor $W_{\mu\nu}$ describes the boson-proton interaction. Its form is not known exactly, since the proton has a complex structure. It is given in terms of the hadronic current operators $J_\mu(x)$ as,

$$W_{\mu\nu}(p,q) = \frac{1}{4m_p}\int\frac{d^4x}{2\pi}e^{iq.x} < p|J_\mu(x)J_\nu(0)|p > \tag{1.12}$$

with the proton mass m_p. Using the arguments of Lorenz invariance and current conservation, the tensor can be constructed in the most generalized form, from two available 4-vectors p^μ and q^ν, the symmetric tensor $g^{\mu\nu}$, the asymmetric tensor $\epsilon^{\mu\nu\alpha\beta}$ and scalars functions which only depend upon the independent scalar variables $p \cdot q$ and Q^2. This leads to the following expression,

$$W_{\mu\nu}(p,q) = F_1(x,Q^2)(-g_{\mu\nu} - \frac{q_\mu q_\nu}{Q^2}) + F_2(x,Q^2)\frac{P_\mu P_\nu}{p.q} - iF_3(x,Q^2)\epsilon_{\mu\nu\alpha\beta}\frac{p^\alpha q^\beta}{p.q} \tag{1.13}$$

With a modified vector P_μ defined as,

$$P^\mu \equiv p^\mu + \frac{p \cdot q}{Q^2}q^\mu \tag{1.14}$$

The hadronic tensor contains three unknown scalar functions F_1, F_2 and F_3, termed as structure functions. At large Q^2 ($\sqrt{Q^2} >> 1/D$, with the proton size $D \sim 3GeV^{-1}$), the structure functions F_1 and F_2 describe the density of the constituents (called partons, assuming that the proton has a substructure) and their momentum inside the proton [6]. They correspond to the elastic form factors in the low Q^2 limit.

The F_3 structure function is vanishing for purely electromagetic interactions, as the leptonic tensor does not contain an asymetric component, which must be added when taking into account the Z exchange, where also the weak contribution to F_2 must be considered [7]. Substituting these tensors in the cross section expression, one arrives at

$$\frac{d^2\sigma^{e^\pm p}}{dxdQ^2} = \frac{4\pi\alpha^2}{xQ^4}[y^2xF_1(x,Q^2) + (1-y)F_2(x,Q^2)] \tag{1.15}$$

Considering only the virtual photon exchange, the process $ep \to e'X$ can be factorized in two parts $e \to e'\gamma^*$ and $\gamma^*p \to X$. The aim of using the electron as a beam is in fact to get a virtual photon which probes the structure of the proton. The total cross section for the later process is:

$$\sigma^{tot}(\gamma^*p \to X) = \sum_\lambda \frac{8\pi^2\alpha M}{W^2 - M^2}\epsilon_\lambda^{\mu *}\epsilon_\lambda^\nu W_{\mu\nu} \tag{1.16}$$

with ϵ_λ^μ being the polarization vector of photon and λ its helicity which contrary to a real photon can have both longitudinal ($\lambda = 0$) and transverse ($\lambda = \pm 1$) components. The cross-section can be decomposed as

$$\sigma^{tot} = \sigma_T + \sigma_L \tag{1.17}$$

Putting the explicit form of the polarization vectors and substituting the expression of $W_{\mu\nu}$ from equation 1.13, the two parts can be written in terms of structure functions,

$$\sigma_T = \sigma_{\lambda=+1} + \sigma_{\lambda=-1} = \frac{4\pi^2\alpha}{Q^2(1-x)} \cdot 2xF_1(x,Q^2) \tag{1.18}$$

$$\sigma_L = \sigma_{\lambda=0} = \frac{4\pi^2\alpha}{Q^2(1-x)}[F_2(x,Q^2) - 2xF_1(x,Q^2)] \tag{1.19}$$

Based on the helicity of the virtual photon, the longitudinal and transverse structure functions of the proton are defined as,

$$F_L(x,Q^2) \equiv F_2(x,Q^2) - 2xF_1(x,Q^2) \tag{1.20}$$

$$F_T(x,Q^2) \equiv 2xF_1(x,Q^2) \tag{1.21}$$

1.3 The Quark Parton Model and the Quark Momentum Distribution Functions

In a system in which the proton is moving with an infinite momentum, the partons find no time available for mutual interactions during the scattering and the proton can be simply pictured as being made up of free massless partons [6]. This picture is called the Quark-Parton Model (QPM), which leads to an simple interpretation of the structure functions in terms of parton densities. Using the Feynman rules, the double differential cross section for an electromagnetic interaction between an electron and the i^{th} pointlike parton of spin 1/2, called quark, carrying a momentum fraction ω $(0 \leq \omega \leq 1)$ of the proton is given by

$$\frac{d^2\sigma_i}{dxdQ^2} = \frac{4\pi\alpha^2}{Q^4} e_i^2 \frac{1}{2}[1 + (1-y)^2]\delta(x-\omega) \tag{1.22}$$

The presence of the Dirac function δ in this cross section, gives a physical meaning to the variables x, as being the momentum fraction carried by the struck quark. If $d\omega f_i(\omega)$ is the probability of finding the i^{th} struck quark in the proton carrying a momentum fraction between ω and $\omega + d\omega$, then the total electron proton scattering cross section will be:

$$\frac{d^2\sigma}{dxdQ^2} = \sum_i \int_0^1 d\omega f_i(\omega) \frac{d^2\sigma_i}{dxdQ^2} \tag{1.23}$$

This factorization of the cross section is only possible for the quark-parton model, where no interaction occurs between the partons. Comparing equations 1.15 and 1.23 we obtain after integrating the δ function, the proton structure functions as being

$$F_1(x, Q^2) = \frac{1}{2} \sum_i e_i^2 f_i(x, Q^2) \tag{1.24}$$

$$F_2(x, Q^2) = \sum_i e_i^2 x f_i(x, Q^2) \tag{1.25}$$

which expresses the structure functions as the weighted sums of the density of all quark i, carrying a fractional momentum x. From the last two equations, we get

$$F_2(x, Q^2) = 2xF_1(x, Q^2) \Rightarrow F_L(x, Q^2) = 0 \Rightarrow \sigma_L = 0 \tag{1.26}$$

which is known as the Callan-Gross relation [8]. Moreover in the quark-parton model, the longitudinal photon cross section vanishes, which means, as the photon is strongly virtual that the partons do not carry any transverse momentum.

However, from the structure functions which are measured experimentally, one can estimate the quark momentum distribution functions and quantify the momentum carried by spin 1/2 partons in the proton. Combining the results from different experiments one finds [9]

$$\sum_q \int_0^1 dx x(q(x) + \overline{q}(x)) = 0.45 \tag{1.27}$$

where $q + \bar{q} = f_i$ for all the different quark and antiquark flavors. This fact (i.e. the right-hand-side is not equal to one) suggests that there are not only spin-1/2 partons in the proton, as only a fraction of the momentum (45%) is carried by them. In the following, we will see, that the remaining proton momentum is carried by the gluons, which are the bosons of the color interactions between the quarks, and which are neglected in the QPM.

1.4 Structure Functions in QCD

In the QPM, the proton contains only spin-1/2 non-interacting partons, the quarks. In QCD, the quarks can have three different "colors" (a more complex type of charge than in Quantum Electrodynamics) and are interacting by exchanging non-abelian gauge bosons called gluons. The strength of the interaction is determined by the strong coupling constant α_s, in a similar way as the coupling constant α in QED, but unlike α in QED, α_s decreases with increasing Q^2. This means that the strong interaction gets "weaker", the smaller the distance in between quarks, leading to "asymptotic freedom" for sufficiently high Q^2. Contrarily to the photon, which is electrically neutral, the gluon by itself carries color which arises from the non-abelian structure of the color field and therefore interacts with other gluons. The inclusion of gluons in calculating the structure functions is described in this section, from which the evolution equations are derived.

1.4.1 *ep*-Interactions at the Order α_s

Figure 1.2 shows the main diagrams which have to be taken into account for the cross-section calculation of the DIS process up to the first order in α_S. The diagram in figure 1.2*a* corresponds to the Born diagram. Taking into account the interactions

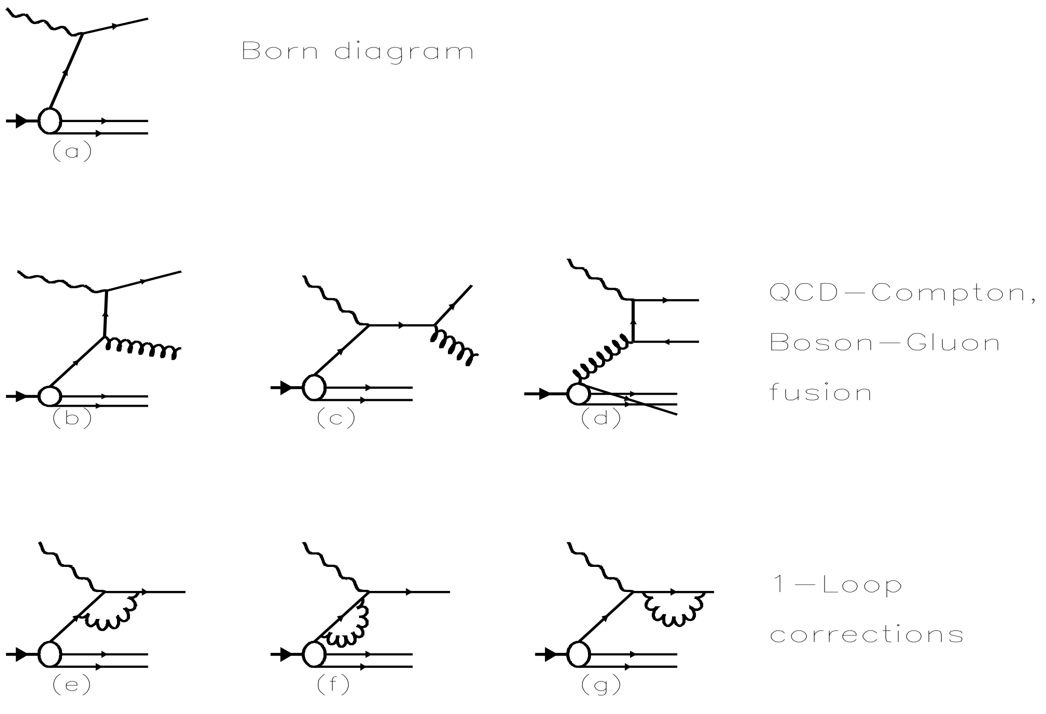

Figure 1.2: *Different processes up to the first order in α_s contributing to the matrix element calculation.*

at the first order of α_s, we have to consider the diagrams 1.2 $b-g$. The diagrams 1.2 b, c correspond to the QCD-Compton processes, where a gluon is radiated before or after the interaction with the photon, where as the diagram 1.2 d shows the interaction via photon gluon fusion. In figure 1.2 $e-g$, the virtual 1-loop corrections are pictured, which have to be taken into account in the cross-section calculation.

From equation 1.13, and using the definition of the longitudinal structure function given in equation 1.20, the structure functions F_2 and F_L can be expressed as function of the hadronic tensor $W_{\mu\nu}$ as

$$\begin{aligned} \frac{F_2(x,Q^2)}{x} &= \left(-g^{\mu\nu} + 3Q^2\frac{p^\mu p^\nu}{(p.q)^2}\right) W_{\mu\nu} \\ \frac{F_L(x,Q^2)}{x} &= -2Q^2\frac{p^\mu p^\nu}{(p.q)^2} W_{\mu\nu} \end{aligned} \tag{1.28}$$

Equation 1.12 can be written in momentum space and for the electron quark scattering where a struck quark carries the momentum fraction ω of the proton, as

$$\widetilde{W}_{\mu\nu}(\omega) = \frac{2\pi^3}{4\omega M}\sum_n \int \prod_{i=1}^{n}[\frac{d^3p_i}{(2\pi)^3 2p_{i0}}] < \omega p|J_\mu^\dagger(0)|n >< n|J_\nu(0)|\omega p > \delta^4(p_n - \omega p - q) \tag{1.29}$$

The tilde over $W_{\mu\nu}$ differentiates the partonic tensor from the hadronic tensor. Here the phase space is for n-final state particles, the δ function expresses the 4-momentum conservation at the vertex and the matrix elements describe the transition amplitude from the initial parton p carrying the momentum fraction ω to n final partons.

First we consider the QCD-Compton process $\gamma^*(q) + q(\omega p) \to q(p') + g(k)$ (figure 1.2 b, c) for its contribution to F_2. For this process in which we have two final state particles, d(PS) is given by the phase space along with the δ function

$$d(PS) = \frac{d^3p'}{(2\pi)^3 2p'_0}\frac{d^3k}{(2\pi)^3 2k_0}\delta^4(p' + k - \omega p - q) \tag{1.30}$$

The matrix elements are calculated using the Feynman rules for figure 1.2 b, c. We introduce the Lorenz invariant quantities for partons as

$$\hat{s} = (p+q)^2, \qquad \hat{t} = (p'-q)^2, \qquad \hat{u} = (p'-p)^2. \tag{1.31}$$

Integrating out the delta function and the azimuthal angle, the phase space reduces to just one single variable $\hat{t}$. After some calculations using the equations 1.28 and 1.29, the contribution to F_2 from the QCD-Compton process terms of invariant variables $\hat{s}$, $\hat{t}$ and $\hat{u}$ is found to be

$$\frac{\widetilde{F}_2^{q,r}(\omega)}{x} = \frac{2\alpha_s}{3\pi}\int_0^{t_{max}} \frac{d\hat{t}}{\hat{s}+Q^2}\left(-\frac{\hat{t}}{\hat{s}} - \frac{\hat{s}}{\hat{t}} + \frac{2\hat{u}Q^2}{\hat{s}\hat{t}} - \frac{6x^2}{\omega^2}\frac{\hat{u}}{Q^2}\right) \tag{1.32}$$

In this expression tilde means the partonic F_2, the superscript q indicates the quark-photon interaction and r the radiation of real gluon before or after the interaction with the photon. The lower limit of the integration is zero and the integral is diverging at this limit. This arises because we have given the real gluon a zero mass. Associating a non zero mass m to gluon prevents the divergence and we can absorb this mass in the definition of the bare quark momentum distribution in the end of our calculations. This way of renormalization is known as the gluon mass regularization (MG) scheme, though there exist other schemes like the dimensional regularization scheme (DR) [9].

To get the proton structure function F_2, we must convolute the partonic $\widetilde{F}_2$ structure functions as

$$\frac{F_2(x,Q^2)}{x} = \sum_q e_q^2 \int d\omega q(\omega) \frac{\widetilde{F}_2(\omega)}{\omega} \tag{1.33}$$

By introducing $z = \frac{x}{\omega}$ and integrating over $\widehat{t}$, we get

$$\begin{aligned}\frac{F_2^{q,r}}{x} = \sum_q e_q^2 \int_x^1 \frac{dz}{z} q\left(\frac{x}{z}\right) \Bigg[\frac{\alpha_s}{2\pi}\left\{\frac{4}{3}\frac{1+z^2}{1-z}\log\left(\frac{Q^2}{m^2}\right)\right\} + \frac{2\alpha_s}{3\pi}\Bigg\{\frac{1+z^2}{1-z}\log(1-z) \\ + \frac{1+z^2}{1-z}(-2\log(z)) - \frac{3}{2}\frac{1}{1-z} + 4z + 1 + \frac{5}{4}\delta(1-z)\Bigg\}\Bigg] \end{aligned} \tag{1.34}$$

In this equation the integral is independent from the regularization scheme, whereas the multiplicative term of $\frac{2\alpha_s}{3\pi}$ is only a function of z and depends on the regularization scheme, besides its process dependence. In order to distinguish among the different schemes and different processes, we put subscripts and superscripts, and call this term for the case of the gluon radiation $f^{q,r}_{F_2,MG}$. The coefficient function $\frac{4}{3}\frac{1+z^2}{1-z}$ of $\log(\frac{Q^2}{m^2})$ however is independent of any scheme of regularization and is a universal function that appears whenever a quark radiates a gluon. We call it the splitting function and denote it as $P^r_{qq}(z)$, where the superscript r specifies the real gluon emission contribution, and represents the probability of finding a quark q, which reduced its momentum fraction x by the fraction z after the emission of a gluon (figure 1.3 a). We note the singularities at $z = 1$, the upper limit of integration, for both $P^r_{qq}(z)$ and $f^{q,r}_{F_2,MG}$, however these singularities will cancel by the inclusion of the virtual gluon emission contributions $P^v_{qq}(z)$ and $f^{q,v}_{F_2,MG}$ (figures 1.2 e, f, g) as we will see in following. So the real gluon emission from the quark adds to F_2 as,

$$\frac{F_2^{q,r}}{x} = \sum_q e_q^2 \int_x^1 \frac{dz}{z} q\left(\frac{x}{z}\right) \left(\frac{\alpha_s}{2\pi} P^r_{qq}(z) \log\left(\frac{Q^2}{m^2}\right) + \alpha_s f^{q,r}_{F_2,MG}\right) \tag{1.35}$$

If we calculate the virtual gluon contribution (figures 1.2 e, f, g), we get the following expression for the radiative (r) and the loop (v) contribution,

$$\begin{aligned}\frac{F_2^q}{x} &= \frac{F_2^{q,r}}{x} + \frac{F_2^{q,v}}{x} \\ &= \sum_q e_q^2 \int_x^1 \frac{dz}{z} q\left(\frac{x}{z}\right) \left(\frac{\alpha_s}{2\pi}\left[\left\{\frac{4}{3}\frac{1+z^2}{1-z} + (2 + \frac{8}{3}\log(\epsilon))\delta(1-z)\right\}\log(\frac{Q^2}{m^2})\right]\right.\end{aligned}$$

$$\begin{aligned} &+ \quad \frac{2\alpha_s}{3\pi}\Bigg[\Bigg\{\frac{1+z^2}{1-z}\log(1-z)+\frac{1}{2}\log^2(\epsilon)\delta(1-z)\Bigg\}+\frac{1+z^2}{1-z}(-2\log(z)) \\ &- \quad \frac{3}{2}\Bigg\{\frac{1}{1-z}-\log(\epsilon)\delta(1-z)\Bigg\}+4z+1-\left(\frac{2\pi^2}{3}+\frac{5}{4}\delta(1-z)\right)\Bigg]\Bigg) \end{aligned} \tag{1.36}$$

By looking at this expression, one finds that each singular term in braces has its counterpart, such that the integration over these individual sums vanishes. If we write the above equation in terms of P and f, the expression becomes

$$\frac{F_2^q}{x} = \sum_q e_q^2 \int_x^1 \frac{dz}{z} q\left(\frac{x}{z}\right)\left(\frac{\alpha_s}{2\pi}P_{qq}(z)\log(\frac{Q^2}{m^2}) + \alpha_s f^q_{F_2,MG}\right) \tag{1.37}$$

with

$$P_{qq}(z) = \left(\frac{4}{3}\frac{1+z^2}{1-z}\right)_+ \tag{1.38}$$

$$\begin{aligned} \alpha_s f^q_{F_2,MG} = \frac{2\alpha_s}{3\pi}\Bigg\{&(1+z^2)\left(\frac{\log(1-z)}{1-z}\right)_+ + \frac{1+z^2}{1-z}(-2\log(z)) \\ &-\frac{3}{2}\frac{1}{(1-z)_+} + 4z + 1 + \frac{2\pi^2}{3} + \frac{5}{4}\delta(1-z)\Bigg\} \end{aligned} \tag{1.39}$$

The subscript + indicates that the corresponding functions are defined such that they do not contain the singularities and their integrals are always 0.

Finally the contribution from the photon-gluon fusion diagram 1.2 *d* is given by

$$\frac{F_2^g(x,Q^2)}{x} = 2\sum_q e_q^2 \int_0^1 \frac{d\omega}{\omega}\Bigg\{\frac{\alpha_s}{2\pi}P_{qg}(z)\log\left(\frac{Q^2}{m^2}\right) + \alpha_s f^g_{F_2}(z)\Bigg\} \tag{1.40}$$

Where the splitting function $P_{qg} = \frac{1}{2}(z^2 + (1-z)^2)$ corresponds to the annihilation of a gluon into a quark-antiquark pair (figure 1.3 c), and the function f is

$$\alpha_s f^g_{F_2,MG}(z) = \frac{\alpha_s}{2\pi}\Bigg\{-2P_{qg}(z)\log(z) - 1 + 3z - 3z^2\Bigg\} \tag{1.41}$$

Four splitting functions can be defined, as pictured in figure 1.3 The two splitting functions, corresponding to the diagrams *b* and *d* of figure 1.3, can be computed in a similar way and have the following expressions:

$$\begin{aligned} P_{gq}(z) &= \frac{4}{3}\frac{1+(1-z)^2}{z} \\ P_{gg}(z) &= 6\left[\frac{z}{(1-z)_+} + \frac{1-z}{z} + \frac{11-\frac{2}{3}n_f}{12}\delta(1-z)\right] \end{aligned} \tag{1.42}$$

where n_f is the number of the flavors, which must be considered for the evaluation of the triple gluon vertex for the P_{gg} splitting function. The P_{gq} splitting function corresponds to a quark emitted by a quark transforming to a gluon.

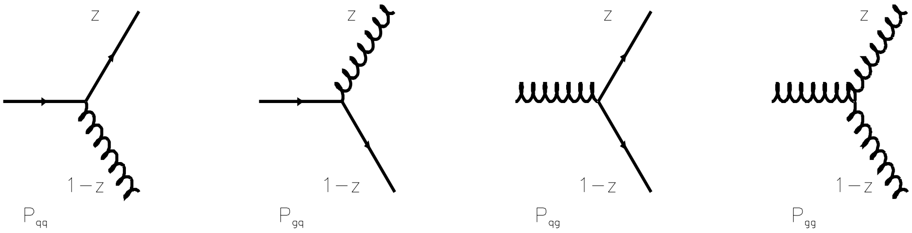

Figure 1.3: *Different processes corresponding to the four splitting functions.*

The structure function F_2 up to the order α_s is obtained by adding F_2^i from all the diagrams of the figure 1.2. Thus by adding equations 1.25, 1.37 and 1.40 we obtain the following expression for F_2,

$$\begin{aligned}
\frac{F_2(x,Q^2)}{x} &= \frac{F_2^{born}(x,Q^2)}{x} + \frac{F_2^q(x,Q^2)}{x} + \frac{F_2^g(x,Q^2)}{x} \\
&= \sum e_q^2 \int_x^1 \frac{dz}{z}\left(q\left(\frac{x}{z}\right) + \overline{q}\left(\frac{x}{z}\right)\right)\left[\delta(1-z) + \frac{\alpha_s}{2\pi}P_{qq}(z)\log\left(\frac{Q^2}{m^2}\right) + \alpha_s f^q_{MG,F_2}(z)\right] \\
&\quad +2\sum e_q^2 \int_0^1 \frac{dz}{z} g\left(\frac{x}{z}\right) x \left[\frac{\alpha_s}{2\pi}P_{qg}(z)\log\left(\frac{Q^2}{m^2}\right) + \alpha_s f^g_{MG,F_2}(z)\right] \qquad (1.43)
\end{aligned}$$

Here g is the gluon density of the proton. In a similar way, the longitudinal structure function F_L is

$$\begin{aligned}
F_L(x,Q^2) &= \frac{F_L^{born}(x,Q^2)}{x} + \frac{F_L^q(x,Q^2)}{x} + \frac{F_L^g(x,Q^2)}{x} \\
&= \sum_q e_q^2 \int_x^1 \frac{dz}{z^3}\left(q\left(\frac{x}{z}\right) + \overline{q}\left(\frac{x}{z}\right)\right)\left[\alpha_s f^q_{F_L,MG}(z) + \alpha_s f^g_{F_L,MG}(z)\right] \qquad (1.44)
\end{aligned}$$

where the f functions are

$$\begin{aligned}
\alpha_s f^q_{F_L,MG}(z) &= \frac{2\alpha_s}{3\pi}2z \\
\alpha_s f^g_{F_L,MG}(z) &= \frac{\alpha_s}{2\pi}2z(1-z) \qquad (1.45)
\end{aligned}$$

The new Q^2 dependent quark distribution functions can be extracted from F_2 using the relation

$$F_2(Q^2,x) = \sum_q e_q^2 \left(q(x,Q^2) + \overline{q}(x,Q^2)\right) \qquad (1.46)$$

resulting in a integro-differential equation.

1.4.2 The DGLAP Evolution Equations

Although we cannot solve equation 1.46 for F_2 we can control the evolution of the parton distribution functions with respect of $\log(Q^2)$ with the help of the equation 1.43. The evolutions of the quark and gluon distribution function are more conveniently put in the double integro-differential equations, called the DGLAP equations after Dokshitzer, Gribov, Lipatov, Altarelli and Parisi [10] and are obtained from equations 1.43 and 1.46

$$\frac{\partial q(x,Q^2)}{\partial(\log Q^2)} = \frac{\alpha_s}{2\pi}(P_{qq} \otimes q + P_{qg} \otimes g) \tag{1.47}$$

$$\frac{\partial g(x,Q^2)}{\partial(\log Q^2)} = \frac{\alpha_s}{2\pi}(P_{gq} \otimes q + P_{gg} \otimes g) \tag{1.48}$$

Here $\otimes$ is defined as

$$P \otimes q = \int_x^1 \frac{dz}{z} P\left(\frac{x}{z}\right) q(z,Q^2) \tag{1.49}$$

Equations 1.47 and 1.48 can be described by diagrams *a* and *b* of figure 1.4 respectively. In a simplified way, we may say that

- the evolution of the quark density with Q^2 depends on the quark density before the emission of a gluon and the gluon density before creating a quark anti-quark pair
- the variation of the gluon density is coupled to the quark density before gluon emission and the gluon density at the triple gluon vertex itself.

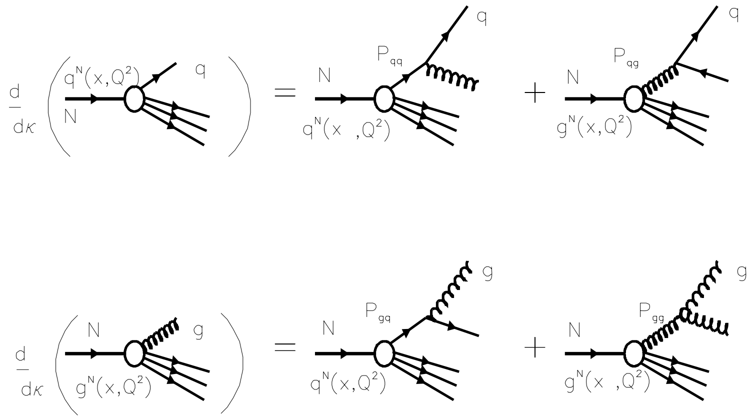

Figure 1.4: *DGLAP equations in leading order stating the rate of change of the quark and gluon distributions with respect to* κ *where* $\kappa = \frac{2}{11-\frac{2}{3}n_f}\log(\alpha(Q_o^2)/\alpha(Q^2))$.

1.4.3 The Leading-Log Approximation

The radiation of a single gluon is not the only process which contributes to the cross-section, multiple gluon radiation as pictured in figure 1.5, must also be considered. In order to compute these contribution we can use a perturbative development. In perturbative QCD, the processes are factorized in short-range phenomena, with $Q^2 > \mu^2_{fac}$, and long-range phenomena, $Q^2 < \mu^2_{fac}$. μ^2_{fac} is called the factorization scale and is chosen such as $\alpha_s(\mu^2_{fac})$ is sufficiently small to allow a perturbative development of the short-range processes.

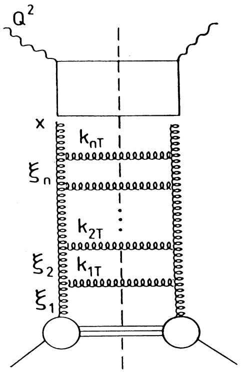

Figure 1.5: *Ladder diagram for multiple gluon radiation.*

Within this framework, F_2 can be expressed as a function of the parton densities as

$$F_2(x,Q^2) = \sum_{i=q,g} \int_0^1 d\xi C_i\left(\frac{x}{\xi}, \frac{Q^2}{\mu^2_{ren}}, \mu^2_{fac}, \alpha_s\right) q_i(\xi, \mu^2_{ren}, \mu^2_{fac}, \alpha_s) \tag{1.50}$$

where we sum over the quark and the gluon densities. The equation depends on two scales: the renormalization scale, which prevents ultraviolet divergences in which the momentum of virtual particles in 1-loop contributions gets infinite (similar to the mass regularization in section 1.4.1 and the factorization scale μ^2_{fac}, which defines the separation into short-range and long-range contribution. In the case of the gluon ladder, gluons emitted with $k_T^2 > \mu^2_{fac}$ will contribute in the coefficient function and be computed in the perturbative development, whereas gluons emitted at $k_T^2 < \mu^2_{fac}$ can not be computed perturbatively and contribute to the parton densities. Due to the factorization scale, the coefficient functions are infra-red stable, which means they will not contain singularities from gluons emitted collinearly.

In order to compute the coefficient functions, only the gluon ladders, being the dominant processes are included. The emitted gluons are supposed to be ordered in longitudinal momentum

$$\xi_1 > \xi_2 > \xi_3 > ...... > \xi_n > x \tag{1.51}$$

and strongly ordered in transverse momentum

$$Q^2 >> k^2_{nT} >> ... >> k^2_{2T} >> k^2_{1T} \tag{1.52}$$

In the leading-log approximation (LLA), only the dominating terms contributing as ${\alpha_s}^n(\log\frac{Q^2}{\Lambda^2})^n$ are considered. This is valid as long as

$$\alpha_s(k_{1T}^2)\log\left(\frac{Q^2}{k_T^2}\right)\sim 1 \tag{1.53}$$

$$\alpha_s(k_{1T}^2)\log\left(\frac{1}{x}\right)\ll 1 \tag{1.54}$$

In NLO, also the terms in $\alpha^{n+1}(\log\frac{Q^2}{\Lambda^2})^n$ are considered.

1.4.4 The Small-x Behaviour

At low x, the evolution of F_2 is driven by the gluon density and the evolution of the gluon density itself is dominated by the contribution from the triple gluon vertex, which leads to the approximation

$$\frac{dg(x,Q^2)}{d\log Q^2}\simeq\frac{\alpha_S}{2\pi}P_{gg}\otimes g \qquad \text{with} \qquad P_{gg}(z)\simeq\frac{6}{z} \tag{1.55}$$

After the derivation with respect to $\log 1/x$, this equation can be rewritten as

$$\frac{\partial^2(xg(x,Q^2)}{\partial\log 1/x\partial\log(\log(Q^2/Q_0^2)}=\frac{12}{\beta_0}xg(x,Q^2) \tag{1.56}$$

and can be solved exactly, leading to a double logarithmic scaling of the gluon density, as

$$xg(x,Q^2)\propto exp\sqrt{\frac{48}{\beta_0}\log\frac{1}{x}\log\left(\log\frac{Q^2}{Q_0^2}\right)} \tag{1.57}$$

The BFKL Equation

The leading log approximation is only valid under the assumption that

$$\alpha_s(Q^2)\log(1/x)\ll 1 \tag{1.58}$$

This condition is not fulfilled when x is becoming very small.
Therefore as $\alpha_s(Q^2)\log(1/x)\sim 1$, the BFKL equations (Balitski, Fadin, Kuraev and Lipatov) were proposed [11], where all the terms in $(\alpha_s\log(\frac{1}{x}))^n$ are summed. This approach needs strong ordering in x, i.e.,

$$x << x_n << ..... << x_2 << x_1 << x_0 \tag{1.59}$$

and weak ordering in transverse momenta

$$Q^2\geq k_T^2\geq k_{nT}^2\geq ...\geq k_{2T}^2\geq k_{1T}^2\geq Q_0^2. \tag{1.60}$$

As at low Q^2 the behaviour of the gluon is dominating the behaviour of F_2, the BFKL equation is describing the evolution of the gluon density with $\log(1/x)$, using the function f defined by the derivated gluon density

$$f(x,k^2) = \left.\frac{d(xg(x,Q^2))}{\log Q^2}\right|_{k^2=Q^2} \tag{1.61}$$

and the evolution with $\log(1/x)$ is given by

$$\frac{\partial f(x,k^2)}{\partial \log 1/x} = \frac{\partial f_0(x,k^2)}{\partial \log 1/x} + \frac{3\alpha_S}{\pi} k^2 \int dk'^2 K(k^2,k'^2) f(x,k') \tag{1.62}$$

where f_0 is a non-perturbative term describing the coupling of the gluon to the proton and K the kernel.

From the BFKL equations, the strong rise of F_2 with decreasing x can be derived by an approximative solution of this equation [12], leading to a divergent gluon density:

$$xg(x,Q^2) \propto x^{-\lambda} \qquad \text{with} \qquad \lambda = \frac{3\alpha_S}{\pi} 4\log(2) \sim 0.5 \qquad \text{at} \qquad \alpha_S = 0.2 \tag{1.63}$$

However recent calculation at the NLO [13] have given large corrections reducing the amount of gluons at low x, which are still under theoretical debate (see for example [14]).

In order to relate the behaviour of the gluon density to F_2, the k_T factorization theorem was developed [15], which can be pictured as seen in figure 1.6.

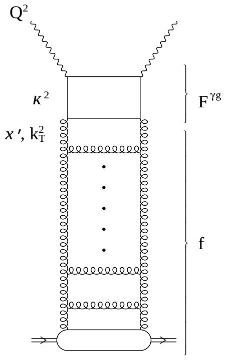

Figure 1.6: *Ladder diagram for multiple gluon radiation, indicating the k_T factorization.*

Within this framework, F_2 can be expressed as:

$$F_2 = F^{\gamma p} \otimes f + F^{np} \simeq \mathcal{C}(Q^2) x^{-\lambda_L} + F^{np} \tag{1.64}$$

where $F^{\gamma p}$ is the characterized by the photon-gluon fusion process convoluted to the derivated gluon density, $F^{np} \sim 0.4$ is a constant non-perturbative contribution at $x \leq 0.05$ and determined from the F_2 behaviour at $x \sim 0.1$ [16]. However, predictions on F_2, from the BFKL inspired models, show a similar behaviour than in the NLO-DGLAP formalism, whereas the prediction on F_L are about a factor of two lower.

1.5 QCD Fits and Parton Distributions

Equations 1.47 and 1.48 do not predict the parton distribution functions at some arbitrary Q^2, but for a given distribution functions at some initial Q_0^2 scale, the DGLAP equations evolve them to an arbitrary scale. QCD fits aim at extracting the parton densities of the proton and the value of α_s. They are derived from the measured F_2 values, and may also take into account other processes in which the parton densities intervene, for example the prompt photon production $pp \to \gamma X$, which depends on the gluon density at high x or the Drell-Yann production $pp \to l^+l^-X$, which is sensitive to the sea quark densities. The result of these fits allows to test pQCD and to predict the cross-sections in yet unmeasured kinematic regions. In order to perform a QCD fit, first the parton densities are parameterized as functions of x. They are then injected in the DGLAP equations (eqs 1.47 and 1.48) at a given value of Q_0^2 and evolved according to these equations in Q^2. The splitting functions P and the coefficient functions C have been computed to NLO. The theoretical F_2 computed from the parton densities, is then adjusted to the data, taking into account the constraints from the quark counting rule on the valance quark densities u_v and d_v

$$\int_0^1 u_v(x,Q^2)dx = \int_0^1 u(x,Q^2) - 2\bar{u}(x,Q^2)dx = 2 \tag{1.65}$$

$$\int_0^1 d_v(x,Q^2)dx = \int_0^1 d(x,Q^2) - 2\bar{d}(x,Q^2)dx = 1 \tag{1.66}$$

and from the momentum sum rule

$$\int_0^1 x(u_v + d_v + g + 2(u_s + d_s + s_s + c_s + b_s))dx = 1 \tag{1.67}$$

where the subscript s indicates the contribution from the sea-quarks. Various groups have performed QCD fits, differing in the chosen input data, the type of parton density parametrization and additional assumptions on parton densities. In the following, two of them are described in more detail.

1.5.1 The MRST Parametrization

In this parametrization due to Martin, Robert, Stirling and Thorne [17], the parton distribution functions are parameterized at a scale $Q_0^2 = 1GeV^2$ as

$$xu_v(x) = a_u x^{\alpha_u}(1-x)^{\beta_u}(1 + b_u\sqrt{x} + c_u x) \tag{1.68}$$

$$xd_v(x) = a_d x^{\alpha_d}(1-x)^{\beta_d}(1 + b_d\sqrt{x} + c_d x) \tag{1.69}$$

$$xS(x) = a_s x^{\alpha_s}(1-x)^{\beta_s}(1 + b_s\sqrt{x} + c_s x) \tag{1.70}$$

$$xg(x) = a_g x^{\alpha_g}(1-x)^{\beta_g}(1+c_g x) \tag{1.71}$$

with 3 active flavors u, d and s. S stands for the total sea quark density. The constraints put on the light sea quarks at $Q^2 = Q_0^2$ are

$$2\bar{u} = 0.4S - \Delta \tag{1.72}$$

$$2\bar{d} = 0.4S + \Delta \tag{1.73}$$

$$2\bar{s} = 0.2S \tag{1.74}$$

which means that the u and d quarks densities contributing t o the sea can be different by Δ and the strange contribution to the sea accounts for 20%. The c and b contributions are only generated above their threshold $Q^2 > m_q^2$ from boson-gluon fusion.

To obtain the parameters of the parton distribution functions, large amount of data points from different experiments i.e. H1, ZEUS, HERMES, BCDMS, NMC, E665 and SLAC was used to cover the maximum possible kinematic region. It was further required to satisfy the neutrino data constraints by comparing with the structure functions $F_2^{\nu n}$ and $xF_3^{\nu n}$ as measured by the CCFR experiment [18]. The parameterized gluon distribution was constrained by the prompt-photon production from the E706 experiment at $x \geq 10^{-3}$. Contrarily to the former parametrization [19] where the light sea was weakly constrained by a single measurement of $\bar{u} - \bar{d}$ at $x = 0.18$ from NA51 [20], the present parametrization is strongly constrained by the Drell-Yann production in the range $0.03 \leq x \leq 0.35$ from the E866 experiment [21]. The CDF measurement of the asymmetry of the rapidity distribution of the charged lepton from $W^{\pm} \to l^{\pm}\nu$ provides a tight constraint on the light valence ratio u/d [22]. The new more precise measurements of $F_2^{\mu p}$, $F_2^{\mu d}$ and $F_2^{\mu d}/F_2^{\mu p}$ by NMC constrains further the parton densities [23]. Finally the parameterized charm quark distribution was required to satisfy the recently measured charm structure function at HERA [24].

1.5.2 The GRV Model

The GRV (Glück, Reya and Vogt) model [25] was developed as a dynamical ("radiative") parton model in order to account for the QCD evolution of the parton densities. This means that all parton densities even the gluons are assumed to have a valence like form at a very low Q^2 scale, typically $\mu^2 \approx 0.3\ GeV^2$. The sea quarks are then generated dynamically via boson-gluon fusion, and were predicted to rise strongly at low x [26, 27, 28] which was confirmed by the very first measurements at HERA. The parton densities are parameterized as following

$$xu_v(x) = a'_u x^{\alpha'_u}(1-x)^{\beta'_u}(1+b'_u\sqrt{x}+c'_u x+d'_u x^{3/2}) \tag{1.75}$$

$$xd_v(x) = a'_d x^{\alpha'_d}(1-x)^{\beta'_d}(1+b'_d\sqrt{x}+c'_d x+d'_d x^{3/2}) \tag{1.76}$$

$$x\Delta(x) = a'_\delta x^{\alpha'_\delta}(1-x)^{\beta'_\delta}(1+b'_\delta x) \tag{1.77}$$

$$x(\overline{u}(x)+\overline{d}(x)) = ex^{\gamma}(1-x)^{\eta}(1+fx) \tag{1.78}$$

$$xg(x) = g' x^{\alpha'_g} (1-x)^{\beta'_g} \tag{1.79}$$

The GRV parametrization assumes the strange quark distribution $s(x) = \overline{s}(x) = 0$ at the initial scale leading to an SU(3) broken sea. The light quarks u, d and s, are supposed massless whereas the heavy quark masses used are

$$m_c = 1.4\ GeV \qquad m_b = 4.5\ GeV \qquad m_t = 175\ GeV \tag{1.80}$$

The remaining constraints are same as in MRST.

1.6 The Transition towards Photoproduction

In QCD, we generally distinguish two major types of interactions, "hard interactions", where we can determine a factorization scale, which is sufficiently important such that perturbative calculations can be performed, and "soft interactions", which can only be described by phenomenological models. In ep scattering, the most natural interaction scale is given by the exchanged photon: for DIS-events at Q^2 greater than a few GeV^2, perturbative calculations can be safely applied, whereas photoproduction processes at $Q^2 \simeq 0$ can be described by Regge theory, as used for example in the model of Donnachie-Landshoff [29], where F_2 is the sum of two Regge trajectories, which are motivated by the contributions of Reggeon exchange (particles carrying non-zero quantum numbers) and Pomeron exchange (particles carrying zero quantum numbers).

With the HERA data at low Q^2, the transition region between the two regimes can be studied explicitally and several approaches were developed in order to describe the behaviour of the cross-section over the full kinematic region. The two most successful models, the Badelek-Kwiechinski model and the ALLM-parametrization are described briefly.

1.6.1 The ALLM Parametrization

The ALLM parametrization (Abramowicz, Levin, Levy and Maor) [30] is the result of a fit on F_2 data from various experiments, photoproduction cross-sections, and the cross-sections from hadron-hadron interactions. The Regge theory inspired fit is based on the idea, that F_2 can be obtained from a Pomerons and a Reggeon contribution as

$$F_2(x, Q^2) = \frac{Q^2}{Q^2 + m_0^2} \left(F_2^{I\!P}(x, Q^2) + F_2^{I\!R}(x, Q^2) \right) \tag{1.81}$$

with

$$\begin{aligned} F_2^{I\!P}(x, Q^2) &= c_P(t) x_P^{\alpha_P(t)} (1-x)^{b_P(t)} \\ F_2^{I\!R}(x, Q^2) &= c_R(t) x_P^{\alpha_R(t)} (1-x)^{b_R(t)} \end{aligned} \tag{1.82}$$

the scale t is defined as

$$t = \log \left(\frac{\log \frac{Q^2 + Q_0^2}{\lambda}}{\log \frac{Q_0^2}{\lambda}} \right) \tag{1.83}$$

The t dependence of the coefficients c_P, c_R, b_P, b_R as well as $\alpha_P(t)$ and $\alpha_R(t)$ is expressed by two parameterized functions, such that this fit contains 23 free parameters, which allow to describe the cross-section measurements from fixed target and the HERA experiments in the whole phase space in x ($3 \cdot 10^{-6} \leq x \leq 0.85$) and Q^2 ($0\ GeV^2 \leq Q^2 \leq 5000\ GeV^2$).

1.6.2 The Badelek-Kwiechinski Model

In the Badelek-Kwiechinski Model (BK) [31], the structure function is composed of a non-perturbative part based on the Vector Meson Dominance Model (VDM) and a perturbative part based originally on the GRV approach, but which can be replaced by any type of NLO QCD parametrization:

$$F_2(x,Q^2) = F_2^{VDM}(x,Q^2) + \frac{Q^2}{Q^2+Q_0^2} F_2^{QCD}(x,Q^2) \tag{1.84}$$

In VDM, the photon is considered as a hadronic system, carrying the quantum numbers of a vector meson. $F_2^{VDM}(x,Q^2)$ contains therefore the contribution of the production cross-section of all light vector mesons, with $M_V^2 < Q_0^2$, Q_0^2 defining the limit between the VDM and the QCD regime and can be expressed as:

$$F_2(x,Q^2) = \frac{Q^2}{4\pi} \sum_V \frac{M_V^4 \sigma_V(W)}{\gamma_V^2 (Q^2+M_V^2)^2} \tag{1.85}$$

where σ_V is the total vector meson-nucleon cross-section and γ_V^2 the coupling constant of the photon to the vector meson. If only a finite number of vector meson is considered, the F_2^{VDM} contribution is vanishing at high Q^2. For $Q_0^2 \simeq 1.2\ GeV^2$ the considered vector mesons are according to their masses ρ, ω and ϕ. The extension of VDM, by taking into account the continuous contribution in the perturbative region of the phase space is called Generalized Vector Meson Dominance Model (GVDM).

1.7 Summary

We have introduced the formalism which relates the structure functions to the strong interaction theory QCD. Using the framework of perturbative theory, the evolution of the structure function can be predicted as a function of $\log(Q^2)$ by the DGLAP evolution equations, and current parametrizations of the parton densities obtained by NLO QCD fits have been presented. At small x, the gluon density is dominating the F_2 behaviour and can be predicted by the LL-approximation to have a double logarithmic scaling behaviour. This approximation however is only valid, if $\log(1/x)$ is small, whereas in the opposite case, the BFKL formalism was proposed. The constraints on the behaviour of F_2 from the DGLAP and the BFKL equations, are not important enough to discriminate them experimentally, and different observables as for example F_L will be necessary in the future in order to establish clearly the underlying dynamics. The transition from perturbative to non-perturbative QCD at very low Q^2 has been discussed in the form of two different models, either using a Regge theory inspired Ansatz or a generalization of the Vector Meson Dominance Model. The results of the measurement presented in this thesis will be compared to the two approaches.

Bibliography

[1] E.D. Bloom et al., **Phys. Rev. Lett.** 23(1969) 930.

[2] M. Breidenbach et al., **Phys. Rev. Lett.** 23(1969) 935.

[3] R.P. Feynman, **Photon-Hadron Interactions**, Reading, MA, Benjamin (1972).

[4] F. Halzen, A.D. Martin, **Quarks and Leptons**, J.Wiley & Sons 1984.

[5] T.P. Cheng, L.F. Li, **Gauge theory of elementary particle physics**, Oxford 1984.

[6] R.G. Roberts, **The structure of the proton**, Cambridge 1990.

[7] J. Blümlein et al., **HERA Workshop, vol 1**, 1987.

[8] C.G. Callan and D. J. Gross, **Phys. Rev. Lett.** 22(1969) 156.

[9] R.D. Field, **Applications of Perturbative QCD** , Addison-Wesley 1989.

[10] V.N. Gribov and L.N. Lipatov, **Sov. J. Nucl. Phys.**15 (1972) 438;
L.N. Lipatov, **Sov. J. Nucl. Phys.**20 (1975) 96;
G. Altarelli and G. Parisi, **Nucl. Phys.**B126 (1977) 298.

[11] E.A. Kuraev, L.N. Lipatov and V.S. Fadin, **Sov. Phys JETP** 45 (1977) 199;
Y.Y. Balǐtsky and L.N. Lipatov, **Sov. J. Nucl. Phys.** 28 (1978) 822.

[12] J. Kwiecinski et al., RAL-90-053 (1990).

[13] V.S. Fadin and L.N. Lipatov, **Phys. Lett.** B429 (1998) 127.

[14] R. Thorne, **Preprint OUTP**-9902 (1999).

[15] S. Catani and F. Hautman, **Phys. Lett.** B315 (1993).

[16] J. Kwichinski, **Report 1620/PH**, IFJ Cracow (1993).

[17] A.D. Martin et al, **hep-ph/9803445**.

[18] CCFR collaboration, W.G. Seligman et al., **Phys. Rev. Lett.** 79 (1997) 1213.

[19] A.D. Martin et al, **Phys. Rev.** D50 (1994) 6734.

[20] NA51 collaboration, A. Baldit et al., **Phys. Lett.** B332 (1994) 244.

[21] E866 collaboration, E.A. Hawker et al., **hep-ex/980301**.

[22] CDF collaboration, A. Bodek at The Cracow International Symposium on Radiative Corrections (CRAD96), Cracow Poland May 1,1996 **Acta Phys. Polon.** B28 (1997) 477.

[23] NMC collaboration, M. Arneodo et al., **Nucl. Phys.** B483 (1997) 3.

[24] H1 collaboration, C. Adloff et al., **Z. Phys.** C72 (1996) 593;
ZEUS collaboration, J. Breitweg et al., **Phys. Lett.** B407 (1997) 402

[25] M. Glück, E.Reya, A. Vogt, **preprint DO**-TH 98/07.

[26] M. Glück, E.Reya, A. Vogt, **Z. Phys.** C53 (1992) 127.

[27] M. Glück, E.Reya, A. Vogt, **Phys. Lett.** B306 (1993) 391.

[28] M. Glück, E.Reya, A. Vogt, **Z. Phys.** C67 (1995)433.

[29] A. Donnachie and P.V. Landshoff, **Z. Phys.** C61 (1994) 139.

[30] H. Abramowicz et al., **Phys. Lett.** B269 (1991) 465;
H. Abramowicz and A. Levy, **DESY-Report** 97-251.

[31] B. Badelek and J. Kwiechinski, **Nucl. Phys.** B370 (1992) 278;
B. Badelek and J. Kwiechinski, **Phys. Lett.** B320 (1994) 50.

Chapter 2

The HERA Accelerator and the H1 Detector

The HERA collider (Hadron Electron Ring Accelerator) is producing electron-proton collisions for the H1 and ZEUS experiments with an electron beam energy of 27.6 GeV and a proton beam energy of 820 GeV, resulting in a center of mass energy $\sqrt{s} = 301\ GeV$. H1 (and similarly ZEUS) is a nearly hermetic multi-purpose detector [1] (see figure 2.1) equipped from inside out with a tracking system, several calorimeters, a superconducting solenoid delivering a magnetic field of 1.2 T and dedicated

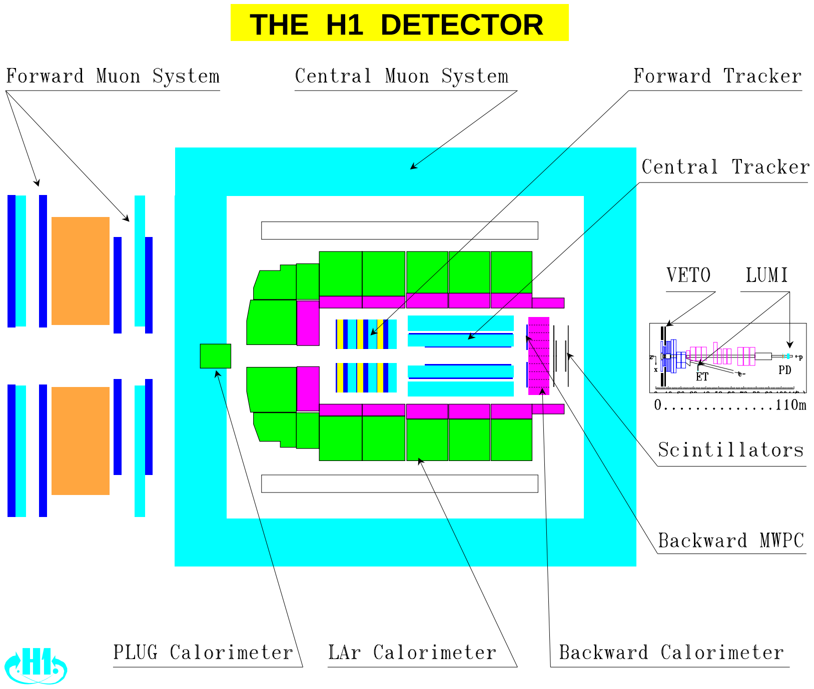

Figure 2.1: *Longitudinal view of the H1 Detector before the upgrade of the backward region.*

muon detectors. The detector is asymmetric, reflecting the asymmetry in the beam energies, with a small calorimeter in the backward region [1], dedicated mostly to the measurement of the scattered electron at low Q^2 and a denser forward region, where mainly the fragments of the proton are observed.

Since 1992 the luminosity increased roughly by a factor of 10 each year from 25 nb^{-1} in 1992 to 35 pb^{-1} in 1997. The accumulated luminosity allows for a precise study of the structure functions especially in the low x and low Q^2 region. In order to improve the precision of these measurements, an upgrade program of the rear part of the H1 detector was undertaken replacing the Backward Proportional Chamber (BPC) by a Backward Drift Chamber (BDC) and the Backward Electro-Magnetic Calorimeter (BEMC) by a 'Spaghetti' Calorimeter (SpaCal).

The present chapter describes briefly the HERA accelerator and the H1 detector. After introducing HERA in section 2.1, section 2.2 describes the luminosity system and the different methods used for the luminosity measurement. Section 2.3 discusses the tracker system and section 2.4 the calorimeter system with emphasis given to the new SpaCal calorimeter as the present analysis relies strongly on this detector. The other subdetectors are not used in this analysis and their description can be found in [1].

2.1 The HERA Accelerator

Before obtaining the final beam energies of 27.6 GeV for the electrons and of 820 GeV for the protons, different steps in pre-acceleration are taken [2], from the bunch formation to the final beam energies (see fig 2.2).

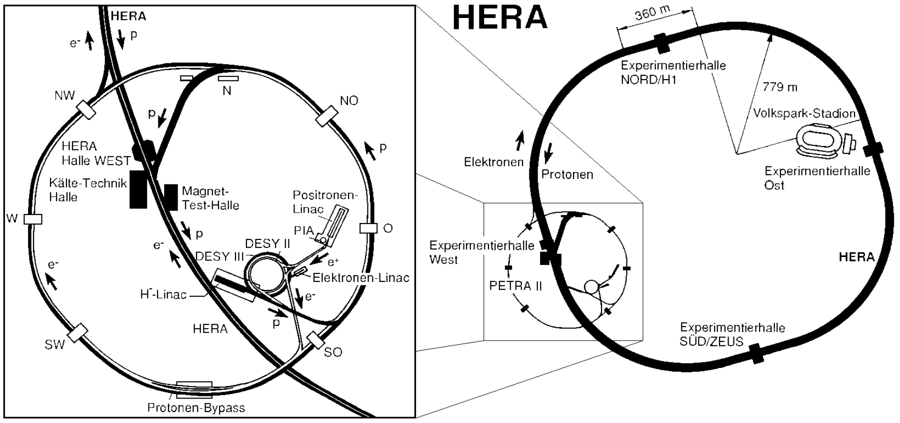

Figure 2.2: *The HERA accelerator with the location of the four experiments and an enlarged view of the preaccelerators.*

For the electrons, first a LINAC injects individual electrons of 500 MeV into a small storage ring which produces single bunches of $\sim$ 60 mA. These bunches

---

[1] The positive z axis is defined w.r.t the proton beam direction

are transferred to DESY II which accelerates them to 7 GeV. Then 70 bunches of 14 GeV are collected in PETRA. These bunches are finally transferred to the main storage ring HERA, where up to 210 bunches are circulating and accelerated to the nominal beam energy.

The protons pass through almost the same kind of processes before attaining the final energies. A different LINAC produces 50 MeV H^- ions, which are accumulated in DESY III. In DESY III, the charge exchange injection takes place within 10 turns of accumulation by stripping off the electrons of the H^- ions passing through a thin foil in order to obtain protons in individual 7.5 GeV bunches which are then transfered to PETRA and cumulated into 70 bunches each of 40 GeV. Finally they are transfered to HERA and accelerated to 820 GeV.

A bunch of whether electron or proton has a Gaussian distribution of particles both in the x- and y-directions [3]. Each bunch has a length of 7.8 mm for the electron beam and $110 - 150$ mm for the proton beam at their maximum energies, determinating the width of the interction vertex distribution in z. Their widths at the interaction points are 0.3 mm (for the electrons) and 0.32 mm (for the protons) while their heights at the interaction points are 0.04 mm and 0.1 mm respectively, leading to an ellipsoidal transverse cross-section. Each bunch contains about 3.5×10^{10} electrons and 10^{11} protons. The spacing between the bunches is 96 ns, leading to a collision frequency of 10.4 MHz Some bunches have no counterpart, called pilot bunches, and used to study beam induced backgrounds.

If we look at the bunch structure of the electrons (see fig 2.3), we see a main peak and besides satellite bunches which are 4.8 ns later and -4.8 ns earlier, than the main bunch. The contribution of these satellite bunches are varying in time and between different fills. As the interactions from these bunches contribute to the luminosity measurements but are cut by the vertex requirement in the analysis, we

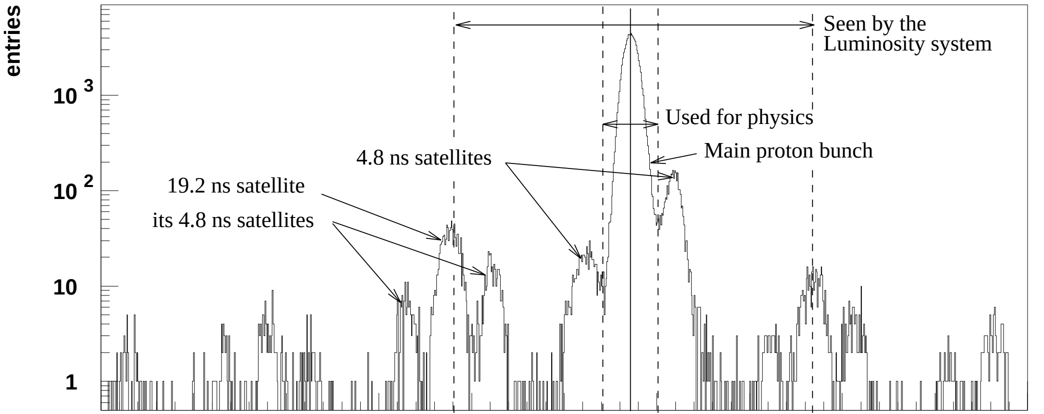

Figure 2.3: *Bunch structure of the electron beam with the main bunch and the satellite bunches. Indicated is the part seen by the luminosity system.*

have to correct for their contribution in the luminosity determination. The mean correction factor is -3.6% for the 95 nominal vertex data.

The main running parameters for HERA in 1995 are summarized in table 2.1 and compared to the performance during the 1994 e^+ running. The performance of the machine improved, especially for the mean proton currents, which is partially related to an increase of the number of stored bunches, but also higher currents in each bunch could be achieved. The design values for HERA are also given.

	1995 e^+	1994 e^+	nominal
lepton energy (GeV)	27.6	27.6	30
proton energy (GeV)	820	820	820
$\langle I_e \rangle$ (mA)	18.4	17.0	60
$\langle I_p \rangle$ (mA)	54.0	41.0	160
number of bunches	174 (+21 pilots)	153 (+21 pilots)	210
peak luminosity ($cm^{-2}s^{-}1$)	6.0 10^{30}	4.3 10^{30}	1.5 10^{31}

Table 2.1: *Main parameters of HERA for the* 1995 *data taking compared to the* 1994 e^+ *running and the nominal values.*

The two interaction regions of the electron and the proton beam are equipped with the H1 detector in the north and with the ZEUS detector in the south. In the east hall, the HERMES detector is installed, where the electron beam is scattered on a gas target. The beam and the target are polarized for studies of polarized structure functions and semi-inclusive measurements on the hadronic final state. In the west hall, the HERA-B experiment uses the proton beam on wire targets and is aiming at observing direct CP violation in the $B\bar{B}$ system.

2.1.1 Kinematic Constraints for HERA-Events

From the HERA-beam energies, we can easily compute the accessible $x-Q^2$ domain for DIS events: the kinematic limit in Q^2 with the available center of mass energy is 90600 GeV^2, whereas at $Q^2 = 1\ GeV^2$ an x value of $1.1 \cdot 10^{-5}$ can be reached. Figure 2.4 shows the lines of constant energy and angle, for both the scattered electron (upper figure) and the "struck quark" in the naive QPM (lower figure) over this kinematic region. The region is delimited by a diagonal, corresponding to the kinematic constraint of $y < 1$. Lines of constant y will be parallel to this diagonal.

The relation between x, y and Q^2, implies that the lowest x values are obtained also at lowest Q^2 and at high y. The reach at low Q^2 is limited by the θ-acceptance of the scattered electron in the backward region: considering an acceptance limit due to the beam-pipe of 2^o, electrons of events with with $Q^2 < 0.1\ GeV^2$ are escaping the backward beam-pipe.

In order to reach low x values, we must be able to detect events at high y, which means at low electron energy. If electrons can be identified with energies down to 3 GeV, $y \sim 0.9$ can be reached, however this is far from being trivial, as the

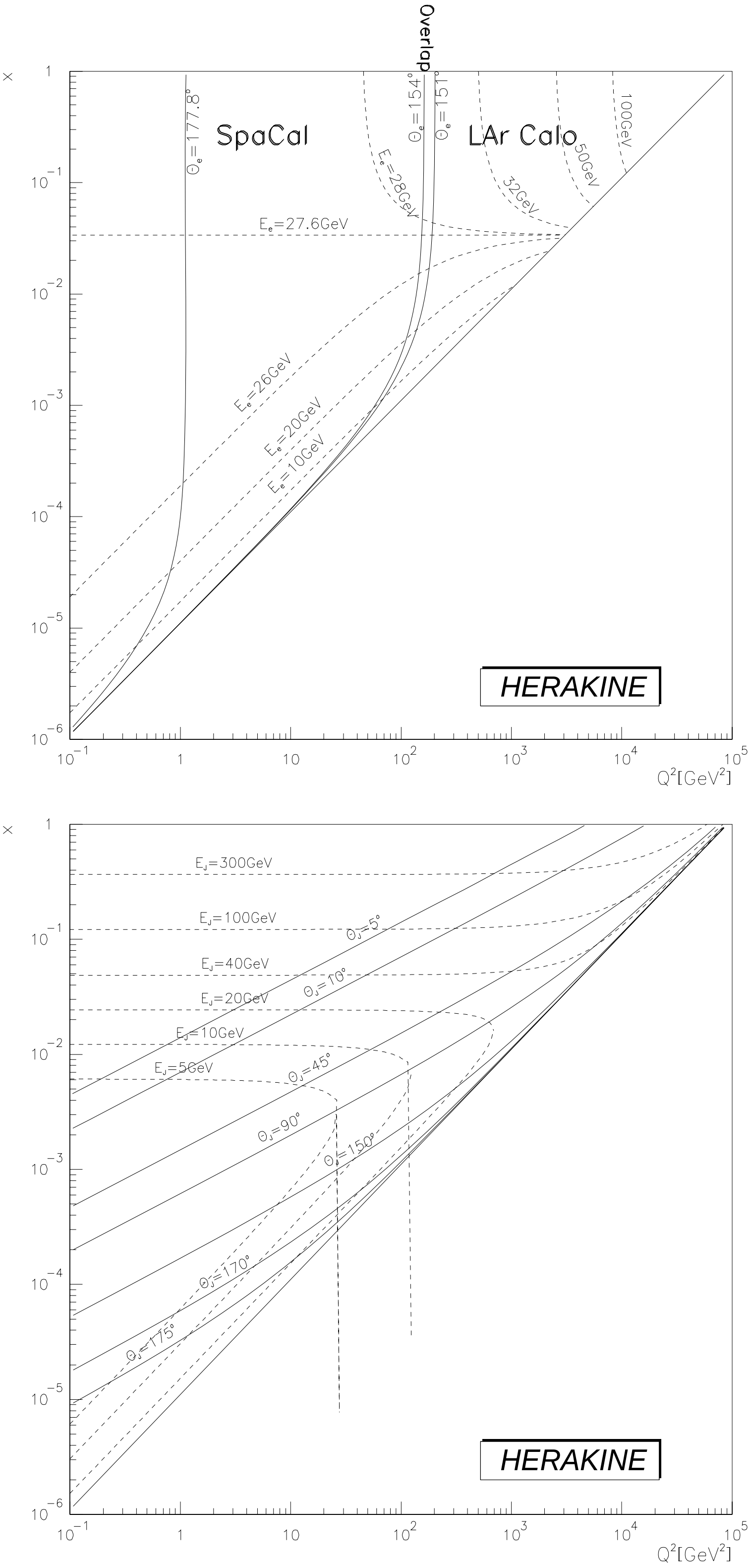

Figure 2.4: *Hera kinematics: x and Q^2 regions as function of the energy and the angle of the scattered electron, indicating the calorimeter in which it is detected (upper plot) and as function of the theoretic energy and angle of the struck quark in the QPM (lower plot).*

electron/pion separation is very difficult at low energy and therefore misidentification can easily occur. This effect is amplified, by the fact that at high y, the struck quark is backscattered, creating an low energetic jet in the backward region of the detector.

At high x, the detection of events is limited by the hadronic final state, which is directed more and more in the forward direction, as we are going towards lower y. The background conditions at HERA however impose the presence of an event vertex measured with the tracking chambers from either the electron or the hadronic final state, imposing therefore a limit on the measurable region towards high x. Besides, the wide range in x covered by a rather small variation in the electron energy, indicates that we must use the hadronic final state information in order to accurately reconstruct the event kinematics, as even small errors on the electron energy will induce huge migration in the $x - Q^2$ plane.

As the cross-section in DIS is varying as $1/Q^4$, we will get the majority of events at low Q^2, i.e. low electron scattering angles. Limiting the event rate, due to a limited amount of trigger band-width, is therefore be done by prescaling trigger for electron candidates in the very backward region.

2.2 The Luminosity System

For the luminosity determination, the cross-section of QED processes which can be computed precisely, are measured and from the comparison with the expected value the luminosity is extracted. At HERA, one can use essentially two methods for the luminosity determination [4]:

- Bethe-Heitler Bremsstrahlung: The Bethe-Heitler process $ep \to e\gamma p$ has a very large cross section of about 100 mb for the emission of a photon at low angles below 17 μrad. This allows for a measurement with a very high statistical precision, but at these angles, the electron and the photon are escaping the main detector and have to be detected in special calorimeters placed further away along the beam pipe.

- QED-Compton: In the elastic $ep \to ep\gamma$ or inelastic $ep \to eX\gamma$ QED Compton process, the scattered electron and photon angles are large and both can be clearly seen in the main detector. The small cross section $\sigma_{vis} \sim 10$ nb however, prevents a good statistical precision. This method is therefore only used for cross-checks [5].

The Luminosity Detector

The electron and photon of the Bethe-Heitler process are detected by the luminosity detector, which consists of an electron tagger and a photon detector (see figure 2.5), located upstream of the main H1 detector [6]. The main electron tagger (ET) for the luminosity system is a 49 channel crystal Cherenkov calorimeter with a cross section area of 15.4 $cm \times 15.4$ cm and a depth of 20 cm, located at $z = -33.4$ m. Two additional new electron tagger ET44 and ET8, analogous to ET but with only

6 channels (2×3 crystals), are situated at $z = -44$ m and $z = -8$ m. These taggers are not used for the luminosity measurement.

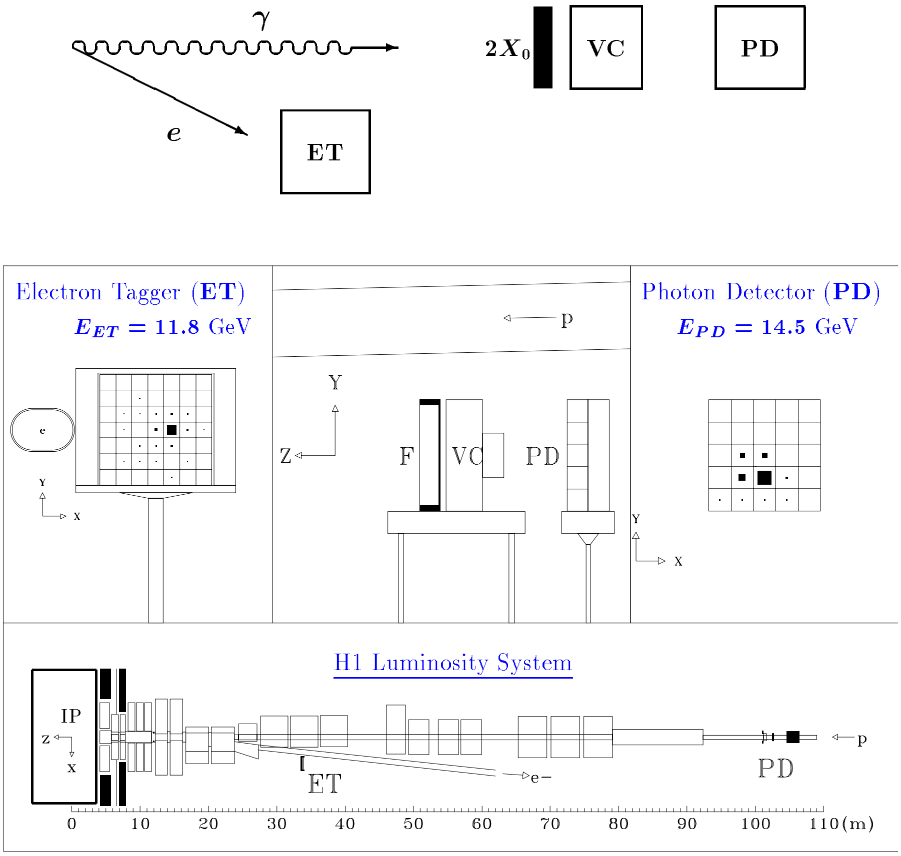

Figure 2.5: *Schematic view of the Luminosity System. Above is indicated the Bethe-Heitler process and the principle of its detection. In the middle, an event seen in the Electron Tagger and the Photon Detector is shown along with the setup of the Veto-Counter and the Photon Detector. Below, the magnets from the interaction point in the main detector to the luminosity detectors are indicated.*

A 25 channels crystal Cherenkov calorimeter with a cross sectional area of 10 $cm \times 10$ cm and a depth 20 cm is used as photon detector (PD) and located at $z = -103.1$ m. A veto counter (VC), a water Cherenkov detector of 28 cm width, is just in front of the PD at $z = -102.8$ m and used as protection against the high synchrotron radiation flux.

The system has high radiation resistance with a good energy resolution of $\sigma_E/E = 15\%/\sqrt{E} \oplus 1\%$, a resolution in x and y of $\sigma_{x,y} = 0.3 - 1.2$ mm and a timing resolution below 3 ns for both ET and PD.

Other Functions of the Luminosity System

Besides the luminosity measurement, these detectors are used to monitor the behaviour of the electron beam. The ET is also used, together with the two additional taggers, to measure electrons in photoproduction events at $Q^2 \approx 0\ GeV^2$. In these events the angular deviation of the electron is so small that it escapes into the beampipe and may then be detected, within their acceptance, by these electron taggers. As these events are the main background at low energy in DIS, the tagged events are used for the background estimation in our event sample.

2.2.1 The Luminosity Determination

The luminosity[2] is obtained from the following formula [6]:

$$\mathcal{L} = \frac{N_{BH}^{ep}(E_\gamma > E_{min})}{\sigma_{BH}(E_\gamma > E_{min})} \tag{2.1}$$

As the system is very close to the beam pipe, there is a large contamination from synchrotron radiation, predominantly at low energies. This background can be avoided by putting a lower limit on the photon energy E_{min}. The choice of a reasonable E_{min} further reduces pile-up effects. The luminosity was corrected for limited geometrical acceptance of the detector and the trigger efficiencies. The number of Bethe-Heitler events N_{BH} are determined in H1 by two different methods.

- **Coincidence (γe) method:** This method uses only events, where the electron and the photon are detected in coincidence. It is very sensitive to small variations in the beam optics due to the limited acceptance of ET, as small changes in the vertical position of the electron beam, may make the electron escape the tagger. However the advantage is its stability against small variations in the trigger threshold. Moreover as one is measuring the energies of both the electron and the photon, a better relative energy calibrations is achieved. In figure 2.6, the correlation of the energy measured in the photon and in the electron detector is shown, where the sum of the two energies should be equal to the beam energy of the electron. In the 1995 data taking this method was used for the online analysis due to these two advantages.

- **Single photon (γ) method:** Here only the information obtained from the PD is used. Due to the larger acceptance of the PD compared to the ET, this method is less sensitive to variations in the beam optics. However, it is less stable against variations in the trigger threshold and a better energy calibration is needed as the relative calibration with the scattered electron is not available. Therefore this method is less adapted for the online analysis, and used for the precise offline determination of the luminosity.

---

[2] $\mathcal{L}$ denotes the total time-integrated luminosity (b^{-1}).

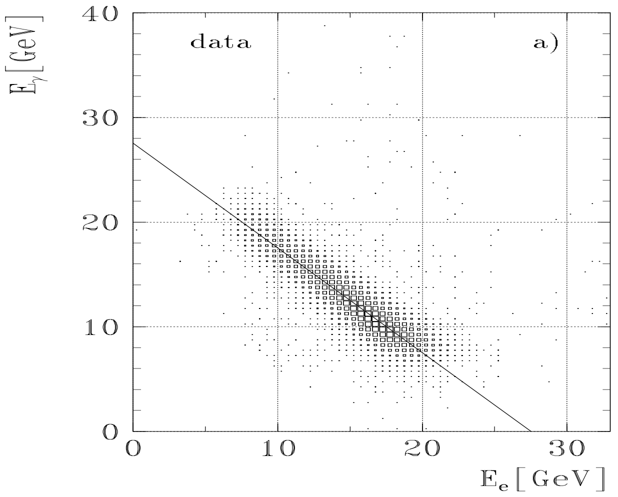

Figure 2.6: *Correlation between the photon energy measured in the photon detector and the electron energy in the electron tagger used for the energy calibration for luminosity system.*

Uncertainties on the Luminosity Measurement

The most important contributions to the uncertainties of the luminosity measurement are coming from the theoretical uncertainty on the calculated cross-section, σ_{BH}, which is 0.47% and from the photon energy calibration and the PD energy resolution, which leads equally to and uncertainty of 0.47 % at $E_{min} = 10\ GeV$. Pile-up effect occur with the emission of more than one BH photon in a single bunch crossing (BC), such that their energies are summed and wrongly estimated as the energy of a single photon. The error estimated from this effect is 0.11 %. The statistical errors from the electron gas background subtraction contribute 0.21% [6].

The total corrections on the on-line luminosity measurements determined from the off-line study are -2.7 ± 1.07 % for the nominal vertex data and -5.4 ± 1.14 % for the shifted vertex data. The satellite bunch corrections determined from the offline analysis for 91 % of the nominal vertex 1995 data (only 'Good' or 'Medium' runs) are -3.6 % with a systematic error of ± 0.4 % from FToF (Forward Time of Flight) measurements and $^{+1.6}_{-0.3}$ % from the limitation of the method used. The total error on the luminosity measurement is 1.97%.

2.3 The Tracking System

The H1 tracking system [7] is used for the detection of charged particle tracks, the measurement of their momenta and the determination of the event vertex. A momentum resolution of $\frac{\delta p}{p^2} \sim 0.3\%\ GeV^{-1}$ and an angular resolution of $\delta\vartheta$, $\delta\varphi < 1\ mrad$ is achieved for the reconstructed tracks. The dE/dx information from the drift chambers can also be used for particle identification. Besides, the tracking system provides information which is used in the event trigger. The complete tracking system, as shown in figure 2.7, is divided into three parts: the forward tracker which is only used for the vertex reconstruction in this analysis, the central tracker and the backward drift chamber.

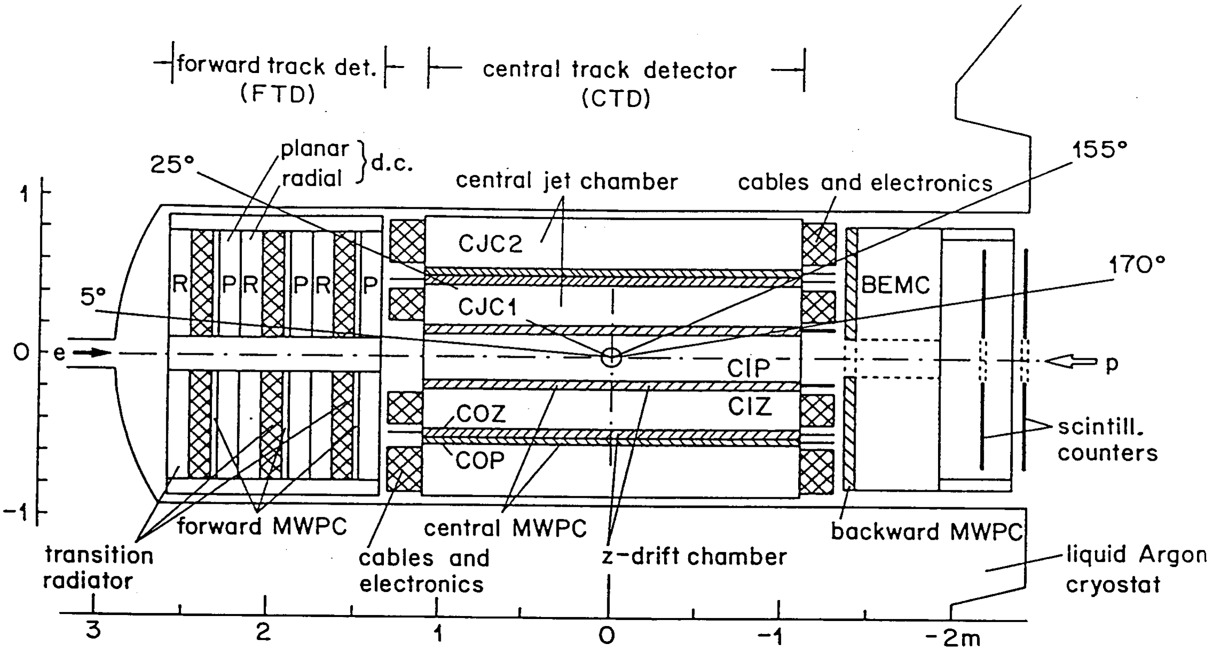

Figure 2.7: *Longitudinal view of the H1 Tracking System before the upgrade program of the backward region.*

2.3.1 The Central Tracking System

The central tracker is a combination of multiwire jet chambers, drift chambers and proportional chambers and covers an angular region between 25^o to 155^o.

The Central Jet Chambers (CJC1, CJC2)

These chambers work according to the following principles:

1. **Primary Ionization:** Incident charged particles are ionizing the gas atoms. If a produced electron has an energy above the ionization threshold ($E_{Ion} \sim 26\ eV$), it causes further ionization.
2. **Drift:** The motion of the electrons and the ions is controlled by applying an electric field (E) between the sense wires and the cathode wires. The produced

electrons drift towards the sense wires with a certain drift velocity depending on the gas used.

3. **Gas Amplification:** Near the sense wire, the electric field changes as $E \propto 1/r$ and reaches values of $E \sim 10^4 - 10^5\ V/cm$. As a result, the electron gains energy and new ions are produced. A large number of these ions near the sense wire produces an avalanche and amplifies the signal.

The central jet chambers are built from two cylindrical co-axial (the beam being the axis) jet chambers [8]. The inner one, CJC1 has a radial coverage from 20 *cm* to 45.2 *cm*, the outer one CJC2 from 52.7 *cm* to 85.5 *cm* and the cylinders are 220 *cm* long centered around the interaction point. chambers are filled with a mixture of Argon(Ar), Ethane(C_2H_4) and water(H_2O) in ratio 50 : 50 : 0.08 at atmospheric pressure in order to increase the primary ionization. The internal structure consists of sense wires, cathode wires, potential wires and field wires, all parallel to the beam. This allows to measure precisely the radial positions, but not the z-position of a track. As shown in figure 2.8, the wires form tilted planes at 30^o to the radial direction. This tilt is provided to compensate the 30^o Lorentz angle in the presence of 1.2 T magnetic field so that in the presence of the high transverse momentum tracks, the drift direction is perpendicular to the field.

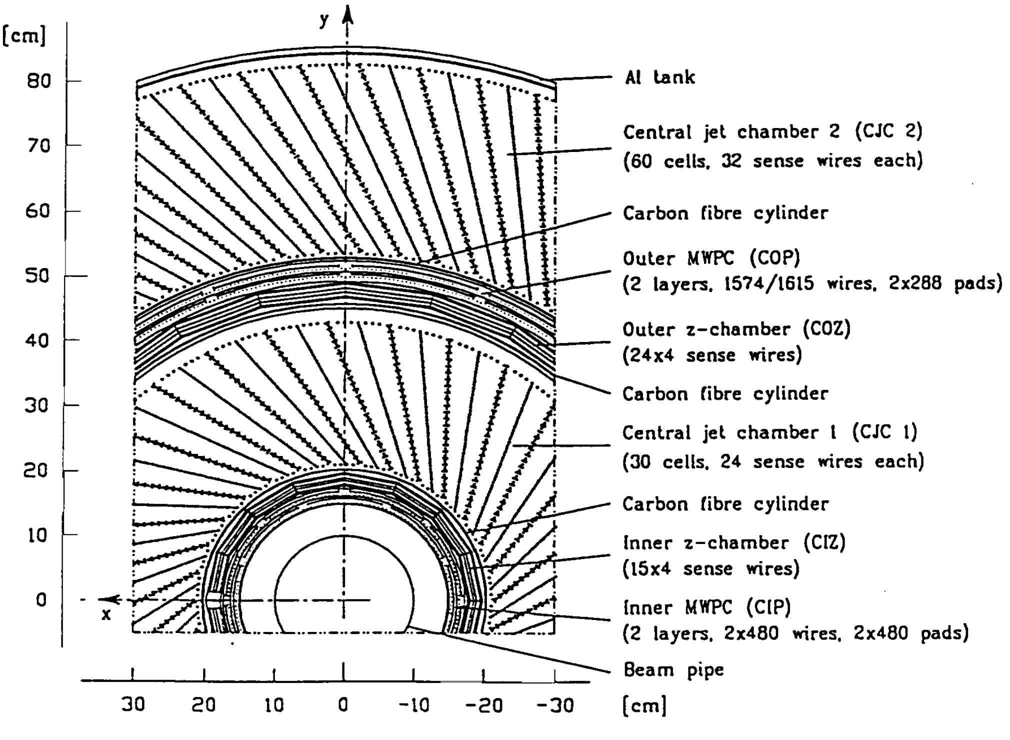

Figure 2.8: *The Central Tracking System, section perpendicular to the beam.*

The above described wire geometry provides a nice transverse resolution of $\sigma_{r\varphi} \sim$ 170 μm. A rough estimation of the z-measurement is done by the charge division method in which the sense wire currents are measured at both ends of the sense wires. This method gives a resolution of $\sigma_z \sim 2.2$ *cm* (i.e. 1% of the wire length). The resolution obtained in the energy loss measurement is $\sigma_{dE/dx} \sim 10\%$.

The Central z-Chambers (CIZ, COZ)

Due to the poor precision in the z-position determination of the CJC chambers, two additional chambers were added, the innermost CIZ, lies in front of CJC1 and the outer one COZ, in between CJC1 and CJC2 (See figure 2.8). The polar angles range covered by CIZ and COZ are $16^o < \vartheta < 169^o$ and $25^o < \vartheta < 156^o$ respectively.

1. CIZ: The chamber forms a 16 faces regular polygon in the cross-section with a thickness of 0.012 radiation length X_o. In the z-direction, the chamber is divided into 15 equal rings, each ring being drift cell 12 *cm* long and 2 *cm* thick, where the wires are mounted along polygons. The wire planes are tilted by 45^o with respect to the beam, tilted backward for the first 9 cells while tilted forward for the remaining 6 cells according to the direction of the crossing tracks. This wire geometry resolves the right-left ambiguity and it eliminates the dependence of the chamber resolution on the crossing angle.

2. COZ: The chamber cross-section is a 24-faces regular polygon. The number of cells and their azimuthal size is the same as in CIZ. The wire planes are not tilted and these planes are aligned perpendicular to the beam. Mirror tracks can be eliminated, as they do not point to the vertex.

In each cell, the soldering of the wires is performed at $\varphi = 0^o$ and amounts to a dead zone in φ of 7.7% of 2π for CIZ and 5.3% of 2π for COZ. The chambers allow for a precision of the measurement in z of $\sigma_z = 260$ μm for CIZ and $\sigma_z = 200$ μm for COZ, while the resolution in $r\varphi$, which is determined by the charge division at the wire ends, is rather poor ($\sigma_{r\varphi}$) of 28 *mm* and 58 *mm* respectively.

The Central Proportional Chambers (CIP, COP)

Next to the z-chambers, two thin cylindrical proportional chambers, CIP and COP (see figure 2.8) are located which give space points for three different triggers [9]. Combining these space point informations with the one from the four planes of the FPC (Forward proportional chambers) and those from the CIZ and the COZ allows for a fast estimation of z-vertex position. The system provides a good timing measurement for the particle tracks with a resolution of 75 *ns* for CIP and 60 *ns* for COP. By looking at their structure, the CIP is divided into sixty sectors in z-direction each of a width $\delta z = 3.65$ *cm* and in eight sectors in φ, each of a width $\delta\varphi = 45^o$ while the outer chamber COP, consists of 18 sectors in z-direction each with a width $\delta z = 12.1$ *cm* and sixteen sections in azimuthal direction with a width of $\delta\varphi = 22.5^o$.

2.3.2 The Forward Trackers

The angular acceptance for the forward trackers [10] (fig 2.7) is $7^o \leq \vartheta \leq 25^o$. The system is composed of three identical supermodules, which are the combination of planar and radial drift chambers and proportional chambers.

The Planar Modules

In the planar drift chambers the wires are parallel to each other (see figure 2.9) and the whole chamber is orthogonal to the beam. The system consists of three planes oriented at 0^0 and $\pm 60^0$, with a total of 1152 channels. The main purpose of the planars is the ϑ measurement with a resolution below 1 *mrad*. The radial resolution is of $150 - 170$ μm while the double track resolution is below 2 *mm*.

The Radial Modules

Three radial wire drift chambers [11, 12] are improving the $r\varphi$ and r reconstructions. The basic structure contains wire strung radially from $r = 15$ *cm* to $r = 76$ *cm* (see figure 2.9). Each radial consists of 48 wedge shaped drift cells in φ.

The Forward Proportional Chambers:

The Forward Proportional Chambers are giving a fast timing information which is used as a veto for interactions, which are produced out of the time-window of an *ep* collision. The information of a the presence of a signal in the forward tracker, assembled to a ray, is used in combination with the CIP/COP information in trigger elements indicating the presence of a vertex.

2.3.3 The Backward Drift Chamber

As stated earlier the former Backward Proportional Chamber (BPC) was replaced before the 1995 data taking by a Backward Drift Chamber (BDC) [15, 16]. The BPC was used to measure the impact points of the charged particles tracks in front of the BEMC with a precision of 1 *mm*. However, being a plane chamber it did not measure the direction and the momentum of the charged particles tracks. This measurement was performed by the central trackers but restricted in acceptance to $\vartheta < 165^o$ given by CJC1.

The newly installed backward drift chamber (BDC) covers the angular region of $153^o \leq \vartheta \leq 177.5^o$. The system (see figure 2.10) contains 4 parallel planes of double layers perpendicular to the z-axis, each plane has 8 equal azimuthal sectors with 44 radial wires per sector thus forming a cobweb geometry . The distance between two wires decreases as one goes from higher to lower radii, in order to cope with the high background rate (beam gas, beam wall) which increases as one goes closer to the beampipe. Each of the four planes is tilted with respect to its adjacent plane by 11.25^o so that the whole detector provides 32 effective φ segments, which are unique segments in 3-dimension. The detector contains the gas mixture of $92.5\% Ar, 5\%$

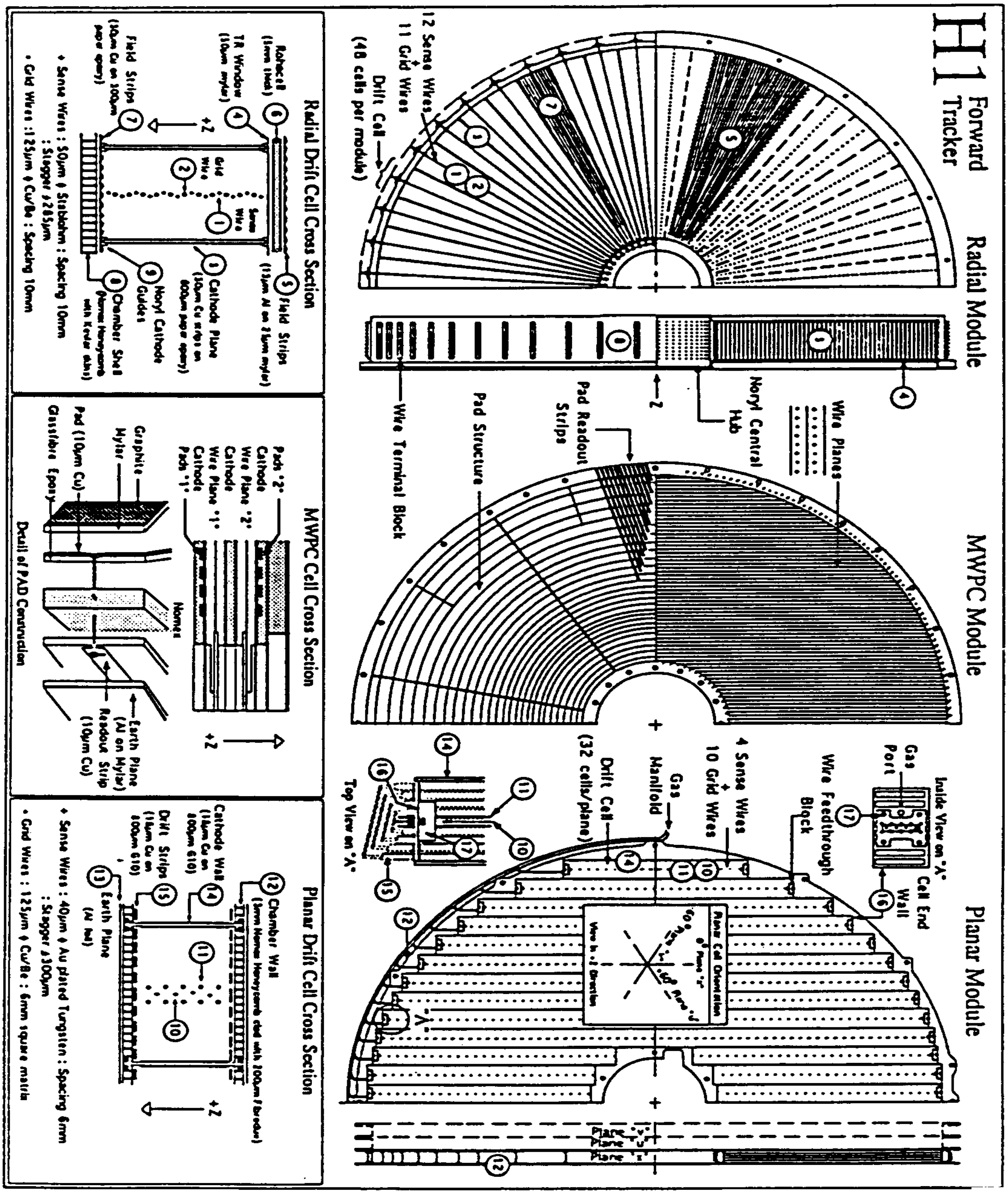

Figure 2.9: *The three different modules of the Forward Tracking System, section perpendicular to the beam and the corresponding cell structures.*

isobutane and $2.5\% NH_3$. The gas mixture provides a reasonable gas amplification factor of 5.10^4 and the drift velocity of ionization electrons is $v_d = 28\ \mu m/ns$ at $E = 1kV/cm$, directed radially.

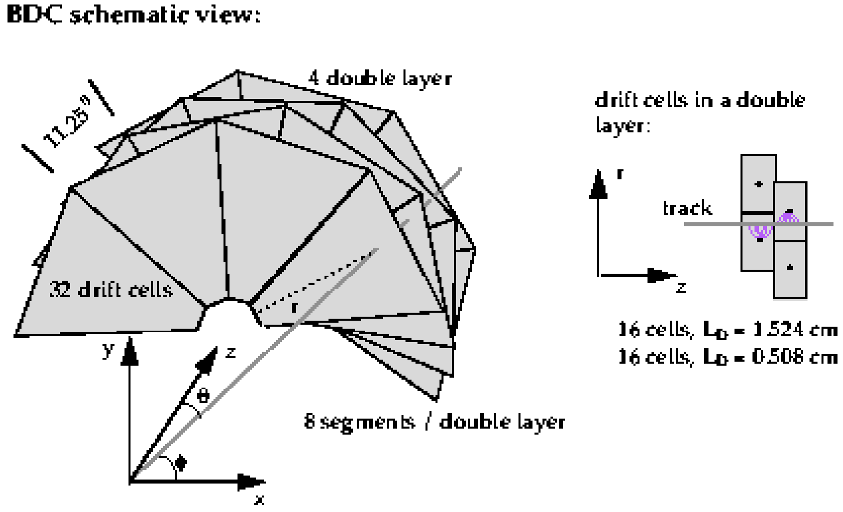

Figure 2.10: *Schematic view of the BDC, showing the arrangement of the* 4 *double layers and the structure of a double layer readout cell.*

The described BDC geometry provides an impact point with a good radial resolution of $\sigma_r \sim 0.4\ mm$ and an azimuthal resolution of $\sigma_\varphi \sim 0.8\ mm$ for non-showering particles while it has a moderate hit resolution of $400\ \mu m$ in ϑ and $1\ mm$ in φ. The double track resolution is $3\ mm$. There is a large amount of dead material in front of the BDC due to the CJC's end walls, electronics and cables with a variable depth from 0.5 to 2 radiation lengths with an inhomogeneous structure. This dead material produces preshowering of the electron in about 60 to 70% of the events. The BDC can measure the energy loss of the electron due to this preshowering by measuring dE/dx with a precision of $\sigma_{dE/dx} \sim 30\%$, but this has not been used for the analysis so far. In the case of showering particles the resolution degrades as $\sigma_r \sim 1.4mm$ and $\sigma_{r\varphi} >\sim 1.5mm$.

The Electron Track Reconstruction

The BDC is a vital detector in the backward direction in order to identify the electron in low Q^2 events. Therefore an electron candidate is only validated, if the electron cluster in the SpaCal can be associated to a track measured in the BDC. In order to use the maximum available information, from the track reconstruction one defines χ'^2 [15], adding to the usual χ^2 criteria, using the distance of the closest approach between tracks and hits, the difference between the electron cluster and a

BDC track,

$$\chi'^2 = \chi^2 + (\frac{\delta\vartheta}{\sigma_\vartheta})^2 + (\frac{\delta(d\varphi/dz)}{\sigma_{d\varphi/dz}})^2 \tag{2.2}$$

Here $\delta\vartheta$ is the difference in the polar angle of the track and the angle from the electron cluster to the vertex and $\delta(d\varphi/dz)$ is the difference in the corresponding slopes. For the electron reconstruction only 5 tracks with minimum χ'^2 are kept and the remaining tracks are rejected. Among these five tracks the electron is selected as one with a minimal projected distance from the SpaCal cluster.

The polar angle resolution depends upon the radial resolution, the resolution in z-vertex and the resolution in z-BDC. As the later two are very small, one can neglect them and hence

$$\sigma_\vartheta = \frac{\sigma_R}{z_{BDC} - z_{vtx}} \tag{2.3}$$

from which one finds a resolution of 0.6 $mrad$ for non-preshowering events. While comparing the data with the simulation, one finds a shift of 0.5 $mrad$ in the angular distribution which is included in the systematic errors for the F_2 measurement.

2.4 The Calorimeters

The tracking systems can only detect charged particles and as the resolution dp/p is proportional to p, the momentum measurement is more accurate for low momentum particles. For sampling calorimeters, where only a fraction of the deposited energy is detected by some active material, the energy resolution $\delta E/E$ varies as $1/\sqrt{E}$, therefore high energetic particles are more precisely measured with a calorimeter, whereas neutral particles can only be measured by the calorimeter. The energy loss as a function of the distance varies as $\sqrt{E}$ for a tracker, while for calorimeters it varies as $\log(E)$. This means that the calorimeters are very compact in order to absorb a particle, whereas trackers only modify slightly the trajectory of a particle. With a high granularity, calorimeters can determine the position of isolated particles and electromagnetic and hadronic particles can be separated by looking at the longitudinal and transverse structure of the measured shower.

5 In High Energy Experiments we use sampling calorimeters

The response time of calorimeters vary, depending on the active material. In the case of scintillators, the response is very fast and precise, as for example in the case of the SpaCal calorimeter, where the timing resolution is about 1 ns. For the liquid Argon Calorimeter, the response time is limited by the drift velocity of electrons in the liquid Argon and the rise time of the electronic signal. However the timing information of calorimeters is used to veto interactions out of the timing window in the trigger system, which is rejecting non-ep background events.

Electromagnetic Showers

A photon of a few MeV will interact with matter either by photoelectric or by Compton effect, while an electron of a few MeV interacts with the detector material via ionization and excitation (Figure 2.11). At energies of several GeV the dominant process for photons is e^+e^- pair production and Bremsstrahlung for electrons. These interactions give rise to electromagnetic cascades.

The total longitudinal length, lateral radius and the starting point of the cascade formation depends on the material of the detector depend on the energy of the particle. One defines the radiation length X_o as the length of material through

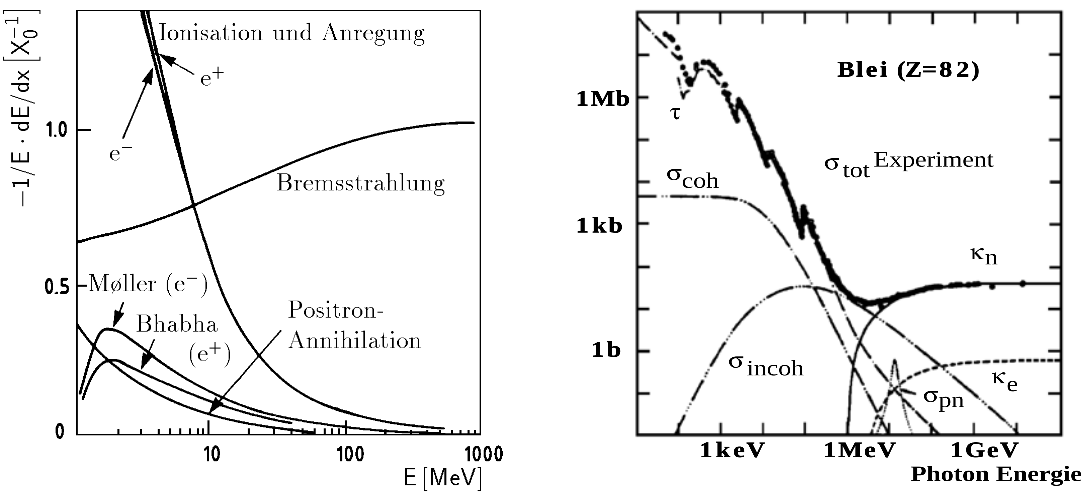

Figure 2.11: *Energy loss by a electron (left) and an photon (right) as a function of the energy in Lead.*

which an energetic electron looses $1 - e^{-1} \sim 67\%$ of its energy by Bremsstrahlung [17]. X_o depends strongly on the material, 5 X_o correspond for example to 45 cm of Al but less than 3 cm of lead, whereas the longitudinal shower development as a function of X_o is nearly independent of the material. For a 10 GeV electron the shower is generally contained in about $25X_o$ [18] The transverse development of an shower is expressed by the Molière radius ρ_M, which is defined as the transverse radius of a shower of an electron after one radiation length. About 95% of the energy of an electromagnetic shower are contained in a cylinder of radius $r = 2\rho_M$, which corresponds to about 3.4 cm for lead.

Hadronic showers

In the formation of the hadronic showers, the interaction between the hadrons and the nuclei of the absorbing material has to be considered in addition [19]. Contrary to the electromagnetic showers, not all the energy of the hadron deposited in the detector can be measured since the energy involved in the breaking up of the interacting nucleons has to be taken into account. This can be compensated either by the choice of the absorbing material [20] or by software reweighting techniques, as performed by H1 [21]. In the case of hadronic showers, one defines the interaction length λ, as the length of the absorbing material through which a hadronic particle looses in average 67% of its energy. For the lateral extension of a hadronic shower, about 95% of its energy are contained in a cylinder with a 1λ radius. The shower of a $10 GeV$ hadron interacting in lead, would extend over about 80 cm which corresponds to 4.5λ longitudinally, and about 35 cm corresponding to 2λ transversally [22]. This shows, that the difference in the formation process between electromagnetic and hadronic showers is reflected in the extension of the showers, which are longer and wider in the case of hadrons. Figure 2.12 shows the lines of constant X_o and λ for the H1 Liquid Argon (LAr) calorimeter.

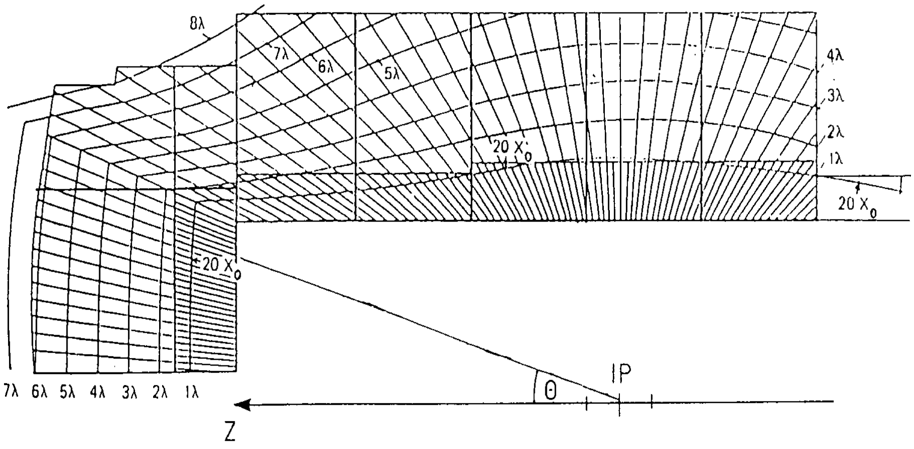

Figure 2.12: *Longitudinal view of the H1 LAr calorimeter. Indicated are lines of constant radiation lengths X_o and interaction length λ.*

The calorimetric coverage of the H1 detector for the measurement of the scattered electron in DIS is given by the SpaCal in the backward direction and the liquid argon calorimeter in the central and forward direction. Figure 2.4 is indicating the angular acceptance of the two calorimeters for the measurement of the scattered electron and the corresponding $x - Q^2$ domain. The SpaCal is covering a region of about 2 orders of magnitude in Q^2, from 1 GeV^2 to 100 GeV^2, whereas with the LAr calorimeter electrons in events with $Q^2 \sim 100 GeV^2$ up to the kinematic limit of $100000 GeV^2$ can be measured. In this analysis we concentrate on events with the electron measured in the SpaCal. The LAr calorimeter is therefore used to measure the main part of the hadronic final state. A small copper-silicon calorimeter, covering the very forward direction ($12.5\ mrad < \theta < 60\ mrad$), the Plug, is only used for background rejection in this analysis.

2.4.1 The Liquid Argon Calorimeter

The central and forward part of the H1 calorimeter system is covered by the LAr calorimeter [23]. The whole system has 7 wheels, each with 8 octants. The calorimeter has in total 44000 channels. It is divided into two parts: the highly segmented electromagnetic section, covers the inner part of the calorimeter (from 20 to 30 radiation lengths) with lead absorber plates of 2.4 mm thickness. It contains about 30784 cells with a variable cell size of an average value of $3 \times 5\ cm^2$. The coarser hadronic section constitutes the outer radial part of the calorimeter (4.5 to 8 absorption lengths) where stainless steel absorber plates of 16 mm are used. It accounts for 13568 cells with an average size of 4×6 cm^2.

The use of liquid argon as active material requires a cryogenic system, which keeps the temperature at 90 K but has the advantage of smaller aging effects than scintillators for example. The high stability and the ease of calibration gives a homogeneous response and therefore a good energy flow measurement. However this needs to keep the electronegative impurities of the Liquid Argon (like O_2) at a very low level ($< 1\%$), which is continuously monitored.

Usually the drift velocity in LAr is very small i.e of the order of 0.4 $cm/\mu s$ at 10 kV/cm. This can be increased by addition of $0.5\% CH_4$, after which an electron drift velocity of $v_{drift} \sim 5$ $mm/\mu s$ is reached at $E = 1$ kV/mm, which is sufficient to provide a reasonable dead time, and leads to a drift time of electrons in liquid Argon of about 200 ns/mm [23]. The induced charge due to ion movements has a very small rise time, so it does not intervene in the signal formation.

The relative high density of liquid Argon ($\rho_{LAr} = 1.4$ g/cm^3) allows to get a high absorption. and has the further advantages of having small ionization energy of $E_{ion} = 23.6$ eV and a high recombination probability, which allows for a high charge collection efficiency.

The resolution for the electromagnetic showers is about $12\%/\sqrt{E}$, whereas a resolution of $50\%/\sqrt{E}$ is achieved for hadronic showers after off-line reweighting. The noise level in the L.Ar calorimeter is low: $\sigma_{noise} = 10 - 30$ MeV in the electromagnetic section and $50 - 100$ MeV in the hadronic section.

2.4.2 The SpaCal Calorimeter

The Spaghetti Calorimeter SpaCal [24] uses the novel technology of embedded scintillating fibers inside lead matrices. These fibers carry the energy information in terms of light signals which are amplified and then converted to electronic signals by photomultipliers (PMT). The fast response allows not only for an energy measurement of the particles but also to measure the timing information.

After a number of test experiments [25, 26] such a calorimeter was finally installed in 1995 in order to cover the backward part of the H1 detector. It replaces the earlier electromagnetic lead/scintillating sandwich calorimeter BEMC and the Time of Flight system (ToF).

The calorimeter consists of two main parts: an electromagnetic section and a hadronic section. The front end of the SpaCal is at -150 cm from the interaction point with an active width of each section of 25 cm and a diameter of 160 cm (see fig 2.13).

The installation of the SpaCal was the result of the upgrade program of the rear part of the H1 experiment. The requirements were to increase the efficiency of the detectors in the backward region, to increase the acceptance, to better estimate the hadronic flow, to reduce the background by improving the e/π separation and a precise measurement of the scattered electron. Following are a few important advantages of the SpaCal over the BEMC [27, 28, 29]:

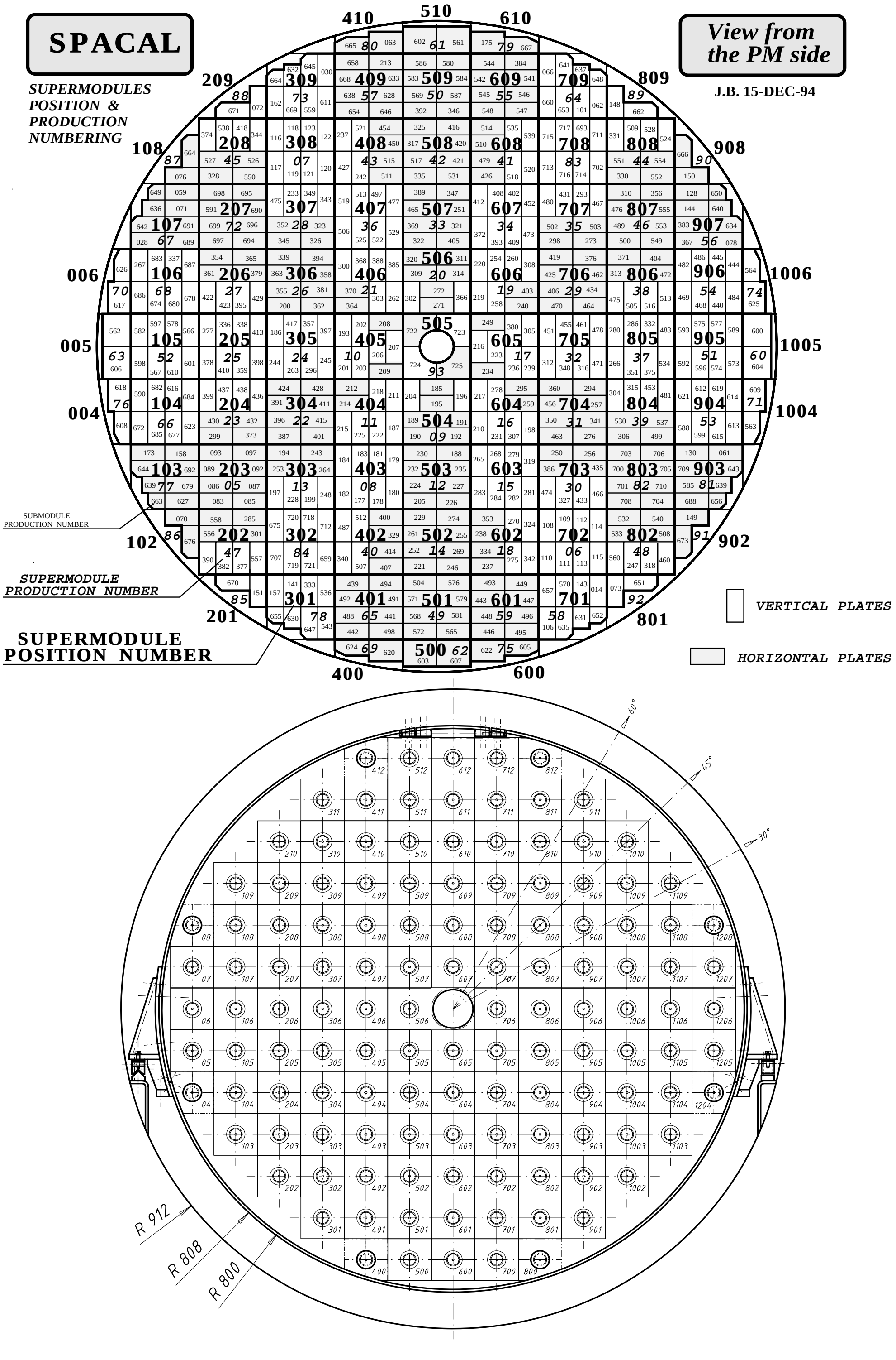

Figure 2.13: *r-φ view of the electromagnetic and hadronic SpaCal indicating the cell structure and for the electromagnetic section the association in submodules and supermodules.*

- **Extended kinematic region**: With the larger angular acceptances of $151^o < \vartheta < 177.5^o$ for the electromagnetic SpaCal and $160^o < \vartheta < 177.8^o$ for the hadronic SpaCal (compared to BEMC for which, the acceptance was $151^o < \vartheta < 176^o$), the detector is able of cover a large kinematic region extending down to low values of x ($\leq 10^{-5}$) and $Q^2(\sim 0.85\ GeV^2)$ (See figure 2.4) as compared to the BEMC where the acceptance reached down to $x \sim 10^{-4}$ and $Q^2 \sim 8.5\ GeV^2$.

- **Increased angular resolution**: Spacal has a higher granularity as compared to the BEMC, with 1192 channels each of a size of $4 \times 4\ cm^2$ for the em-part, while the old calorimeter BEMC had only an electromagnetic part with 88 channels each of a size of $16 \times 16\ cm^2$. Thus the SpaCal has a high resolution of a few mm in position which gives a resolution of $1 - 2\ mrad$ on the polar angle of the scattered electron.

- **Accurate energy measurement**: The electromagnetic energy resolution is $7.5\%/\sqrt{E}$ ($10\%/\sqrt{E}$ in case of BEMC). This results in improvements in the systematics on F_2.

- **Electron identification**: A better electron identification is very important in order to lower the energy threshold in the selection of DIS events. Due to the two separate sections of the calorimeter, the separation of electrons from pions and therefore the suppression of the photoproduction background is achieved more efficiently.

- **Hadronic energy measurement**: The presence of an hadronic section allows for a better measurement of the hadronic energy flow in the backward direction and therefore a better measurement of the kinematic variables from the hadronic final state especially at high y. Due to the choice of the fiber/lead ratio, the SpaCal is a nearly compensating calorimeter with a energy resolution for hadrons of $30\%/\sqrt{E}$ compared to $80\%/\sqrt{E}$ for the BEMC.

- **Time resolution**: The hadronic calorimeter acts also as a timing device. It measures the time of the particle with respect to the HERA clock with a resolution of 1 ns which allowed to abandon the former Time of Flight (ToF) system. The arrival time of the upstream particles arising from the beam - gas interaction is smaller than for DIS ep scattering at the interaction point and they can therefore be rejected.

- **Small radiation length and Moliere radius**: The electromagnetic and hadronic parts of SpaCal have a radiation length X_0 of 9 mm and 8.5 mm, interaction lengths λ of 25 cm and 24.6 cm and Moliere radii ρ of 2.55 cm and 2.36 cm respectively compared to the BEMC calorimeter which has an interaction length of 21.7 cm and a Moliere radius of 3.4 cm.

- **Good efficiency in high magnetic field environments**: In the presence of the strong magnetic field of 1.2 T, a sufficient voltage gain of the photomultipliers of 10^4 (100 times less than without this field) has been reached. This is achieved by using special MESH photomultipliers [25].

The electromagnetic (em) and the hadronic (had) sections of the calorimeter are constructed in a similar way. The r-φ view of both sections of the calorimeter in shown in figure 2.13. The em-part of the detector consists of 60 supermodules each of a size of $16.26 \times 16.26 \times 25\ cm^3$ and a number of special shaped outer modules to fill the gaps in order to construct a rounded shaped detector. In the radial position around the beam pipe of the electromagnetic SpaCal is filled with 12 special cells of different sizes and shapes in order to accommodate the beampipe structure plus 4 veto layers of circular arcs inside these cells (see fig 2.14). A supermodule is composed of 8 rectangular shaped submodules (see fig 2.15) and further each submodule consists of two cells each of size $4.05 \times 4.05 \times\ 25\ cm^3$. This leads to 16

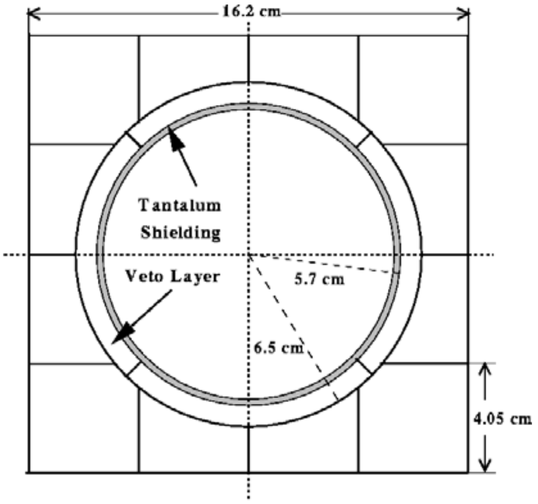

Figure 2.14: *The cell shape of the SpaCal Insert and the Veto layers, covering the innermost part of the electromagnetic SpaCal.*

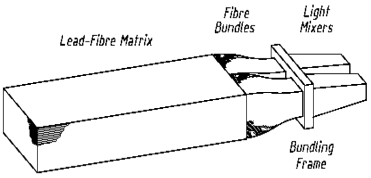

Figure 2.15: *An electromagnetic SpaCal submodule.*

cells per supermodule, giving total a total of 1192 channels for the electromagnetic part. The hadronic part of the SpaCal consists of 128 single modules. Each module is considered as a single cell of the square shaped cross-section with a volume of $11.93 \times 11.93 \times 25\ cm^3$.

The front part of each submodule (hadronic module) consists of 52 (65) lead plates oriented longitudinally to the beam direction with a cross section of $8.1 \times 4.05\ cm^2$ ($11.93 \times 11.93\ cm^2$). The thickness of each plate is $7.8\ cm \pm 10\ \mu m$. The plates have 90 (54) grooves engraved in the longitudinal direction where the lead fibers are fitted in. There are 4680 (3510) scintillating fibers in each supermodule (hadronic module) which have a diameter of $0.5\ mm$ ($1\ mm$) giving a lead to fiber ratio of $2.3 : 1$ ($3.4 : 1$) which gives Pb/Fiber density of $7.3\ g/cm^3$ ($7.7\ g/cm^3$). The front end of each fiber is polished and mirrored. At the rear part, the fibers emerge of the matrix and are bundled in two parts of equal number. A bundle has a length of $7\ cm$($8\ cm$) and is separately held in a bundling frame. The bundle ends are coupled by an air gap of $0.3\ mm$ to the light mixers. The purpose of these mixers is to randomize and concentrate the light onto the photo-cathode of the PMT (fig 2.16). Finally the light-mixers are glued to the photomultipliers which convert the light of each cell to an electric pulse. Each supermodule is connected to a HV source and a which provides an adjustable voltage of $1\ kV$ to the PMT.

In addition, each supermodule is connected to a Calibration and Monitoring unit (CAM) [30]: as the PMT's are not stable within a few hours, their gain has to be monitored continuously. For this purpose, the CAM-modules are sending short light pulses from LEDs via a fiber and a lightmixer to the PMTs with a frequency of $1 Hz$. In the same time the light pulses from the LEDs are read out by Photodiodes (PD). Differences in the variation in the signal seen by the PDs compared to the signal seen by the PMTs, can be attributed to gain variations are a directly used in the offline-reconstruction for gain corrections.

All supermodules are assembled in a $8\ mm$ thick Al vessel.

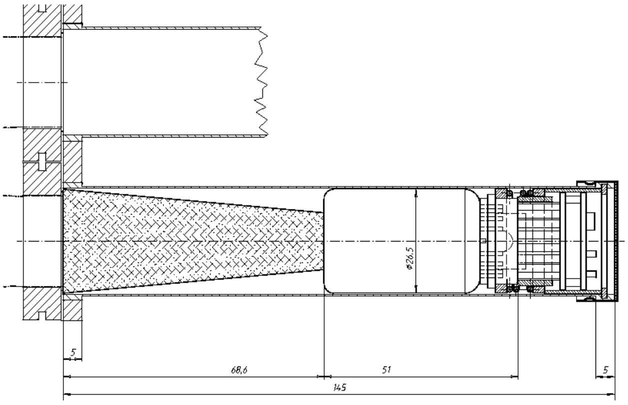

Figure 2.16: *Lightmixers in front of the Photomultiplier tubes.*

2.4.3 The SpaCal Readout and Trigger

The front-end electronics (FE) of the SpaCal aims at measuring the arrival time of the particle with respect to the HERA clock and to send the data in form of energies and timings for a triggered bunch crossing to the H1 Data Acquisition (DAQ). The general view of the SpaCal read out and trigger system is shown in the block diagram in figure 2.17.

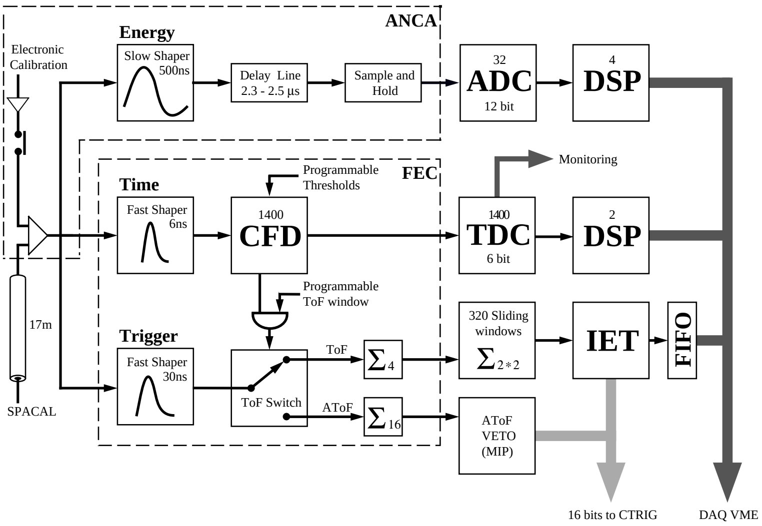

Figure 2.17: *The Spacal Readout and Trigger System.*

The amplified signals from the PMT are taken to the FE electronics. Here the signals are reshaped and divided into three branches, the energy read out, the time measurement and the trigger readout.

From the first branch i.e. the energy read out, the signal is taken to a delay line of 2.3 μs to 2.5 μs, from where it goes to the sample and hold circuit. If an event is selected, the energy read out branch information is sent to the Analog to Digital Converters (ADC) and finally to the Digital Signal Processors (DSP) for pedestal subtraction and the conversion from ADC-counts to energy. The ADCs read out the energies with two gains, gain 1 and gain 4. An inter gain calibration is applied in the DSP to the ADC counts.

From the time measuring branch, the signals are sent into Constant Fraction Discriminators (CFD). The timing information from the CFDs are taken to Time to Digital Converter (TDC) where taking signal to the DSPs. Also the beam structure is monitored and an analysis of the hit frequency is performed continuously with the TDC. In principal the timing information for each cell could be used in cluster algorithms, in order to reject cells which are not in time. However this information is not reliable for low energy cells. Using this information the trigger branch separates the time of flight (ToF) from the out of time of flight (AToF) events.

The principal topological characteristic of a DIS event is the presence of a scattered electron. The IET is based on a rough identification of an electron candidate, based on ToF energy sums in sliding windows, each window corresponds to 4×4 cells (in total 320 windows) of the electromagnetic spacal. Three possible energy thresholds, between 100 MeV and 23 GeV, can be set to the $IET0$, $IET1$ and $IET2$ trigger elements, to which the energies of the sliding windows are compared. If an 'electron candidate' of the corresponding threshold is found, a cluster bit is set for each of the different thresholds and sent to the central trigger logic (CTL). For 1995 data taking the thresholds were set to 5 GeV, 8 GeV and 23 GeV respectively.

2.5 Summary

HERA is a unique facility for producing ep interactions at high center of mass energies and the first collider of hadron-lepton beams. The asymmetry in the beam energies is directly reflected in the shape of the H1 and ZEUS detectors. The nearly hermetic detectors allow for a precise measurement of the scattered electron in Deep Inelastic Scattering, but also of the most relevant part of the associated hadronic final state. The choice a highly segmented liquid Argon calorimeter for the H1 detector permits a good detection of electromagnetic and hadronic particles, which is supplemented by the tracking devices. In 1995, the installation and commissioning of new subdetectors in the backward region, namely the BDC and the SpaCal, was completed and both detector components were reaching the expectations: an extension of the geometrical acceptance, a more precise measurement of the energy and the position of the scattered electron and an improved coverage for the detection of hadrons in the backward region.

Bibliography

[1] H1 Collaboration, **The H1 Detector at HERA**, Internal Report DESY H1-96-01.

[2] B.H. Wiik, **Proceedings of the workshop, 'Physics at HERA'** , vol. 1 (1991) ed. W.Buchmuller and G. Ingelman.

[3] M. Conte, W.W. MacKay, **An Introduction to The Physics of Particle Accelerators**, World Scientific 1991.

[4] H1 Collaboration, T.Ahmad et al.,**Z. Phys.** C66 (1995) 529.

[5] S. Kermich, **Ph.D. thesis**, Orsay 1994.

[6] H1 Collaboration, T.Ahmad et al., **Luminosity Measurements in the H1 experiment at HERA**, Proceedings of the 28th ICHEP'96, Warsaw, July 1996.

[7] H1 Collaboration, I.Abt, **Nucl. Instr. and Meth.** A386 (1997) 348.

[8] J. Bürger et al., **Nucl. Instr. and Meth.** A279 (1989) 1217.

[9] K. Müller et al., **Nucl. Instr. and Meth.** A312 (1992) 457.

[10] G.A Beck et al., **Nucl. Instr. and Meth.** A283 (1989) 471.

[11] H. Grassler et al., **Nucl. Instr. and Meth.** A323 (1991) 401.

[12] H. Grassler et al., **Nucl. Instr. and Meth.** A283 (1989) 622.

[13] J.M. Bailey et al., **Nucl. Instr. and Meth.** A323 (1992) 184.

[14] H. Grassler et al., **Nucl. Instr. and Meth.** A310 (1991) 535.

[15] J.Katzy, **Ph.D. Thesis** (in German), Heidelberg 1997.

[16] B.Schwab, **Ph.D. Thesis** (in German), Heidelberg 1996.

[17] PDG'98, C. Caso et al., **Eur. Phys. J** C3 (1998) *and references therein.*

[18] R. Wigmans, **NIKHEF** H/87-12 (1987).

[19] R. Wigmans, **Nucl. Instr. and Meth.** A259 (1987) 389.

[20] R. Wigmans, **CERN-PPE** 91/39(1991).

[21] H.P. Wellisch et al, **preprint MPI-PhE/94-03** (1994).

[22] J.F. Laporte, **Ph.D. Thesis** (in French), Orsay 1991.

[23] H1 Calorimeter Group, B.Andrieu et al., **Nucl. Instr. and Meth.** A336 (1993) 460.

[24] H1 Spacal Group, E. Barrelet et al., **Nucl. Instr. and Meth.** A346 (1994) 137;
H1 Spacal Group, T. Nicolls et al., **Nucl. Instr. and Meth.** A386 (1997) 397.

[25] H1 Spacal Group, T.Nicolls et al., **Nucl. Instr. and Meth.** A374 (1996) 149;
H1 Spacal Group, E. Barrelet et al., **Nucl. Instr. and Meth.** A346 (1994) 137;
R.Wigmans, **Nucl. Instr. and Meth.** A315 (1992) 299.

[26] H1 Spacal Group, T.Nicolls et al., **Nucl. Instr. and Meth.** A404 (1998) 265.

[27] M.Weber, **Proceedings of the Beijing Calorimetry Symposium** 1994.

[28] G. Muller, **Proceedings of the 5th Int. Conf. on Calorimetry in HEP**, 1994.

[29] H1 Spacal Group, T. Nicolls et al., **DESY Red Report 96-013** 1996.

[30] J. Janoth,**Ph.D. Thesis**, Heidelberg (1996).

[31] S.Spielmann, **Ph.D. Thesis** (in French), Orsay 1996.

Chapter 3

Data Selection and Simulation

For the structure function measurements, the selection of DIS events from the entire event sample, and a precise description of the detector by Monte Carlo simulation are of fundamental importance. This chapter mainly discusses how the data acquisition and the event selection are performed. In the measurement, the Monte Carlo simulation is used for acceptance corrections, efficiency calculations, radiative corrections and the unfolding of the data, the remaining photoproduction background is subtracted statistically using the simulation therefore the description of Monte Carlo programs used is presented in this chapter. The different event signatures, including the different sources of background are discussed in section 3.1. In section 3.2 we discuss the data acquisition system and the trigger system. Section 3.3 describes the selection of data. Section 3.4 presents the run selection. In section 3.5 the Monte Carlo simulations are described.

3.1 Event Signatures

At HERA the recognition of DIS events is in general based on the identification of the scattered electron, which is seen in the detector as an isolated electromagnetic cluster. Two major sources of background to DIS occur: photoproduction background, which corresponds to ep events at $Q^2 \simeq 0$ and non ep-background, mainly induced by the beam conditions.

3.1.1 DIS Events

The DIS events seen by the H1 detector allow not only for the identification of the scattered electron, but also for the measurement of a major part of the hadronic final state. If we consider the electron-proton interaction as being the exchange of a virtual photon between the electron and a parton by breaking up the proton, we expect the hadronic final state to contain a current jet, produced by the struck quark and a remnant jet from the residual proton, which will be directed in proton beam direction.

Figure 3.1 is showing a DIS at $Q^2 = 2.7\ GeV^2$ and $x = 2.8 \cdot 10^{-4}$, where the electron can be seen in the SpaCal calorimeter, the current jet in the central region of the detector and the remnant jet around the beampipe in the forward direction.

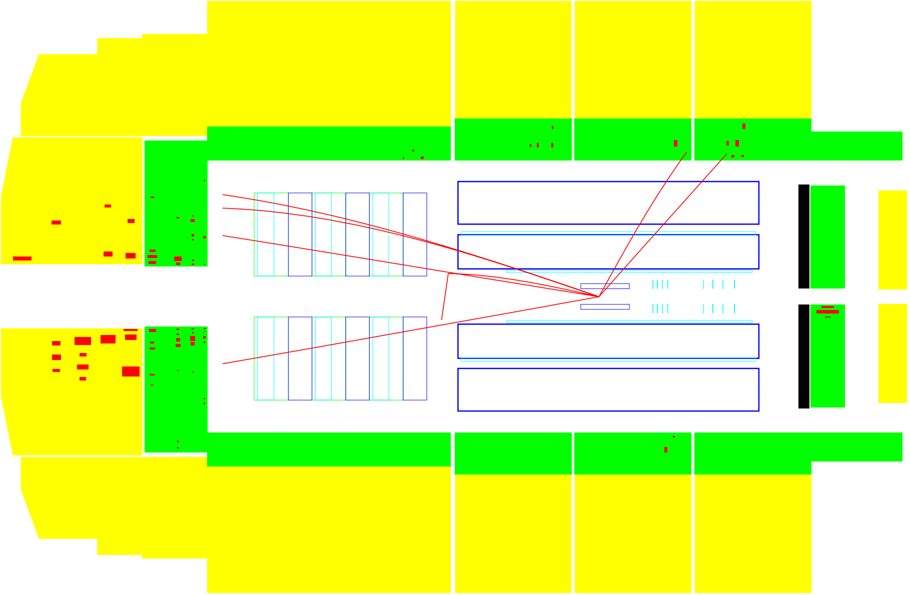

Figure 3.1: *DIS event with scattered electron in SpaCal* $Q^2 = 2.7\ GeV^2$ *and* $x = 2.8 \cdot 10^{-4}$.

Events at higher Q^2, at electron energies below the kinematic peak, are essentially characterized by an increased scattering angle of the electron, and for $Q^2 \simeq 100 GeV^2$, the electron will be detected in the liquid Argon Calorimeter, whereas for $Q^2 \simeq 0.5 GeV^2$ the electron is escaping in the backward beampipe (see also figure 2.4). Decreasing y, and therefore increasing x, will direct the current jet more and more in the forward direction, whereas low x events have low energetic jets directed in the central and backward direction. An example of an low x event is shown in figure 3.2, where the combination of being at low Q^2 and low x leads to an very "unjetty" behaviour of the hadronic final state.

Besides this very simple picture of the behaviour of DIS events, the presence of gluons in the proton can be directly seen, if a hard gluon radiation or photon-gluon fusion occurs, and a third jet is observed in the events. This effect is however more pronounced in events at high Q^2 as can be seen in figure 3.3, where the electron is detected in the liquid Argon calorimeter.

3.1.2 Photoproduction background

For $Q^2 \leq 10^{-2}\ GeV^2$, the photon exchanged is quasi real, which means the electron has only a very small scattering angle and it escapes therefore through the beam pipe. The hadrons produced in such an event can mimic an electron in the backward region and lead to a misidentification, especially for events at high y, an example of such an event is shown in figure 3.4. Depending on the way the fake electron is

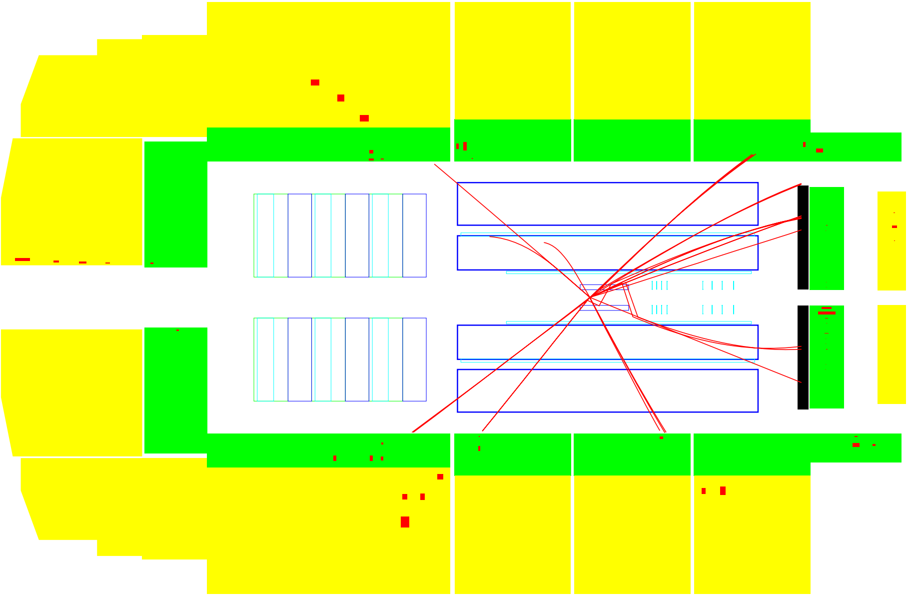

Figure 3.2: *DIS event at low* $Q^2 = 1.3\ GeV^2$ *and low* $x = 4.2\ 10^{-5}$.

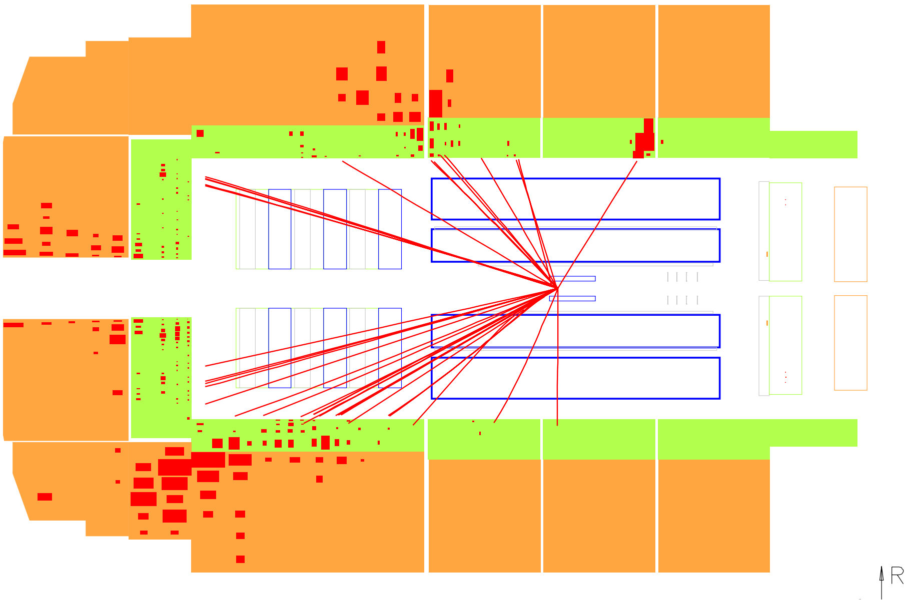

Figure 3.3: *DIS event at high* Q^2 *(electron in liquid Argon) with a supplementary jet from a hard QCD-Compton or photon-gluon fusion process.*

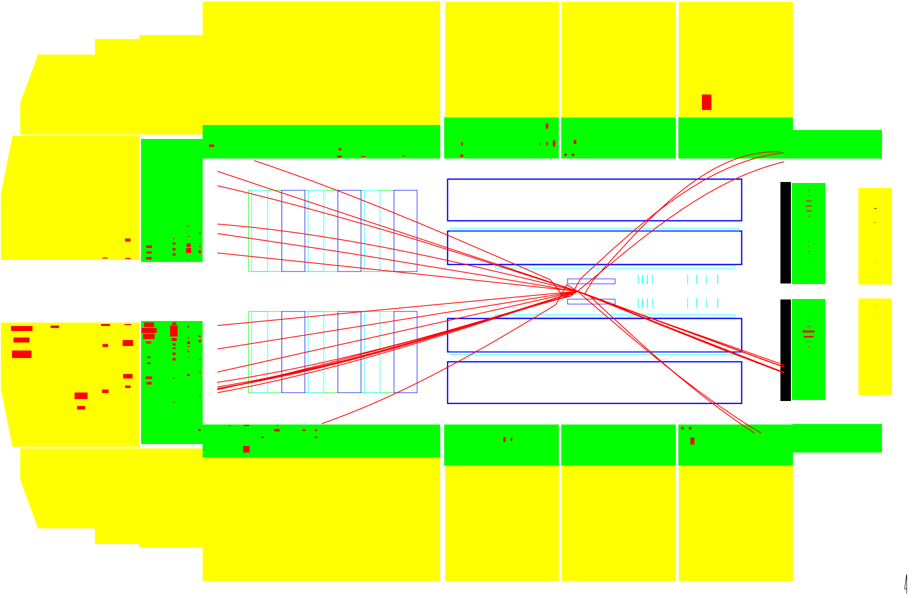

Figure 3.4: *Tagged photoproduction event with misidentified fake electron in the Spacal of* $E' = 8.3\ GeV$.

produced, we can classify the γp background as follows,

- A charged pion can be misidentified as an electron, being a charged particle, it produces a track and especially at low energy it may be contained in the electromagnetic part of the calorimeter.
- The neutral pions have a very short life-time i.e. $\tau \sim 0.87.10^{-16} s$ and decay into two photons before reaching the calorimeter. The photons produce electromagnetic clusters, but leave in general no tracks in the BDC, except if they convert to an e^+e^- pair or start showering in the dead material in front of the BDC.
- The overlapping of a photon and a charged pion may effect the DIS sample. A high energy cluster is induced by the photon and a charged track is measured from the pion, thus giving an image of a fake electron.

The fake electrons are mainly produced at low energy and we try to minimize these γp backgrounds by different requirements in the events selection. A presence of at least one BDC track associated to a cluster in SpaCal, removes non-converted photons, whereas pions have usually a larger transverse cluster size than electrons and leave also more energy in the hadronic section and can be rejected by selecting events where the cluster of the electron candidate has a limited lateral and longitudinal shower size. The energy and the longitudinal momentum conservation leads us to

$$\frac{\sum_i (E_i - P_{z,i})}{2E_e} = 1 \tag{3.1}$$

where i indicates the sum over detected particles in the event. The escaping electron in the backward direction of the beam pipe reduces the left side of this equation and by putting a lower limit of 0.634 we further reduce the photoproduction background.

3.1.3 Non-*ep* background

The rate of non-ep background production at HERA is several orders of magnitude higher than the production of DIS events. The major part is due to beam induced interactions like beam-gas collisions or beam-pipe wall collisions. The production rate is about 50 kHz (compared to a rate of DIS low Q^2 events of about 1 Hz only) and varying with the beam conditions, i.e. highest in the beginning of a luminosity fill. A typical event of beam-gas interaction is shown in figure 3.5. These events are in most of the cases produced upstream and can be rejected by requiring a correct timing measurement from different devices (Veto-Counters, SpaCal, Central Tracking System) or a correct vertex position.

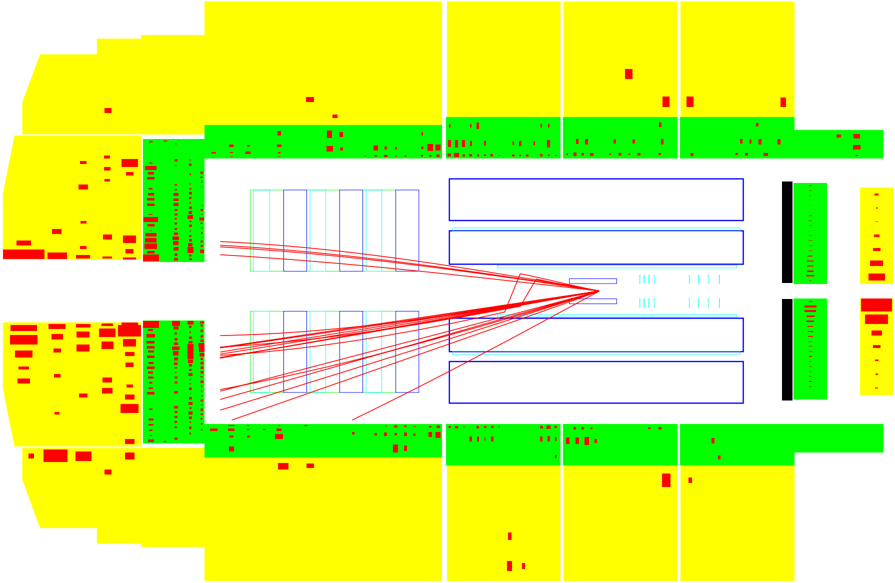

Figure 3.5: *Beam-gas event.*

Synchrotron radiation, which is produced by the inclination of the electron beam a couple meters in front of the interaction region, can leave energy depositions of about 5 GeV especially in the region close to the beampipe of the SpaCal calorimeter (figure 3.6). A cumulation of such events, called “Hot Spot” [1], was observed during the 1995 running, as the increased geometric acceptance of the SpaCal covered for the first time the given region and are creating unacceptable high trigger rates. As the synchrotron radiation is in time with the electron beam, these events can not be simply rejected by a timing requirement, and changes in the beam optics did not

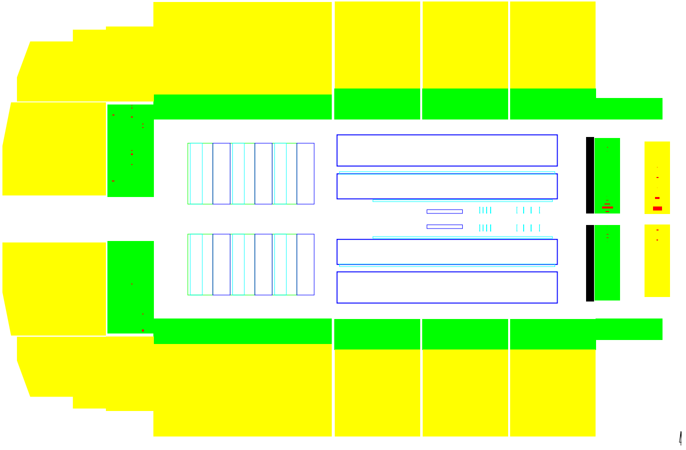

Figure 3.6: *"Hot Spot" Event.*

removed this Hot Spot, but only shifted it. The final way out consisted in taking this innermost cells out of the SpaCal trigger.

A final background contribution is due to showering muons, either from beam halo muons or cosmic muons, (figure 3.7 is showing a halo muon event). Most of

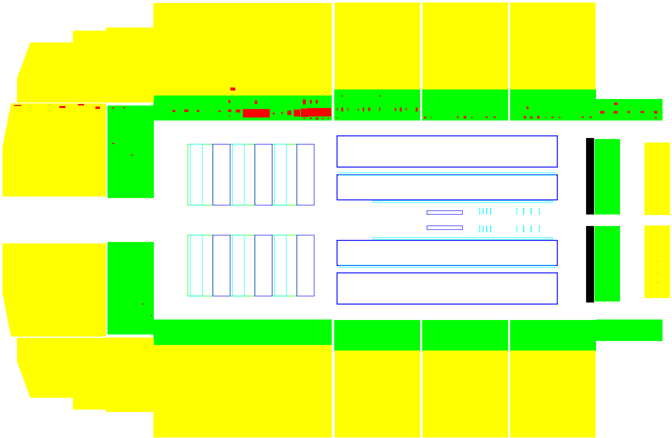

Figure 3.7: *halo muon event.*

these events are easily rejected by the timing and vertex criteria, but for example overlap of muons with photoproduction or Bethe-Heitler events may fake DIS events. Besides being background, special runs are taken either with no beams for cosmic muons, or with stable proton beam for halo muon events, which can be considered as Minimum Ionizing Particles and can therefore be used for calibration purposes (see section 4.2.4).

3.2 The Data Acquisition and the Trigger System

The complex signals from different physical processes provide distinct properties for an event, and the identification of their characteristics allows to select these events with the trigger system and to record them through the Data Acquisition. By looking at some rough figures, one can see how challenging the task is for the data acquisition and the trigger system of H1 [2] (see figure 3.8). There are about $270,000$ channels from all subdetectors which requires about 3 $Mbyte$ of memory per event. The multi-bunch beams have a collision frequency of 10.4 MHz which gives a time separation between bunch crossings of 96 ns. All the information from the detector subsystems is in form of analog signals before they are converted in digital signals and synchronized to the corresponding bunch crossings (BC) and finally formated and written to tape.

The trigger system of H1 has to perform several tasks. The asymmetric beam energies at HERA gives strongly forward-directed event, which can easily be faked by beam-gas interactions.

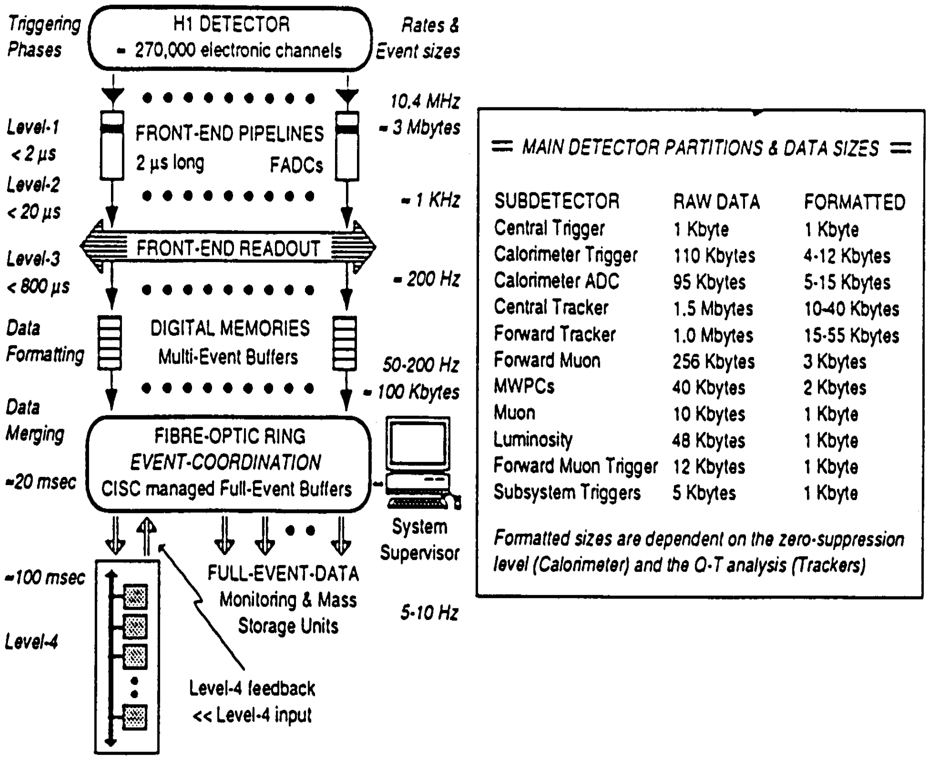

= MAIN DETECTOR PARTITIONS & DATA SIZES =

SUBDETECTOR	RAW DATA	FORMATTED
Central Trigger	1 Kbyte	1 Kbyte
Calorimeter Trigger	110 Kbytes	4-12 Kbytes
Calorimeter ADC	95 Kbytes	5-15 Kbytes
Central Tracker	1.5 Mbytes	10-40 Kbytes
Forward Tracker	1.0 Mbytes	15-55 Kbytes
Forward Muon	256 Kbytes	3 Kbytes
MWPCs	40 Kbytes	2 Kbytes
Muon	10 Kbytes	1 Kbyte
Luminosity	48 Kbytes	1 Kbyte
Forward Muon Trigger	12 Kbytes	1 Kbyte
Subsystem Triggers	5 Kbytes	1 Kbyte

Formatted sizes are dependent on the zero-suppression level (Calorimeter) and the Q-T analysis (Trackers)

Figure 3.8: *Overview of H1 DATA acquisition (DAQ) system.*

The H1 trigger and data acquisition system consists of four different levels: L1 is a primary dead-time free fast trigger level. L2 is based on the information of the L1 trigger, but analyzing the information more thoroughly using neural network algorithms (L2NN) or combining topological information (L2TT). L3 is used for the event building. L4 is the Filter Farm which uses simplified algorithms from the reconstruction program in order to achieve further rejection before writing to tape. In the following, the different levels are described.

3.2.1 The Trigger and Event Processing Levels

- **L1:** The L1 trigger is a front end pipeline system, where signals are shaped, discriminated, digitized and synchronized to the HERA clock. The information about the general properties of an event are contained in trigger elements (TE) which are Boolean expressions. Their total number is 192 with 16 TE for each subdetector. These elements tell for example, about the presence of charged tracks, their multiplicity, momentum, and distance of closest approach to the nominal vertex, about energy depositions in the electromagnetic and hadronic calorimeters and hits in the muon chambers. The trigger towers in the calorimeter pointing to the interaction vertex and the fast signals of the MWPC allow for a rough estimation of the vertex position.

  The trigger elements are taken to the central trigger system (CTL) consisting of VME boards, where they are logically (AND) combined by programmable coincidence circuits into 128 subtriggers.

  The trigger information is divided in different classes, i.e. physics triggers, monitor triggers (for testing and monitoring events) or cosmic trigger (cosmic muons used for calibration purposes). If required, the rate of each subtrigger can be downscaled independently. This leads to a compromise of useful data, a reasonable trigger rate and a low dead time. Finally a logical (OR) combinations of selected subtriggers gives the L1 signal.

  For the structure function measurements, the subtriggers based on the signature of an electron (in SpaCal or LAr) are used. Along with the timing information from the SpaCal, and the information about the topology of the hadronic final state, this leads to a powerful rejection of the background. Other interaction types are also identified at L1, e.g. the imbalance of p_t characterizes charged current events, jet signals indicate high Q^2 DIS or hard γp interactions and the presence of muons in the muon system may be due to heavy quark production.

  The response of some subdetectors may be slow, for example, the maximum drift time for the tracking chamber is 11 BC, the charge collection and integration of the LAr calorimeter is 13 BC and even delays of several BC may occur from the cable length (20 m standard cable gives 100 ns of delay). The final decision time for an event to be kept or rejected is about 2 μs (24 BC). Further time is needed to distribute this signal and to stop various subdetector pipelines (PL) or else the memory will be overwritten and the information for the relative BC will be lost. The length of the PL for various subdetectors is between 27 to 35 BCs. The output event rate of L1 is about $1kHz$.

- **L2:** (This level is not used for the present analysis as it was not implemented for the 1995 data) L2 consists of a Neural Network trigger (L2NN) and a Topological Trigger (L2TT) along with additional subtriggers and performs a more complex analysis of the events where topological trigger informations from individual subdetectors are combined. The calculation power of several microprocessors and massive use of parallel decision algorithms eases the rapid triggering. The neural network approach uses the advantage of multidimensional correlation between TEs from different subdetectors. The topological information is especially useful to reject the so called "Hot Spot" events, which have an energy deposition in the SpaCal close to the beam-pipe, induced by the electron beam. The decision time for an event to be kept or rejected is 20 μs and the event rate reduced to 200 Hz.

- **L3:** The L3 level is used for the event building: the time consuming readout of the detector elements i.e. digitization of analog energy deposits in the calorimeters, hit search using algorithms based on digital drift chamber information and zero suppression, are performed at this level. As a result the event size is largely reduced and only useful detailed information are recorded. For the calorimeter the use of a parallel farm of digital signal processors (DSP) performs the zero-suppression, pedestal subtraction, gain correction and calibration. The time taken by this level is 800 μs which results in an event rate of 50 Hz and an event size considerably reduced to 100 *kbytes* per event. If the event is rejected, the PL is reactivated immediately, else the event goes to the next level.

- **L4:** The level L4 uses a filter farm consisting of a parallel array of processor boards. For the first time there is a full online access to the raw data of an event and a first reconstruction, using simplified software from the off-line reconstruction is performed, with one event per processor board. After the event is processed completely, the L4 keep or reject decision is made. A genuine ep-scattering event is then sent to the memory buffers. The reconstruction time of an event is of about 800 ms and the L4 reduces the event rate to 5 Hz while the event size goes down to 40 *kbytes* per event.
  Online monitoring: At this level the calibration constants are determined and by use of an online event display and monitoring histograms the quality of the data are continuously checked. In the end, through an optical fiber link events are sent to the computer center for data logging.

- **L5:** The off-line reconstruction is performed on this level. The event processing may take place several times and at different places (External Laboratories). After the reconstruction the events are preselected and classified. Non-classified events are rejected. The events are then stored in two different formats:

1. POT (Production on Output Tapes): All the information is available from raw data (as hits in the tracking chambers for example), to reconstructed data (i.e. tracks) and the physical observables as momentum, mass, energies, time etc. and written on tapes.
2. DST (Data Summary Tapes): An event size reduction is made and only the most useful information is kept, which yields an event size of 10 *kbytes*, and can be stored on disk, allowing for a fast access of the analysis program to the data.

3.2.2 The Trigger Selection

We use three SpaCal based subtriggers, S_0, S_2 and S_3, for our event selection, which are based on the presence of an electron candidate in the SpaCal. In 1995, both S_0 and S_2 apply the same constraint on the SpaCal inclusive electron trigger i.e. the validation of the $IET1$ trigger element is required, which corresponds to a minimum energy of 1 GeV in a window of 4×4 electromagnetic cells, while S_3 requires $IET2$ which means a minimum energy 23 GeV. There are no other constraints on S_0 and S_3, but S_2 further demands a reconstructed vertex in the interaction region from the forward or the central trackers.

As the total L1 trigger rate should be below 10 Hz, prescales were applied for the low Q^2 DIS events. The rates of these triggers are about 2.5, 7 and 2 Hz respectively, after prescaling, with mean prescale factors of 30 for S_0, 2 for S_2 and 4 for S_3.

In our selection, the main trigger was S_2, which has the lowest prescale due to the vertex requirement. S_0 which corresponds to a minimal biased trigger, completed this selection and prevents for biases introduced by the vertex requirement. About 4 % of the events are triggered by S_0 and not by S_2. Finally, S_3 has a much lower prescale, as it is triggering on events with a very energetic electron candidate and allows especially to have no losses in the kinematic peak, where the events are used for the energy calibration of the detector. About 0.5 % of additional events are triggered by S_3, but not by the other two triggers.

3.3 Event Samples

The present analysis is based on reconstructed DST events belonging to the inclusive low Q^2 DIS event classes, determined at L5 (class 10 and 11 in the H1 nomenclature), where the class 10 contains monitoring events and class 11 the physics events. The physics class 11 requires:

- an electromagnetic cluster in the SpaCal with an energy $E > 4$ GeV
- the energy weighted cluster radius ECRA < 4 cm,
- a reconstructed z-vertex from the tracking system within 40 cm of the nominal position.

For events with an electron candidate between 24 GeV and 30 GeV no vertex is required (kinematic peak saver), as essentially no background is expected at this high energies and these events are belonging to the kinematic peak, which is used for the energy calibration of the SpaCal.

For the monitoring class, which is used to control the efficiency of the cuts of the physics class, only events are considered not belong already to the class 11. For each cut which is not fulfilled, additional criterias are required in order to select the most interesting candidates. The basic criteria for class 10 requires an electromagnetic cluster in the SpaCal of 5 GeV, with an energy weighted cluster radius $ECRA < 4.5$ cm. Events with an electromagnetic cluster with a radius above 4.5 cm are accepted, if there is no reconstructed vertex, in order to study the vertex reconstruction efficency, but still a good timing determined with the SpaCal. To limit the beam-induced background in this sample, the energy in the veto layer has to be less than 4 GeV and the energy in the hadronic section of the SpaCal is below 30 GeV.

In order to allow studies of events with low energetic electrons, which will allow F_2 measurements at high y, the events with energy between 2 GeV and 4 GeV in the SpaCal are also accepted if, the cluster radius is less than 4.5 cm, the vertex and timing requirements are fulfilled and the energy in the veto layer is less than 1 GeV, as well as the energy in the hadronic section lower than 30 GeV.

From the events of this two classes, we are producing ntuples, where about 100 words per event are stored. In the Paris analysis chain [3], three different reduction steps $r0$, $r1$ and $r2$ are then performed on the ntuple level, which reduces the CPU-time needed for interactive studies of the data.

The $r1$ and $r2$ level are requiring,

- electron energy $E > 6.5 GeV$
- energy weighted cluster radius $ECRA < 5$ cm
- fiducial cut on the electron cluster or on the associated track position projected in the plan of the BDC at 8 $cm < R < 70$ cm
- the vertex position has to be:
    - **for r1**: within 35 cm around the nominal position, if the vertex is reconstructed by the tracking system
    - **for r2**: within 30 cm and a vertex must be reconstructed by tracking system

Figure 3.9 compares the energy distribution of the scattered electron for these three levels. About a factor of 4 is gained by comparing the processing time of the $r0$ and $r1$ levels. The cuts applied on this preselection are slightly larger than the final cuts, in order to allow calibration procedures without border effects. The use of the $r1$ sample is limited to the determination of the vertex reconstruction efficency.

The selection of the final events is mainly based on a more refined electron identification based on estimators related to the shower shape or the presence of a

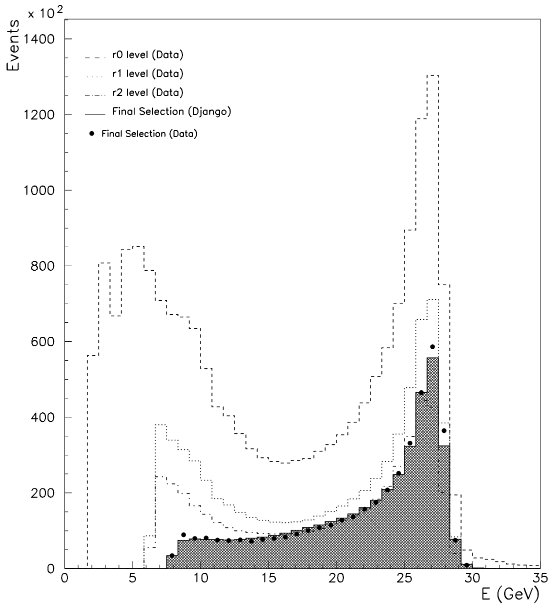

Figure 3.9: *Scattered electron energy comparison at level* $r0$ *(solid line),* $r1$ *(dashed line) and* $r2$ *(dotted line) and after the final selection cuts.*

track associated to the cluster of the electron candidate. The final selection requires the following criterias:

- a reconstructed vertex within 30 *cm* around the nominal position.
- $\sum_i E_i - P_{z,i}/2E_e$ over all particles in the event must be greater than 0.634.
- the presence of an electron-candidate of at least 7 *GeV* in the SpaCal.
- a track associated to the cluster of the electron candidate within 2.5 *cm* (EBDC).
- the energy weighted shower radius of this cluster to be lower than 3.5 *cm* (ECRA).
- the fraction of energy in the hadronic section of the electron cluster to be below 2% (EHAD).
- the SpaCal timing information to be within 10 *ns* around the nominal position.
- the position of the associated track has to be within the fiducial volume of the BDC, i.e. $8.7\ cm < R_{BDC} < 70\ cm$, where R_{BDC} is the radius of the electron-track position in the BDC plane.

The estimators used for the electron identification are described in more detail in chapter 4, but figure 3.10 is showing the distributions of the main estimators used and indicating the cuts applied.

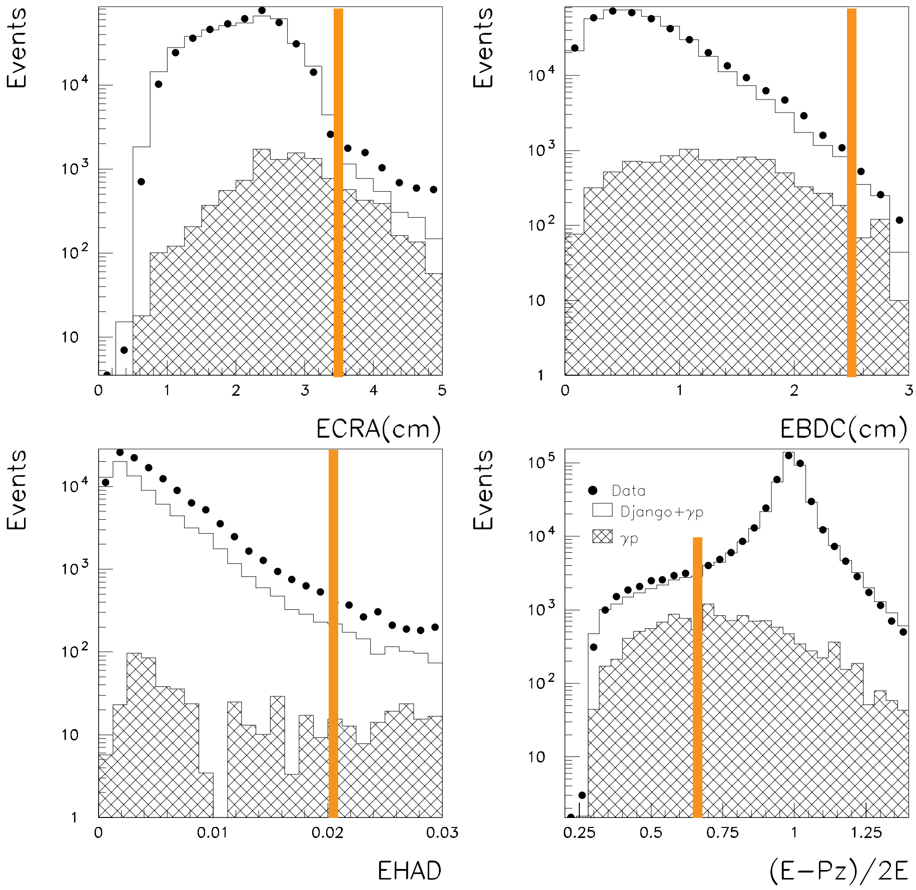

Figure 3.10: *Estimators used for the event selection. The vertical lines indicate the cut values.*

3.4 The Run Selection

We do not use all the runs taken during data-taking but impose a selection based on the presence of active parts of the detectors and followed by a detailed study of the number of events expected for a given luminosity. The information of the presence of different subdetectors in an event and of their HV status are collected by the Slow Control System and are stored in the database, which also includes the online luminosity information. The basic unit of our run selection is the “luminosity fill” which corresponds to one filling of HERA with protons and positrons. A luminosity fill usually lasts for about 9 to 12 hours and is divided in maximum four different phases, determined by the background conditions and each phase is characterized by a default set of subtriggers and their prescales. Moreover each trigger phase is divided in runs, for which the detector conditions are stable. The selection criteria for a run to be considered are following:

- Trigger phase > 1: The Trigger Phase 1 is set immediately after the beam ramping ends, when most of the subdetectors are still not in operation: the

HV for the drift chamber, for example, can only be switched on, after stable beam conditions are reached. Usually there are a few runs for each luminosity fill under these circumstances, which have been excluded from this analysis.

- Good or Medium Run quality: A run is good, medium or bad, depending on the detector stability i.e. the number of high voltage trips in the tracking detectors, the number of operational systems etc. A run is classified Good or Medium if all essential subdetectors like the LAr and the SpaCal calorimeters, the drift chambers and the luminosity system are operational. We are selecting only Good or Medium runs.
- High-voltage-bit selection: The Slow Control System writes to the database, when a subdetector is not at its nominal High Voltage within the 20 seconds after a HV drop. Therefore when a subdetector is partially off during a run, not the whole run has to be rejected, but only the part in which the HV is off and the luminosity is corrected accordingly.
- Events yields: The number of events per unit of luminosity is an important quantity and should be constant as it is directly proportional to the cross-section. The greater the number of events, the better will be its precision, therefore all the runs with a luminosity below 0.2 nb^{-1} are rejected. Among all other runs we select a run i if,

$$\sigma_i = \sqrt{N_i}(1 - \frac{(N/\mathcal{L})_{tot}}{(N/\mathcal{L})_i}) < 4 \tag{3.2}$$

The total luminosity for the 1995 run period from the database (online) was found to be 4936.6 nb^{-1} for a total of 2890 runs. However only 641 runs could be used in the following, as many runs were affected by the BDC and the SpaCal commissioning, and classified "poor" as the related information was not reliable. The total off-line luminosity using the photon method after the trigger phase selection and the run quality selection was 1157 nb^{-1}. During our analysis we rejected 9.1% of the total luminosity due to HV bit correction. A total luminosity of 8.4 nb^{-1} from 124 runs was rejected by the constraint to have luminosity per run greater than 0.2 nb^{-1}. Besides this criteria, 30 runs were rejected which had a higher luminosity than 0.2 nb^{-1}, but no events were found, which corresponding to a total luminosity of 51.56 nb^{-1}. A total number of 11 runs were rejected by the above mentioned 4-sigma criteria corresponding to a luminosity of 53.15 nb^{-1}. The proton satellite bunch correction was estimated to be $(-3.6^{+1.6}_{-0.3})$%. After these corrections we were left with 931.61 nb^{-1}. Taking into account the trigger prescales, this corresponds to a luminosity of 657.35 nb^{-1}. Figure 3.11 shows the variations in the events per luminosity as a function of runs after the trigger selection S_2 and the HV bit corrections with all other selections described above being applied. The rate is of 272.48 events/nb^{-1} with a width 10.1 events/nb^{-1}.

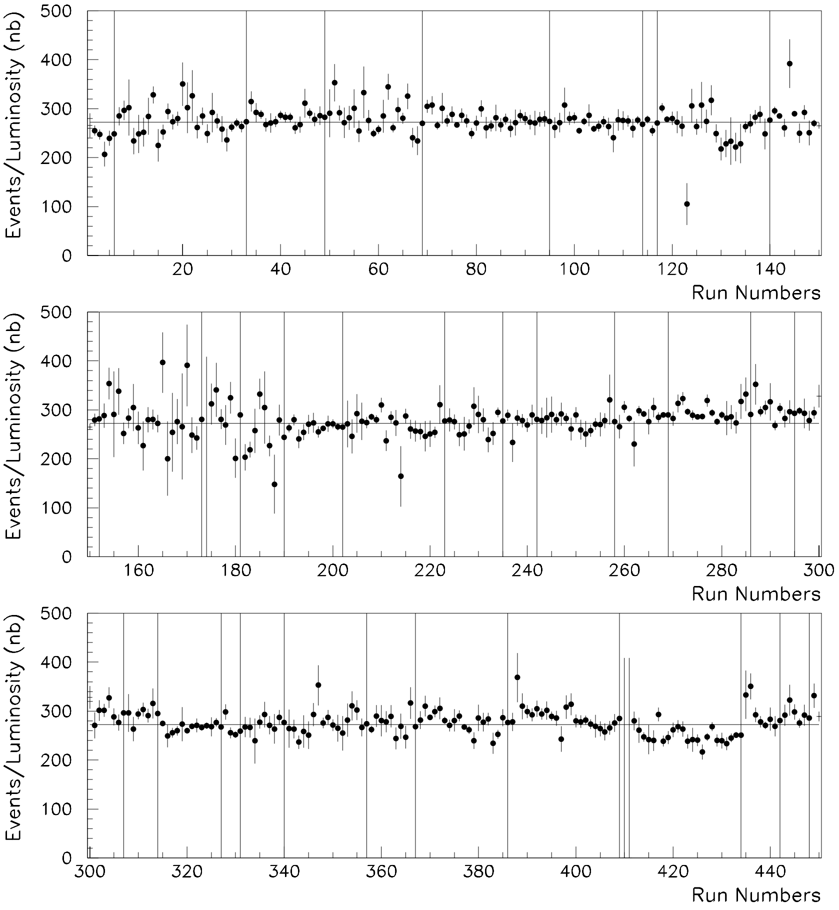

Figure 3.11: *Event per luminosity for selected luminosity runs for subtrigger* S_2 *and after applying the HV bits correction.*

3.5 The Monte Carlo Simulation

In order to correct the data for detector effects, MC simulation is widely used in high energy physics. The Monte Carlo simulation uses random number techniques in order to simulate physical processes. This is not only useful in order to estimate the detector response, but also to evaluate for example the cross sections which can not be computed analytically, as it is done by a big variety of event generator programs. However the events observed in the detector, which are containing all subdetector responses and which are obtained after some sophisticated selection criteria can not be compared with a simple event generator MC without taking the full detector response into account. There are two important steps in the simulation process. Firstly, events are generated for the processes of the particle production to be studied. Secondly, the detector response to the scattered particles is simulated in detail, i.e., when a particle propagates through a detector all the effects like bending in the magnetic field, the interaction in detector material and the response in the active detector elements, are taken into account. These two steps of the event simulation are described in detail below.

3.5.1 The Event Simulation

Events are generated for different physical processes i.e. at HERA photoproduction, deep inelastic scattering, diffraction process allow for the prediction of the cross-sections of processes beyond the Standard Model like Supersymmetry or leptoquark production.

DIS events

The DIS cross-section can be evaluated as function of x and Q^2 for the elastic electron-quark scattering at the Born level. However higher order processes in α e.g. photon radiation (figure 3.12), or higher order QCD processes, like photon-gluon fusion and QCD Compton (see section 1.4.1) or even further higher order processes like QCD cascades are also contributing to the measured cross section. These processes can be factorized and are part of different programs interfaced by DJANGO [3].

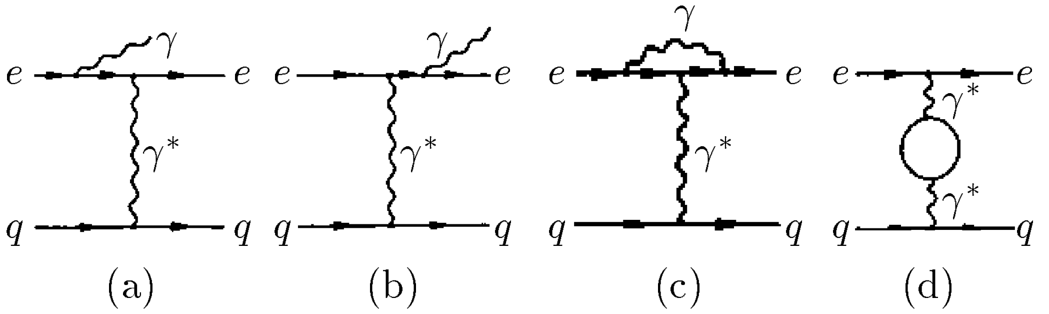

Figure 3.12: *Diagrams for photon radiation considered up to the first order in α for neutral current lepton-quark scattering. Photon-emission from (a) the initial lepton and (b) the final lepton. (c) loop correction for the lepton line and (d) the propagator.*

1. The Electromagnetic Interaction:

   The HERACLES program [14] generates on the partonic level, the processes $eq \to eq(\gamma)$. For the hard scattering the exact matrix element is computed, and in the Q^2 range we are interested, the Z exchange is neglected. The radiative contributions up to order $O(\alpha)$ are implemented coming from Initial State Radiation (ISR) and Final State Radiation (FSR) of a photon from the lepton line (figure 3.12 a,b) and virtual one-loop diagrams (figure 3.12 c,d). The radiative corrections from the quark line are not taken into account.

In order to avoid large virtual QED corrections, which lead to negative non-radiative cross-section, the constraint $y(1-x) \geq 0.004$ has been imposed. The x and Q^2 dependence of the cross section is evaluated by using the GRV504 [17] parton density parameterization from the PDFLIB [18]. The light quarks are considered massless, target mass effects and higher twist effects have been neglected, and F_L was put equal to zero.

2. QCD Radiation:

   The exact calculation of the eq cross-section is not possible beyond first or maximum second order in α_s [4]. Even though the higher orders in QCD do not contribute significantly to the cross-section, they have a major influence on the characteristics of the hadronic final state. Several approximations exist in order to include the higher orders in QCD. Among them two commonly used are:

   - The parton showering (PS) method [5]: A quark before and after a hard scattering can produce a cascade of gluon radiation. The production of the Initial Parton Shower (IPS) and the Final Parton Shower (FPS) is different in that the initial partons are close to the mass-shell in IPS and in the gradual shower production, the virtuality of the daughters increases i.e. the parton becomes more and more space-like while the radiated gluon becomes more and more time-like while contrarily in FPS the scattered parton is usually time-like giving rise to a series of cascades with successively decreasing virtuality till a cut-off where the cascade production stops. The FPS is well understood and experimentally tested in $e^+ \, e^-$ interactions while IPS is experimentally less well-established.
   - The color dipole model (CDM) [6]: Here the point color charge of the scattered quark q and the extended color charge of remnant diquark $q\ \bar{q}$ can be treated as a color dipole radiating a gluon. As a result of the radiation of a single gluon, two color antennas are formed (quark-gluon and gluon-diquark) and to a good approximation the emission of a second softer gluon can be treated as the radiation from two independent dipoles, the third gluon from three independent dipoles.

   Figure 3.13 is comparing the transverse energy flow measured with the H1 detector [7] with different predictions for gluon radiation and the prediction with the Quark Parton Model, where no gluons are included. The Color Dipole Model gives the best description and its implementation in the ARIADNE [19] program is used in the Monte Carlo mode of the presented analysis.

3. Hadronisation:

   After the generation of the partons, phenomenological fragmentation models like the string model [8] or the cluster model [9] are used to simulate the observed hadrons. In our simulation the LUND-string model, implemented in the JETSET program [20] was used, where a narrow string is formed between

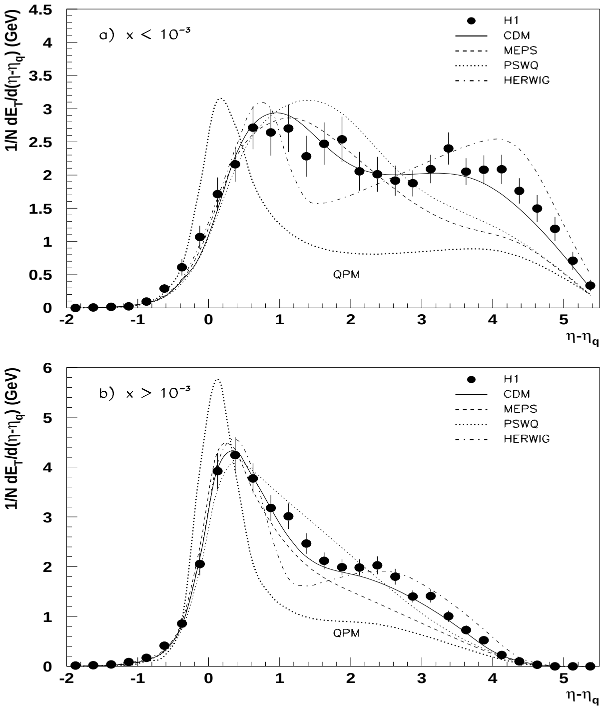

Figure 3.13: *Transverse energy flow E_T in the laboratory system as a function of the pseudorapidity distance to the 'current quark' $\eta - \eta_q$ for events with a) $x < 10^{-3}$ and b)$x > 10^{-3}$ [7].*

the two colors of the outgoing partons with a uniform energy density. The increasing tension in the string breaks it in two parts, thus creating a new $q\bar{q}$ pair, hadronising into a meson.

The common uncertainties in the MC arise from the quark masses which enter in the hard subprocess matrix elements, the choice of the parton density functions, the choice of the evolution order (LO, NLO), the cutoff between the perturbative (QCD-radiation) and the non-perturbative part (hadronisation) and from beam remnants treatments.

Photoproduction events

The PHOJET Monte Carlo was used in the context of the presented measurement with the aim to study the background initiated by photoproduction. Studies of photoproduction processes have shown, that an accurate description can be achieved with this program [21]. One can divide the photoproduction processes into two main categories: 'soft' collisions with $p_T << 1-2\ GeV$ and the hard scattering with very large p_T. The hard processes are of two types:

- Direct γ interactions: The photon is considered as a usual gauge particle which mediates the electromagnetic interaction.
- Resolved γ-interactions: The photon exhibits the features of a composite particle like a normal hadron and so the concept of the photon structure arises

In principle we can separate the direct and the resolved processes by looking at the event topology. In case of direct photon process there is very little energy of the final state in the electron directions while in contrast in the resolved process one can find some energy in the backward direction corresponding to the photon remnants.

As the cross section of the photoproduction process is very high, and we are only interested in the background contribution, the 'turbo' setup is used: events are preselected for the detector simulation, requiring a high energetic particle in the backward direction , which could lead to an electron misidentification.

3.5.2 The Detector Simulation

The 4-vectors of the generated particles are taken as input for the detector simulation. The H1 simulation uses GEANT [10], which is a program package that includes all important interactions of particles with matter. The electromagnetic interactions are parametrized in the H1FAST program [11]. The interactions of hadrons are based on the GHEISHA simulation program [12]. Further input to the simulation are, the detailed description of the detector including geometry, the material composition and the magnetic field B. The generated events are then tracked through the detector and at each step (e.g. each mm of a particle track) a decision is made for the kind of interaction that will occur. For various possible processes a relative probability is defined and then selected and simulated using a random number generator. The step size is adjusted to the detector granularity: a small step size needs large computing time for the simulation but gives a more reliable description of the detector. The tracking includes the response of the active material i.e. the energy deposition and the digitization is also simulated. The final simulation output has the same format as that of the data and is then processed through the same reconstruction and analysis chain as the real data.

In this analysis two Monte Carlo samples are used (based on the DJANGO program): The MC reconstructed and simulated at DESY with $300k$ events of 289.3 nb^{-1} luminosity and the MC reconstructed and simulated in PARIS with $1000k$ events of 831.25 nb^{-1} luminosity. The photoproduction Monte Carlo produced at DESY contains about 130 k events with a luminosity of 150.7 nb^{-1}.

3.6 Summary

The very fast beam-crossing at HERA and the high background rates, are a particular challenge for the trigger and the data acquisition systems of the HERA experiments. However the clean signature of DIS events allow an efficient selection, mainly based on the identification of the scattered electron. Starting from the trigger level $L1$, where the electron identification is reduced to the presence of an energy deposition in the electromagnetic part of the calorimeter, the shower shape and the track requirements are more and more refined up to the final event selection. The residual non-ep background is estimated from visual scanning of parts of the final event sample, to be below 1% and the remaining photoproduction background is simulated by the PHOJET-event generator. In order to determine the corrections for the geometrical acceptance and the efficiencies, DIS-events have been generated by the DJANGO program, and have been fully simulated and reconstructed, corresponding to nearly twice the luminosity of the data-sample. The luminosity from 1995 running, which could be used for the data analysis at low Q^2, had to be carefully selected and corresponds only to about 1/5 of the total luminosity accumulated, due to the commissioning of the new subdetectors.

Bibliography

[1] P. Zini, **Ph. D. Thesis** (in French), University of Paris 6 (1992).

[2] H1 Collaboration, I. Abt et al., **NIM** A386 (1997) 310.

[3] U. Bassler, G. Bernardi, B. Gonzalez-Pineiro, I. Ayyaz , *H1 Note in preparation.*

[4] D. Graaudenz, N. Magnussen, **Proceedings of the Workshop 'Physics at HERA'**, eds. W. Buchmüller and G.Ingelman, vol1, DESY (1992) 261.

[5] B.R. Webber, **Ann. Rev. Nucl. Part. Sci.** 36 (1986) 253.

[6] B. Andersson, G. Gustafson, L. Lönnblad, **Nucl. Phys.** B339 (1990) 393.

[7] H1 Collaboration, I. Abt et al., **Z. Phys.**C63 (1994) 377.

[8] B. Andersson et al., **Phys. Rep.** 97 (1983) 31.

[9] S. Catani, G. Marchesini, B. R. Webber, **Nucl. Phys.** B349 (1991) 635.

[10] R. Brun et al, GEANT3 User's Guide, **CERN-DD/EE** 84-1,Geneva (1987).

[11] S. Peters, **Ph. D. Thesis** (in German), University of Hamburg (1992).

[12] H. Fesefeld, **GHEISHA, RWTH Aachen**, PITHA 86/05 (1986).

[13] G.A. Schuler, H. Spiesberger, **Proceedings of the Workshop 'Physics at HERA'**, eds. W. Buchmüller and G.Ingelman, vol3, DESY (1992) 1419.

[14] A. Kwiatkowski, H. Spiesberger and H.J. Möhring, **Comp. Phys. Comm.** 69 (1992) 155.

[15] G.Ingelman, **Proceedings of the Workshop 'Physics at HERA'**, eds. W. Buchmüller and G.Ingelman, vol3, DESY (1992) 1366.

[16] A. Arbuzov et al., **Comp. Phys. Commun.** 94 (1996) 128.

[17] M.Glück, E.Reya, A. Vogt, **preprint DO-TH** 98/07.

[18] H. Plothow-Besch, **User Manual**, CERN W5051.

[19] L. Lönnblad, **Comp. Phys. Comm.** 71 (1992) 15.

[20] T. Sjöstrand, **CERN-TH-6488** (1992)

[21] H1 Collaboration, S. Aid et al., **Z.Phys.** C70 (1996) 17.

Chapter 4

Data treatment and analysis

As the measurement of F_2 is based on the double differential cross-section as a function of the kinematic variables x and Q^2, it is necessary to select the suitable events free from background and to reconstruct the kinematic variables. Therefore the scattered electron has to be identified and its energy and angles have to be measured precisely along with those of the particles belonging to the hadronic final state.

This chapter basically consists of four main sections. The section 4.1 describes the reconstruction of the kinematic variables using the electron method, the sigma method and the electron-sigma method and discusses the errors in each method. In the next section we discuss the electron identification. In this context, the estimators are introduced to achieve a better electron finding efficiency and the efficiencies of the identification is discussed. In the same section we describe the electron calibration in detail. The section 4.3 treats the hadronic final state reconstruction. The SpaCal noise along with possible treatments for its suppression are discussed. The section 4.4 is devoted to the vertex reconstruction, where the vertex re-weighting procedure is described in detail, the correction for the beam-tilts is shown and the vertex reconstruction efficency discussed.

4.1 The Reconstruction of Kinematic Variables

At H1, compared to many fixed target experiments, we have the possibility of different methods for the reconstruction of the kinematic variables due to available information from both the scattered electron and the hadronic final state i.e. angles and energies of the particles belonging to the hadronic final state, not escaping through the forward beampipe. This gives us four independent measured quantities E' and θ from the scattered electron and Σ and $p_{T,h}$ from the hadronic final state, in order to reconstruct two independent kinematic variables.

Although two types of reconstructions are most commonly used i.e. the electron method and the Σ-method, we will use the new eΣ method for the F_2 measurement. The main kinematic reconstruction methods used by H1 are:

- **Electron (e) Method:** The method uses E' the energy of the scattered electron and θ its angle. The kinematic variables y, Q^2 and x are reconstructed as,

$$y_e = 1 - \frac{E'(1-\cos\theta)}{2E} \tag{4.1}$$

$$Q^2_e = 4EE'\cos^2\frac{\theta}{2} \tag{4.2}$$

$$x_e = \frac{Q^2_e}{sy_e} \tag{4.3}$$

The resolution of these variables depend on the resolutions in E' and θ. This method is very precise in the high y region while in the low y region it has large uncertainties, since

$$\frac{\delta y_e}{y_e} = \frac{1-y_e}{y_e}\left(\frac{\delta E'}{E'} \oplus \frac{\delta\theta}{\tan\theta/2}\right) \tag{4.4}$$

contains y in the denominator. So for small y, the errors become very large.

- **Hadron (h) Method [1]:** This method uses the energy and the angle information from the final state hadrons only. If we define $\Sigma = \sum_i (E_i - p_{z,i})$ and $p_{T,h} = \sqrt{(\sum_i p_{x,i})^2 + (\sum_i p_{y,i})^2}$, where we sum over all hadronic final state particles i, we can express

$$y_h = \frac{\Sigma}{2E} \tag{4.5}$$

$$Q^2_h = p^2_{T,h}/(1-y_h) \tag{4.6}$$

The method gives a good y measurement at low and medium y ($y < 0.2$) while it degrades at high y and a poor Q^2 measurement. This is due to the loss of hadrons in the beam pipe which affects strongly $p_{T,h}$, where the energy lost is weighted by the angle of the lost particle, as $\sin x_i \to x_i$ for $x_i \to 0$, whereas Σ is less affected by the losses, as they are weighted only by $x_i^2/2$ as $1-\cos x_i \to x_i^2/2$ for $x_i \to 0$. Therefore the h-method is only used for charged current events, where the outgoing neutrino can not be detected.

- **Double-Angle (DA) Method [2]:** The method uses only angular information from the electron and the hadronic final state with the hadronic angle γ defined as

$$\tan\frac{\gamma}{2} = \frac{\Sigma}{p_{T,h}} \tag{4.7}$$

y and Q^2 can be derived as

$$y_{DA} = \frac{\tan\frac{\gamma}{2}}{\tan\frac{\gamma}{2} + \tan\frac{\theta}{2}} \tag{4.8}$$

$$Q^2_{DA} = 4E^2\frac{\cot\frac{\theta}{2}}{\tan\frac{\gamma}{2} + \tan\frac{\theta}{2}} \tag{4.9}$$

y_{DA} is independent of the initial electron energy and therefore not affected by initial state radiation, but Q^2_{DA} depends quadratically on it. The method has reasonable resolution at medium y ($0.05 \leq y \leq 0.3$) and is precise at high Q^2 ($Q^2 > 100\ GeV^2$).

At the first order this method is independent of any absolute energy calibration and is therefore used for the energy calibration of scattered electron using the relation

$$E'_{DA} = 2E \frac{\sin\gamma}{\sin\gamma + \sin\theta - \sin(\gamma + \theta)}. \tag{4.10}$$

- **Sigma (Σ) Method [4]:** This method uses the information from both the scattered electron and the final state hadron system according to,

$$y_\Sigma = \frac{\Sigma}{\Sigma + E'(1 - \cos\theta)} \tag{4.11}$$

$$Q^2_\Sigma = \frac{E'^2 \sin^2\theta}{1 - y_\Sigma} \tag{4.12}$$

$$x_\Sigma = \frac{Q^2_\Sigma}{s y_\Sigma} \tag{4.13}$$

Contrary to the electron method, the errors on y are given by,

$$\frac{\delta y_\Sigma}{y_\Sigma} = (1 - y_\Sigma)(\frac{\delta\Sigma}{\Sigma} \oplus \frac{\delta E'}{E'} \oplus \frac{\delta\theta}{\tan\theta/2}) \tag{4.14}$$

There is no $1/y$ term in the error propagation therefore this method gives a good precision in the y reconstruction at small values. At high y the large errors $\frac{\delta\Sigma}{\Sigma}$ are compensated by $1 - y$ term.

For the electron method we expect large radiative corrections from the initial state radiation of photons, which do not give the correct incident electron energy and enter directly in the calculation of the kinematic variables. If we look for example at the y reconstruction for the electron method, the initial energy of the electron is smaller, when a photon was radiated, than the one used in the formula, and the events are therefore migrating towards high y. In the Σ method, the use of the energy momentum conservation is made to replace the incident electron energy in the y calculation as

$$2E = \Sigma + E'(1 - \cos\theta) \tag{4.15}$$

and it has therefore small radiative corrections [3], as can be seen in figure 4.1. In fact, we are using in the Σ-method three independent variables, E', θ and Σ, but are computing in addition the initial electron energy.

To compare the resolution of the $e-$ and the $\Sigma-$method, we have divided the kinematic domain into three parts i.e. the small y region ($0.01 < y < 0.1$), the medium y region ($0.1 < y < 0.5$) and the high y region ($y > 0.5$). In figure 4.2, we compare x_{rec}/x_{gen} for simulated events. The first row shows the e-method, the second the Σ-method. The e-method gives a good x reconstruction at large

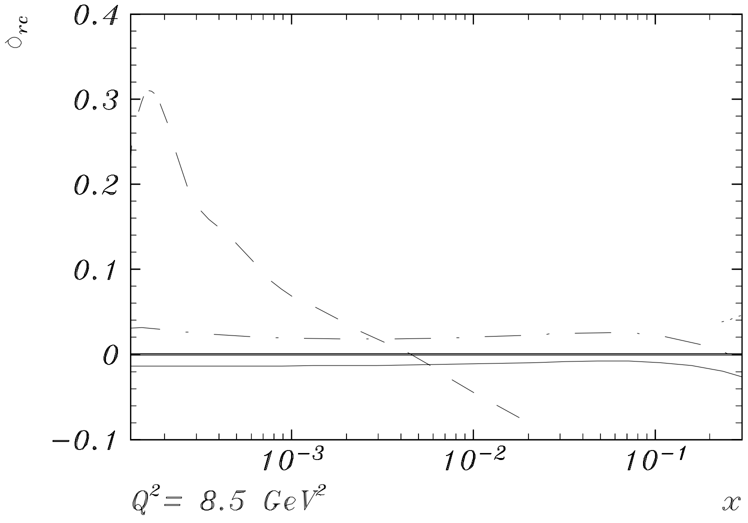

Figure 4.1: *Radiative corrections at* $Q^2 = 8.5$ GeV^2 *for e- (dashed line),* Σ*- (thin solid line) and e*Σ*-method (dash-dotted line) for* $x \geq 10^{-4}$ *[4]. The thick solid is indicating no radiative corrections.*

y, however it degrades rapidly as one moves to small y. The Σ-method gives a good y reconstruction throughout. Although the resolution gets worse at low y, the distributions stays mainly Gaussian and centered.

In the Q^2 reconstruction (figure 4.3), the Σ-method has the largest resolution at high y, however the Q^2 reconstructed from the electron gives a very good resolution in the whole y region.

- Electron-sigma ($e\Sigma$) method [5]: This method is a mixture of the electron method and the sigma method. The fact that the electron method has a better reconstruction of Q^2 and the Σ method a better reconstruction of x allows a combination of Q_e^2 and x_Σ and defines the electron-sigma method as $Q^2_{e\Sigma} = Q^2_e$ and $x_{e\Sigma} = x_\Sigma$. In this method y is given by

$$y_{e\Sigma} = \frac{Q_e^2}{s x_\Sigma} = \frac{2E\Sigma}{(\Sigma + E'(1-\cos\theta))^2} \tag{4.16}$$

  Compared to the $\Sigma-$ method the y is rescaled by the factor $2E/(\Sigma + E'(1 - \cos\theta))$, which improves the y reconstruction as can be seen in figure 4.4, where we compare y_{rec}/y_{gen} for the three reconstruction method. It is interesting to notice, that event though we used the energy-momentum conservation in the y reconstruction, and introduce therefore a sensitivity to initial photon radiation, the radiative corrections stay rather small and constant in x (figure 4.1).

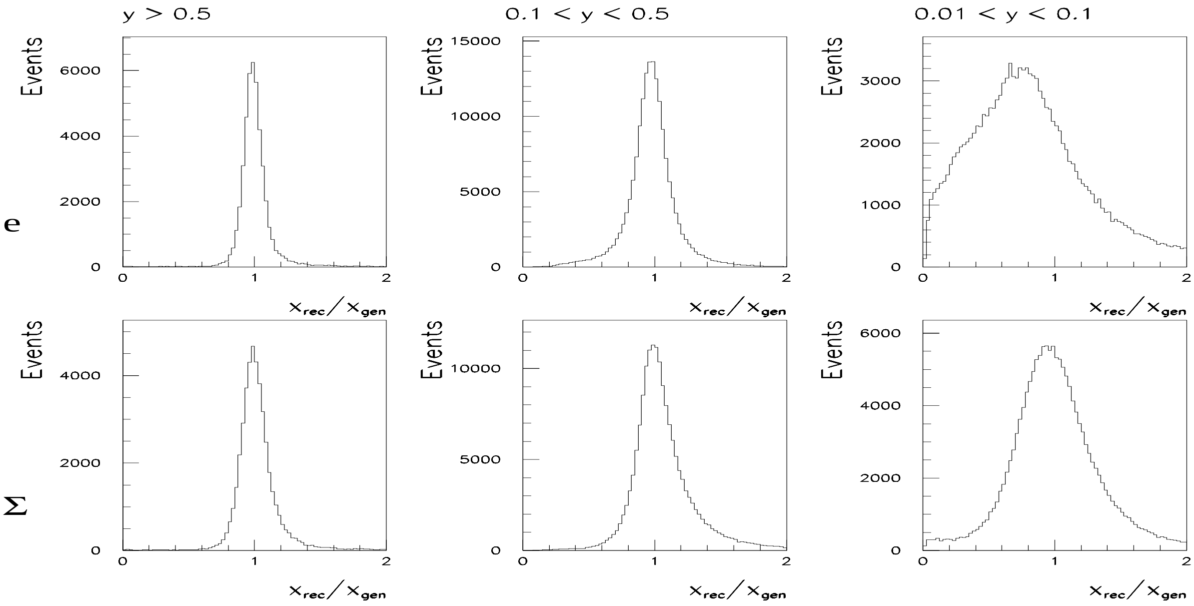

Figure 4.2: *Reconstruction results by looking at* x_{rec}/x_{gen} *using (1)e-method and (2)* Σ*-method in three different kinematic regions i.e.* $0.5 < y_{gen}$, $0.1 < y_{gen} < 0.5$ *and* $0.01 < y_{gen} < 0.1$.

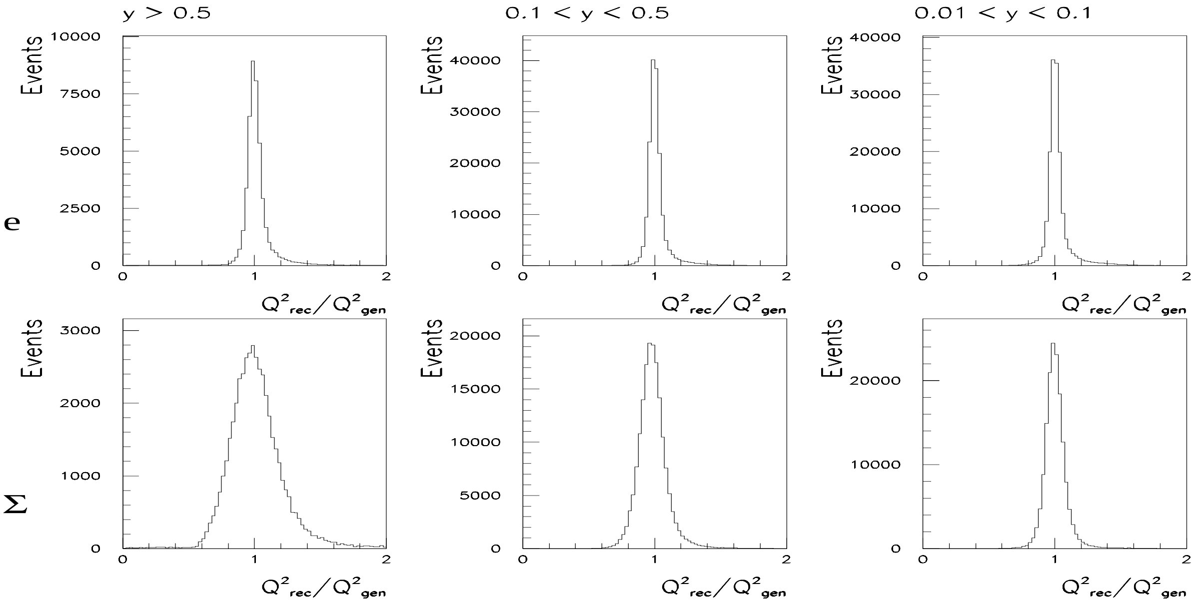

Figure 4.3: *Reconstruction results by looking at* Q^2_{rec}/Q^2_{gen} *using (1)e-method, (2)* Σ*-method in three different kinematic regions i.e.* $0.5 < y_{gen}$, $0.1 < y_{gen} < 0.5$ *and* $0.01 < y_{gen} < 0.1$.

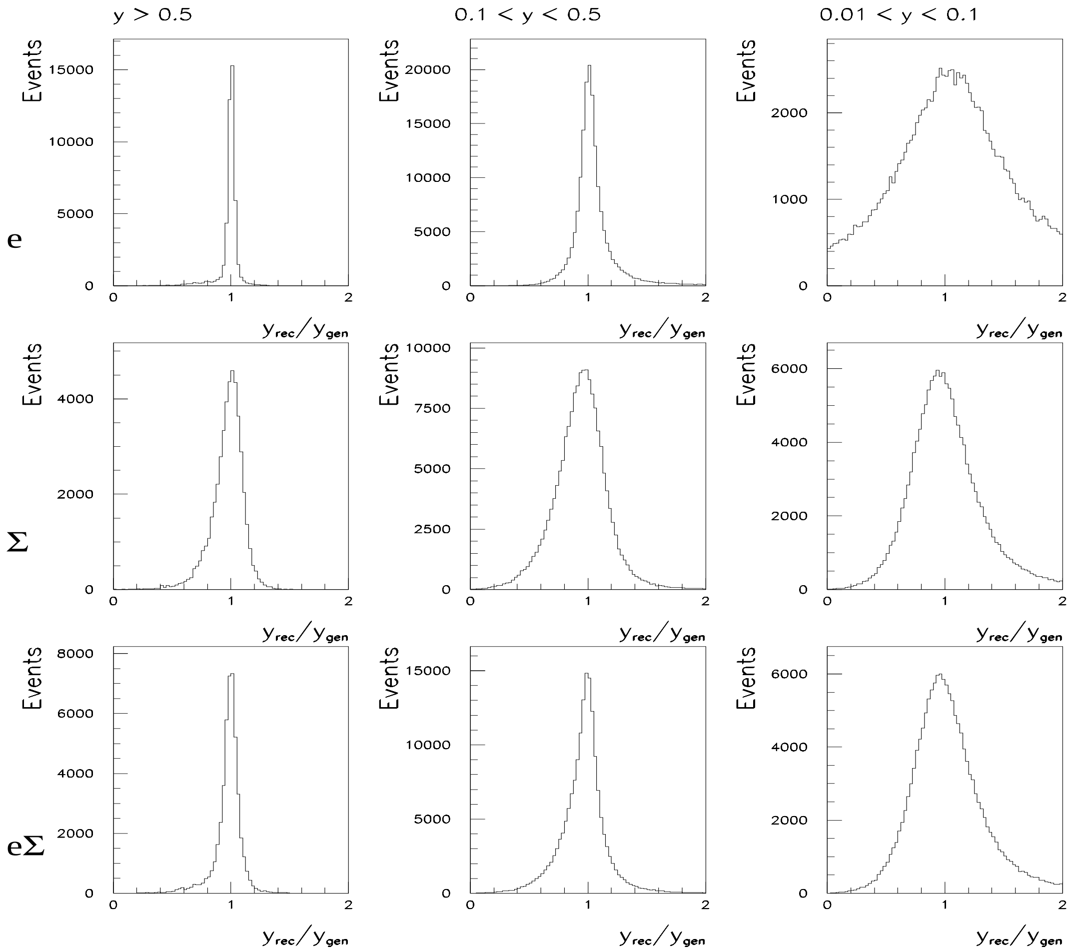

Figure 4.4: *Reconstruction results by looking at* y_{rec}/y_{gen} *using (1)e-method, (2)* Σ*-method and (3) e*Σ*-method in three different kinematic regions i.e.* $0.5 < y_{gen}$, $0.1 < y_{gen} < 0.5$ *and* $0.01 < y_{gen} < 0.1$.

4.2 The Electron Identification

The selection of DIS events is based on the identification of a scattered electron. Electrons are characterized as being isolated clusters in the electromagnetic section of the calorimeters, therefore electromagnetic clusters of at least 7 *GeV* are considered as 'electron seeds'. If another cluster is found within a cylinder of 8.5 *cm*, pointing to the event vertex, it is merged to the seed cluster and forms an electron candidate.

4.2.1 Electron Estimators

An electron candidate is validated, by evaluating the energy weighted shower radius ECRA, the leakage of energy in the hadronic section of SpaCal EHAD and the distance to the closest BDC track, EBDC. The values on which we cut, have always to be a compromise of getting a pure sample without loosing efficiency.

ECRA

The electron shower radius is defined from the distance of each cell to the shower center of gravity weighted by its energy. We define the linear energy weighted shower radius as

$$ECRA = \frac{1}{E}\sum_i E_i \mid \vec{r_i} - \vec{r} \mid \tag{4.17}$$

Here $\vec{r}$ gives the position of the shower center of gravity with respect to the interaction vertex and $\vec{r_i}$ is the position vector of the center of a cell i of the shower, E_i are the corresponding energies and E is the total energy of the electron

If we look at the energy dependence of ECRA (Figure 4.5), we observe that for larger electron energies the ECRA distribution is more narrow while for smaller electron energies it is broader. This is only partially explained by the fact, that the proportion of fake electron increases at low energy, as clusters from pions are larger than those from electromagnetic particles. The contamination from fake electrons can be increased by not asking for a track in the BDC in front of the cluster. We observe that the absence of the BDC track makes the ECRA distribution broader (figure 4.6).

ECRA shows a very strong dependence on the SpaCal impact point (figure 4.7) reflecting the correlation of ECRA with the SpaCal cell structure. We can change the definition by defining an effective cluster radius which is larger than the cell granularity, by modifying the linear energy weighting by a logarithmic weighting. This has not been implemented in this analysis, but is used for the analysis of the 1996/1997 data.

The width of ECRA is larger in the data than in the simulation due to the imperfect shower description in the MC. The adjustment of the Monte Carlo is done with a shift of 0.1 cm and an additional smearing factor of 1.05 (figure 4.8), after this smearing we have a better description of the data by the simulation. However since we apply a cut of 3.5 cm on ECRA, the efficiency of this cut, which is discussed in section 4.2.3, is not strongly affected.

EBDC

As a charged particle, the scattered electron should leave a track in the BDC in front of the SpaCal, therefore the distance of the closest BDC track to the shower center of gravity is a powerful estimator for the electron identification and to reject photoproduction background (see section 3.1.2). As the position measurement of the BDC is more precise than the one achieved with the SpaCal, we are using this information for the determination of the scattering angle as well.

EBDC is the distance in the $r\varphi$ plane of the closest BDC track to the electron cluster, which been projected to the BDC-plane. EBDC and ECRA are correlated, if ECRA is large, the center of the gravity of the cluster is less precise and hence this results in a broader EBDC distribution.

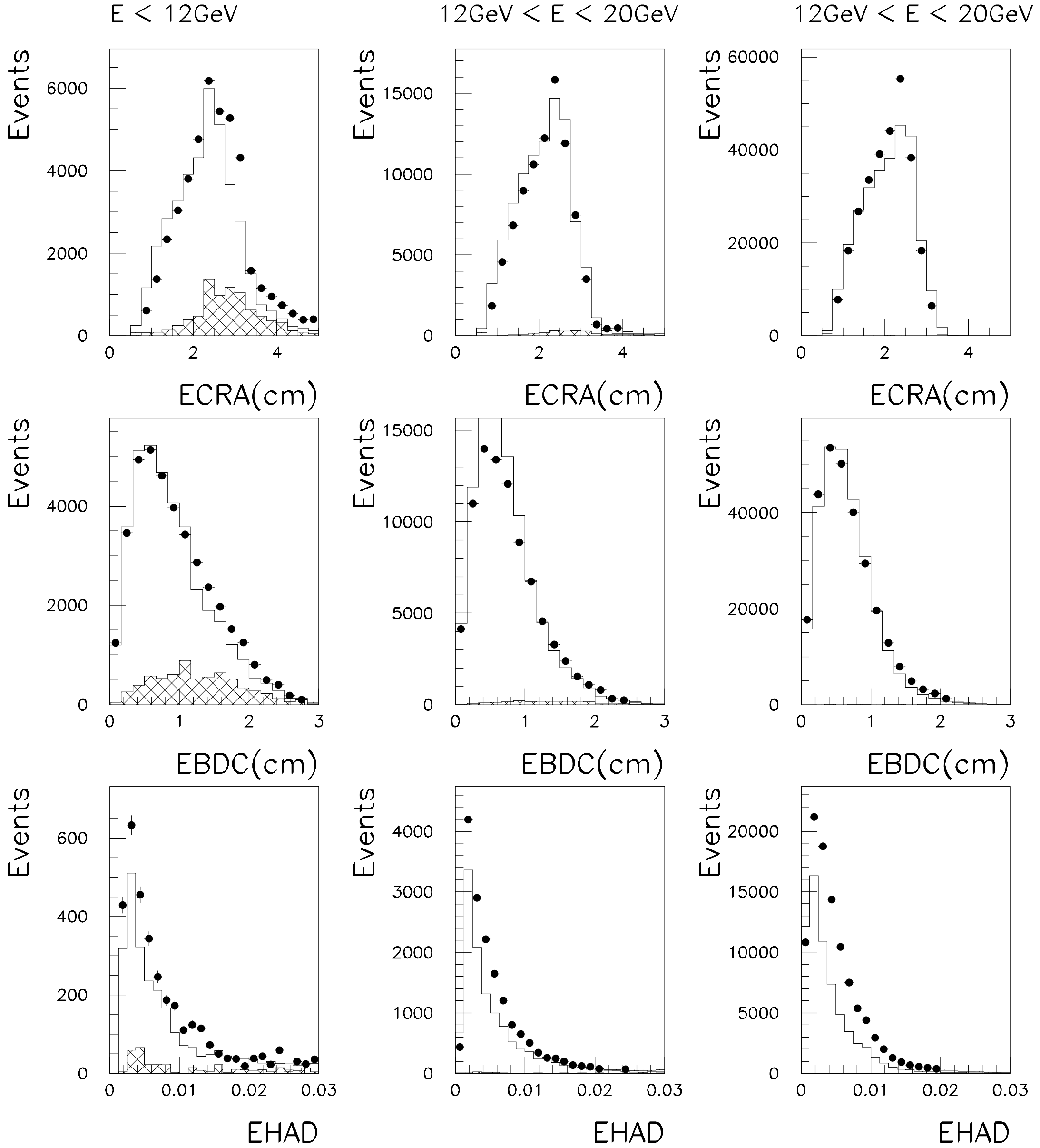

Figure 4.5: *Energy dependence of the estimators is shown for three scattered electron energy ranges (1) $E < 12\,GeV$ (first column); (2) $12\,GeV < E < 20\,GeV$ (second column); and (3) $20\ GeV < E < 30\ GeV$ (third column). The points are for data and the lines for MC. In each estimator the behaviour of the data and the MC is similar. In first row, the significant response to the E of ECRA is noted.*

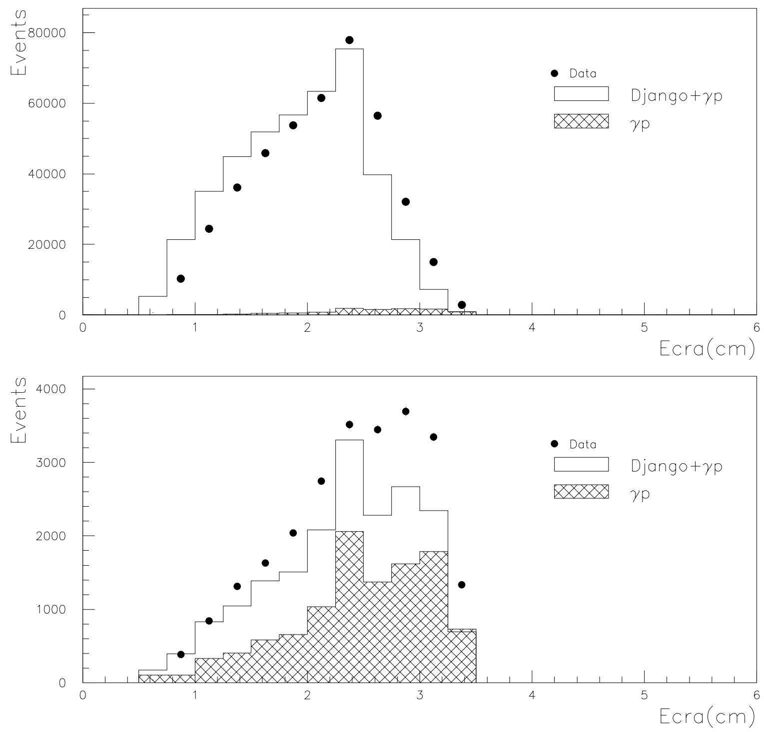

Figure 4.6: *The upper plot shows the distribution of ECRA for the electron candidate with BDC tracks while the lower plot represents those without BDC tracks.*

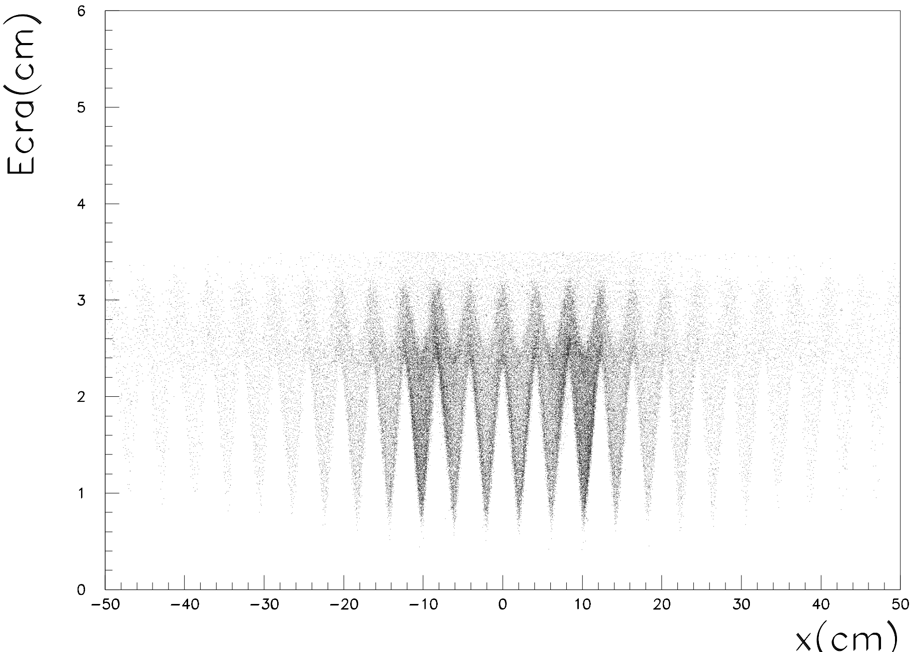

Figure 4.7: *A strong dependence of ECRA on the scattered electron impact point can be seen by looking at ECRA versus x-coordinate of the impact-point in SpaCal.*

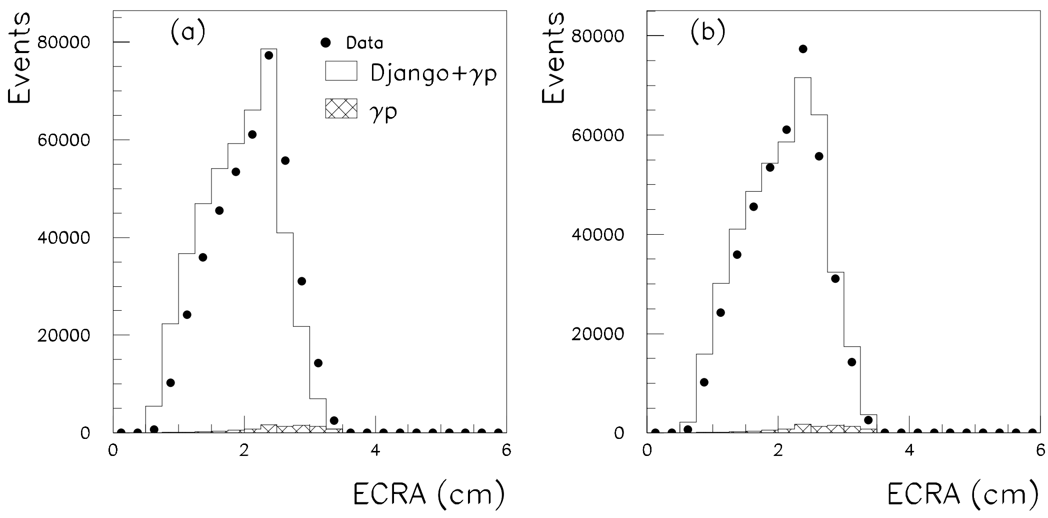

Figure 4.8: *(a) ECRA distribution before smearing. Here the simulation does not reproduce data both at small and large ECRA values but at maximum position, and (b) ECRA distribution after a shift of* 0.1 *cm and an additional smearing by a factor* 1.05*, of the simulation, allow for a better description.*

Figure 4.9 is showing the distribution of EBDC, as well as the distribution projected in the radial direction $EBDC_r$ and the azimuthal direction $EBDC_{r\varphi}$. The EBDC distribution is slightly broader in the data than in the simulation, which can be related to presence of more multiple track events in the data. $EBDC_r$ is slightly shifted in the data, whereas $EBDC_{r\varphi}$ is well centered in both cases. As the resolution of EBDC is dominated by the resolution of the SpaCal cluster position, and essentially no difference in the width of $EBDC_r$ and $EBDC_{r\varphi}$ is observed, a cut of $EBDC < 2.5\ cm$ is applied.

EHAD

Electromagnetic particles produce “shorter” showers than hadrons (see section 2.4), therefore the fraction of the energy in the hadronic section of the SpaCal (EHAD) helps to discriminate between electrons and charged pions.

More precisely, EHAD is defined as the fraction of energy in the hadronic section within a cylinder of 16 *cm* radius, in which we merge the clusters around an electron candidate seed. In the standard H1 reconstruction the clusters of the electromagnetic and hadronic sections are not linked together.

As electrons may also leave sometimes some energy in the hadronic section, we apply a conservative cut on EHAD < 0.02 (See figure 4.10). In this figure the majority of events, which do not deposit energy in the hadronic calorimeter (EHAD=0) are not considered. One observes more leakage into the hadronic section in the data than in the Monte Carlo, resulting from an inaccurate shower description already mentioned.

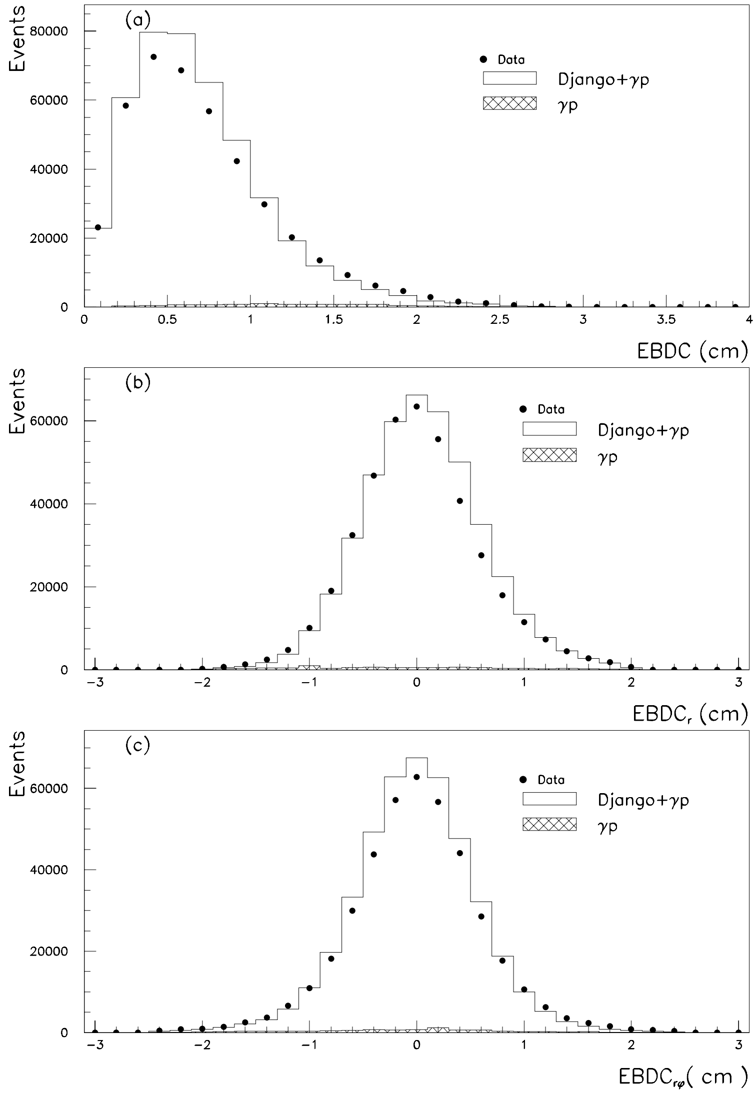

Figure 4.9: *(a)EBDC distribution, (b) its radial component of $EBDC_r$, and (c) its azimuthal component of $EBDC_{r\varphi}$.*

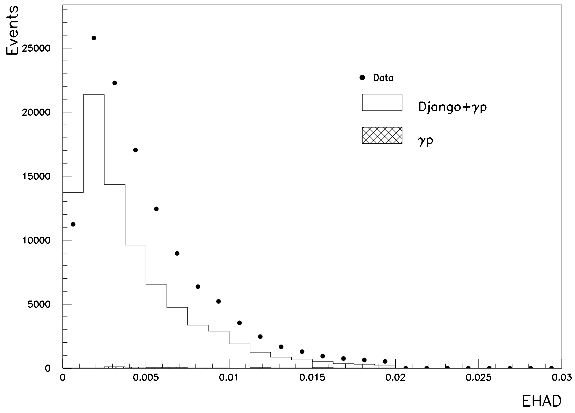

Figure 4.10: *EHAD distribution for events with energy in the hadronic part of the SpaCal.*

4.2.2 The Normalization of the Photoproduction Background

In ep scattering at HERA, the photoproduction process where the exchanged photon is almost real and the scattered electron is emitted at very small angle, is the dominant process in $e-p$ interactions and is creating fake electrons if these events are at high y. A small fraction of these events is detected by the electron tagger (ET). To correctly subtract the photoproduction from our data sample we can compare the tagged PHOJET events with the e-tagged events in the data. We do this by comparing the ECRA distributions and get a global normalization factor of 0.54 for PHOJET, which corresponds to the geometrical acceptance of ET. In figure 4.11 we check the results and find a nice agreement between data and the simulation. The normalization with respect to the luminosity is compared to a normalization to the total number of events in the sample. The uncertainty on the number of photoproduction events, estimated from the simulation and statistically subtracted bin by bin from the event sample is taken to be 30% of the subtracted number of events.

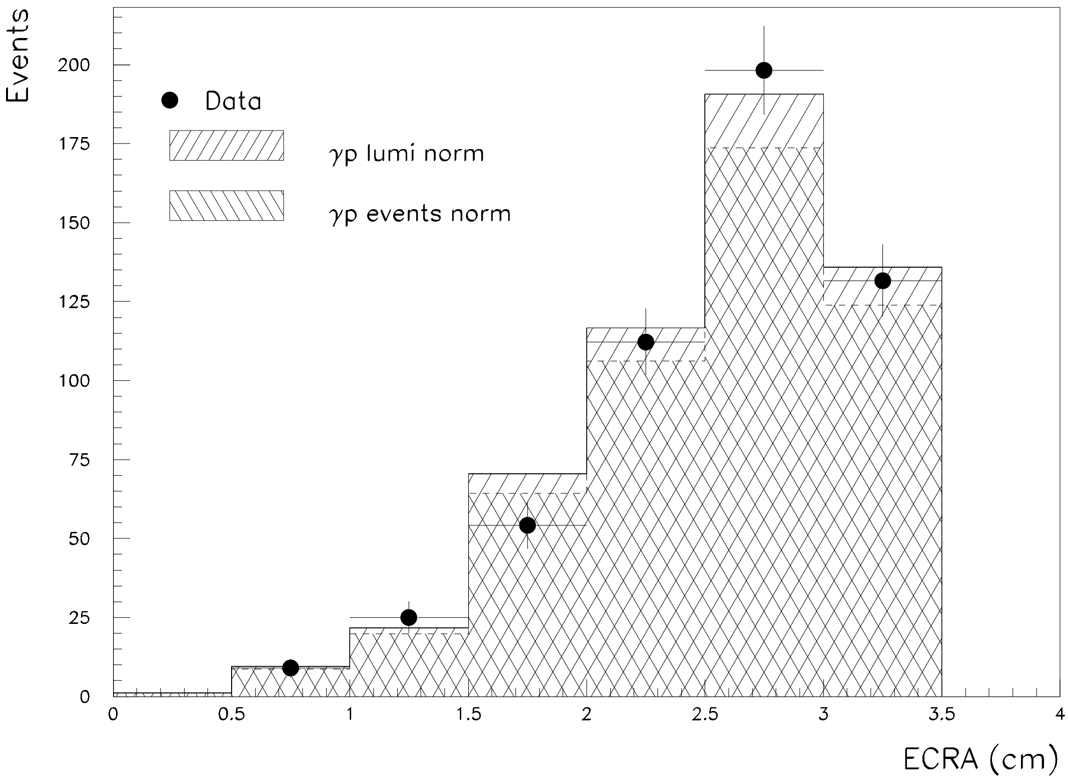

Figure 4.11: *Distributions of ECRA for e-tagged events for the data (dots) compared to PHOJET. The right hatched histogram is corresponding to the normalization taking into account the electron tagger acceptance (labeled luminosity norm), whereas the left hatched histogram (labeled event norm) is corresponding to an normalization to the total number of events.*

4.2.3 Electron Identification Efficiencies

In order to evaluate the quality an estimator, we can study its rejection power of background events and the losses induced on genuine events. As we are using the Monte Carlo Simulation in order to measure F_2, it is important, that the applied cuts do not introduce any bias and therefore that the Monte Carlo is able to describe the behaviour of the data with respect to the different cuts.

After the cuts on the existence of a vertex and the conservation of $E - p_z$, the remaining background contribution is essentially due to photoproduction events. We are studying therefore the efficiencies for each individual estimator in terms of the fraction of the number of events with all cuts applied to the number of events with all cuts applied except the one for the corresponding estimator, for the data, the simulation of DIS events (DJANGO) and the mixture of the simulated DIS and photoproduction events, where the two Monte Carlo samples are weighted according to the luminosity and the normalization factor previously determined for the PHOJET.

These ratios are determined in the same bins of x and Q^2 using the $e\Sigma$-method for our F_2 measurement. On the Monte Carlo simulation of DIS events, these ratios are indicating the inefficiencies of a cut, where as differences between the data and the mixed DIS/photoproduction Monte Carlo are contributing to the systematic errors on the F_2 measurement.

1. ECRA: Inefficiencies arising in the event selection due to ECRA are only observed at low x, high y, where the electron is at low energy. This is also the region, where we expect the photoproduction background. Elsewhere the efficiency is practically 100% in both Data and MC (figure 4.12).

   In the low x region, the inefficiencies on the DIS MC events are below 5%, while we are rejecting about 5% of background events coming from photoproduction at low Q^2. Our simulation, which includes DIS and photoproduction describes the data within 3% in these bins. For the 3 very low Q^2 bins, which are affected by the geometric acceptance of the detector, deviations between data and MC are not only observed in the lowest x bin, but 5 of the 6 bins in these regions show deviations up to 5%. As this corresponds also to the lowest energies, the broadening of the ECRA distribution discussed earlier explains this behaviour.

2. EBDC: The track-cluster link efficiency, relies on the track finding efficiency, the accurate cluster reconstruction and track reconstruction. As for ECRA, the lowest efficiency is at low x, but it rises more slowly and even in the plateau region a $1-2\%$ inefficiency is present (figure 4.13). In the low x region, the inefficiency reaches between $3-7\%$, rejecting $2-10\%$ of photoproduction background events. In the low Q^2 range from 2.5 to 10 GeV^2, where we have the highest precision, the description of the data by the MC is accurate. At lower Q^2, the inefficiency is higher in the data, between $5-10\%$ in the lowest x bins, but also noticeable at higher x values. At higher Q^2, $Q^2 = 15$ GeV^2 and 20 GeV^2, the MC has a higher inefficiency at low x, but reaches the plateau region faster than the data. Even in the plateau region a difference in the

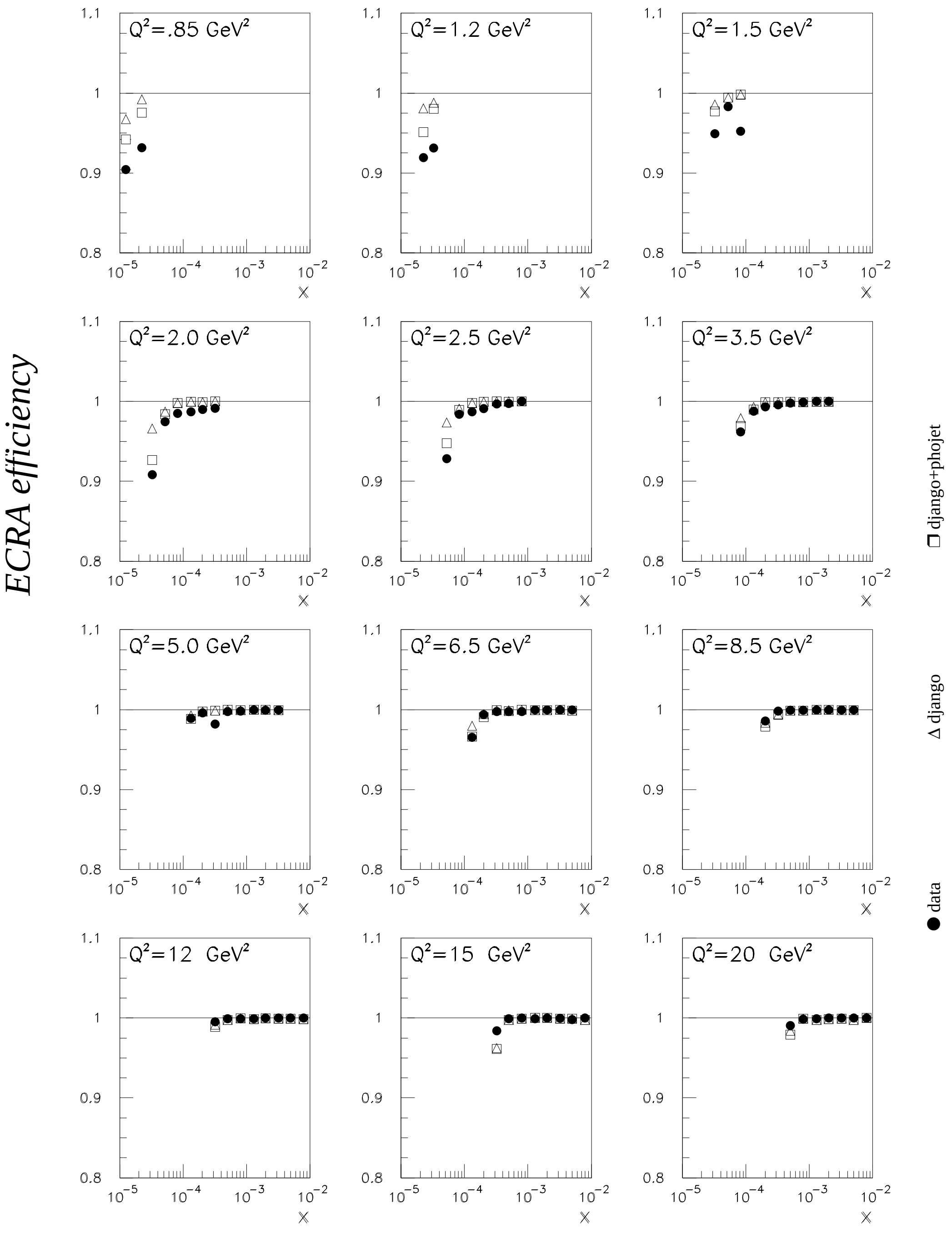

Figure 4.12: *ECRA efficiency in bins of x and Q^2 ($e\Sigma$-method) in data (solid circles), in DJANGO (open triangles) and in DJANGO+PHOJET (open squares).*

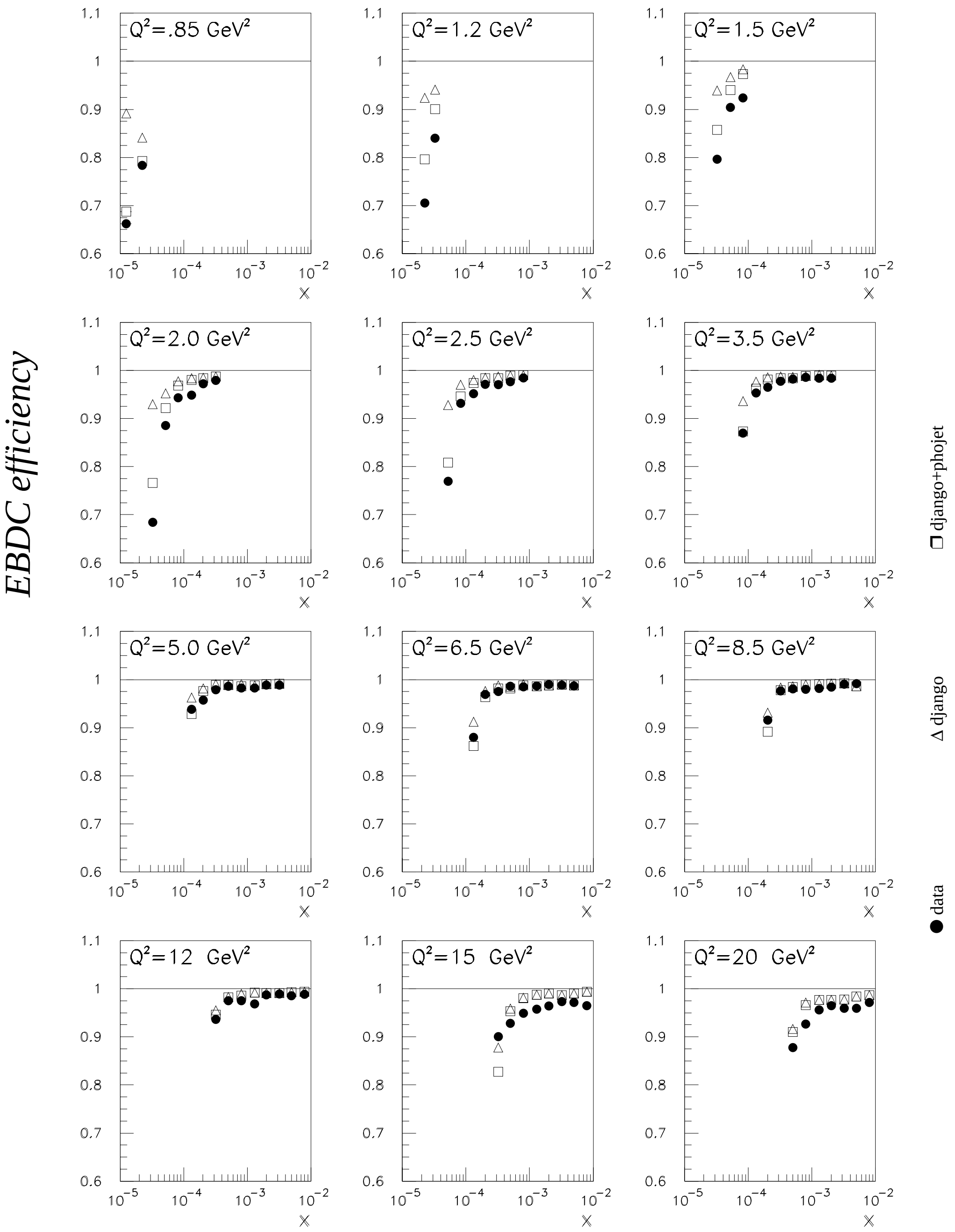

Figure 4.13: *EBDC efficiency in bins of* x *and* Q^2 *(e*Σ*-method) in data (solid circles), in DJANGO (open triangles) and in DJANGO+PHOJET(open squares).*

data-MC comparison of $2-3\%$ is observed. This inefficiency was traced back to a miscalibration in the BDC during the 1995 running, which was affecting the outer BDC-cells which have a larger size than the inner cells [7].

3. EHAD: The inefficiency due to leakage of electron in the hadronic section of the SpaCal, shows in general a similar behaviour as that of the previous two estimators (figure 4.14). The inefficiency on MC events at low x is generally below 5%, with a rejection power of at most 5%. The description of the data by the simulation is good. Slight deviations are mostly observed in the three lowest Q^2 bins.

In the bins of $Q^2 \geq 2\ GeV^2$, the number of events observed in the data has been corrected by the product of the difference between the data and the simulation (DIS+photoproduction) for these three efficiencies. The biggest effect of this correction is coming from the EBDC efficency at $Q^2 \geq 12\ GeV^2$, where we clearly observe an inefficiency from the drift chamber. The lowest Q^2 bins were not corrected for these efficiencies, where the influence from non-ep background may be more important, as we are looking in this region for low energetic electrons at the edge of the geometrical acceptance of the detectors, and the uncertainty on the correct description of the photoproduction background at this low Q^2 values is higher. For all the bins, the difference of the efficiency between data and simulation has been included in the systematic error.

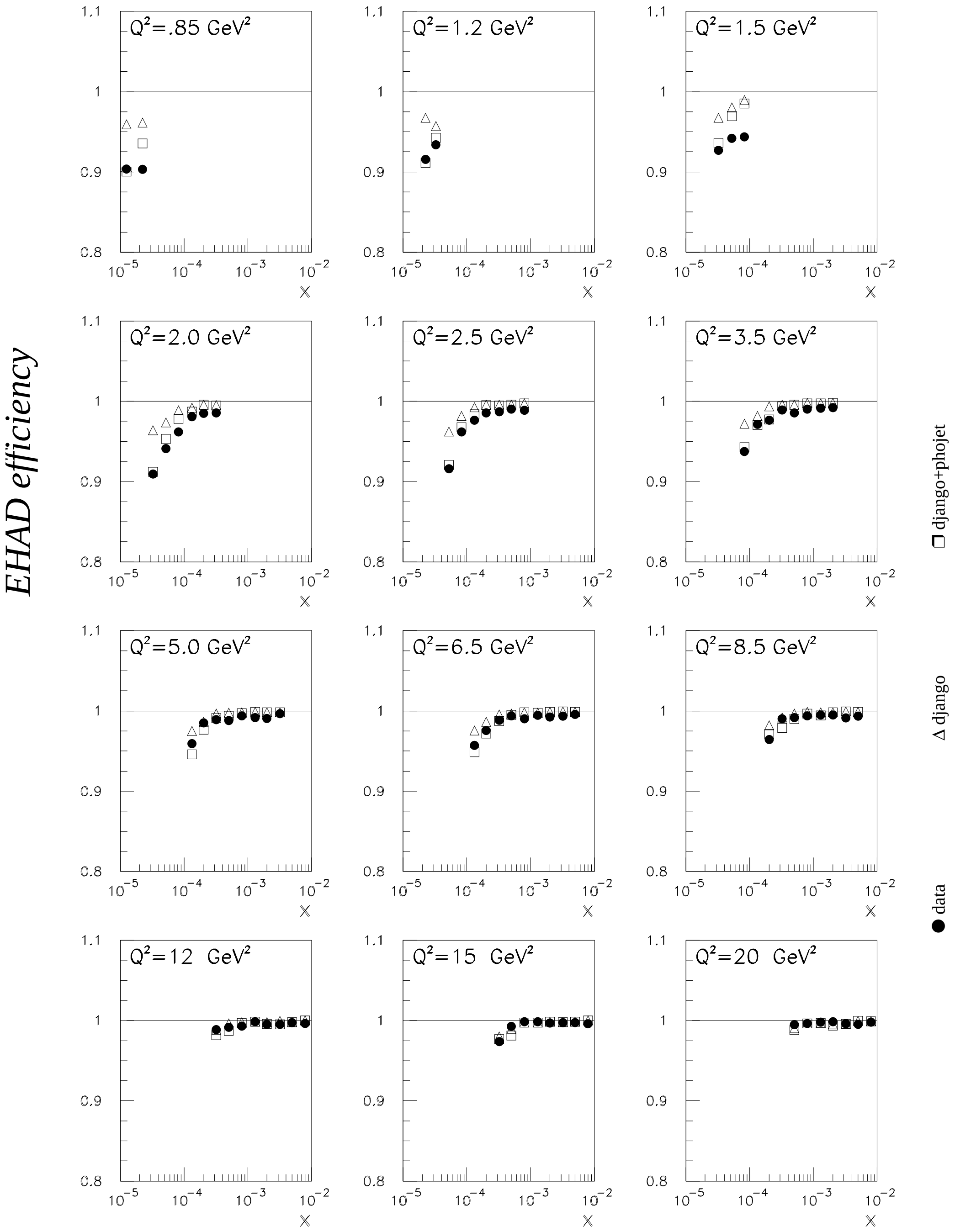

Figure 4.14: *EHAD efficiency in bins of* x *and* Q^2 *(e*Σ*-method) in data(solid circles), in DJANGO(open triangles) and in DJANGO+PHOJET(open squares).*

4.2.4 The Electron Energy Calibration

One of the major systematic error sources of the F_2 measurement is arising from the energy measurement of the scattered electron in both the e- and the Σ-method. A precise calibration of the SpaCal calorimeter is therefore crucial for the precision of our measurement. The absolute calibration of the SpaCal used test beam data at fixed beam energies [8] which allowed to determine the calibration factors from ADC counts to energies with an accuracy of 5%. The intercalibration of the SpaCal electronics channel and the two gains used for the readout is obtained with an electronic pulser system. The gain of the photo-multipliers is constantly monitored with the so called CAM-system (see section 2.4.2). These data is treated in a separate data stream and used in the SpaCal reconstruction program [9]. The energy at the output of the reconstruction is measured with an accuracy of 7%.

In order to improve this precision several techniques for an off-line calibration can be used. At first a cell-wise calibration was produced using the kinematic peak method and and minimum ionizing particles (MIP) as halo muons and cosmic muons [10]. In this procedure the calibration coefficient found is associated to the hottest cell in the cluster. An uncertainty of 2% is reached with these methods and the obtained factors were applied during the ntuple production. In order to improve this result, the detector is divided in 20 rings and 8 azimuthal sectors, and a refined adjustment of the kinematic peak with respect to the Monte Carlo simulation and the generated energy is performed. This allows to correct effects induced by the cell borders and edges.

The Double Angle Method and QED Compton Events allow for an estimation of the remaining systematic error and the linearity of the calorimeter. After a brief discussion of the different methods, the ring-wise so called “final calibration”, will be exposed in more details.

1. Kinematic peak method:
   Figure 2.4 is showing the kinematic plane in x and Q^2 indicating the lines of constant energy and scattering angle of the electron. One notices the line of the scattered electron energy equal to the beam energy, and the slow variation of the energy in this phase space region. This fact leads to an accumulation of events around the beam-energy, and corresponds to the quasielastic scattering of the electron at 27.6 GeV off a quark with the same energy.

   As the position of the kinematic peak does not depend on the structure function input, we can use it for the adjustment of the energy response. A sufficient number of kinematic peak events is accumulated in the inner region of the SpaCal where the cross-section is highest. Figure 4.15 is showing the energy distribution before and after the cell-wise kinematic peak calibration.

   For these events the energy of the scattered electron can also be reconstructed using the Double Angle method: as mentioned in section 4.1, the angular measurement of the electron and the hadrons can be used for the reconstruction of the scattered electron energy. This method is used for event samples at higher Q^2, when the kinematic peak vanishes slowly and becomes less prominent.

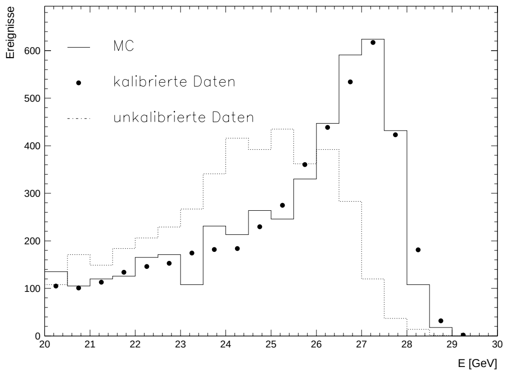

Figure 4.15: *Energy distribution before and after cell-wise calibration using the kinematic peak method [11].*

2. Minimum Ionizing Particles (MIP):
   In the formation of an electromagnetic shower, the Bremsstrahlung process is dominating at energies of about 50 MeV (see figure 2.11). For muons, the Bremsstrahlung process is suppressed by a factor of $1/m_\mu^2$, as their mass m_μ is 200 times higher compared to the mass of an electron. Therefore the muons are depositing energy only via ionization processes in the absorber material and can be considered as minimum ionizing particles. The expected energy deposition is following a Landau distribution for minimum ionizing particles [12], and can be computed accordingly.

   Halo muons, which are formed around the proton beam, have horizontal incidence and deposit 150 MeV per cell in the electromagnetic section of the SpaCal and 400 MeV in a hadronic cell [11]. Special Runs with stable proton beam were taken, in order to accumulate clean halo muon events and to adjust the energy in the outer region of the SpaCal.

   Coming mostly from the vertical direction, cosmic muons deposit less energy in the spacal, as they are passing through less absorber material (see figure 4.16). The energy deposition is only 55 MeV per cell in the electromagnetic SpaCal and 200 MeV in the hadronic section, therefore the calibration with cosmic muons is more difficult than with halo muons. Nevertheless higher statistic can be obtained from special runs without any beam.

3. QED Compton method:
   QED Compton events have the same underlying diagram than radiative events, but the hard scale is given by the electron-photon interaction, instead of the electron-proton interaction. Therefore two electromagnetic clusters, an electron and a photon are detected in the SpaCal or in the SpaCal and the electron tagger (ET). The sum of their energies should be equal to the electron beam energy. Reconstructing one of the final energies with the double angle method is giving a reference energy and the kinematic constraint can then be used for

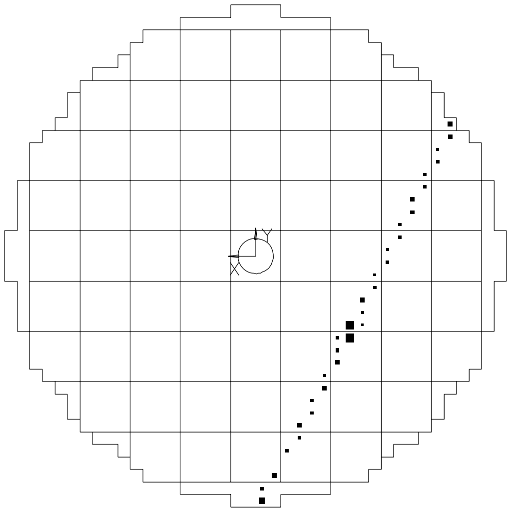

Figure 4.16: *Cosmic muon seen in the SpaCal using for the cell-wise calibration. [11].*

the calibration [13]. If one of the electromagnetic clusters is seen in the ET, this energy can directly be used as a reference energy, as the ET has been calibrated using Bethe-Heitler events (see section 2.2). The calibration with QED Compton events allows to establish an error on the linearity of the energy measurement (figure 4.17), which is 3% at $E = 10\ GeV$.

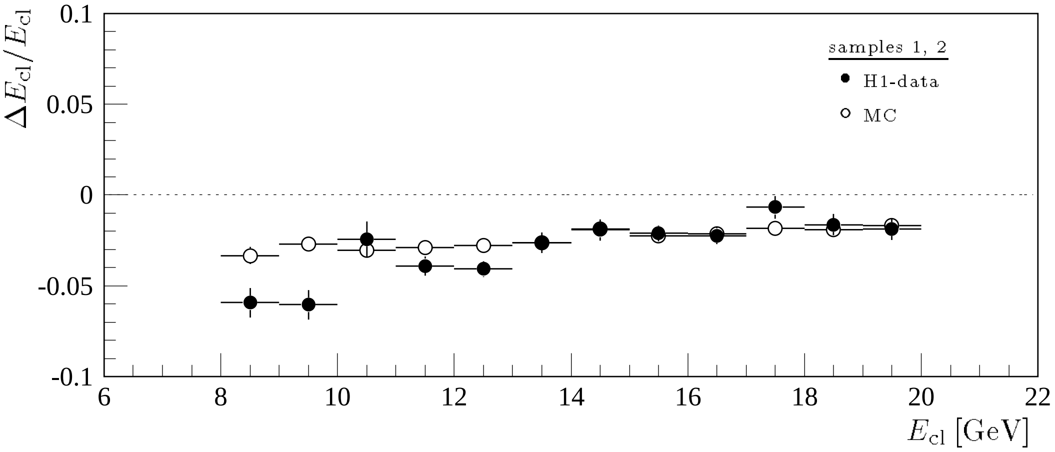

Figure 4.17: *Linearity of the SpaCal as determined with QED Compton events as a function of the cluster energy for data and Monte Carlo [14].*

The Final Calibration for the F_2 Extraction:

The final calibration is performed for a precise correction of local effects in the detector. For this calibration, done at the analysis level, the kinematic peak method is used. The event selection is the same as the general one introduced in chapter 3 with an additional requirement for the selection of the kinematic peak events of $y_h < 0.05$. For final state radiative events on the generator level of the MC, the scattered electron energy is redefined as the sum of the scattered electron energy and the radiated photon energy as they are detected in the same cluster on the reconstruction level. Moreover, for $4\ GeV < W_{gen} < 8\ GeV$ the event weight is doubled for MC in order to correct for the non-simulation of events below $W_{gen} < 4\ GeV$, as the hadronisation step can not be performed there.

For the calibration, the electromagnetic SpaCal is divided into radial and azimuthal sections. The 8 azimuthal sectors are of equal sizes of 45^o each while the 20 radial sections are of varying sizes in order to keep sufficient statistical precision even in the outer part of the SpaCal where the cross-section is smaller. An event belongs to a particular section if the BDC-hit associated to the scattered electron lies in that particular section. In this way miscalibration effects, which could affect the cluster position are not influencing the calibration procedure.

The zone by zone comparison of the kinematic peak distributions for the data and the reconstructed Monte Carlo in figure 4.18 show discrepancies, both in the peak values and in the width of the distributions. The fit of these distributions result in general in a wider distribution for the data at low radii as shown in figure 4.19, where the result of a Gaussian fit is shown, performed to the kinematic peak distribution for the data, the reconstructed MC and the generated MC .

The energy distribution at the generator level is narrower, as it does not include detector effects degrading the resolution. The biggest difference between the generated and the reconstructed energy is visible in the most inner part of the SpaCal, corresponding to the non-quadratic cells of the Insert, where the energy reconstruction is affected by the limit of the detector and partial losses in the beam-pipe. The mean positions of the generated energy versus the reconstructed are described within 2%. Comparing the reconstructed energy in the data and the MC, one observes shifts in the mean position up to 1%, and a better resolution in the MC than in the data of 10% to 20%.

Our calibration procedure consists in (1) adjusting the mean position of the kinematic peak distribution to the generated value (this value is independent of the structure function) and (2)smearing the MC distribution to the same width as that of data. In order to achieve this, we are comparing Gaussian fits to all three distributions, to the kinematic peak distribution in the data, in the reconstructed MC and the generated MC. The calibration factors for each zone are obtained from the mean positions of the Gaussian as,

$$c_i^j = \frac{\langle E_{gen} \rangle - \langle E_j \rangle}{\langle E_j \rangle} \tag{4.18}$$

for i^{th} zone with j=data or MC while E_{gen} is the generated energy. The additional

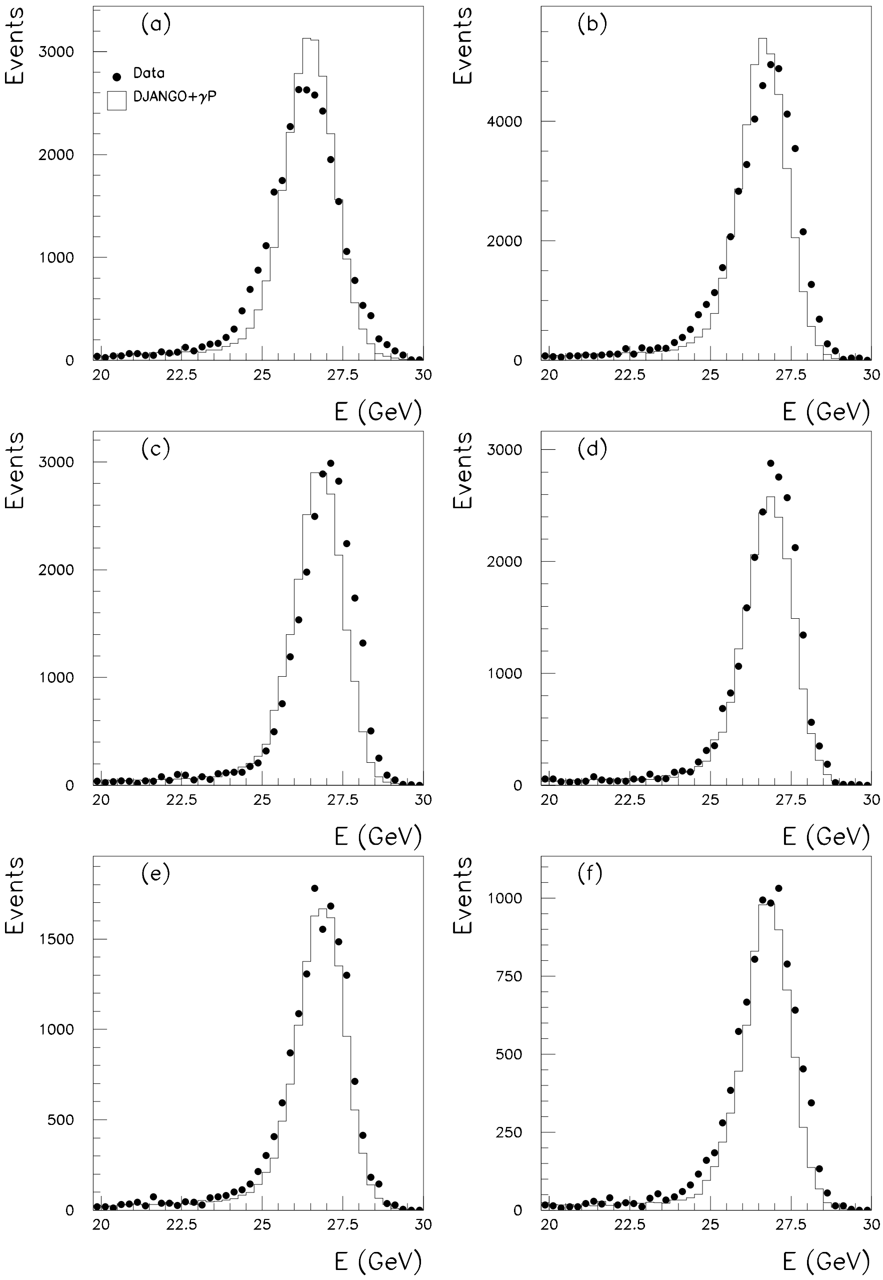

Figure 4.18: *Kinematic energy distribution for (i)data (dots) and (ii)MC-reconstructed (solid line), before calibration in different radial zones of the SpaCal i.e. (a)*$R < 9 cm$, *(b)* $9\ cm < R < 11\ cm$, *(c)* $11\ cm < R < 13\ cm$, *(d)* $13\ cm < R < 16\ cm$, *(e)* $16\ cm < R < 20\ cm$ *and (f)* $20\ cm < R < 25\ cm$.

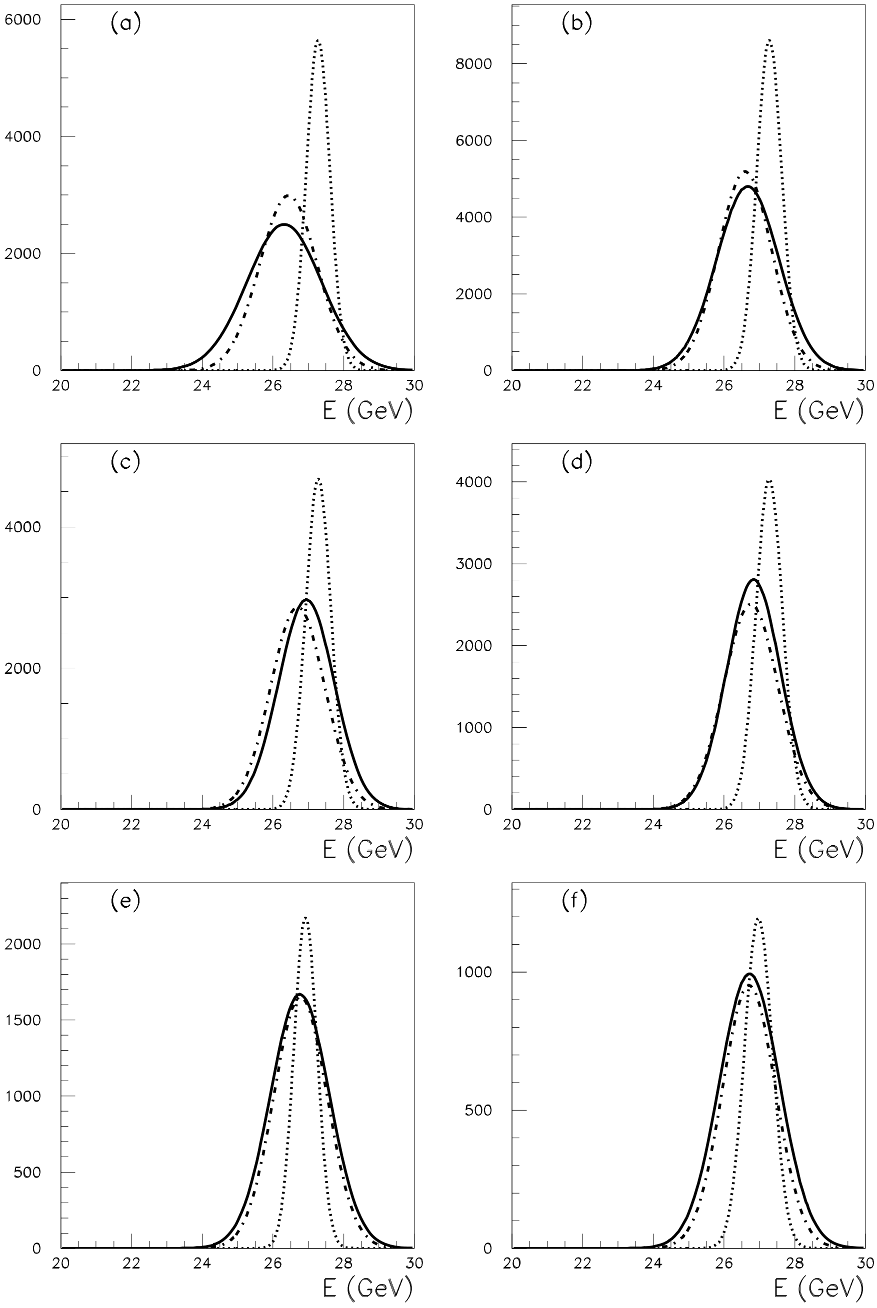

Figure 4.19: *Gaussian fit to zone by zone kinematic peak distribution for (i) data (full line), (ii) the MC-reconstructed (dashed-dotted line) and (iii) the MC-generated (dotted line), before calibration in the same six zone as described in figure 4.18.*

smearing factors for Monte Carlo are obtained from the width of the Gaussian by,

$$s_i = \sqrt{\sigma^2_{i,data} - \sigma^2_{i,MC}} / \langle E_{MC} \rangle \tag{4.19}$$

for the i^{th} zone. In figure 4.20, we see the results of our calibration procedure by comparing the kinematic peak distribution in six different radial zones and in figure 4.21 the whole energy spectra in these zones. Although the peak values are well adjusted, differences in the event yields are observed especially in the intermediate energy regions. This calibration of both data and Monte Carlo and the smearing of the Monte Carlo leads to the final scattered electron energy spectrum in figure 4.22 which shows good agreement between data and MC and a reduced uncertainty of 1%.

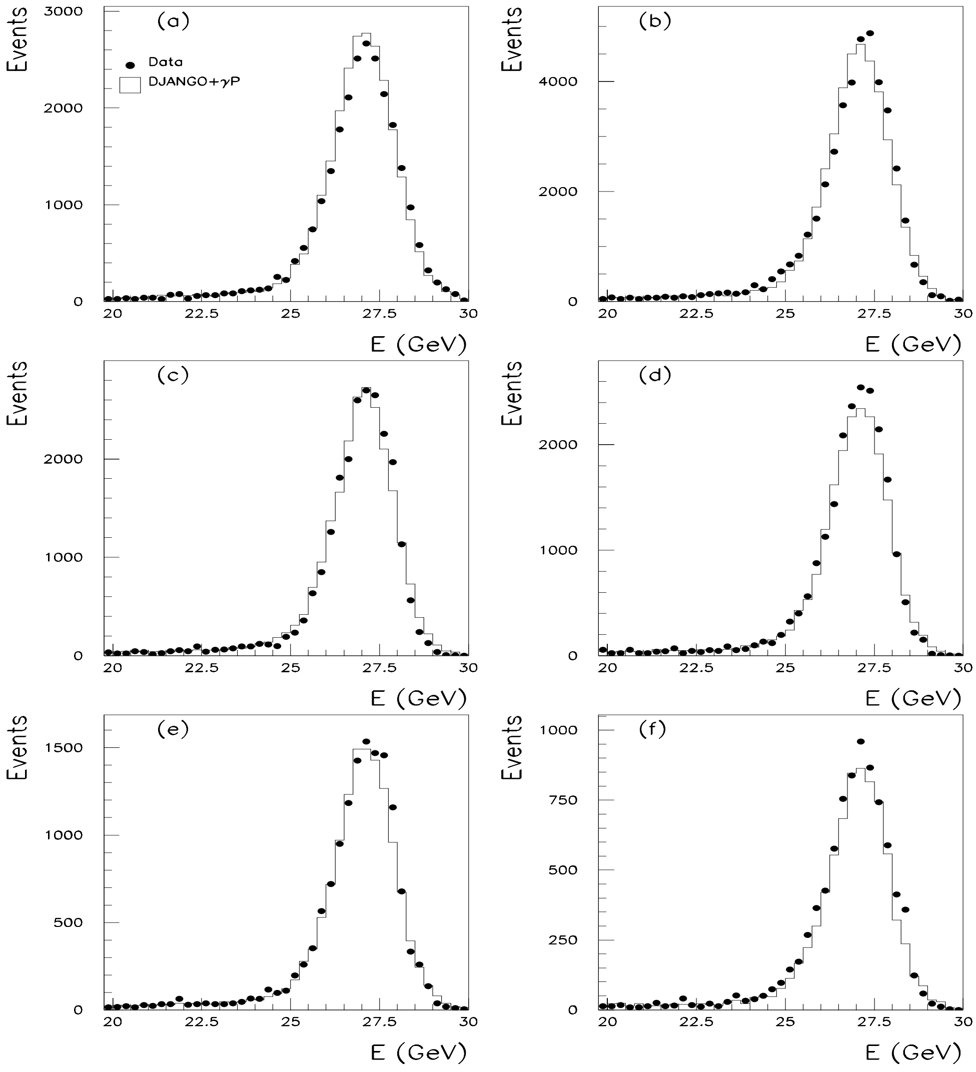

Figure 4.20: *Zone by zone kinematic peak distribution (i)data (dotted), (ii)MC-reconstructed , after calibration.*

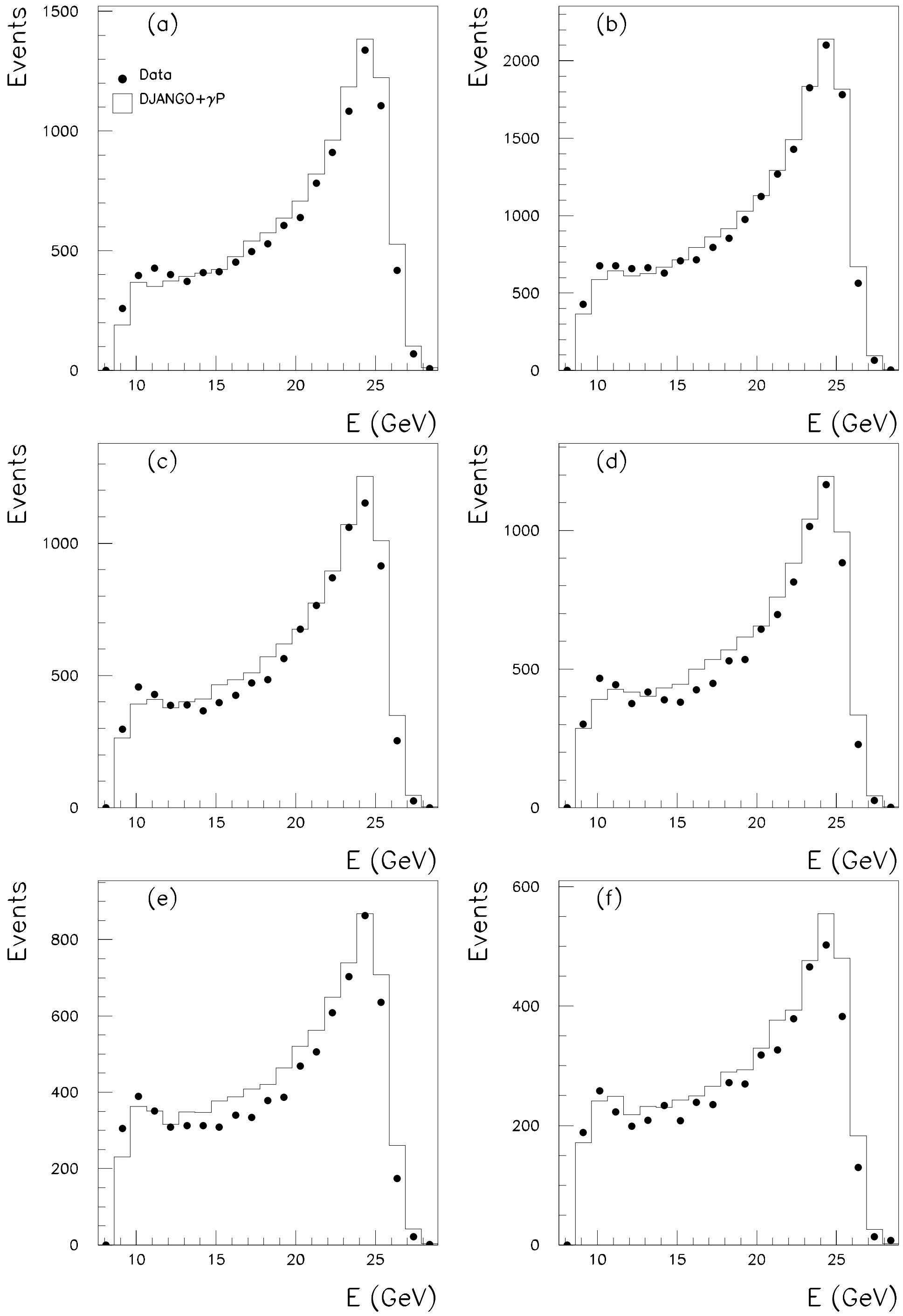

Figure 4.21: *Zone by zone electron energy distribution (i)data (dotted), (ii)MC-reconstructed, after calibration for the events not belonging to the kinematic peak.*

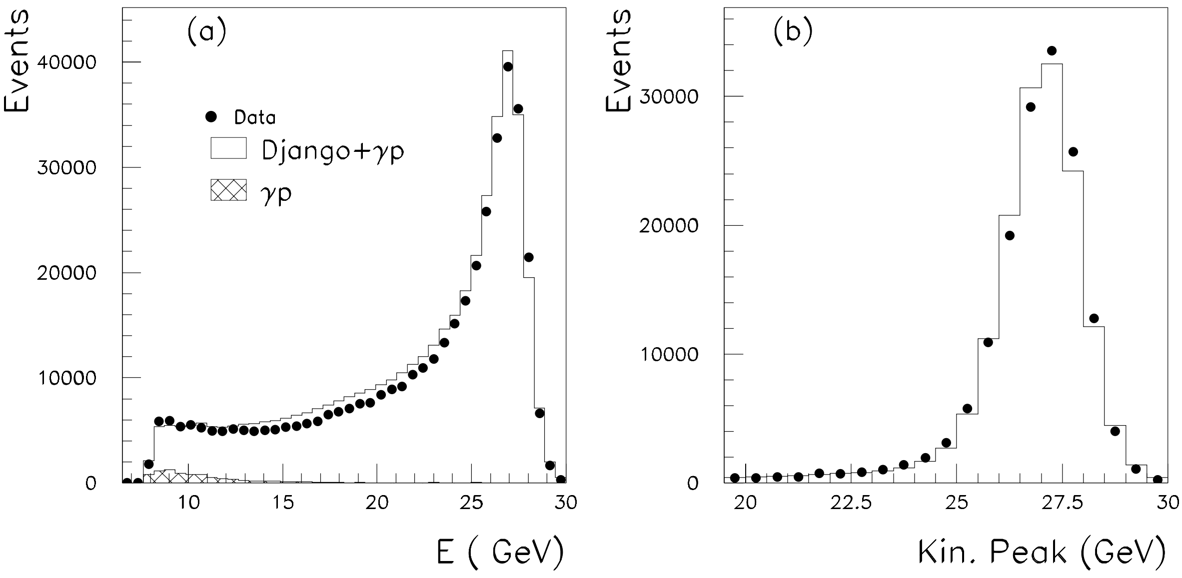

Figure 4.22: *Electron energy distribution after calibration for (a) whole energy spectrum and (b) kinematic peak distribution.*

4.3 The Hadronic Final State Reconstruction

4.3.1 The Track and Cell Combination

At low energies, the measurement of the particles momenta from the trackers is more reliable than the energy measurement from the calorimeters: the resolution of the track measurement behaves as $\delta p/p \propto p$ compared to the calorimeter resolution $\delta E/E \propto 1/\sqrt{E}$ and thresholds effects may prevent the detection of soft particles by the calorimeter. Therefore the reconstruction of the hadronic variables using both calorimetric cells and tracks improve the results and different procedures to combine them were established.

In the present analysis the H1KINE program was used [15], where the tracks are added to the sum of the hadronic final state energies if their momentum is below 2 *GeV* with a p_T of at least 100 *MeV*, in order to avoid curling tracks. Only central tracks pointing at the inner surface of the Liquid Argon calorimeter are used. In order to avoid double counting of energy a cylindric mask is applied to the calorimeter in the prolongation of the track with a radius of 15 *cm* in the electromagnetic section and 25 *cm* in the hadronic section.

In figure 4.23, we show the ratio y_{rec}/y_{gen}, for MC events using the cells-only and the cell and tracks reconstruction, as a function of the generated y.

In the high and medium y range, the cells and tracks method shows a ratio close to 1, whereas the cells only method undershoots the expectation by up to 15%. Splitting the reconstructed y in its different contribution from the Liquid Argon, the tracks and the SpaCal, one sees that the track contribution is most

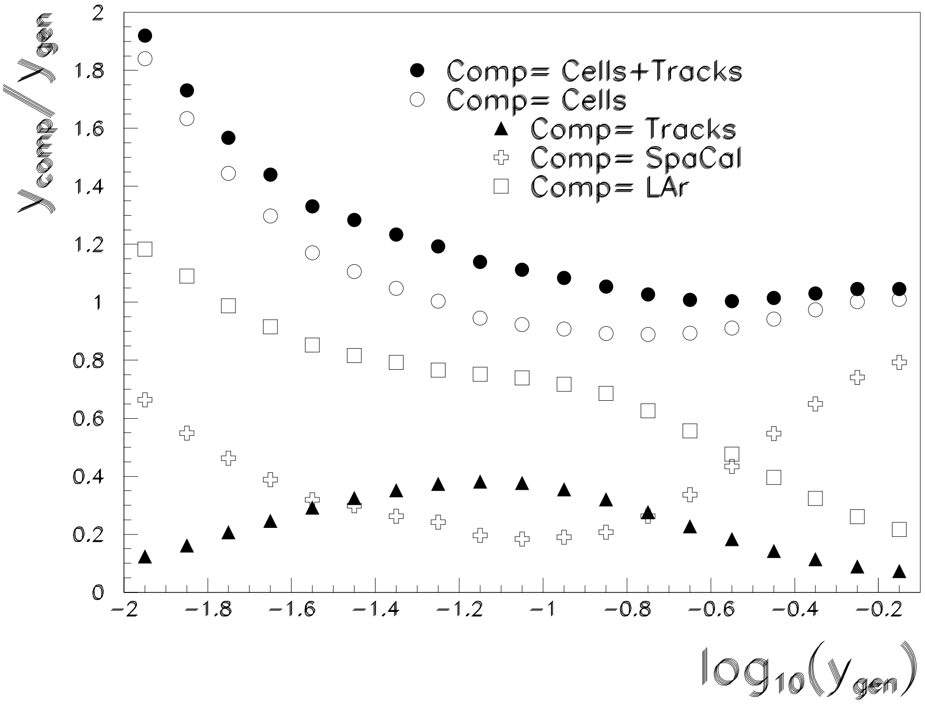

Figure 4.23: *The comparison of* y_h *from the different parts of the H1 detector with* y_{gen} *as a function of* y_{gen}*.*

important in this region. The SpaCal contributes most at high y, when the hadronic final state is expected to go in the backward direction, but one observes also an important contribution at low y, which is due to noise and discussed in more detail in section 4.3.2. A similar rise is also observed in the Liquid Argon contribution, both increasing artificially y_{rec}/y_{gen}. Figure 4.25 compares the different contributions with respect to the reconstructed y for data and MC. The systematic errors associated to the energy measured is 4% for the Liquid Argon and 3% for the tracks. Figure 4.24 shows the ratio $pt_{h,com}/pt_e$, where $pt_{h,com}$ corresponds to the pt carried by either the liquid Argon or the tracks, and the variation which is due to a shift of the amount of systematic error quoted in the positive or negative direction. The ratios are not as well described when these shifts are applied.

4.3.2 Noise Studies in the SpaCal

The reconstruction of y from the hadronic final state sums up the $E - p_z$ of all energy depositions not belonging to the scattered electron. Although the main part of the energy belonging to the hadronic final state is carried by the liquid Argon, the contribution of the SpaCal ($y_{h,SpaC}$) may have a considerable influence, as each energy contribution in the SpaCal enters with nearly a factor 2 in the $E - p_z$ summation i.e

$$y_i = E_i(1 - \cos\theta_i) \rightarrow 2E_i \qquad as \quad \theta \rightarrow 180^o. \tag{4.20}$$

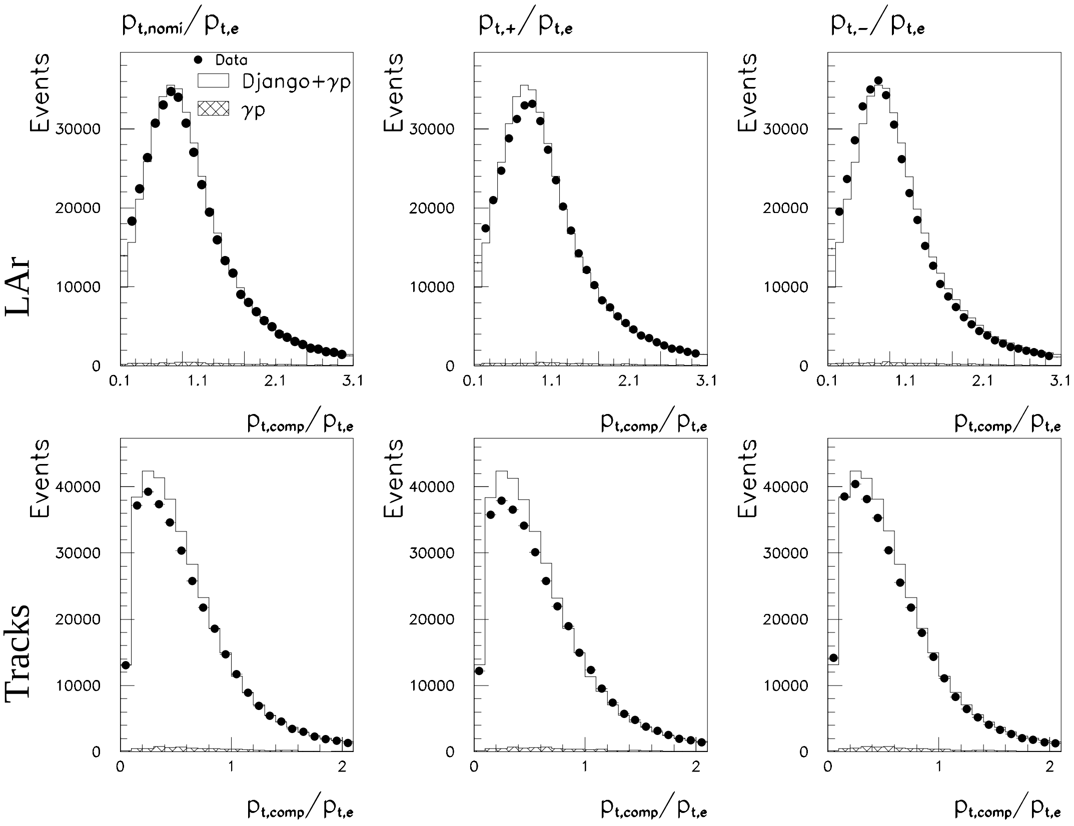

Figure 4.24: *$pt_{h,com}/pt_e$ for the contribution to pt_h, carried by the liquid Argon and the tracks. The first column is showing the nominal contribution, whereas the second (third) column corresponds to a positive (negative) shift on the energy in the data of quoted the systematic error (4% for the liquid Argon and 3% for the tracks).*

This plays a role in essentially two kinematic domains (1) at high y, where the energy flow of the hadronic final state is directed in the backward region of the detector and the contribution of $y_{h,SpaC}$ reaches up to 80 % (figure 4.25), (2) at low y, where noise in the SpaCal can deteriorate considerably the y reconstruction. Although the overall description of the energy flow in the SpaCal by the Monte Carlo is satisfactory, an improvement in the noise reduction allows for a better purity and stability at low y and therefore an extension of the F_2 measurement (see section 5.3.1 for definition and discussion).

In this section we will discuss strategies for the noise suppression in the SpaCal in order to improve the extension of the F_2 measurement towards low y. Possible sources for noise in the SpaCal may occur from back scattering particles, synchrotron radiation close to the beam pipe, random electronic noise in the detector or hot cells. Another source which can deteriorate the reconstruction at low y is energy which belongs to the scattered electron, but which is not contained in the cluster and falsely absorbed in the hadronic final state.

If we look at the $y_{h,SpaC}$ contribution (in figure 4.25), both data and MC are

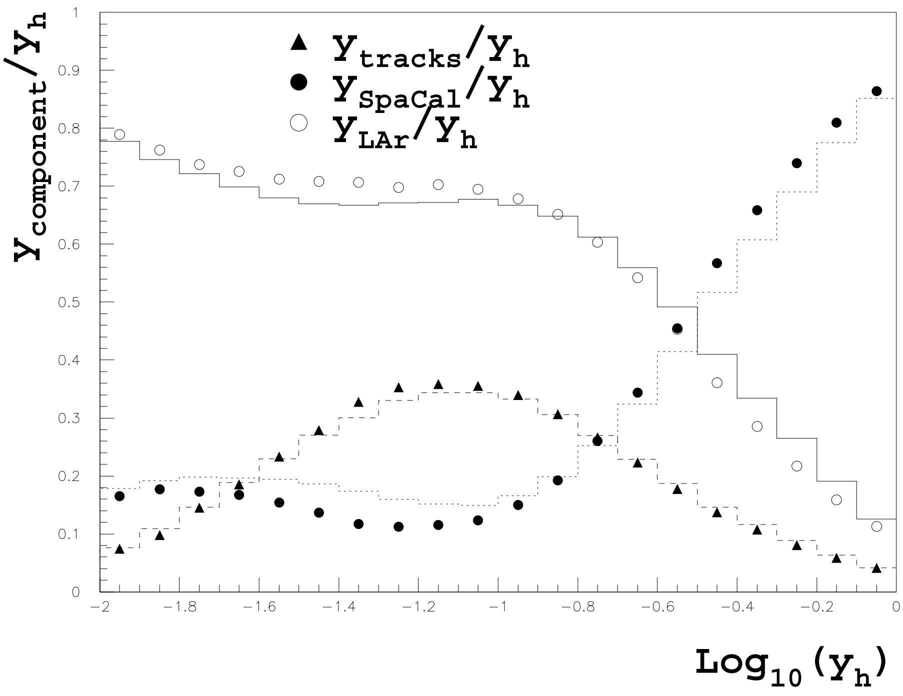

Figure 4.25: *The figure shows the contribution to the measured value of* $\log_{10}(y_h)$ *from different detector components. The relative contribution of the track chambers (solid triangle), the SpaCal (solid circle) and the LAr (open points) along with the MC contribution (lines) in each case can be seen.*

rising at small values of y, which is not expected from the current jet direction in this kinematic region. Looking at the energy found in the SpaCal cells (figure 4.26), we notice a sharp cut at about 15 MeV. This cut is due to the pedestal subtraction applied during the event building at level L3 (section 3.2). The pedestals are determined from random trigger events and are reflecting the electronic noise. A cut of 2σ the pedestal width, which is about 7 MeV, is applied on each cell, leaving some negative energies, which extend down to -50 MeV, as observed in the data. In the case of the liquid Argon calorimeter, similar effects exist, but files containing random trigger events are superposed to the simulation, thus the MC events are equally containing negative energies. This has not been the case for the 1995 simulation of the SpaCal, but was included in more recent simulations.

In order to study the different noise contributions, we reconstructed a subsample of events in data and Monte Carlo, applying various algorithms for the identification of the different noise sources. Figure 4.27 is showing the effect of these algorithms on the $y_{h,SpaC}$ distribution.

A simple global noise cut consists in rejecting all cells below 50 MeV. Such a cell would contribute to y with maximally 0.003. At high y, where the SpaCal contributes substantially, these low energy cells can be safely neglected. In addition the description of the cell energy in the electromagnetic section and the hadronic section

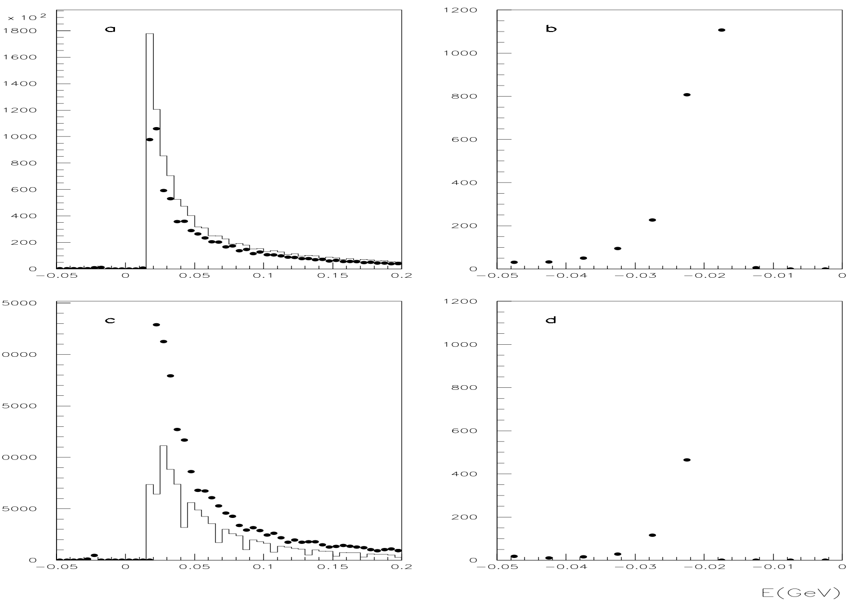

Figure 4.26: *Distribution of the SpaCal cell energies. Figure (a) shows the distribution of the cell energies in electromagnetic part. In (b), same distribution is zoomed for the negative energy cells. Similarly the lower two plots (c) and (d) are for the hadronic part. In simulation (denoted by line) there are no negative energy cells but in data (filled circles) we find a contribution from a few negative cells.*

at low energy is rather bad (figure 4.26). Less cells than expected are observed in the electromagnetic section and an excess in the hadronic section. With the cut at 50 MeV, we cut out the most important part of this region in the electromagnetic part, whereas we rise the cut at 100 MeV in the hadronic part (figure 4.27 a).

The INSERT is the innermost part of the electromagnetic SpaCal (section 2.4.2). Being very close to the beam-pipe, the INSERT is exposed to a wide range of background especially synchrotron radiation and backscattering particles, but also wide-angle initial state radiation. Its exclusion removes most of the rise at small $y_{h,SpaC}$ (figure 4.27 b), which is seen in both data and the simulation (figure 4.27 a). The origin of this rise, can therefore be traced back to initial state QED radiation, which is included in the Monte Carlo simulation.

However the behaviour of $y_{h,SpaC}$ shows still differences in the data and in Monte Carlo. Some isolated cells with energies between 50 and 100 MeV (we call them cold cells) have been found by a visual scan of these events. They are also considered as noise and are rejected by an algorithm, which requires at least one energetic cell of energy greater than 100 MeV within 40 cm from a cold cell. The effect of this cut is rather small, but the behaviour of $y_{h,SpaC}$ improved slightly at small y (figure 4.27 c).

After having removed almost all possible sources of noise in the energy measurements, the leakage of energy from the scattered electron into the hadronic final

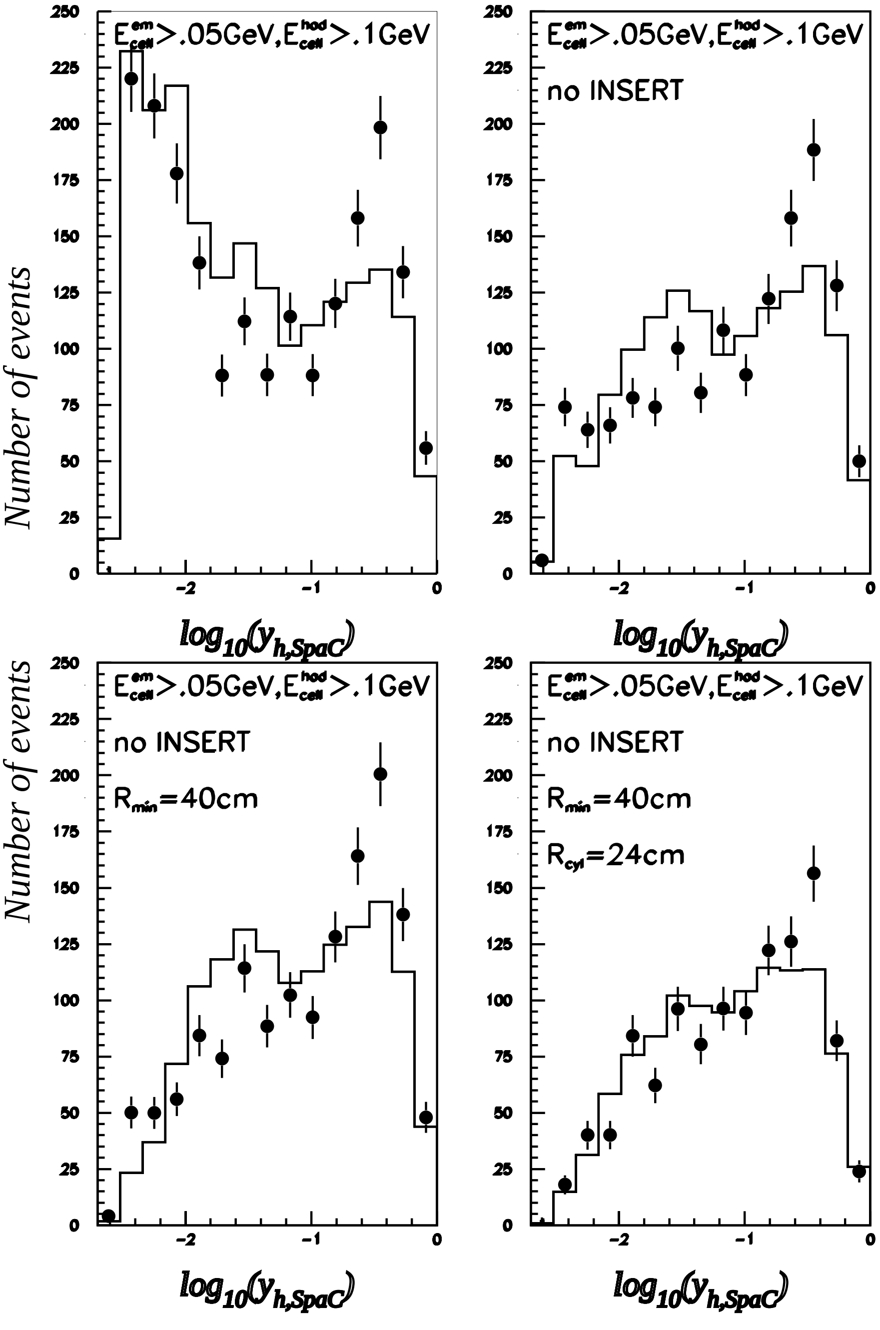

Figure 4.27: *Effect of various noise identification algorithms on the distribution of* $y_{h,SpaC}$*: (a) cut on cell energy of 50 MeV in the electromagnetic section and 100 MeV in the hadronic section. (b) excluding the energy in the SpaCal INSERT. (c) excluding low energetic, isolated cells. (d) increasing the radius defining the electron candidate.*

state was investigated. In general an electron is easily identified as a compact isolated electromagnetic cluster in the SpaCal. However this cluster can be spread out, especially at low energy, in such a way that the electron is even split into two clusters. Leakage of the electron energy into the hadronic section of the SpaCal may occur on the other hand, and form a separate cluster in the hadronic section of the SpaCal, which is not linked to the cluster in the electromagnetic part by the default reconstruction. These clusters are linked in our program by a “cylinder” algorithm.

A cylinder is defined with its axis along the center of the hottest cluster and the event vertex. Figure 4.28 is showing a schematic view of an electron candidate, with the hottest cluster in black in the electromagnetic section of SpaCal and smaller neighbouring clusters around. Indicated is the cylinder axis, pointing to the vertex and the boarders of the cylinder, where all the clusters whose centers lie within a radius R_{cyl} around this axis are merged together. For the above study of the SpaCal noise, we took the cylinder radius of $R_{cyl} = 8.5\ cm$. However we see a significant improvement in the $y_{h,SpaC}$ distribution if we increase this radius up to 24 cm (figure 4.27 d).

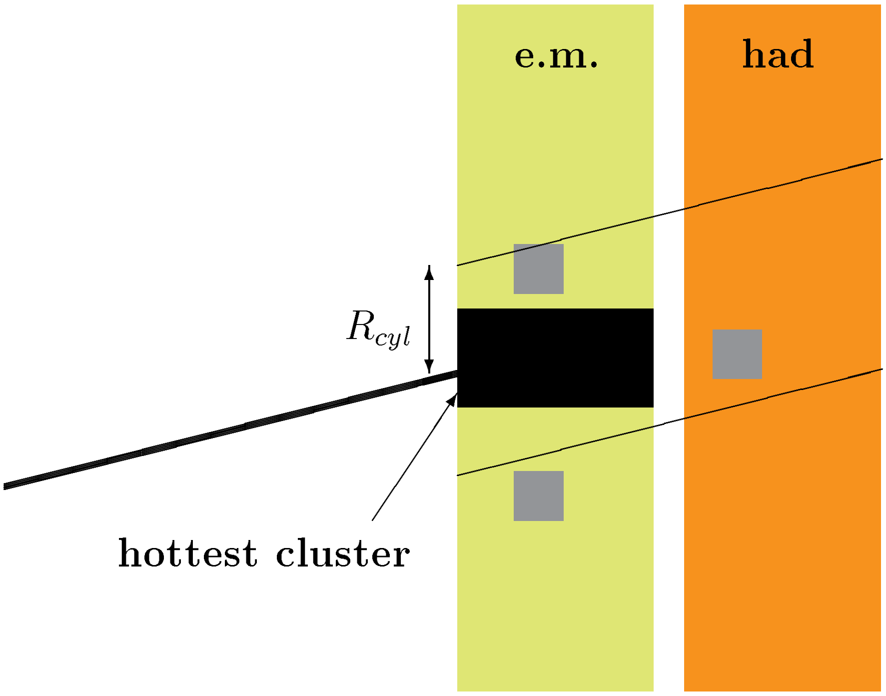

Figure 4.28: *Schematic picture of the cylinder algorithm used to merge the clusters around an electron-candidate in the SpaCal.*

By studying the distribution of the electron energy within a cylinder of variable radius, we can optimize the cylinder used for the electron definition. Figure 4.29 is showing the number of events with energy in a cylinder of variable radius R_{cyl} apart the energy in the hottest cluster. For a subsample of 1200 events, we have about

300 events with energy in a cylinder of a radius of $R_{cyl} = 7.5\ cm$ besides the energy of the hottest cluster. Increasing the radius, the number of events increases up to 700, which is more than the half of the sample at a cylinder radius of $R_{cyl} = 18\ cm$. Increasing the radius beyond this value, doesn't add anymore energy to the electron candidate, and no more additional events are found. In the simulation the number of events with energy outside of the hottest cluster is lower than in the data, about 15%, but continues to rise slightly even if the radius is increased beyond 18 *cm*.

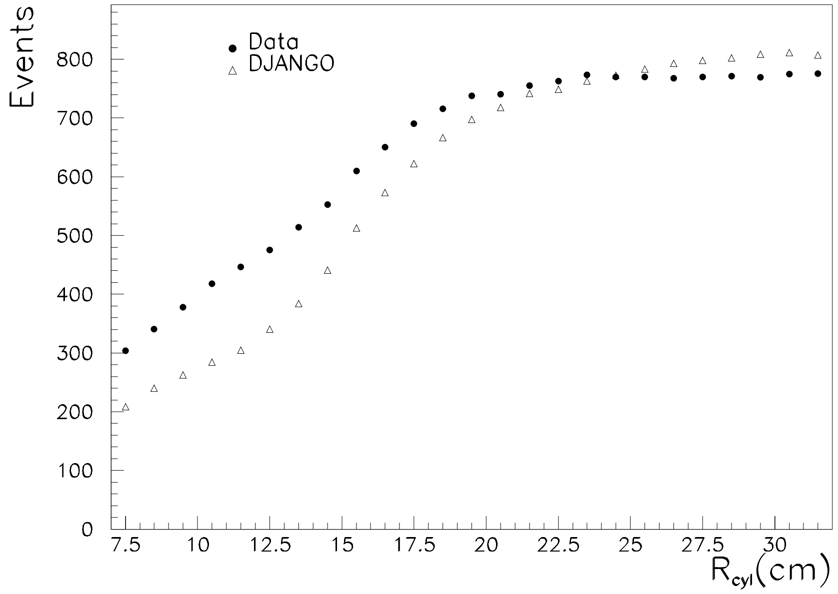

Figure 4.29: *The distribution of the events as a function of the cylinder radius in data (solid points) and MC(open triangles).*

For these events, figure (figure 4.30) is showing the total energy E within the cylinder (figure 4.30(a)), the energy of the hottest cluster E_{hot} (figure 4.30(b)), the energy in the hadronic section E_{had} (figure 4.30(c)) and the energy in the electromagnetic section discarding the hottest cluster E_{em}(figure 4.30(d)), as a function of the cylinder radius. For each value of the cylinder radius, only the events having energy in the cylinder besides the hottest cluster are entering the distribution. The distributions are showing the mean values of the considered quantity for these events. Looking at the different distributions we can see that:

- Increasing the cylinder radius adds mainly energy to low energetic cluster: the mean energy in the cylinder and of the hottest cluster of the electrons with energy outside of the most energetic cluster, is decreasing (figure 4.30 a,b).
- The energy contained in the cylinder apart of the hottest cluster is about 0.5% (figure 4.30 a). This corresponds in average to an additional energy

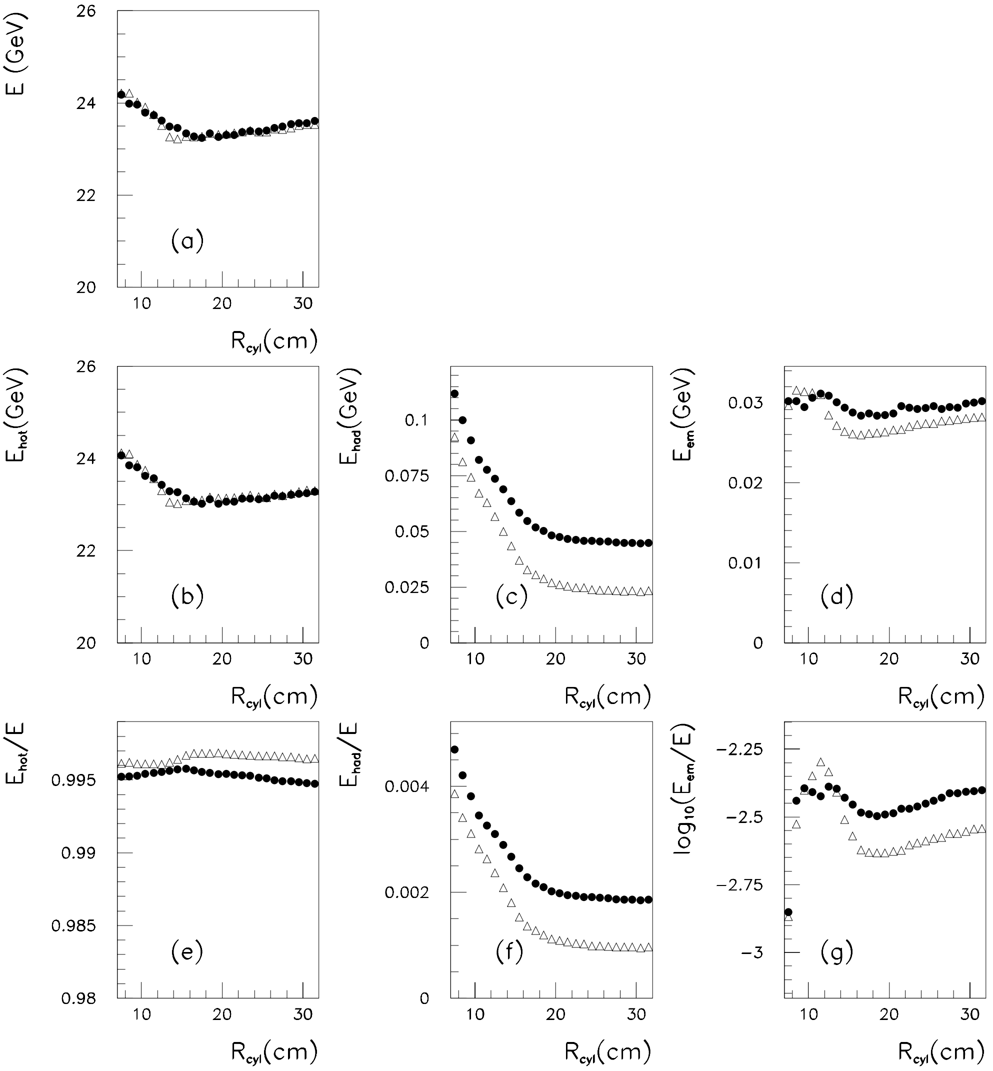

Figure 4.30: *Scattered electron energy (E) versus cylinder radius (R_{cyl}): E_{had} is the contribution from the hadronic part, E_{hot} the energy of the hottest electron cluster and E_{em} the remaining electromagnetic energy from low energy clusters (dots are for data and open triangles for MC).*

below 100 MeV in the hadronic section (figure 4.30 c) and about 30 MeV in the electromagnetic section(figure 4.30 d).

- The hadronic part of the electron energy contained in the cylinder, gets smaller with an increase of R_{cyl}. E_{had} is smaller in the simulation than for the data, reflecting the discrepancy in the cell energies observed in figure 4.26.
- The evolution of the mean energy in the cylinder and in the hottest cluster are well described by the simulation. The difference in the ratio E_{hot}/E is of the order of 0.2%.

The energy in the cylinder around the electron may be due to final state radiation of the scattered electron, where low energetic emitted photons are not associated to the electron cluster, as in general the behaviour is reproduced by the simulation. The discrepancy from noise is rather small, as the SpaCal has in general very low noise. Increasing the cylinder radius for the definition of the scattered electron can on the other hand have the drawback on increasing the amount of misidentification from pions, therefore we decided to keep $R_{cyl} = 8.5\ cm$ for the electron definition and we apply an empiric suppression of the $y_{h,Spac}$ contribution, removing 2.5% of the electron energy from the energy associated to the hadronic final state in the SpaCal. The resulting $y_{h,Spac}$ distribution compared to the distribution before any suppression was applied can be seen in figure 4.31. The shape of the distribution after the suppression is described to an acceptable level by the simulation and its shape corresponds to the expected behaviour, which is not the case before the suppression was applied.

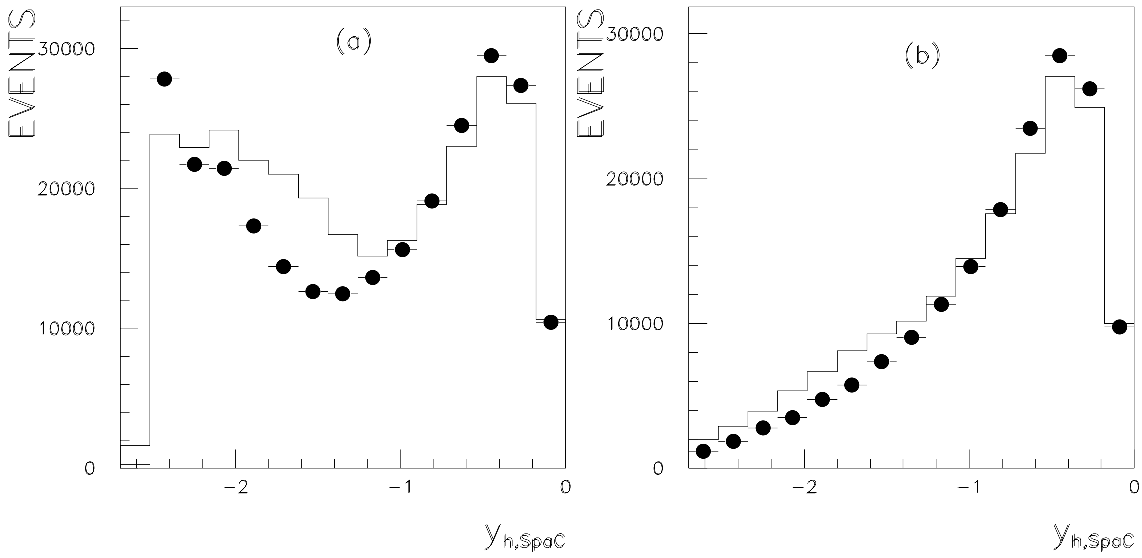

Figure 4.31: $y_{h,Spac}$ *distribution before and after a suppression of* 2.5% *of the scattered electron energy was applied.*

The final systematic error attributed on the energy of the hadronic final state in the SpaCal is 7%. As the SpaCal contribution is most visible in the y variable and most important at high y, we are comparing in figure 4.32 the ratio y_{SpaC}/y_e

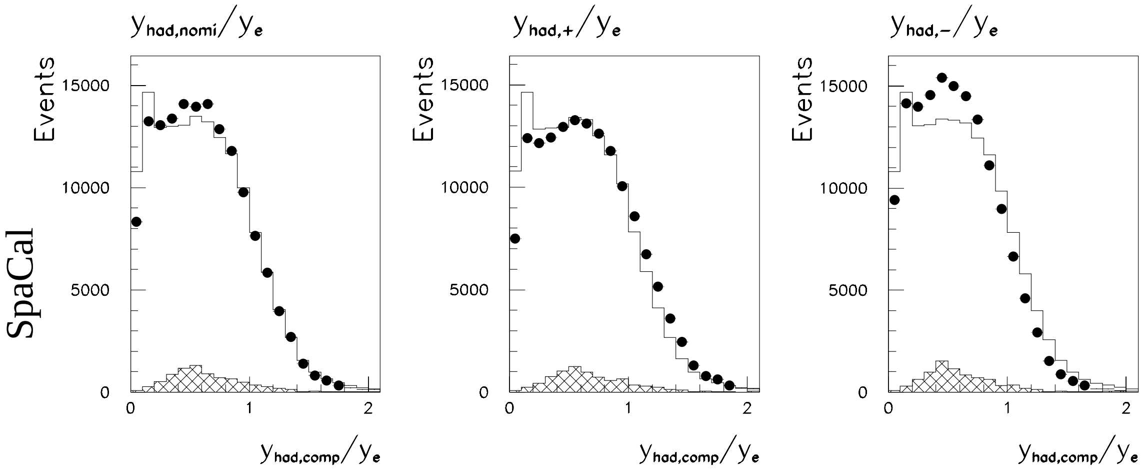

Figure 4.32: y_{SpaC}/y_e *for* $y_e > 0.1$. *The first column is showing the nominal contribution, whereas the second (third) column corresponds to a positive (negative) shift on the energy in data of the quoted* 7% *systematic error.*

for $y_e > 0.1$. The best agreement between data and MC is again found in the first column, whereas a positive or a negative shift degrades the description. The overall quality of the reconstruction of the hadronic final state and the kinematic variables can be seen in figure 4.33. Overall a good agreement between data and MC is achieved. The tail at low y_h/y_e is due to events with initial photon radiation.

4.4 The Vertex Reconstruction

The vertex of an event is reconstructed using the track information from the central and the forward tracking system. For the z-position of the central vertices, the tracks are first reconstructed from the CJC information only and then fitted to a common vertex [16]. Afterwards the precision of the θ-reconstruction is improved, using the information of CIZ/COZ. The typical error on the z-vertex position from central tracks is 0.48 *cm*, whereas the forward trackers give less precise positions with $\delta z \sim 3.25$ *cm*. The vertex position in x and y are obtained by fitting the vertices of a few hundred events and have a mean slope in dx/dz of -1.8 *mrad* and in dy/dz of 1.5 *mrad* which correspond to the tilt of the electron beam and the tilt of the tracking chamber to the ideal beam axis. The tilt of the electron beam is necessary in order to produce the crossing of the electrons and protons, which are stored in two separate rings. These tilts of the beams are produced by magnets outside the detector and they vary depending upon the beam condition, but are generally small compared to the tilt of the chamber. The tilts are not included in the simulation,

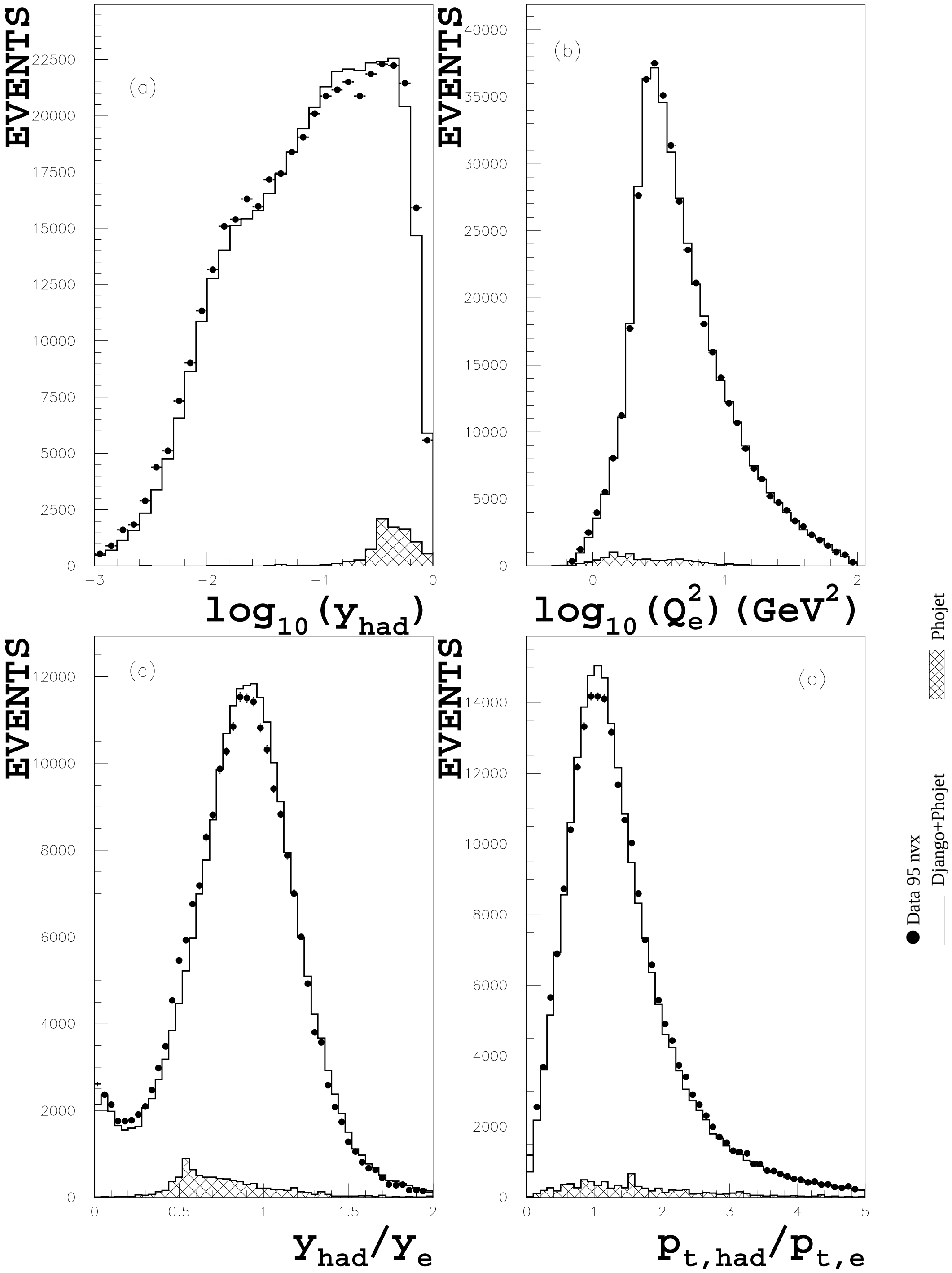

Figure 4.33: *Reconstruction of the kinematic variables: (a) is showing the distribution of* y_h*, (b)* Q_e^2*, (c) the ratio* y_h/y_e *for* $y_e > 0.1$ *and (d)* pt_h/pt_e*. The normalization is done according to the luminosity.*

only a constant off-set corresponding to the mean x-, y-position of the beam at the position of the SpaCal is put in the Monte Carlo.

4.4.1 The Vertex Reweighting

The global z-vertex distribution (figure 4.34) differs between data and Monte Carlo, both in their mean position and in the widths of the distribution.

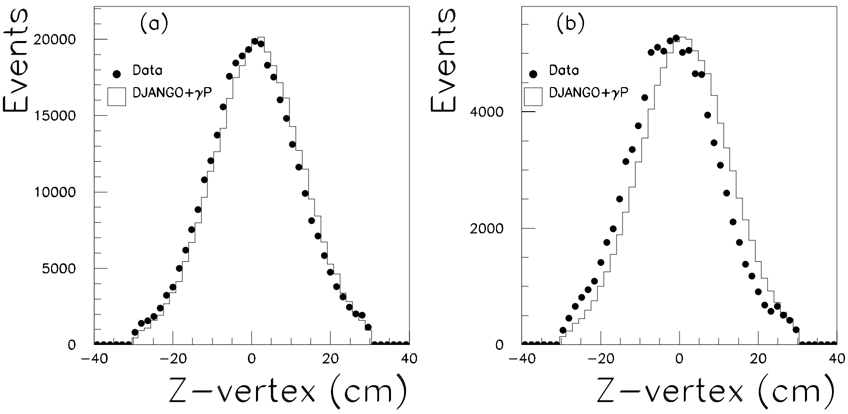

Figure 4.34: *z-vertex distribution (a)BSV and (b)ASV, in the later case a large shift is found between data and MC.*

During the 1995 running some data was taken with a shifted vertex, which implied a major change in the beam optics. If we look at the vertex for the data taking, before the shifted vertex (BSV) and after (ASV), the mean position of the z-vertex distribution changed from 0.54 *cm* for the BSV period to a mean position of -1.24 *cm* during the ASV period, while the width stayed the same at 11.4 *cm*. In the simulation the mean position of the $z - vertex$ is fixed to 1.22 *cm* and smeared to a width of 11.3 *cm*. Therefore cuts made on position variables determined from tracks on the detector level such as z_{BDC} or R_{BDC}, are effecting different θ and Q^2 regions in the data and in the simulation and can introduce biases in the F_2 extraction.

In order to study in more detail eventual changes in the positioning of the z-vertex, we can look at the mean position of the vertex distribution as a function of the run number (figure 4.35). A clear correlation of changes in the z-vertex position and the different stores of HERA ("luminosity fills") indicated by vertical lines, can be observed. The variations of the z-positions are varying from $+9$ *cm* to -5 *cm* among the different stores. As these differences in the running conditions can not be included in the simulation, a re-weighting procedure is applied in order to take these effects into account.

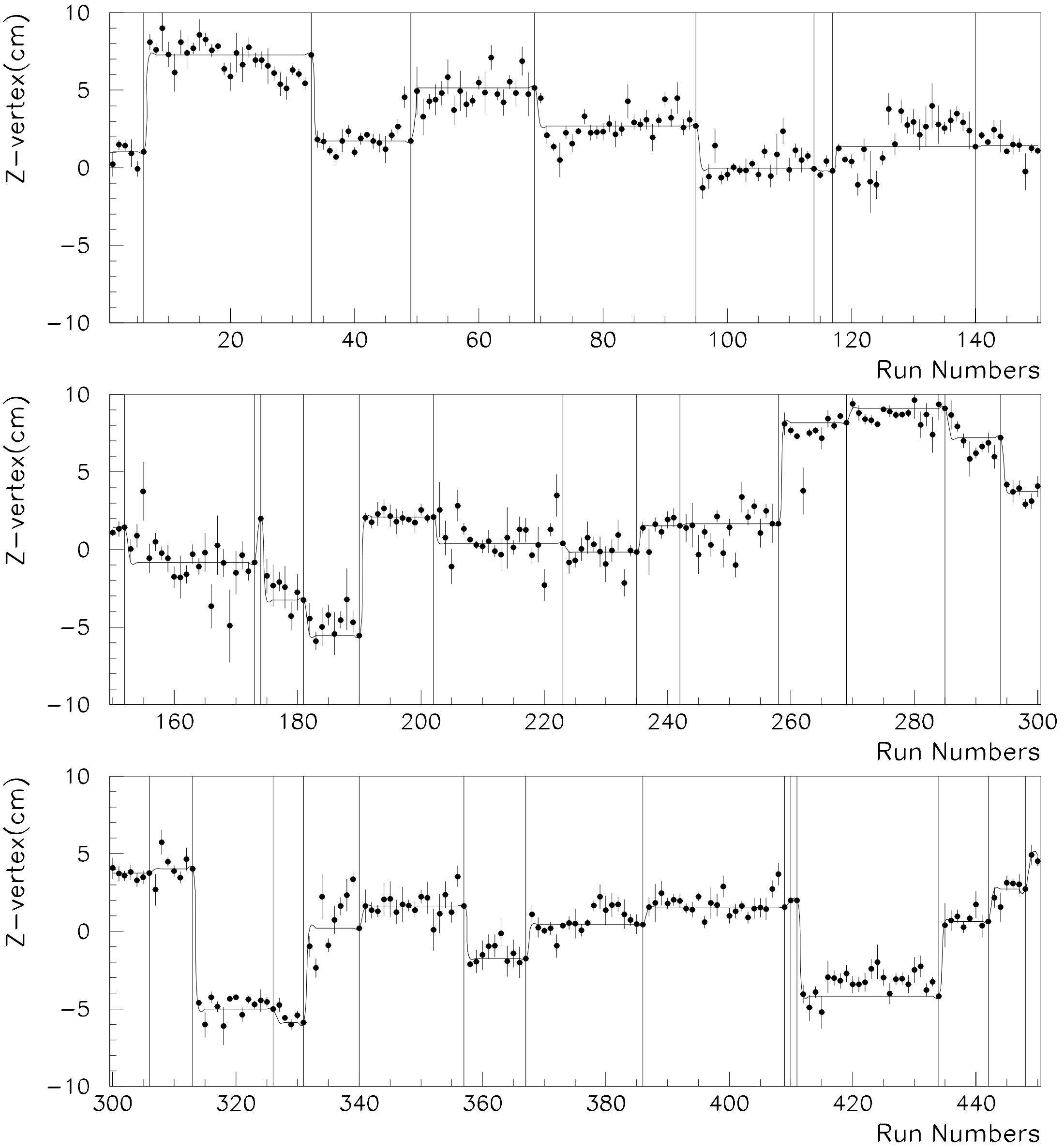

Figure 4.35: *z-vertex mean position as function of runs. From run-number 410 on-wards the fills correspond to the period ASV.*

The Reweighting Procedure

For the re-weighting of the vertex distribution in the simulation, Gaussian fits are made to each luminosity fill of data and to the entire MC. For the data, these Gaussian are normalized to the luminosity of the corresponding fill. The Gaussian for the two cases are,

$$w_{data}(l, z_{vertex}) \equiv \frac{\mathcal{L}_l}{\mathcal{L}_{tot}} \frac{1}{\sqrt{2\pi}\sigma_d(l)} exp\Big[-\frac{(z_{vertex} - m_d(l))^2}{2\sigma_d^2(l)}\Big] \tag{4.21}$$

for l^{th} luminosity fill, with $\mathcal{L}_l$ the luminosity of the fill, $\mathcal{L}_{tot}$ the total luminosity, m_d the mean value of the z-position of the vertex and σ_d the width (subscript d denotes data); and

$$w_{MC}(z_{vertex}) \equiv \frac{1}{\sqrt{2\pi}\sigma_m} exp\Big(-\frac{(z_{vertex} - m_m)^2}{2\sigma_m^2}\Big) \tag{4.22}$$

for the Monte Carlo (subscript m for MC).

The weight for a Monte Carlo event at a given z-vertex position is then determined by the ratio of the sum of all Gaussian from the different luminosity fills and the Gaussian from the MC as

$$w(z_{vertex}) = \frac{\sum_l w_{data}(l, z_{vertex})}{w_{MC}(z_{vertex})} \tag{4.23}$$

This weighting procedure adjusts at the same time, the shift and in the width between data and Monte Carlo distribution. The total z-vertex distribution before and after the re-weighting procedure can be seen in figure 4.36.

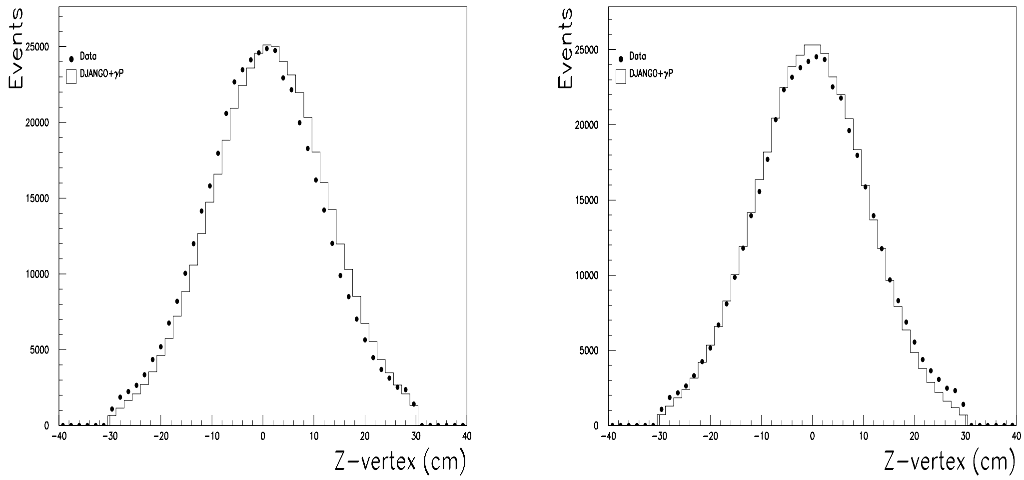

Figure 4.36: *z-vertex distribution (a)before re-weighting and (b)after re-weighting.*

The mean position in the MC changed from $z = 1.4$ cm to -0.1 cm and the width from 11.2 cm to 11.7 cm, which is now in good agreement with the data (mean=

0.1 *cm*, width=11.8 *cm*) although slight differences are still visible at the edge of the distribution arising from non-Gaussian effects in the forward vertex reconstruction (figure 4.37).

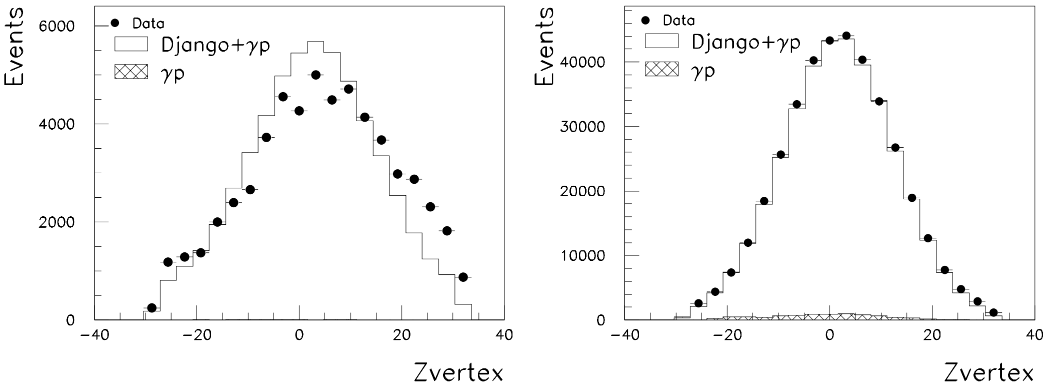

Figure 4.37: *z-vertex reconstructed from (a)forward and (b)central trackers.*

4.4.2 The x-,y-Vertex Positions and the Beam-Tilt

The x- and y-vertex positions are determined from a fit to the vertices of a few hundred events. As can be seen in figure 4.38, the x and y positions of the vertices

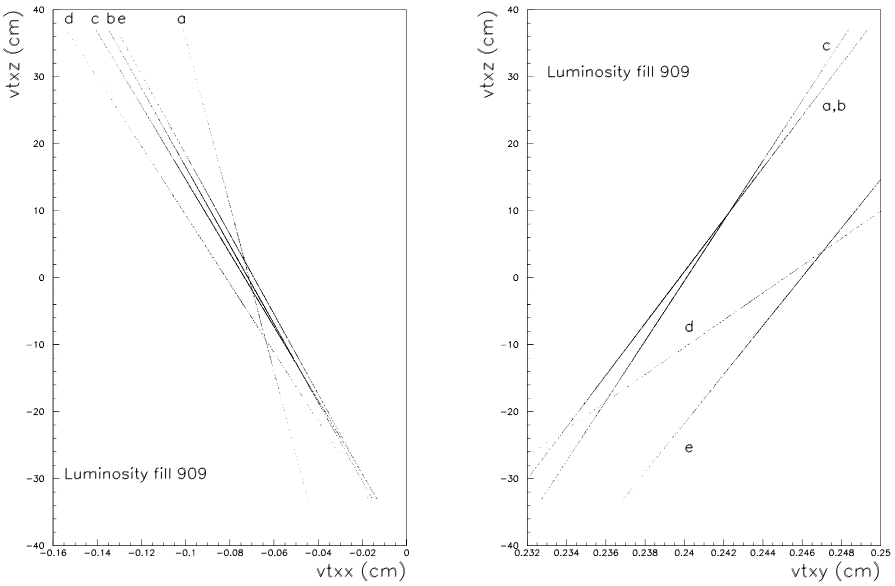

Figure 4.38: *Correlation of x- (left) and y-vertex (right) versus z-vertex for luminosity fill 909 in runs (a)125960, (b)125961, (c)125962, (d)125963 and (e)125964.*

in a given run at different positions of the z-vertex are lying along one line, corresponding to the electron beam-tilt and the tilt of the tracking chamber with respect to a reference line. Figure 4.39 is showing the x- and y-vertex position before and after the shifted vertex running. A mean position of -0.08 cm BSV and 0 cm ASV in x and of 0.25 cm BSV and 0.23 cm ASV in y is visible.

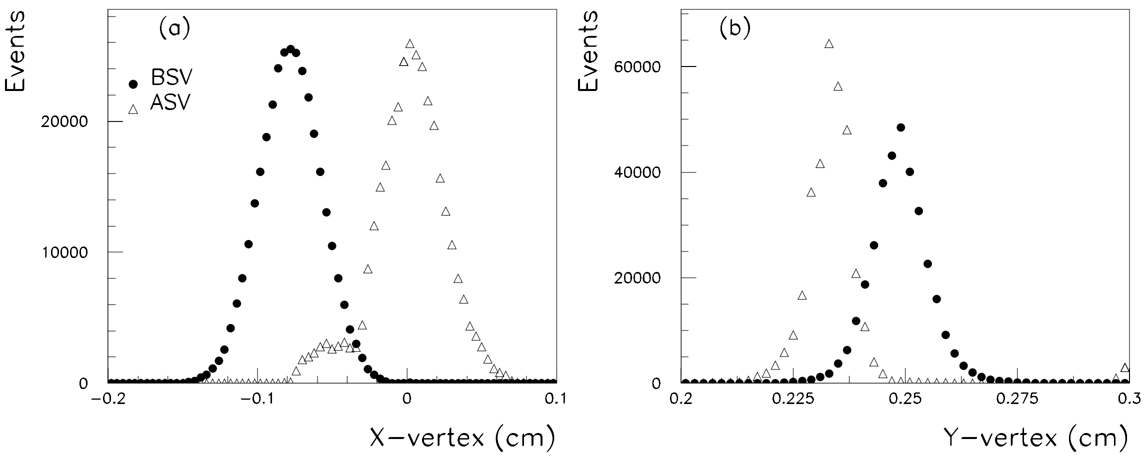

Figure 4.39: *(a)x-vertex distribution and (b)y-vertex distribution for BSV(solid circles) and ASV(open triangles).*

The complete vertex information is taken into account for the determination of the position of the energy depositions of the final state particles, while for the electron position also the tilt is taken into account. The x, y and z positions of the electron determined from the tracking are corrected according to the formula,

$$x_{new} = \frac{1.}{\sqrt{1+(\frac{dx}{dz})^2}}(x - \frac{dx}{dz}z) \tag{4.24}$$

$$y_{new} = \frac{1.}{\sqrt{1+(\frac{dx}{dz})^2}}\frac{1.}{\sqrt{1+(\frac{dx}{dz})^2+(\frac{dy}{dz})^2}}(-\frac{dx}{dz}\frac{dy}{dz}x + (1+(\frac{dx}{dz})^2)y - \frac{dy}{dz}z) \tag{4.25}$$

$$z_{new} = \frac{1.}{\sqrt{1+(\frac{dx}{dz})^2+(\frac{dy}{dz})^2}}(\frac{dx}{dz}x + \frac{dy}{dz}y + z) \tag{4.26}$$

The effect of this correction can be seen in figure 4.40, which is showing the φ-distribution of the scattered electron after the tilt correction. Although we get a better description between the data and the MC after this correction, we still see a sinusoidal behaviour in both data and MC of this distribution. This effect is due to the fiducial cut of the inner BDC-radius: as this cut is centered on the horizontal axis but the events are centered around an axis ex-centered by the x/y vertex position, a sinusoidal shape is produced. In order to get a flat behaviour in φ, as expected from physics, we are cutting on the radius determined from the ϑ-position of the electron.

Figure 4.41 is showing the φ distribution (b), y_h distribution (c), $p_{t,h}$ distribution and (d), y_h/y_e distribution for the data taking periods before the shifted vertex

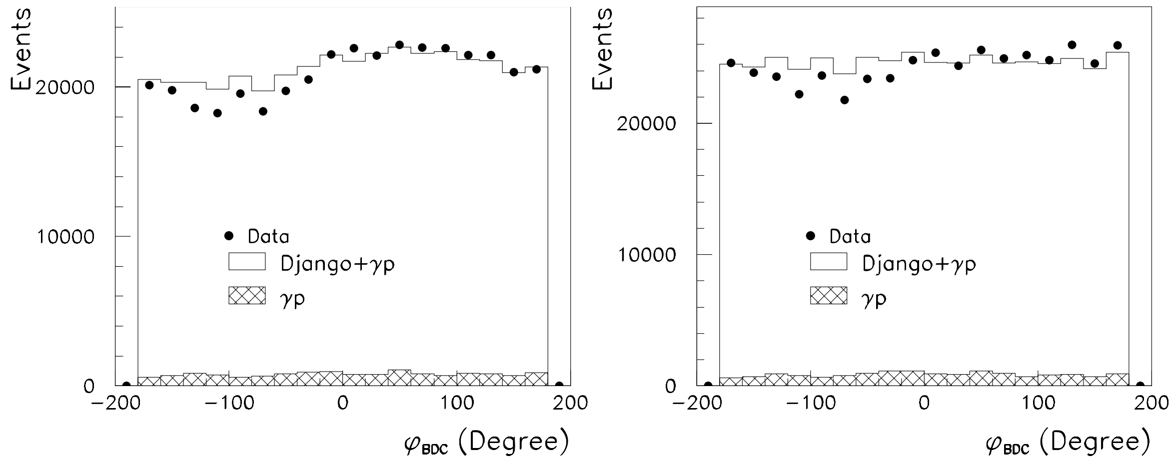

Figure 4.40: *Azimuthal angle φ distribution with (right) and without (left) effective BDC cut.*

run (BSV) and after the shifted vertex run (ASV). No notable difference in these distributions can be found after the corrections procedures previously described were applied.

4.4.3 The Vertex Reconstruction Efficiency

The vertex efficiency is determined by looking at the ratio of events with vertex and events without vertex. As the vertex requirement is rejecting an important fraction of non-ep background, other selection cuts non-related to the vertex reconstruction must be re-enforced in order to compare the data to the Monte Carlo. Therefore we put a cut on the timing requirement of the Plug calorimeter, between 35 ns and 45 ns for the data. Figure 4.42 is showing this efficiency in the bins of x and Q^2. The vertex efficency is in fact related to the y value, more than to x, which can be easily computed from the relation $x = Q^2/sy$, and implies that the highest x in each bin are approximatively always at the same y value of $y \sim 0.01$ and the highest x bins at $y \sim 0.5$.

Down to $y = 0.1$ the vertex efficiency shows a flat behaviour with an efficiency of 95 to 98%, which is well described by the simulation. At low y ($y < 0.05$) however, the efficiency drops rapidly and faster in the Monte Carlo than in the data. This drop is due to the topology of the events in this kinematic region. At low y, the hadronic final state is directed to the forward direction, leaving no more tracks in the tracking detector and therefore a vertex can not be reconstructed anymore. This is specially true at low Q^2, where also the electron is at low angle and therefore leaving no track in the tracking detectors (Figure 4.43).

The difference in data and MC may arise from various sources:

1. at low y, the y reconstruction may be strongly influenced by noise, and migration from events at very low y without vertex towards higher y can degrade

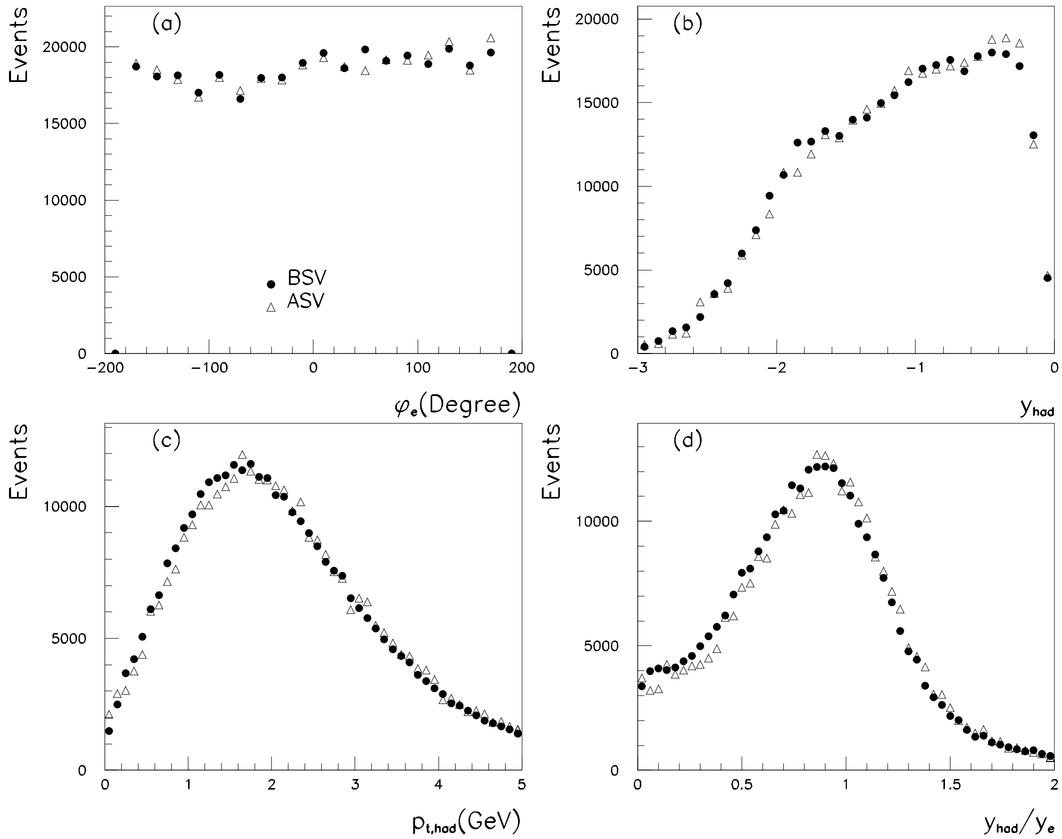

Figure 4.41: *Comparison of BSV-period (solid circles) and ASV-period (open triangles) for (a) φ distribution (b)y_h distribution (c)$p_{t,h}$ distribution and (d)y_h/y_e distribution.*

the vertex reconstruction efficency. This effect has been observed looking at the vertex reconstruction efficency with and without suppressing y_{SpaC} and a significant improvement has been found after the suppression was applied. Residual noise even in the liquid Argon Calorimeter, which may not be the same in data and MC, may still create a discrepancy between the data and the MC efficency.

2. at low y the fraction of events with a vertex reconstructed with the forward tracker increases, which are however less well understood (Figure 4.37 for z-vertex for central and forward vertices).

In the final results only bins were selected, where the vertex efficiency in data and MC agree better than 5%. No correction for the difference between data and simulation has been applied but a 5% systematic error has been included in the F_2 determination.

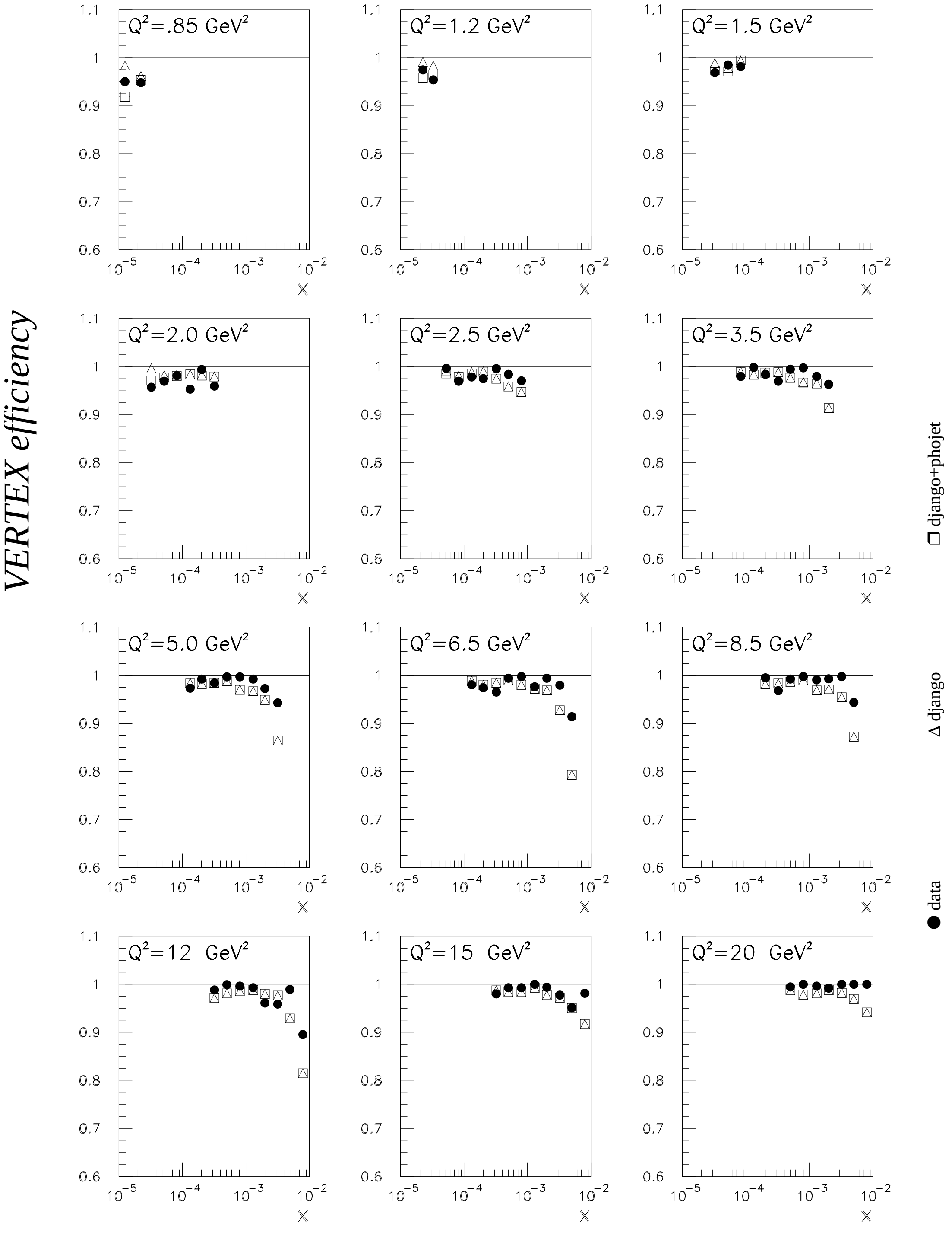

Figure 4.42: *Vertex reconstruction efficiency plotted as a function of Q^2 and x (obtained with the $e\Sigma$-method) in data (dots), DJANGO (open triangles) and DJANGO+PHOJET (open squares).*

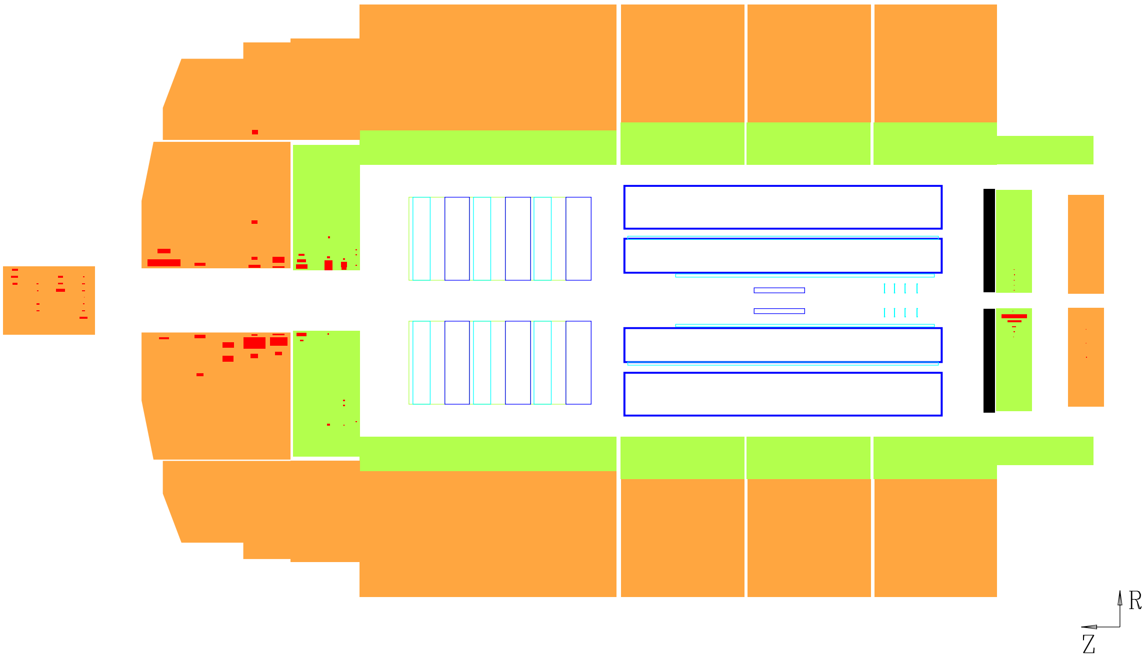

Figure 4.43: *Event Display of an event with no vertex and with* $Q^2 = 4.1$ *GeV^2 and y=0.007.*

4.5 Summary

The correct measurement of the structure function relies not only on the event selection, but also crucially on the reconstruction of the kinematic variables from the scattered electron and the hadronic final state. Therefore we had a close look in this chapter to the estimators used for the electron identification, on which the event selection mainly relies. The efficiencies due to the cuts on these estimators were compared between the data and the simulation. From this comparison correction factors were determined and the size of the correction included in the systematic error. The electron calibration was improved compared to the cell-wise calibration and a systematic error of 1% derived for electrons in the kinematic peak region and the electron angle corrected for effects of the "beam-tilt". The reconstruction of the hadronic final state was improved by reducing the contribution of y_{SpaC} at low y, which allowed for a significant improvement of the vertex reconstruction efficency. The most relevant kinematic distribution are described by the simulation at a satisfactory level, permitting therefore an extraction of the structure function.

Bibliography

[1] A. Blondel and F. Jacquet, **Proc. Study of an *ep* Facility for Europe,** ed. U. Amaldi, DESY 79/48 (1979)391.

[2] S. Bentvelsen et al, **Proc. Workshop Physics at HERA, Vol. 1,** eds. W. Buchmüller and G. Ingelman, DESY(1992)23.

[3] A. Arbuzov et al., **Comp. Phys. Comm.** 94 (1996) 128.

[4] U. Bassler, G. Bernardi, **NIM** A361 (1995) 197.

[5] U. Bassler, G. Bernardi, **preprint hep-ex/9801017**.

[6] J.Katzy, **Ph.D. Thesis** (in German), Heidelberg 1997.

[7] R. Wallny, **Ph.D. thesis** , Heidelberg *in preparation.*

[8] E. Barrelet et al., **NIM** A346 (1994) 137.

[9] S. Schleif, **Ph.D. thesis**, Heidelberg (1998).

[10] A. Meyer, **H1-Note** H1-12/97-532 (1997).

[11] C. Arndt, **Diploma thesis**, Hamburg (1995).

[12] W.H. Leo, **Techniques for Nuclear and Particle Physics Experiments**, Spinger Verlag, (1994).

[13] S. Kermiche, **Ph.D. thesis**, Orsay (1994).

[14] R. Maracek, **Ph.D. thesis**, Kosice (1998).

[15] U. Bassler, G. Bernardi, H1KINE - Users Guide, Software note H1-51-06/95 (1995).

[16] Volker Blobel, Stephen Burke, Stephan Egli, Gaby Raedel, Alexander Glazov, **The new tracker bank scheme** , Software note H1-47-06/94 (1994).

Chapter 5

The F_2 Measurement

In order to transform the measured number of events in bins of x and Q^2 into the physical quantity F_2, we use an iterative Monte Carlo unfolding. This method needs a correct description of the data by the simulation, which was obtained in the previous chapter. In this chapter the F_2 measurement is presented in several steps.

In section 5.1, we briefly discuss the mathematical method for the F_2 measurement. The iteration procedure implies the reweighting of the MC with the extracted structure function which will be discussed in section 5.2. The section 5.3 describes the bin selection for the F_2 measurement and the section 5.4 gives the detailed description of the systematic error sources. In section 5.5 the results will be presented and be compared with the previous H1 results and F_2 measurements from other experiments are gathered.

5.1 The Monte Carlo Method

As already discussed in chapter 1, F_2 is derived from the Born cross-section, where the interaction between electron and proton takes place through a single photon exchange without any contribution from diagrams involving higher powers of α, such that the coupling is controlled by the QED coupling constant α. In DIS the interaction takes place through processes of all orders and practically it is impossible to isolate the Born process. For this reason we absorb the radiative corrections in a factor δ_{RC} which have also been included in the cross-section calculation of the MC.

The relation between the double differential Born cross-section $d\sigma/dxdQ^2$ and F_2 can be written as

$$\left.\frac{d^2\sigma(x,Q^2)}{dxdQ^2}\right|_{Born} = \kappa(R)F_2(x,Q^2) \tag{5.1}$$

The kinematic factor κ is defined as,

$$\kappa(R) = \frac{2\pi\alpha^2}{Q^4x}(2(1-y)+\frac{y^2}{1+R}) \tag{5.2}$$

and the Born cross-section obtained by applying corrections for QED-radiation

$$\left.\frac{d^2\sigma(x,Q^2)}{dxdQ^2}\right|_{Born} = \frac{d^2\sigma(x,Q^2)}{dxdQ^2}(1+\delta_{RC}) \tag{5.3}$$

In addition to the kinematic terms, κ contains $R = F_L/(F_2 - F_L)$. The longitudinal structure function F_L has been recently estimated by H1 [6] but in this analysis we used F_L parameterization by Badelek and Kwiecinski [7]. In the Badelek-Kwiecinski model $F_L \propto O(Q^4)$ such that the $Q^2 = 0$ singularity in the hadronic tensor is canceled and in addition the total longitudinal cross-section vanishes in $Q^2 \to 0$ limit to ensure that a real photon do not contribute to σ_L.

The radiative corrections are estimated by MC. They are obtained from the comparison of the Born cross-section to the total cross section. The radiative correction factor δ_{RC} is

$$\delta_{RC} = \frac{\int_\Box \frac{d\sigma_o^{MC}(x,Q^2)}{dxdQ^2}dxdQ^2}{\int_\Box \frac{d^2\sigma^{MC}(x,Q^2)}{dxdQ^2}dxdQ^2} - 1 \tag{5.4}$$

where σ_o^{MC} denotes the Born cross-section, and σ^{MC} the radiative cross-section, both obtained from Monte Carlo Simulation. F_2 is measured in the bins of x and Q^2 at the center of a bin taking into account the correction due to the cross section measured in the whole bin. The bin size correction factor is estimated from the Born cross section from MC as,

$$c^\Box = \frac{\left.\frac{d\sigma_o^{MC}(x,Q^2)}{dxdQ^2}\right|_{x_c,Q_c^2}}{\int_\Box \frac{d^2\sigma_o^{MC}(x,Q^2)}{dxdQ^2}dxdQ^2} \tag{5.5}$$

So equation 5.1 for the center c of the bin $\Box$ becomes,

$$c^\Box(1+\delta_{RC})\int_\Box \frac{d^2\sigma^{data}(x,Q^2)}{dxdQ^2} = \kappa(R)F_2^{data}(x_c,Q_c^2) \tag{5.6}$$

The differential cross section $d^2\sigma^{data}(x,Q^2)/dxdQ^2$ takes the detector acceptances and the efficiencies into account,

$$\int_\Box \frac{d^2\sigma^{data}(x,Q^2)}{dxdQ^2}dxdQ^2 = \frac{N^{\Box,data} - N^{\Box,\gamma P}}{A^\Box \epsilon^\Box \mathcal{L}^{data}} \tag{5.7}$$

Here $N^{\Box,data}$ is the number of the data events in the $\Box^{th}$ bin, $N^{\Box,\gamma P}$ is the estimated number of photoproduction events $A^\Box$ is the detector acceptance, $\epsilon^\Box$ the selection efficiency and $\mathcal{L}^{data}$ is the total integrated luminosity. The number of the photoproduction events, $N^{\Box,\gamma p}$ is obtained from the PHOJET Monte Carlo and was shown in the previous chapter to describe the amount of photoproduction events seen in the limited acceptance of the electron tagger as well as to accommodate the overall description of the data sample.

From equation 5.6, F_2 is extracted as

$$F_2^{data}(x_c, Q_c^2) = \frac{1}{\kappa(R)} c^{\Box,MC} (1 + \delta_{RC}^{\Box,MC}) \int_\Box \frac{d^2\sigma^{data}(x, Q^2)}{dx dQ^2} \tag{5.8}$$

$$= \frac{1}{\kappa(R)} \frac{\frac{d\sigma_o^{MC}(x,Q^2)}{dxdQ^2}|_{x_c,Q_c^2}}{\int_\Box \frac{d^2\sigma^{MC}(x,Q^2)}{dxdQ^2} dx dQ^2} \int_\Box \frac{d^2\sigma^{data}(x, Q^2)}{dx dQ^2} \tag{5.9}$$

In the same way as for the data, the Monte Carlo cross-section in a bin can be written as

$$\int_\Box \frac{d^2\sigma^{MC}(x, Q^2)}{dx dQ^2} dx dQ^2 = \frac{N^{\Box,MC}}{A^\Box \epsilon^\Box \mathcal{L}^{MC}} = \frac{N_{gen}^{\Box,MC}}{\mathcal{L}^{MC}} \tag{5.10}$$

and using the relation

$$\frac{d^2\sigma_o^{MC}(x, Q^2)}{dx dQ^2}|_{x_c,Q_c^2} = \kappa F_2^{MC}(x_c, Q_c^2) \tag{5.11}$$

we get

$$F_2^{data}(x_c, Q_c^2) = \frac{N^{\Box,data} - N^{\Box,\gamma P}}{N^{\Box,MC}} \frac{\mathcal{L}^{MC}}{\mathcal{L}^{data}} F_2^{MC}(x_c, Q_c^2) \tag{5.12}$$

under the assumption that

$$A^{\Box,data} \epsilon^{\Box,data} = A^{\Box,MC} \epsilon^{\Box,MC} \tag{5.13}$$

But as the acceptance, and also the efficiency are depending on the structure function itself, we can only use this method if the structure function used in the Monte Carlo is as close as possible to the measured structure function. Therefore we iterate the determination of $N^{\Box,MC}$ and F_2^{MC} until the obtained structure function F_2^{data} remains unchanged.

5.2 The F2 Reweighting Procedure

In the iterative method of the F_2 measurement, each time a new F_2 is measured, it is given as an input to the Monte Carlo. As it is practically difficult to resimulate the entire MC for each iteration, the MC is reweighted on an event by event basis. The weight for an event is defined as the ratio of the new parametrization cross-section to the MC differential cross section as following:

$$W(x_{gen}, Q_{gen}^2) = \frac{d^2\sigma^{par}}{dx dQ^2}(x_{gen}, Q_{gen}^2) / \frac{d^2\sigma^{gen}}{dx dQ^2}(x_{gen}, Q_{gen}^2) \tag{5.14}$$

Here the subscript *gen* indicates the corresponding generated quantities. $d^2\sigma^{gen}/dxdQ^2$ is the cross-section used for the MC generation, $d^2\sigma^{par}/dxdQ^2$ is the cross section obtained from the parametrization of the measured cross section. For the MC generation the GRV94 parametrization was used. In the MC generation, F_L was set to 0, but for the extraction of F_2, the Badelek-Kwiecinski model was used. As a best estimate of F_2, the fit to the shifted vertex and the H1 1995 data was used [8]. The

F_2 fit was made according to the following parameterization by Badelek-Kwiecinski [7] in which F_2 is split into photoproduction and DIS parts as,

$$F_2(x, Q^2) = C_{VDM} F_2^{VDM} + \frac{Q^2}{Q^2 + Q_0^2} F_2^{QCD}(\bar{x}, Q^2 + Q_0^2) \tag{5.15}$$

Where $\bar{x} = (Q^2 + Q_0^2)/(W^2 + Q^2 + Q_0^2)$. The fit parameters in equation 5.15 are the normalization of the vector meson term C_{VDM} and the meson mass cut-off parameter Q_0^2 which are found to be 0.77 GeV^2 and 0.45 GeV^2 respectively after the fit was made to the previous F_2 measurements of H1 and of the fixed target experiments NMC and BCDMS to cover the entire x-region. In the kinematic region of the present measurement, the VDM part has only a marginal influence. The DIS part is obtained with the parametrization of a NLO QCD fit.

5.3 The Bin Selection

The accurate bin selection is important for the F_2 measurement, as a large bin size may shadow physics, a very small bin size leads to statistical fluctuations and high correlation between the bins due to migration. The binning can be defined linear, logarithmic or exponential depending upon the behavior of the quantity to be measured. As the variation of F_2 is logarithmic in Q^2, we choose a logarithmic binning in both x and Q^2. The number of bins per decade must be related to the resolution of the kinematic variables and has been chosen to be 8 bins per decade in Q^2 and 4 bins per decade in x, the Q^2 resolution being approximately twice as good as the resolution in x. The bin boundaries and bin centers in Q^2 and x are given in table 5.1 and 5.2.

Q^2	.74990	1.0000	1.3340	1.7780	2.3710	3.1620	4.2170	5.6230
Q_c^2		.85000	1.2000	1.5000	2.0000	2.5000	3.5000	5.0000
Q^2	7.4990	10.000	13.340	17.780	23.710			
Q_c^2	6.5000	8.5000	12.000	15.000	20.000			

Table 5.1: *Table defining the boundaries and the centers of the bins in* Q^2

x	.0000100	.0000158	.0000251	.0000398	.0000631
x_c		.0000130	.000020	.000032	.00005
x	.000100	.000158	.000251	.000398	.000631
x_c	.00008	.00013	.00020	.00032	.0005
x	.00100	.00158	.00251	.00398	.00631
x_c	.0008	.0013	.0020	.0032	.005
x	.01000				
x_c	.0080				

Table 5.2: *Table defining the boundaries and the centers of the bins in* x

In order to determine the bins in which we can perform the F_2 measurement, the migration of events were studied using different methods for the kinematic reconstruction with simulated events.

5.3.1 Acceptance, Purity and Stability

In order to quantify the migration effects,the notion of stability, purity and acceptance are introduced [1].

The Stability

The ratio of the number of events which are both reconstructed and generated in the same bin to the number of events generated in that bin is called stability. In these terms, the stability is related to the resolution of the reconstruction of a kinematic variable. Figure 5.1 shows the stability for the electron, the Σ and the $e\Sigma$-method. The electron method reaches the highest stabilities at low x, but it decreases rapidly towards medium and large x. The Σ method has a lower stability in general (about 50%) but a more flat behavior and allows to reaches higher x in the measurement. The $e\Sigma$ method lies between the two methods, showing a stability nearly as high as the electron method at low x and a slightly better behavior as the Σ method at high x, as it combines the excellent Q^2 reconstruction of the electron method with the stable x-behavior of the Σ-method.

The Purity

The purity is the ratio of the number of events which are both reconstructed and generated in the same bin to the number of events reconstructed in that bin. Figure 5.2 shows the purities for the three reconstruction methods. The behavior of the three methods is similar to that of the stability.

The Acceptance

The smeared acceptance is defined as the ratio of the number of events reconstructed to the number of events generated in a bin (figure 5.3) after all cuts have been applied. The quantity depends upon the geometry as well as the detector resolution and gives in some sense the basic matrix for the unfolding of the measured quantity towards the physics, therefore the acceptance should have values close to 1. However this is not sufficient for our bin selection criteria: as the acceptance is the ratio of stability over purity, an acceptance close to 1 can be reached although the migrations are high and the stability and purity low.

The Bin Selection:

Table 5.1 shows 15 selected bins in Q^2 with edges and centers of all bins. Similarly, table 5.2 shows 14 selected bins in x with their edges and centers. These selected bins and the corresponding number of events in each bin, for the three different methods after applying a 40% criteria on the stability and the purity for the electron method and a 30% criteria for the Σ and the $e\Sigma$ method, are further shown in figure 5.4 in the $x - Q^2$ plane.

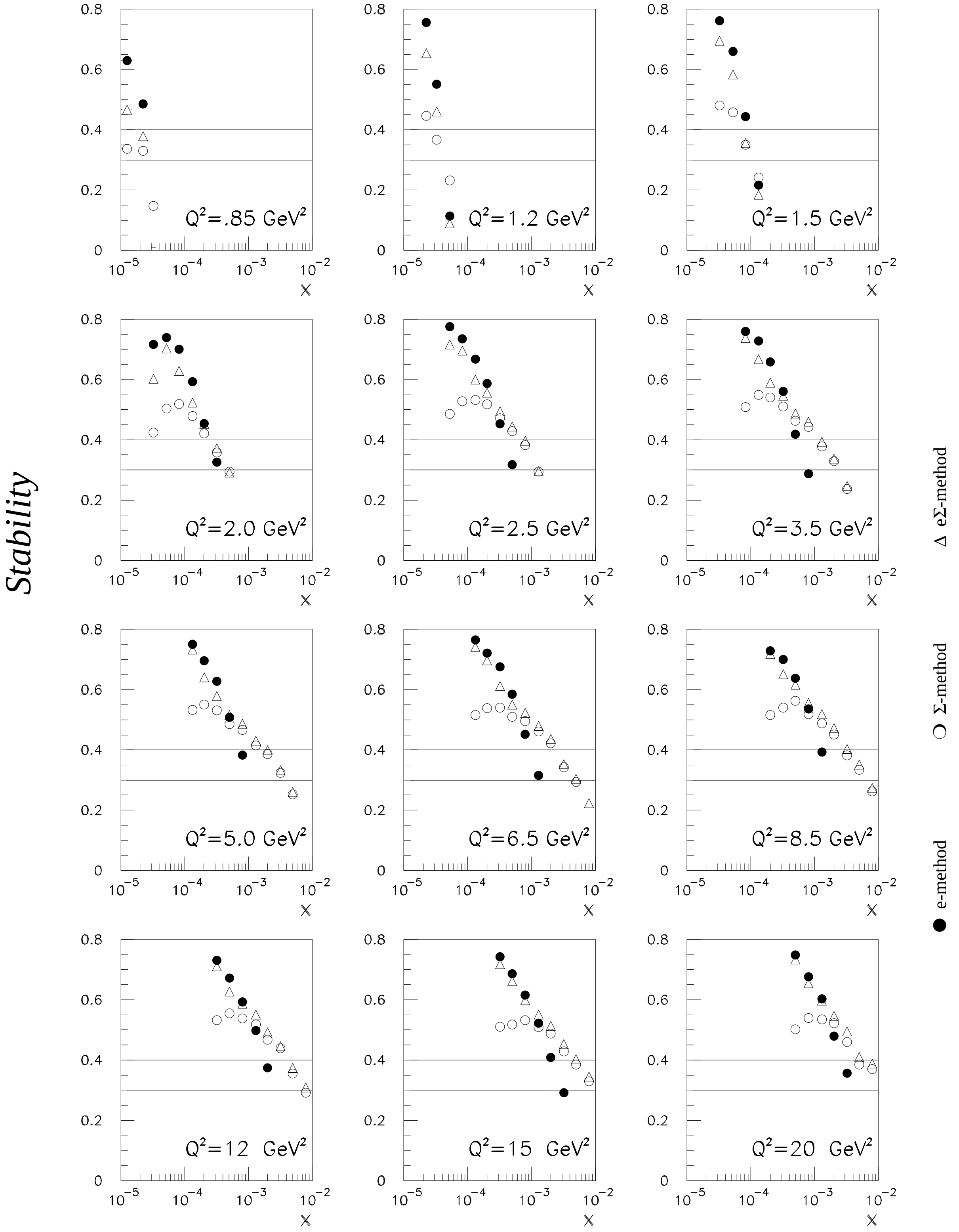

Figure 5.1: *Stability for (1)e- method (dots), (2) Σ- method(open circles) and (3) eΣ-methods (open triangles) is shown in different Q^2 bins as a function of* $\log_{10}(x)$. *The upper line at 0.4 is the lower limit for e-method while lower line at 0.3 is the lower limit for both Σ- and eΣ- methods*

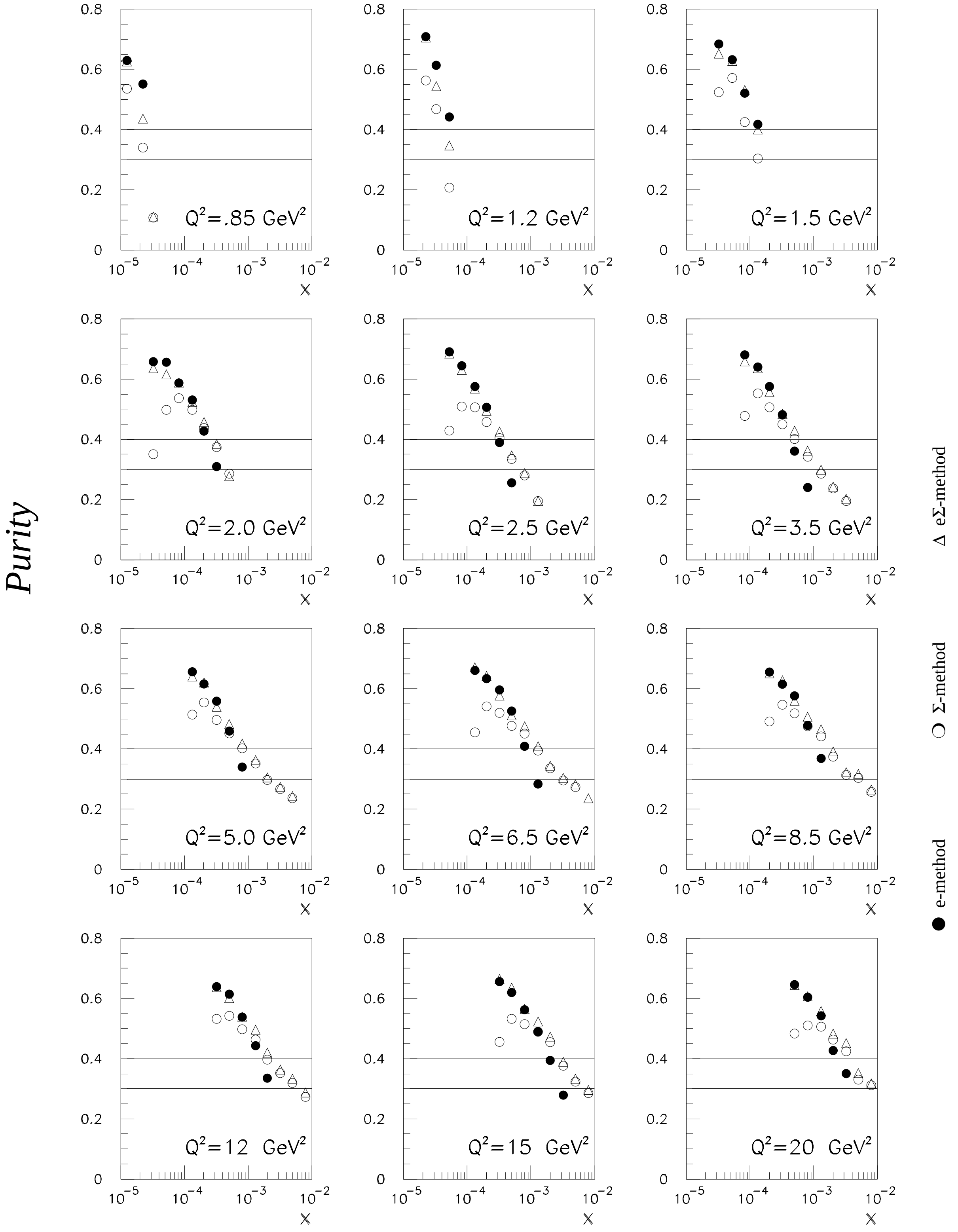

Figure 5.2: *Purity for (1)e- method (dots), (2)Σ- method(open circles) and (3)eΣ- method (open triangles) is shown as a function of* $\log_{10}(x)$ *for different* Q^2 *bins. Upper line at 0.4 is the lower limit for e-method while lower line at 0.3 is the lower limit both for Σ- and for eΣ- methods.*

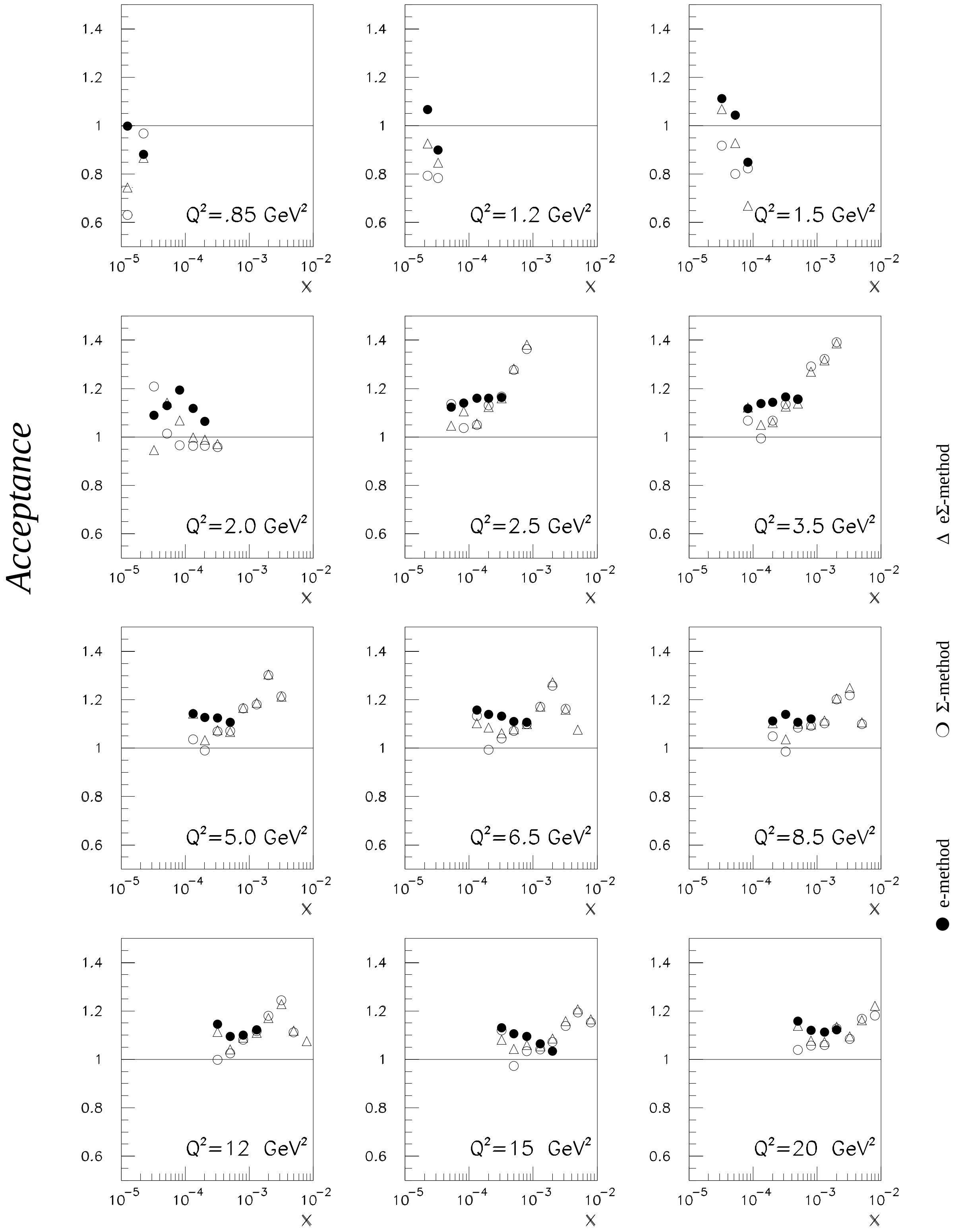

Figure 5.3: *Acceptance as a function of* $\log_{10}(x)$ *in bins of* Q^2 *for (1)electron method (dots), (2) sigma method(open circles) and (3) e*Σ*-method (open triangles).*

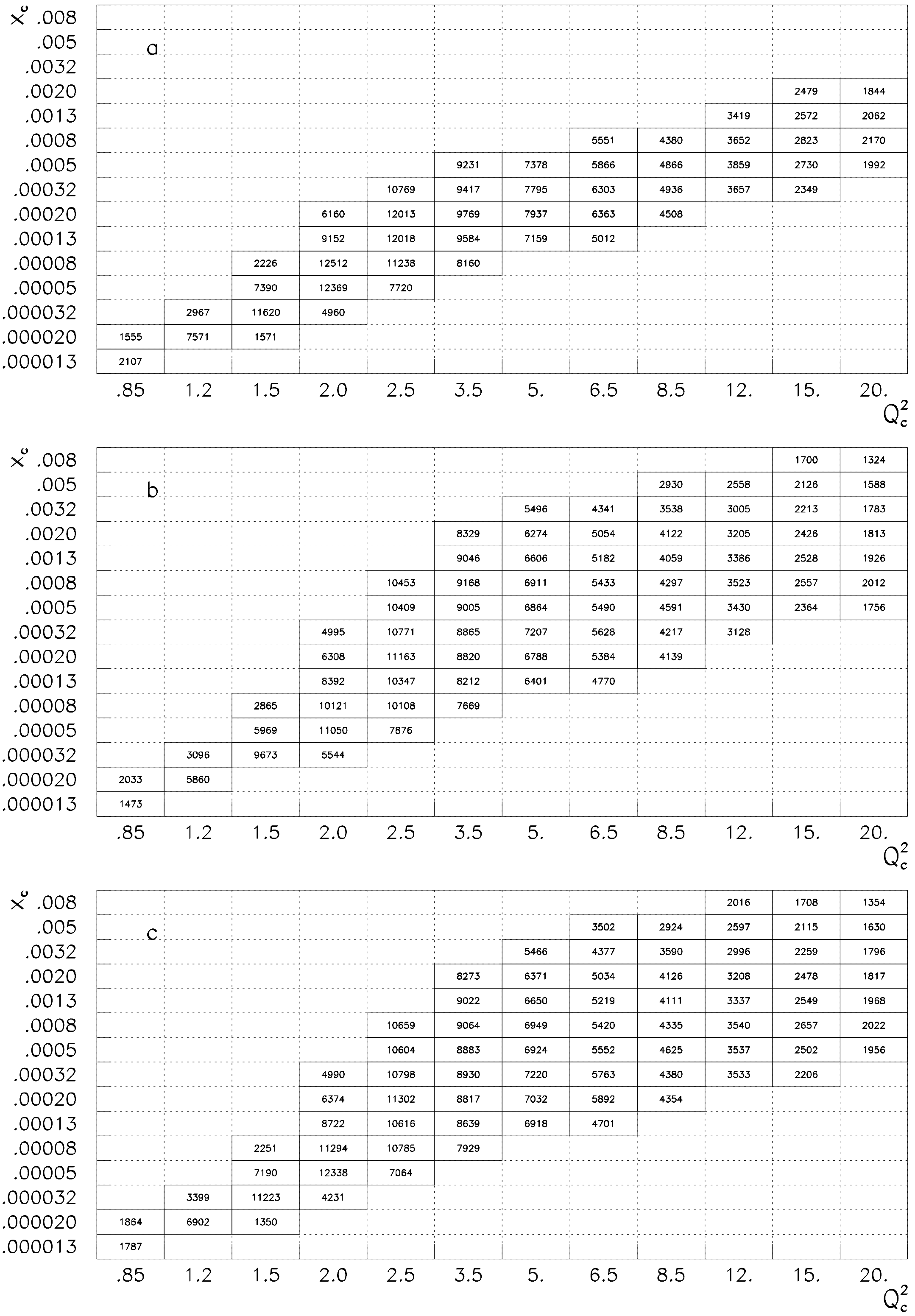

x^c \ Q^2_c	.85	1.2	1.5	2.0	2.5	3.5	5.	6.5	8.5	12.	15.	20.
.008												
.005												
.0032												
.0020											2479	1844
.0013										3419	2572	2062
.0008								5551	4380	3652	2823	2170
.0005						9231	7378	5866	4866	3859	2730	1992
.00032					10769	9417	7795	6303	4936	3657	2349	
.00020				6160	12013	9769	7937	6363	4508			
.00013				9152	12018	9584	7159	5012				
.00008			2226	12512	11238	8160						
.00005			7390	12369	7720							
.000032		2967	11620	4960								
.000020	1555	7571	1571									
.000013	2107											

x^c \ Q^2_c	.85	1.2	1.5	2.0	2.5	3.5	5.	6.5	8.5	12.	15.	20.
.008											1700	1324
.005									2930	2558	2126	1588
.0032							5496	4341	3538	3005	2213	1783
.0020						8329	6274	5054	4122	3205	2426	1813
.0013						9046	6606	5182	4059	3386	2528	1926
.0008					10453	9168	6911	5433	4297	3523	2557	2012
.0005					10409	9005	6864	5490	4591	3430	2364	1756
.00032				4995	10771	8865	7207	5628	4217	3128		
.00020				6308	11163	8820	6788	5384	4139			
.00013				8392	10347	8212	6401	4770				
.00008			2865	10121	10108	7669						
.00005			5969	11050	7876							
.000032		3096	9673	5544								
.000020	2033	5860										
.000013	1473											

x^c \ Q^2_c	.85	1.2	1.5	2.0	2.5	3.5	5.	6.5	8.5	12.	15.	20.
.008										2016	1708	1354
.005								3502	2924	2597	2115	1630
.0032							5466	4377	3590	2996	2259	1796
.0020						8273	6371	5034	4126	3208	2478	1817
.0013						9022	6650	5219	4111	3337	2549	1968
.0008					10659	9064	6949	5420	4335	3540	2657	2022
.0005					10604	8883	6924	5552	4625	3537	2502	1956
.00032				4990	10798	8930	7220	5763	4380	3533	2206	
.00020				6374	11302	8817	7032	5892	4354			
.00013				8722	10616	8639	6918	4701				
.00008			2251	11294	10785	7929						
.00005			7190	12338	7064							
.000032		3399	11223	4231								
.000020	1864	6902	1350									
.000013	1787											

Figure 5.4: *Event distribution in bins selected for* F_2 *in case of (a) e-method, (b)* Σ*-method and (c)e*Σ*-method. These plots are for MC.*

The difference in the criteria is justified by the strong migrations in the electron method due to radiation and to the steeper variation in both quantities for the electron method.

The final results will be presented in the $e\Sigma$-method, as this method covers the highest number of bins with the best performances. The e and the Σ method are used to cross-check the results as a good agreement between the two indicates an accurate calibration of the detector as well as a correct handling of the radiative corrections.

5.4 Systematic Errors

The systematic errors can be divided in two parts: correlated systematic errors, as for example errors due to a miscalibration affecting the measurement by migrations, which will increase the number of events in one bin, but at the same time decrease it in another bin and therefore create correlations between the bins. Uncorrelated errors allow for independent fluctuations in each bin.

5.4.1 Correlated Systematic Errors

These errors are determined by studying the migrations due to different effects of mismeasurements by comparing the acceptances after having shifted the measured quantities within the precision of their determination. The studied error sources are the electron energy scale, the electron angle and the hadronic energy scales. The results are only shown for the $e\Sigma$- method as we will present our final results for this method. In order to compute the systematic error, we compute the acceptance after all cuts (selection cuts plus fiducial cut) with and without modifying the quantity we want to study.

It should be noted that the selection cuts are applied on the modified quantities. $\delta F_2/F_2$ is obtained by,

$$\frac{\delta F_2}{F_2} = \frac{A - A^{\pm}}{A} \tag{5.16}$$

A being the smeared acceptance as defined in section 5.3.1. The determined errors are asymmetric taking into account a positive and a negative shift of the studied quantity.

The Electron Energy Scale:

From the distribution of the electron energy after the calibration procedure, we can claim to know the precision of the electron energy around the kinematic peak up to 1%. At lower energies ($\sim 10\ GeV$), dedicated studies were made using QED-Compton events (see 4.17) which show an accuracy of 3%. Therefore we are varying the electron energy between 1 and 3% linearly as function of the electron energy between 30 and 10 GeV for the determination of the systematic error contribution. The result is shown in figure 5.5. The filled circles correspond to a positive shift, whereas the open triangles correspond to a negative shift. The effect is biggest in the bin at lowest x, where the cut on the electron energy influences directly the population of a bin. Towards higher x, the effects are decreasing with a crossing point between the positive and the negative shift and leveling out at an error of about 2% on F_2.

The Electron Angle

The accuracy of the electron angle measurement has been determined to be better than 1 *mrad* [2]. This leads to a nearly constant error on F_2 of about 1.5% (figure 5.6). The influence of this error is sizeable at low y and at low Q^2, where the limit of the angular acceptance is reached.

The Hadronic Energy Scale

For the measurement of the hadronic final state, we are using three different subdetectors, which are measuring independently the energy and must, therefore, be considered as independent error sources. Most of the energy of the hadronic final state is measured in the liquid Argon calorimeter. After the calibration, the description of the data by the MC is better than 4%. The contribution from tracks is known with an accuracy of 3% and the energy carried by the SpaCal is known with a precision of 7% (see figures 4.24, 4.32). Figures 5.7 to 5.9 are showing the effect on F_2 of these three error sources.

The Luminosity

The most correlated error is coming from the luminosity measurement, as it moves all points up and down by the same amount. The luminosity determination is discussed in chapter 2. The systematic error arising from the luminosity measurement is 1.97% and not included in the total error bars.

5.4.2 Uncorrelated Systematic Errors

The Electron Identification Efficiency:

To select the electrons in the data, we used three estimators ECRA, EBDC and EHAD as discussed in the earlier section of this chapter. The systematic errors resulting from this selection is generated by the different behavior of the data and the MC and are about 2% in the main region of the measurement and 4% at low x.

The Photoproduction Background

The uncertainty in the subtraction of the photoproduction background is 30% of the subtracted photoproduction background. It affects only on the low x-bins particularly for small Q^2. The resulting uncertainty in F_2 measurement is about 6% in this region.

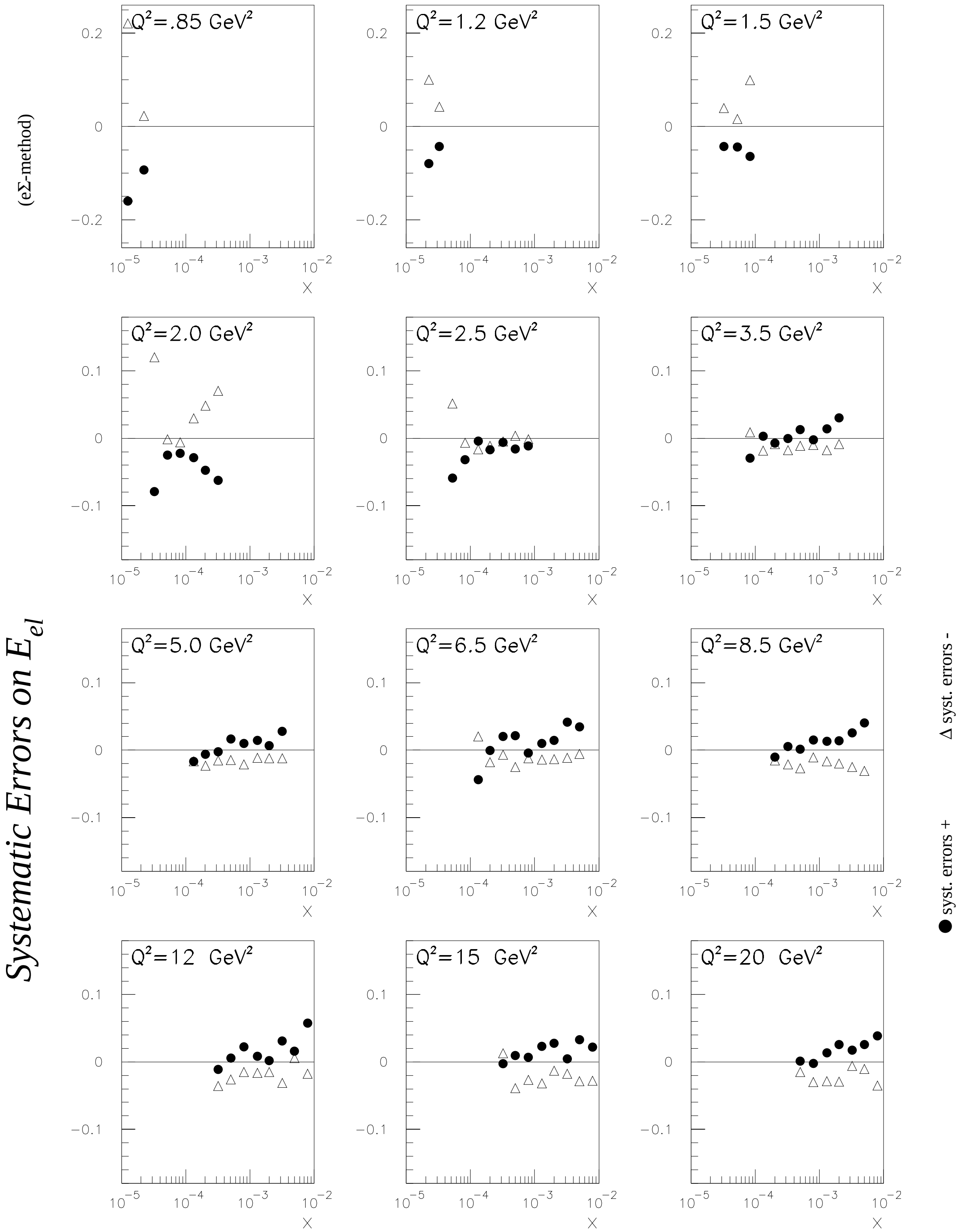

Figure 5.5: *Systematic errors as function of* $\log_{10}(x)$ *in bins of* Q^2 *for* $e\Sigma$*- method due to errors in scattered electron energy measurements.*

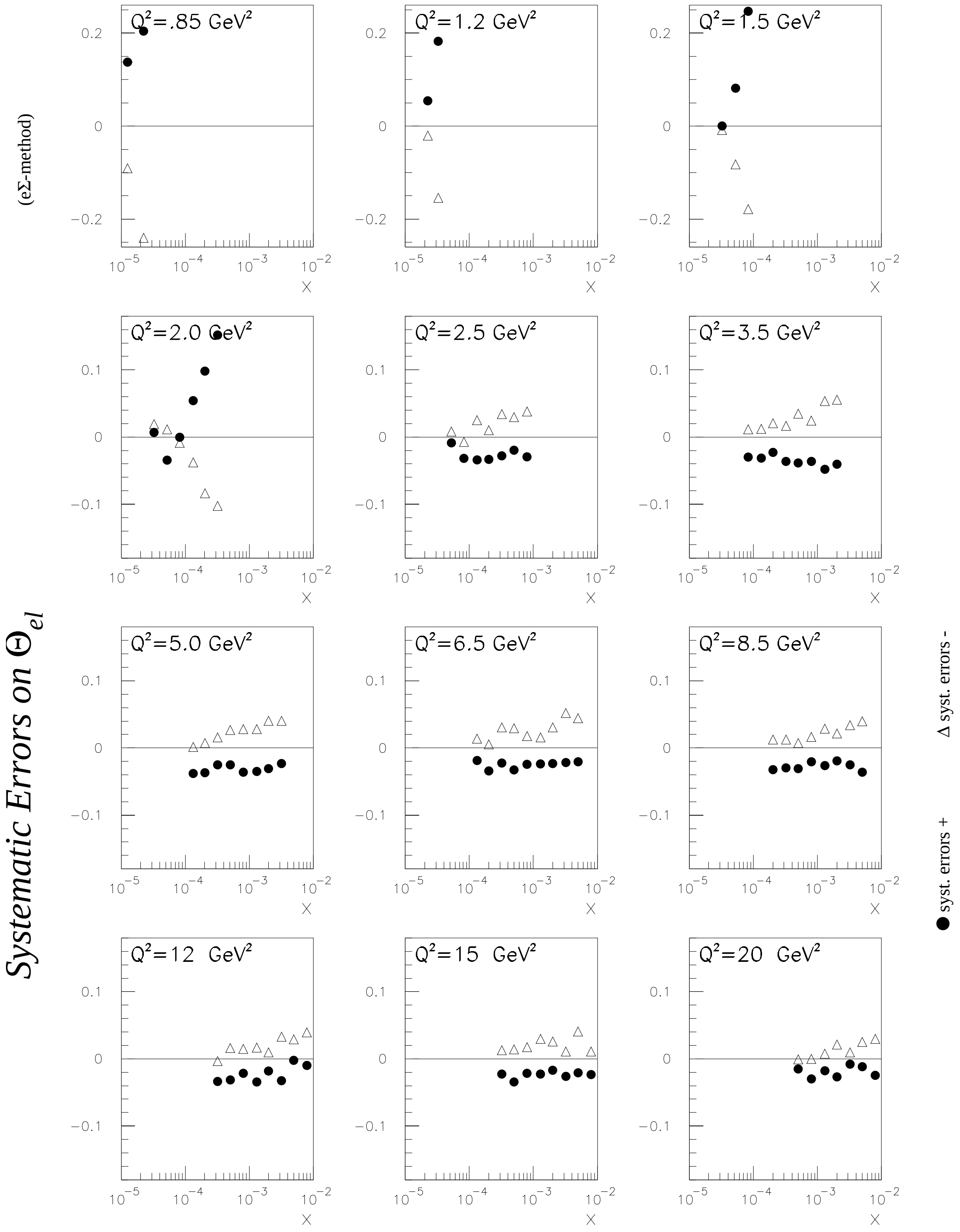

Figure 5.6: *Systematic errors as function of* $\log_{10}(x)$ *in the bins of* Q^2 *in* $e\Sigma$*- method due to errors in scattered electron angle measurements.*

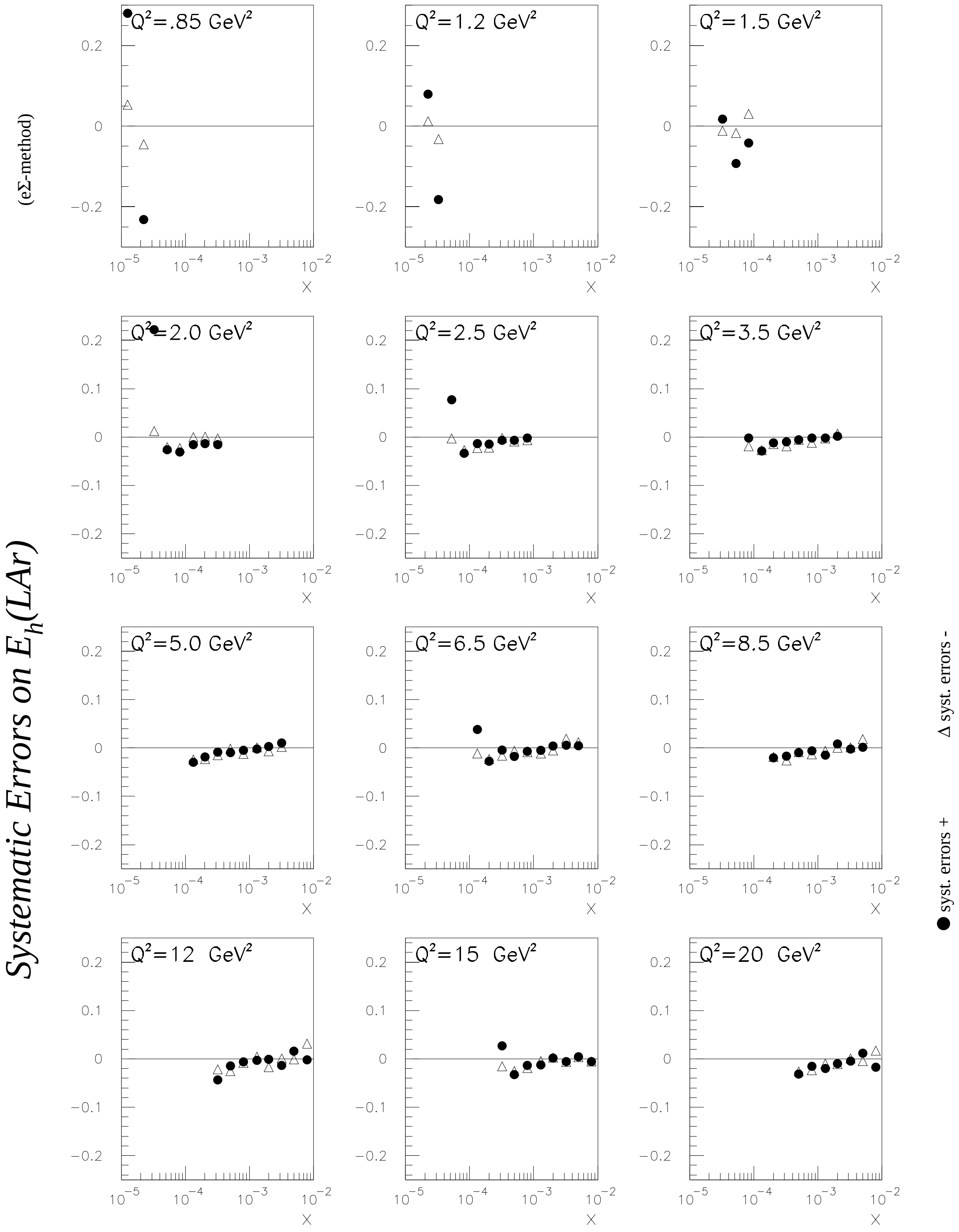

Figure 5.7: *Systematic errors as function of* $\log_{10}(x)$ *in the bins of* Q^2 *in* $e\Sigma$*- method due to final state hadron energy measurements in LAr calorimeter.*

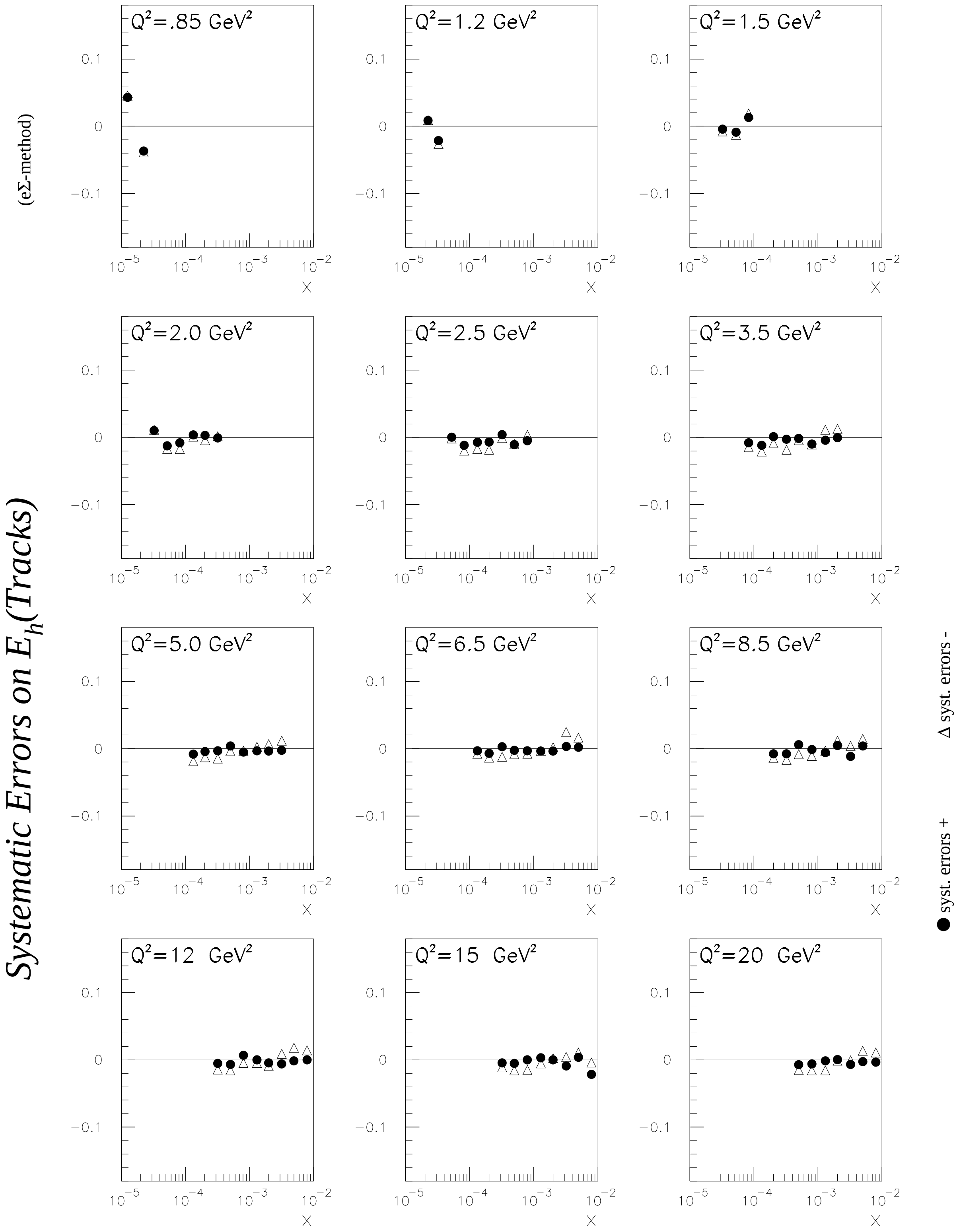

Figure 5.8: *Systematic errors as function of* $\log_{10}(x)$ *in the bins of* Q^2 *in* $e\Sigma$*- method due to errors on final state hadron energy measurements from trackers.*

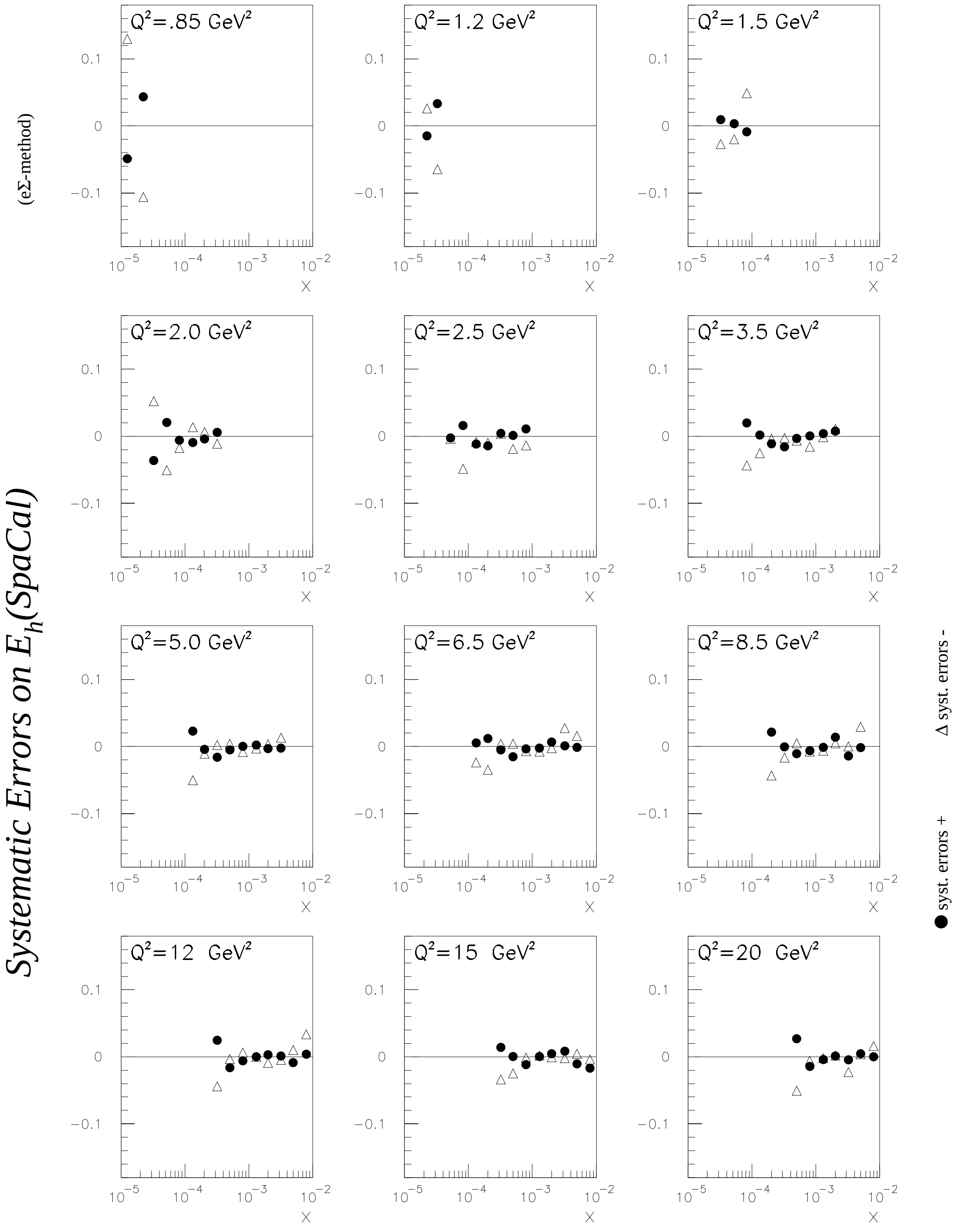

Figure 5.9: *Systematic errors as function of* $\log_{10}(x)$ *in the bins of* Q^2 *in* $e\Sigma$*- method due to errors on final state hadron energy measurements from SpaCal.*

The Vertex Reconstruction Efficiency

The vertex reconstruction efficiency causes about 5% systematic errors in F_2 at low y. Bins where the vertex efficiency differs by more than 5% are excluded from the measurement.

The BDC Efficiency

The electron track finding efficiency of the BDC is 2% [2].

The Radiative Corrections

The uncertainty for the radiative correction is determined by comparing the radiative corrections computed from the DJANGO program [3], δ_{DJG}, where events with and without taking into account the radiative processes are generated in all bins, and analytical calculations, which can be done using the HECTOR program [4], δ_{Hec}. The result obtained [5] using the same structure function as for the F_2 extraction is shown in figure 5.10. An uncertainty of 2% for the radiative corrections is taken for all bins.

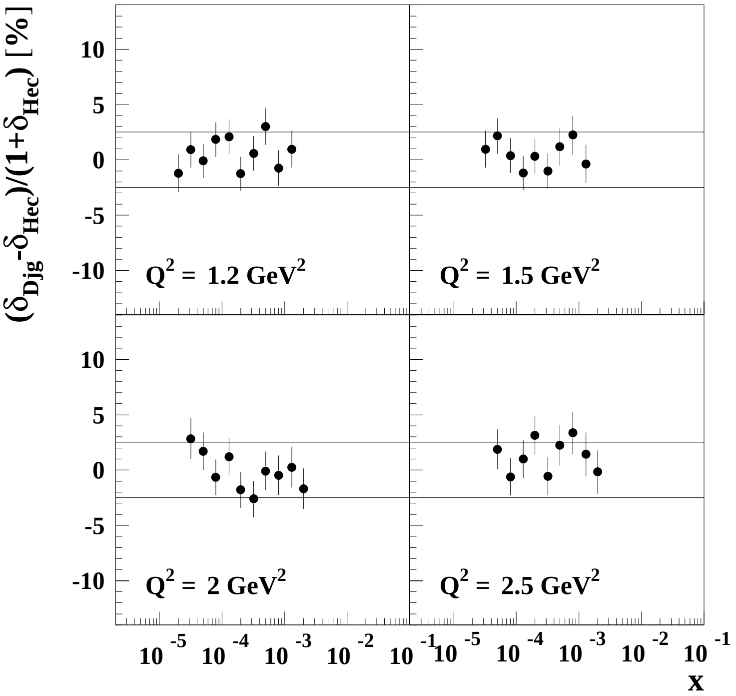

Figure 5.10: *Difference in radiative corrections as determined from the DJANGO program and the HECTOR program in four bins of* Q^2.

5.5 Results

We present the structure function F_2 as a function of x ($2.10^{-5} < x < 10^{-2}$) in different bins of Q^2 from 0.85 GeV^2 to 20 GeV^2. Figure 5.11 compares the results from e- and Σ- methods. The e-method is limited to the small x-values (see section 5.4) whereas Σ-method covers the entire x-region according to the purity and stability criterias discussed previously. The Σ-method which relies on the hadronic final state measurements as well as on the scattered electron 4-momentum is consistent with the electron method in the intermediate bins of x. This indicates that the calibration as well as the radiative corrections are well understood.

The results using the $e\Sigma$-method is shown in figure 5.12 and table 5.3 is giving the values of F_2, the erros and the used value of R.

The obtained results from this method, thus covers the entire kinematic range. The general behaviour of F_2 shows an increase as x decreases. This increase towards low x is smaller at small Q^2 whereas it becomes stronger as Q^2 increases. At the low y, the bad vertex efficiency limits the F_2 measurement, where at high y the increasing amount of photoproduction background imposes a limit on the energy of the electron, and therefore on the kinematic region. The inner error bars show the statistical error and outer error bars the total errors which are obtained by adding statistical errors and systematic errors quadratically. The high error in the highest y-points in each bin of Q^2 is partly due to the contribution from photoproduction, but also from the error on the electron energy measurement.

The result is compared to three parameterizations: The dotted line is showing H1-NLO-QCD fit to the 1994 data, which is set to a constant value for the small x-values where the fit is not validated [10]. The Badelek-Kwiecinski inspired NLO-QCD fit including H1 measurement of the 1995 shifted vertex data [8] is denoted by the solid line which is also used as an input parametrization for our F_2 measurement. The dashed line is showing the latest ALLM-parametrization [11], includes H1 and ZEUS data at low Q^2. The differences within these parametrizations are rather small, and they are in good agreement with the presented measurement.

5.5.1 Comparison with Previous H1 Measurements

During the 1994 [10] and the 1995 [8] running period, data was taken with a special beam setting in which the z-vertex position was shifted by $+70cm$. This enabled the experiments to cover the very low Q^2 between 1.5 GeV^2 and 6.5 GeV^2 and down to x values of (down to 6.10^{-5}) in 1994 and between Q^2 of 0.35 GeV^2 to 3.5 GeV^2 in 1995 after the upgrade of the backward region of the detector. Besides on the 1994 data a special analysis was performed on events with initial state radiation, where the effective initial electron energy is lower than the nominal beam energy, allowing therefore to reach low Q^2 values but at higher x compared to the shifted vertex data. The kinematic reach of the nominal vertex data taken with the BEMC was at $Q^2 = 12\ GeV^2$, although a special run with a special trigger setup, allowed to take data with the inner triangles of the BEMC and pushed this limit down to $Q^2 = 8.5\ GeV^2$.

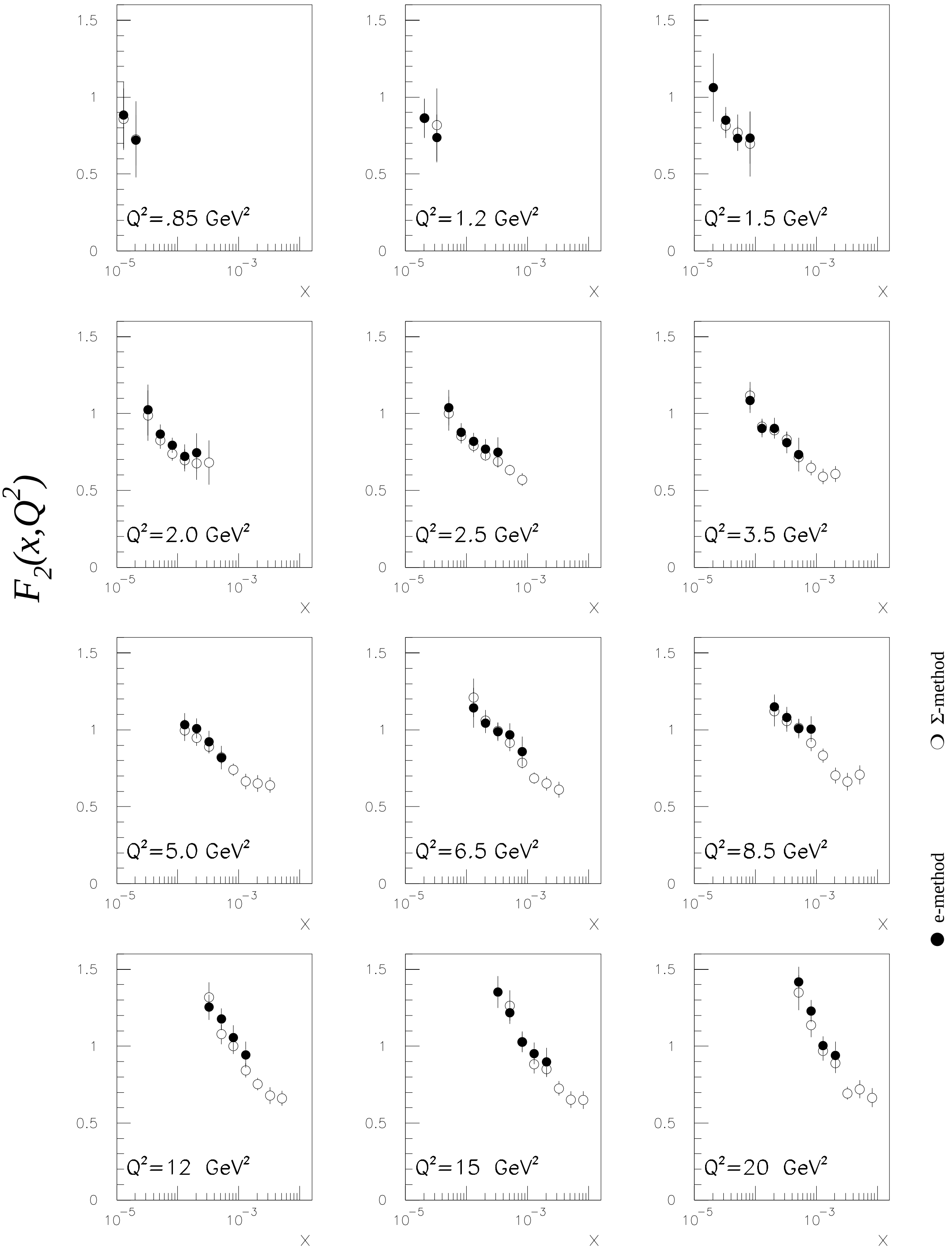

Figure 5.11: *F_2-1995 e- and Σ- method for nominal vertex. The error bars are showing the total error. The agreement between these two methods indicates that the calibration of the detector is under control.*

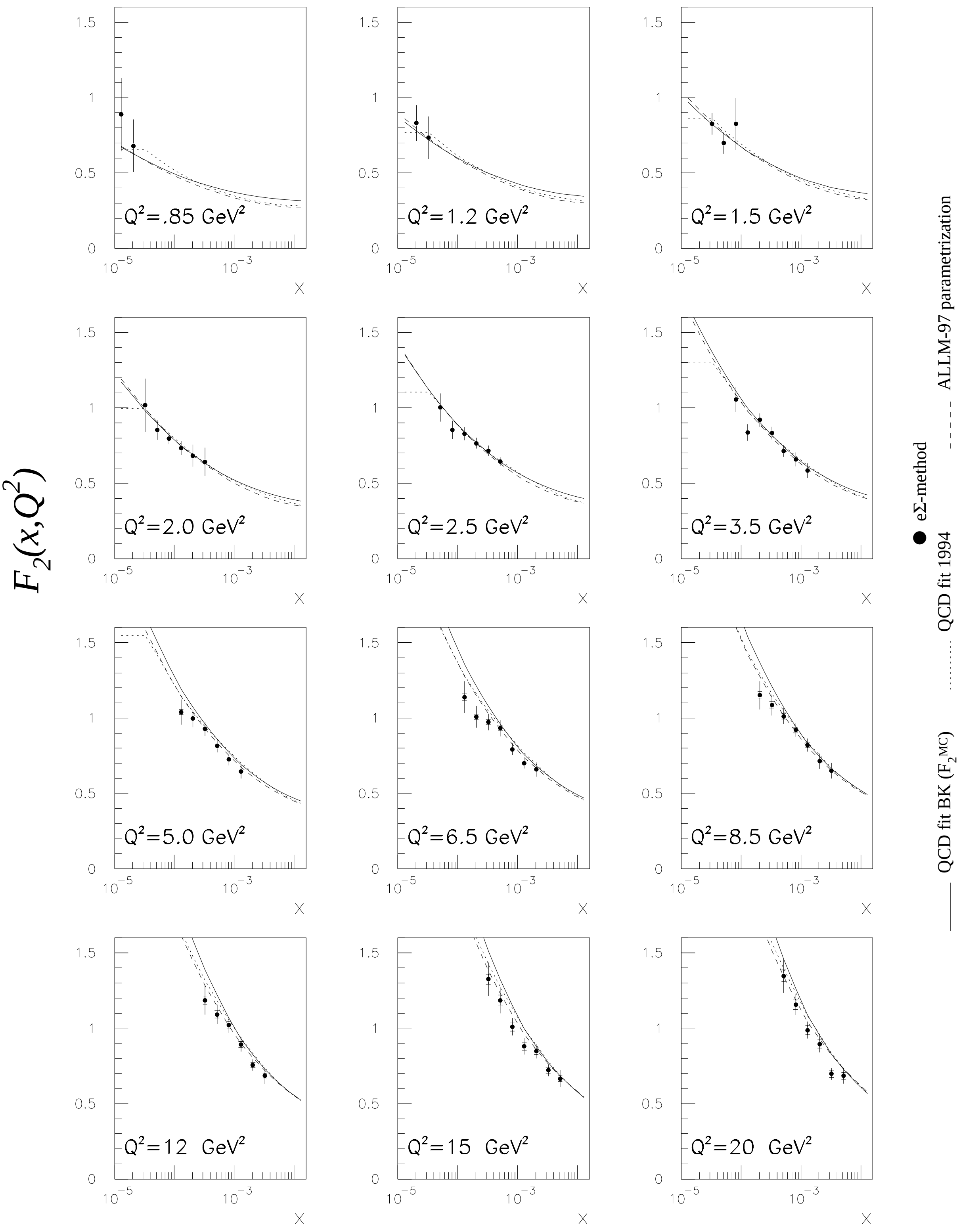

Figure 5.12: *F_2-1995 eΣ- method from nominal vertex data. The error bars are showing the total error. The measured points are compared to the QCD fit on the 1994 data, the QCD fit using the Badelek-Kwichinski approach to the 1995 shifted vertex data and the most recent ALLM parametrization.*

In figure 5.13, we compare our result (closed circles) with the shifted vertex results from 1995 results (open triangles) and with the 1994 results (open squares) above $Q^2 = 1.5\ GeV^2$. In the overlapping region, the agreement of the three measurements are good, although the new F_2 values are slightly below those of 1994 in the high Q^2 bins ($Q^2 = 12 - 15\ GeV^2$). The uncertainty in our measurement is reduced by about 20% in the low Q^2 region compared to the 1994 measurement mainly as a result of using the new detectors, SpaCal and BDC, in the backward direction (compared to the 94-data which used BEMC and BPC) and due to the increase of the total integrated luminosity by a factor of 10 with respect to the 1994 shifted vertex run.

5.5.2 Comparison with Results from Other Experiments

The ZEUS collaboration performed similar F_2 measurements at low Q^2 than H1, namely with the data taken in 1994 [12, 13], where the nominal and shifted vertex data as well as the initial state radiation events were analyzed. With this data, Q^2 values down to 2.5 GeV^2 were reached at $x = 4 \cdot 10^{-5}$. In 1995 a small sampling calorimeter (BPC - Beampipe Calorimeter) was installed in the very backward region of the ZEUS detector. With this additional device the transition region between photoproduction and Deep-Inelastic Scattering was explored reaching Q^2 values from 0.11 GeV^2 to 0.65 GeV^2 at x between $2 \cdot 10^{-6}$ and $2 \cdot 10^{-5}$ [14], which are lying below the kinematic region of the presented measurement. In figure 5.14 the ZEUS-1994 results are compared to our measurement and both are in good agreement even in the high Q^2 region between 12 GeV^2 and 20 GeV^2.

Besides the HERA experiment numerous fixed target experiments have previously measured the F_2 structure function. With a lower center of mass energy than HERA, these experiments are measuring equally in the low Q^2 region, but at higher x values. Shown on figure 5.14 are the SLAC proton and deuteron measurements , which are covering at large x-values and small Q^2 values ($Q^2 \leq 6.5\ GeV^2$), the BCDMS proton and deuteron measurements [15] the large x ($x \geq 0.1$) and larger $Q^2 (\geq 8.5\ GeV^2)$ and the E665 measurements [16] in the medium x region($x \sim 0.01$). Although the kinematic region of these measurement is not overlapping with the HERA measurements in this Q^2 region, a smooth extrapolation of F_2 from these measurements to the HERA measurements is achieved. This can be seen by the good accommodation that the ALLM parametrization is giving for all the data points available. Shown is also the H1 QCD-fit from 1994, which is higher than the ALLM parametrization at $Q^2 > 5\ GeV^2$. We conclude that H1 results agree well with the ZEUS results and further we find a smooth continuation from the fixed target measurements towards the low x region at HERA.

5.6 Summary

We have presented a new F_2 measurement using the 1995 nominal vertex data, where for the first time the SpaCal calorimeter and the BDC drift chamber were used. As

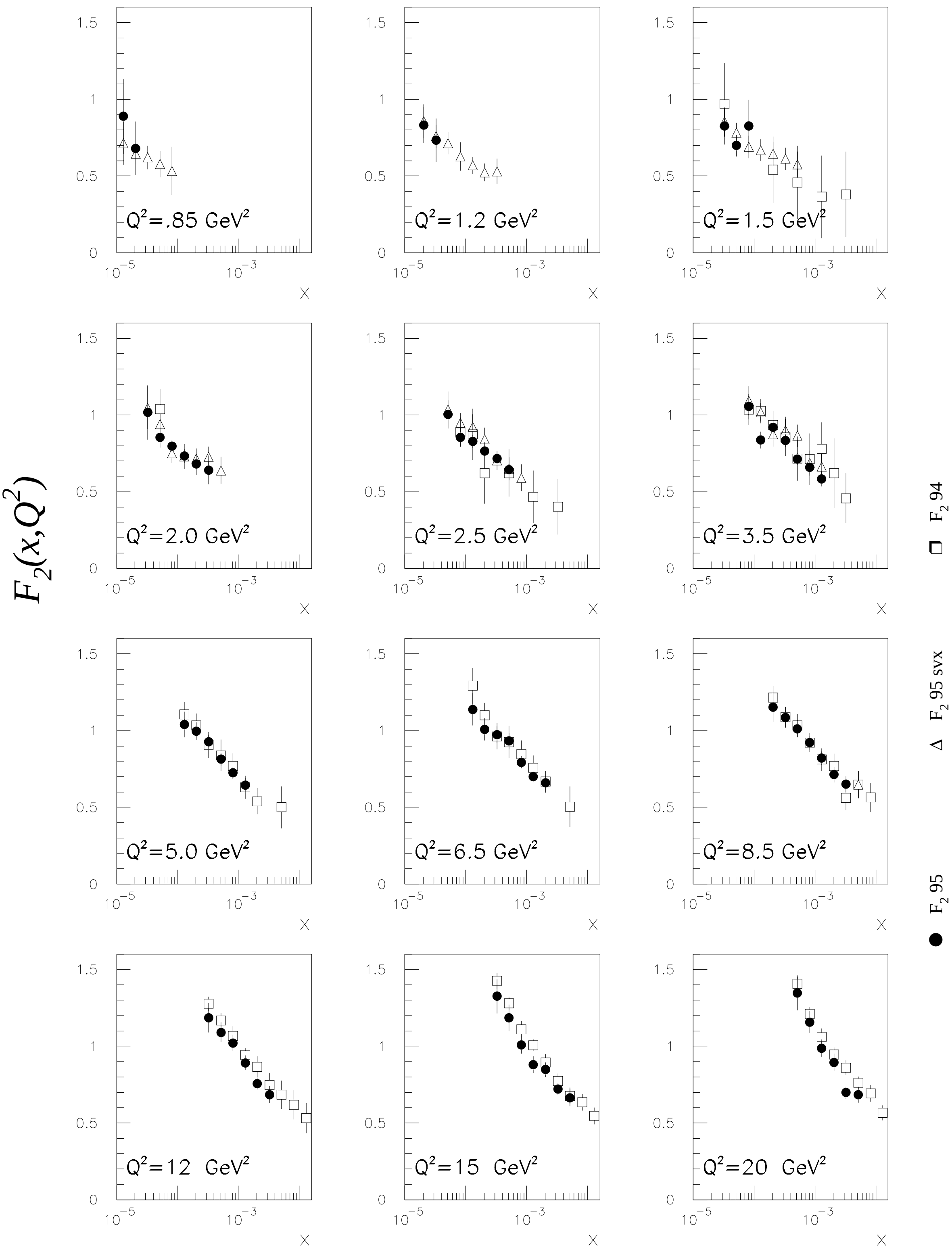

Figure 5.13: *Comparison of the new measurement with the 1994 measurement (open squares) using shifted vertex data, initial state radiation events and nominal vertex data and the 1995 shifted vertex data (open triangles). The error bars are showing the total errors.*

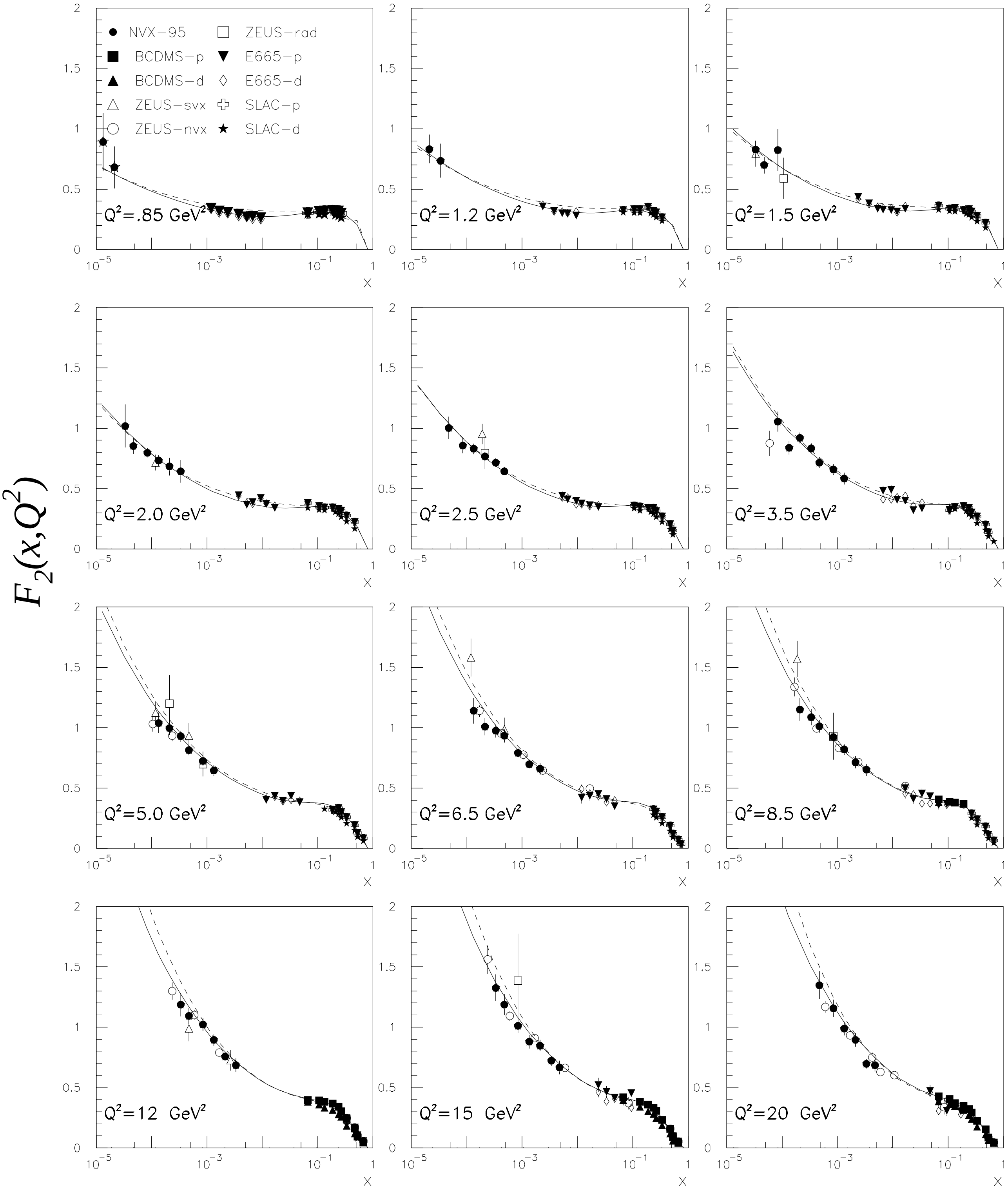

Figure 5.14: *Comparison with other experiments: The ZEUS measurements are in the same kinematic region and in good agreement with the presented results. The fixed measurement of the fixed target experiments lie a higher x values. All results are accommodated by the latest fit from the ALLM collaboration (full line) but at high Q^2 and low x below the fit using the Badelek-Kwichinski approach to the 1995 shifted vertex data (dashed line).*

a result, even with the data taken at nominal vertex, Q^2 values down to .85 GeV^2 and x down to $2 \cdot 10^{-5}$ have been reached. The measurement is presented in 12 bins of Q^2 and 14 bins in x, spanning from $Q^2 = .85\ GeV^2$ to $Q^2 = 20\ GeV^2$, and from $x = 2 \cdot 10^{-5}$ to $x = 0.013$. The result is compared to previous H1 and ZEUS measurements both from nominal and shifted vertex data, to which it is in good agreement. Compared to these results, smaller errors are reached, especially in the kinematic region which was formerly only covered by shifted vertex measurements.

The measurement is showing the characteristic rise of F_2 with decreasing x, even in the lowest Q^2 bins. The strength of rise of F_2 is increasing with increasing Q^2, which corresponds to the expected behaviour from perturbative QCD. The agreement with NLO-QCD fits has been shown and in particular with the latest ALLM parametrization. This agreement shows also the smooth transition between the measurements from fixed target experiments at low Q^2 and the HERA data.

Q^2 (GeV^2)	x	y	R	F_2^p	δ_{tot} (%)	δ_{sta} (%)	δ_{cor} (%)	δ_{cor}^E (%)	δ_{cor}^θ (%)	δ_{cor}^h (%)	δ_{unc} (%)	$\delta_{unc}^{\gamma P}$ (%)	$\delta_{unc}^{R_c}$ (%)	δ_{unc}^{MC} (%)	δ_{unc}^{misc} (%)
.85	.000013	.722	.193	.889	27.3	.3	26.1	19.0	11.420	10.2	8.0	9.2	2.0	3.4	7.0
.85	.000020	.469	.187	.681	25.5	.0	24.8	5.8	22.200	8.6	5.9	3.7	2.0	3.2	4.6
1.20	.000020	.663	.233	.831	14.2	.8	12.4	9.0	3.750	2.2	6.8	7.3	2.0	1.7	6.3
1.20	.000032	.414	.225	.734	19.2	1.5	18.4	4.2	16.880	5.7	5.2	1.7	2.0	2.3	4.2
1.50	.000032	.518	.253	.826	8.7	.9	6.7	4.1	.435	2.5	5.5	4.6	2.0	1.2	4.9
1.50	.000050	.331	.245	.699	10.0	1.0	8.9	3.0	8.175	1.7	4.4	.9	2.0	1.5	3.7
1.50	.000080	.207	.238	.728	23.6	.8	23.2	8.2	21.285	4.1	4.5	.2	2.0	2.5	3.1
2.00	.000032	.690	.288	1.017	17.5	1.3	15.9	10.0	1.325	5.1	7.2	11.2	2.0	1.9	6.6
2.00	.000050	.442	.278	.853	7.7	1.1	5.8	1.3	2.310	4.8	4.9	1.9	2.0	1.1	4.4
2.00	.000080	.276	.269	.748	5.0	.9	2.7	1.4	.435	2.3	4.1	.3	2.0	1.1	3.4
2.00	.000130	.170	.262	.691	6.7	.7	5.5	2.9	4.605	.2	3.9	.0	2.0	1.3	3.0
2.00	.000200	.110	.256	.657	11.0	.6	10.3	4.8	9.115	.7	3.8	.1	2.0	1.4	2.9
2.00	.000320	.069	.252	.628	14.9	.5	14.3	6.7	12.700	.1	3.8	.1	2.0	1.6	2.8
2.50	.000050	.552	.302	1.003	9.3	1.2	7.2	5.6	.840	.5	5.8	4.5	2.0	1.3	5.2
2.50	.000080	.345	.291	.829	7.4	1.3	5.8	1.9	1.945	5.0	4.4	1.0	2.0	1.1	3.8
2.50	.000130	.212	.282	.793	5.5	1.1	3.7	1.0	2.940	1.9	3.9	.5	2.0	1.1	3.2
2.50	.000200	.138	.275	.740	4.9	.9	3.0	1.4	2.160	1.6	3.7	.1	2.0	1.1	3.0
2.50	.000320	.086	.269	.700	4.9	.8	3.2	.5	3.080	.7	3.7	.0	2.0	1.1	2.9
2.50	.000500	.055	.264	.631	4.7	.8	3.0	1.0	2.460	1.3	3.6	.0	2.0	1.1	2.8
2.50	.000800	.035	.261	.572	7.1	.7	3.5	.6	3.360	.6	6.2	.0	2.0	1.1	5.7
3.50	.000080	.483	.319	1.036	7.9	1.3	5.8	1.9	2.070	4.4	5.2	2.5	2.0	1.2	4.7
3.50	.000130	.297	.307	.897	6.1	1.4	4.2	1.1	2.150	3.4	4.2	.7	2.0	1.2	3.5
3.50	.000200	.193	.297	.899	5.0	1.3	2.9	.8	2.150	1.8	3.9	.2	2.0	1.2	3.1
3.50	.000320	.121	.289	.818	5.0	1.3	3.1	.9	2.650	1.4	3.7	.0	2.0	1.2	2.9
3.50	.000500	.077	.282	.711	5.5	1.4	3.9	1.2	3.665	.6	3.7	.0	2.0	1.2	2.9
3.50	.000800	.048	.275	.646	7.1	1.3	3.3	.6	3.040	1.1	6.2	.0	2.0	1.2	5.7
3.50	.001300	.030	.270	.580	8.3	1.3	5.3	1.6	5.085	.1	6.2	.0	2.0	1.2	5.7
3.50	.002000	.019	.266	.605	8.3	1.3	5.3	2.0	4.805	1.2	6.2	.1	2.0	1.2	5.7
5.00	.000130	.425	.326	1.062	7.9	1.6	6.1	1.7	1.955	5.2	4.9	1.7	2.0	1.2	4.2
5.00	.000200	.276	.314	.982	5.8	1.5	3.8	1.5	2.180	2.5	4.1	.9	2.0	1.2	3.4
5.00	.000320	.173	.302	.911	5.0	1.5	2.8	.9	2.020	1.7	3.8	.1	2.0	1.2	3.0
5.00	.000500	.110	.292	.808	5.1	1.6	3.0	1.5	2.590	.1	3.7	.1	2.0	1.3	2.9
5.00	.000800	.069	.283	.716	5.5	1.6	3.7	1.5	3.210	1.0	3.7	.0	2.0	1.3	2.8
5.00	.001300	.042	.274	.635	7.3	1.7	3.5	1.3	3.150	.7	6.2	.0	2.0	1.3	5.7
5.00	.002000	.028	.267	.620	7.4	1.7	3.7	.9	3.565	.6	6.2	.0	2.0	1.3	5.7
5.00	.003200	.017	.260	.636	7.7	1.7	4.1	2.0	3.165	1.7	6.2	.0	2.0	1.4	5.7
6.50	.000130	.552	.335	1.173	8.8	1.7	6.5	3.2	1.625	2.2	5.8	4.9	2.0	1.5	5.2
6.50	.000200	.359	.322	1.022	7.1	1.8	5.2	.9	1.975	4.5	4.5	1.3	2.0	1.3	3.8
6.50	.000320	.224	.308	.969	5.7	1.7	3.6	1.4	2.660	2.0	4.0	.1	2.0	1.4	3.2
6.50	.000500	.144	.296	.934	5.8	1.7	4.0	2.3	3.115	.7	3.8	.2	2.0	1.4	3.0
6.50	.000800	.090	.285	.782	4.9	1.8	2.6	.8	2.090	1.2	3.8	.0	2.0	1.4	2.9
6.50	.001300	.055	.274	.696	4.9	1.9	2.5	1.2	1.975	.3	3.8	.8	2.0	1.4	2.8
6.50	.002000	.036	.264	.658	7.2	1.8	3.1	1.4	2.710	.4	6.3	.0	2.0	1.5	2.7
6.50	.003200	.022	.255	.613	8.4	2.0	5.2	2.7	3.690	2.5	6.3	.0	2.0	1.6	5.7
6.50	.005000	.014	.246	.690	8.0	2.0	4.5	2.0	3.230	2.4	6.3	.0	2.0	1.8	5.7
8.50	.000200	.469	.327	1.178	7.9	2.0	5.6	1.3	2.245	4.5	5.2	2.2	2.0	1.5	4.6
8.50	.000320	.293	.312	1.106	6.2	2.0	4.0	1.3	2.095	3.2	4.3	.4	2.0	1.5	3.5
8.50	.000500	.188	.298	1.011	5.2	1.8	2.7	1.4	1.920	1.3	4.0	.1	2.0	1.5	3.1
8.50	.000800	.117	.285	.909	5.0	2.0	2.5	1.3	1.835	1.1	3.9	.0	2.0	1.6	2.9
8.50	.001300	.072	.271	.810	5.3	2.0	3.2	1.5	2.740	.5	3.8	.0	2.0	1.6	2.8
8.50	.002000	.047	.260	.708	7.1	2.0	2.7	1.7	2.035	.5	6.3	.0	2.0	1.6	2.7
8.50	.003200	.029	.248	.646	8.0	2.2	4.3	2.5	2.920	1.9	6.3	.1	2.0	1.7	5.7
8.50	.005000	.019	.237	.697	9.2	2.2	6.2	3.6	3.780	3.4	6.4	.0	2.0	1.9	5.7
12.00	.000320	.414	.315	1.180	8.2	2.3	6.1	2.3	1.845	5.1	4.9	1.3	2.0	1.7	4.2
12.00	.000500	.265	.299	1.094	6.1	2.2	3.7	1.6	2.375	2.2	4.3	.5	2.0	1.7	3.4
12.00	.000800	.166	.283	1.012	5.3	2.2	2.7	1.9	1.820	.4	4.0	.0	2.0	1.7	3.0
12.00	.001300	.102	.268	.873	5.4	2.3	3.0	1.2	2.555	.9	3.9	.0	2.0	1.8	2.9
12.00	.002000	.066	.254	.752	5.0	2.4	1.9	.9	1.405	1.0	3.9	.0	2.0	1.8	2.8
12.00	.003200	.041	.239	.686	8.4	2.5	4.8	3.1	3.265	1.7	6.4	.0	2.0	1.9	2.7
12.00	.005000	.027	.225	.658	7.2	2.5	2.1	1.1	1.550	.8	6.4	.0	2.0	2.0	5.7
12.00	.008000	.017	.211	.731	9.3	2.6	6.2	3.8	2.470	4.2	6.5	.0	2.0	2.3	5.7
15.00	.000320	.518	.315	1.492	7.4	2.3	4.1	.8	1.775	3.4	5.7	1.2	2.0	2.1	4.9
15.00	.000500	.331	.299	1.162	7.5	2.8	5.1	2.4	2.430	3.8	4.6	.5	2.0	2.0	3.7
15.00	.000800	.207	.282	.974	5.9	2.8	3.0	1.7	1.945	1.6	4.2	.0	2.0	2.0	3.1
15.00	.001300	.127	.265	.854	6.4	3.0	4.0	2.8	2.605	1.1	4.1	.0	2.0	2.0	2.9
15.00	.002000	.083	.250	.825	5.8	2.7	3.1	2.0	2.130	.8	4.1	.0	2.0	2.1	2.9
15.00	.003200	.052	.234	.713	5.5	2.9	2.2	1.1	1.845	.4	4.1	.0	2.0	2.2	2.8
15.00	.005000	.033	.219	.655	8.4	2.9	4.5	3.1	3.060	1.2	6.5	.0	2.0	2.3	2.7
15.00	.008000	.021	.202	.634	8.2	3.2	3.8	2.5	1.730	2.3	6.6	.0	2.0	2.5	5.7
20.00	.000500	.442	.297	1.342	8.5	2.9	6.0	.8	.760	5.9	5.3	.5	2.0	2.3	4.4
20.00	.000800	.276	.280	1.104	6.4	3.0	3.4	1.6	1.510	2.5	4.5	.3	2.0	2.2	3.4
20.00	.001300	.170	.261	.966	5.9	3.0	2.7	2.1	1.260	1.2	4.3	.0	2.0	2.3	3.0
20.00	.002000	.110	.245	.891	6.4	3.1	3.7	2.8	2.385	.3	4.3	.0	2.0	2.4	2.9
20.00	.003200	.069	.228	.685	5.8	3.6	1.5	1.2	.870	.4	4.3	.0	2.0	2.5	2.8
20.00	.005000	.044	.211	.670	7.9	3.4	2.7	1.8	1.840	.9	6.6	.0	2.0	2.6	2.7
20.00	.008000	.028	.193	.649	9.5	3.7	5.6	3.7	2.710	3.2	6.7	.0	2.0	2.8	5.7

Table 5.3: *Proton structure fuction $F_2^p(x,Q^2)$ with total (δ_{tot}) error, statistical error (δ_{stat}), correlated (δ_{cor}) systematic error, and its contributions from a variation of the electron energy scale ($\delta_{cor}^{E^+}$), the polar electron angle($\delta_{cor}^{\theta^+}$), the hadronic energy scale ($\delta_{cor}^{h^+}$); uncorrelated (δ_{unc}) systematic error, and its contributions from the photoproduction background substraction ($\delta_{unc}^{\gamma p}$), the radiative correction ($\delta_{unc}^{R_c}$), the Monte Carlo statistical errors correction (δ_{unc}^{MC}) and the remaining miscellaneous contribution (δ_{unc}^{misc}).*

Bibliography

[1] B. G. Pineiro, **Ph.D. thesis**, Paris 1995.

[2] J. Katzy, **Ph.D. thesis**, Heidelberg 1997.

[3] G.A. Schuler, H. Spiesberger, **Proceedings of the Workshop 'Physics at HERA'**, eds. W. Buchmüller and G.Ingelman, vol3, DESY (1992) 1419.

[4] A. Arbuzov et al., **Comp. Phys. Commun.** 94 (1996) 128.

[5] F. Lehner, **Ph.D. thesis**, Hamburg (1998).

[6] H1 Collaboration, C. Adloff et al.,**Phys. Lett.** 393B (1997) 452.

[7] B. Badelek and J. Kwiecinski, **Phys. Lett.** B295(1992) 263.

[8] H1 Collaboration, C. Adloff et al.,**Nucl. Phys.** B497 (1997) 3.

[9] B. Badelek, J. Kwiecinski and A. Stasto, **DTP/96/16** (1996).

[10] H1 Collaboration, S. Aid et al., **Nucl.Phys.** B470 (1996) 3.

[11] H. Abramowicz, A. Levy **DESY-97-251** (1997).

[12] ZEUS Collaboration, M. Derrick et al., **Zeitschrift f. Physik** C69 (1996) 607.

[13] ZEUS Collaboration, M. Derrick et al., **Zeitschrift f. Physik** C72 (1996) 399.

[14] ZEUS Collaboration, M. Derrick et al., **Physics Letters** B 407 (1997) 432.

[15] BCDMS Collaboration, A.C. Benvenuti et al., **Phys. Lett.** B223 (1989) 485 and **Phys. Lett.** B237 (1990) 592.

[16] E665 Collaboration, M.R. Adams et al., **Phys. Rev.** D54 (1996) 3006.

Prospects

The installation of the new backward detector devices, the SpaCal and the BDC, was successfully completed in 1995 and the aims of extending the kinematic region and improving the systematic accuracy could be reached. However, due to the commissioning of these two subdetectors, an important part of the luminosity delivered by HERA could not be used for the analysis of low Q^2 DIS. In 1996, some trigger problems occurred in the inner SpaCal region, such that an important fiducial cuts had to be applied. A combination of the 1995 measurement in the low Q^2 domain as presented in this thesis, and the 1996 measurement at higher Q^2 was therefore presented as a preliminary result at the ICHEPS'97 at Jerusalem.

In 1997, the H1 experiment was further improved with the installation of the Backward Silicon Tracker (BST). This device allows for the full use of the SpaCal geometric acceptance, beyond the limits of the BDC and for an improved electron identification. The analysis of the data from this run is still ongoing, as important efforts had to be made in order to achieve a correct alignment of the different Silicon disks. With a ~ 10 times higher statistic and a very smooth running, where all detector devices were in fully operational conditions, a very high precision measurements, with errors on F_2 between $2-4\%$ is close to be reached.

After the year 2000, an upgrade program for HERA is ongoing, which will permit an increase of the accumulated luminosity per year from $30-40$ pb^{-1} to ~ 150 pb^{-1}. The emphasis will be put on the high Q^2 measurements and on exclusive processes, which are nowadays still limited in statistics, such that low Q^2 events will be downscaled to avoid saturation of the trigger rates. The aim for the structure function measurements will be to achieve an electron calibration at 0.5%, a θ measurement at 0.5 $mrad$ and an error on the hadronic energy scale of 2%. With such a precision the gluon density can be extracted with an uncertainty of about 1% at low x.

Finally, running at different beam energies would allow for the measurement of the longitudinal structure function and polarizing the electron and the proton beam would give the possibility to measure in yet unexplored kinematic regions the polarized structure functions of the proton.

Acknowledgments

First of all I would like to thank Marcel Banner who accepted me to work at the "Laboratoire de Physique Nucléaire et de Hautes Energies (LPNHE)".

I thank all the members of H1 group of the laboratory with whom I shared useful discussions. I also thank Etienne Barrelet who introduced me the group H1 of LPNHE and later-on for his encouragement during my thesis.

The Physics working group ELAN of H1 was instrumental in providing me very useful discussions over data analysis.

It will be injustice not to mention the contributions of Gregorio Bernardi for the completion of this work. It was his guidance and experience, especially at the start of my thesis, that motivated me to start this research with great interest.

I am thankful to all the members of the jury: Marcel Banner, Marie-Claude Cousinou, Claude Guyot, Michel Jaffre et Francois Vannucci for accepting this task and also for their contributions. I specially thank Claude Guyot and Michel Jaffre for accepting to be the reporters of my thesis and for their useful comments.

In the end I would like to present special thanks and regards to the director of my thesis Ursula Bassler. Without her support and interest I would have never been able to complete this work. Her patience, during this work, is worth mentioning.